UNIVERSITY OF PAVIA

DEPARTMENT OF ELECTRICAL, COMPUTER AND BIOMEDICAL ENGINEERING

Ph.D. School in Electronics, Computer Science and Electrical Engineering

Ground stations evolution for next generation data links at microwave frequencies for Earth observation and space missions

Doctoral Dissertation of:

MATTEO MARCHETTI

Supervisor:

Prof. Marco Pasian

Academic cycle XXXIV

2018/2021

Sommario

La presente Tesi, sviluppata in collaborazione con l'Agenzia Spaziale Europea (ESA, Darmstadt, Germania), è incentrata sullo studio dei principali aspetti critici legati all'implementazione e all'utilizzo di nuove bande di frequenza nelle stazioni di terra appartenenti dell'ESA dislocate in vari punti del pianeta. Queste frequenze, comprese tra 22 e 27 GHz, nella cosiddetta banda K, verranno utilizzate nel prossimo futuro per stabilire collegamenti radio ad alta velocità. Grazie al loro utilizzo sarà possibile garantire un nuovo canale di comunicazione in grado di fornire l'adeguata velocità di trasmissione necessaria per trasmettere verso la Terra la sempre crescente mole di dati raccolti dalle future missioni spaziali, in maniera rapida ed efficiente. Queste missioni includono principalmente i satelliti per l'osservazione della Terra (i.e. MetOP-SG, METeorological OPerations - Second Generation), le sonde inviate in vari punti del sistema solare (i.e. Euclid) o persino missioni lunari con equipaggio. In particolare, la Tesi descrive il lavoro svolto per due diversi progetti: il progetto SNOWBEAR e un altro relativo alle antenne Deep Space (DSA), facenti parte della rete ESTRACK di ESA.

SNOWBEAR (Svalbard grouNd Station for Wide Band Earth Observation Data Reception) è stato uno studio finanziato dalla missione MetOp-SG nell'ambito del programma di osservazione della Terra di ESA. Lo scopo principale di SNOWBEAR era quello di valutare le prestazioni, in ricezione, di un collegamento radio ad alta velocità implementato sfruttando la banda di frequenze a microonde attorno ai 26 GHz. Questo collegamento radio di nuova generazione verrà infatti utilizzato per la trasmissione di dati dal satellite verso una stazione di terra installata alle isole Svalbard, quindi in un ambiente polare, per massimizzare il numero di orbite visibili. Allo stato dell'arte nell'ambito dei satelliti per l'osservazione della Terra nessun collegamento per il download dei dati raccolti utilizza queste frequenze (il collegamento del satellite JPSS-1 è in banda K ma non sono reperibili pubblicazioni in merito).

Nello specifico, si è voluto principalmente comprendere l'impatto degli agenti atmosferici sulle prestazioni del collegamento in ricezione, con particolare enfasi sull'attenuazione indotta dalla pioggia e dall'accumulo di neve sul radome. Inoltre, SNOWBEAR ha permesso anche di espandere il know-how nella costruzione, integrazione e validazione di stazioni di terra in grado di tracciare satelliti veloci durante tutte le loro orbite giornaliere. In particolar modo è stato possibile testare il funzionamento di vari sottosistemi che compongono la stazione e che sono stati studiati negli ultimi anni dall'ESA, come per esempio l'antenna parabolica di 6.4 metri di diametro, capace di lavorare nelle bande S e K, il suo sistema di puntamento a 3 assi, il radome multistrato posto a copertura dell'antenna, gli amplificatori a basso rumore raffreddati criogenicamente, il sistema di tracciamento in banda S/K.

Al fine di ottenere questi risultati, ad una fase di integrazione, conclusasi a fine 2018, è

seguita una campagna di raccolta dati, della durata di 2 anni (dicembre 2018 - dicembre 2020), durante la quale sono stati registrati numerosi parametri di interesse durante il passaggio del satellite JPSS-1 della NASA sopra la stazione.

La Tesi segue i vari step che si sono susseguiti durante questo percorso di Dottorato. Successivamente ad una introduzione generale del progetto e delle strategie adottate dall'autore per raggiungere gli obiettivi prefissati, segue la descrizione del modello di bilancio di collegamento usato per stimare le performance del canale di trasmissione dati in ricezione.

La teoria generale di un bilancio di collegamento è stata dapprima studiata dall'autore e poi applicata a questo caso specifico per la creazione di un software capace di tenere conto di tutte le diverse parti che entrano in gioco nel caso reale, dalle specifiche del satellite passando per la stima alcuni parametri atmosferici fino alla stazione di terra e alle performance delle diverse catene di ricezione dati.

Questo modello software è stato continuamente migliorato durante la campagna di misure e utilizzato principalmente per stimare le performance del collegamento in ricezione che sono state poi confrontate con le misurazioni reali e tutti gli altri parametri, in particolare quelli atmosferici, per estrarre informazioni utili in caso di importante attenuazione del segnale e conseguente calo delle prestazioni.

Viene poi offerta anche una panoramica sulle modalità di acquisizione dei dati, presentati vari problemi relativi ad essa e come sono stati risolti per non alterare le successive analisi. Infine vengono esposte le statistiche generali sui dati raccolti, sia di carattere operativo (i.e. pass acquisiti correttamente o persi e per quale motivo) che riguardanti attenuazione e rapporto segnale/rumore, divisi per fasce di elevazioni o periodo temporale. Nelle conclusioni vengono infine discussi i principali risultati ottenuti, in particolare riguardanti l'impatto che la neve accumulata sul radome ha sulle prestazioni generali del sistema e alcune considerazioni, sia lato progettazione della stazione sia lato procedure operative atte a massimizzarne l'efficienza nell'acquisizione dei dati. Queste considerazioni potranno eventualmente essere tenute in conto dall'agenzia o da chiunque voglia realizzare questo tipo di stazione di terra in modo da progettarla al meglio avendo questo studio già affrontato una serie di possibili problemi e soluzioni.

Il secondo progetto affrontato dall'autore in questa Tesi ha riguardato uno studio di fattibilità atto a valutare come espandere la capacità delle DSA, aggiungendo delle nuove bande di frequenze e avendo allo stesso tempo il minimo impatto possibile sulle prestazioni di quelle attualmente installate ed operative. Attualmente, l'ESA gestisce una rete di tre antenne DSA, installate a New Norcia (DSA1), Cebreros (DSA2) e Malargue (DSA3), tutte dotate di un'ottica Beam Waveguide (BWG) che illumina un riflettore principale di 35 metri che possono operare nelle bande S, X, K e Ka. Ma, come per SNOWBEAR, data la sempre crescente necessità di elevate velocità di trasmissione dati e la nuova allocazione delle frequenze raccomandata dall'International Telecommunication Union, per le missioni future è necessario spostare sia il canale di telemetria e controllo (TTC) sia il canale dati, dalle bande S/X attualmente utilizzate alle nuove bande X/K. Pertanto, per garantire una comunicazione full-duplex nelle bande X/K in tutti e tre le DSA, è necessario ripensare il layout di ciascuna BWG per implementare le nuove bande dove mancano. Per fare ciò, è necessario usare delle superfici selettive in frequenza, note come specchi dicroici. Nel caso particolare delle DSA vengono impiegati solo specchi dicroici induttivi che garantiscono una risposta di tipo passa-alto, progettati come aperture periodiche in uno

schermo metallico. Questo è dovuto principalmente al fatto che queste antenne lavorano con potenze di trasmissione molto elevate e in ricezione necessitano di temperature di rumore estremamente basse, escludendo quindi l'uso di qualsiasi materiale dielettrico per la fabbricazione degli specchi.

Nella Tesi, viene inizialmente fatta una introduzione generale del progetto, descrivendo tutte le attuali configurazioni di ogni BWG, unitamente alle loro possibili nuove implementazioni, specificando quali siano state ritenute le migliori. Viene poi presentata un'indagine approfondita, fatta dall'autore, di vari specchi dicroici, ognuno con un diverso numero di strati, forma e dimensioni delle aperture oltre che tecniche di fabbricazione, in modo da valutarne la risposta in frequenza nelle bande di interesse e identificare il miglior compromesso tra prestazioni, facilità di realizzazione e costi. Per un'analisi preliminare, la loro risposta in termini di coefficienti di trasmissione, riflessione e cross-polarizzazione è stata ottimizzata per l'angolo di incidenza nominale di 30 gradi, sotto l'ipotesi di illuminazione con una singola onda piana (SPW, Single Plane Wave), permettendo di ottenere una panoramica generale delle prestazioni di ogni dicroico. Utilizzando un software commerciale apposito (GRASP) basato sul metodo dell'ottica fisica (PO) sono state poi simulate le performance delle antenne nei vari casi in termini di diagrammi di radiazione, G/T, lobi laterali e cross-polarizzazione, per avere un'idea di quale configurazione si presenti come l'opzione migliore. Da questa fase preliminare sono stati selezionati come migliori due modelli di specchi e una configurazione per ciascuna antenna. L'ipotesi di singola onda piana considerata nella fase preliminare non è del tutto adeguata per un sistema operante con un fascio focalizzato e/o quando la legge di illuminazione non è ideale come nelle BWG. In questo caso, è importante prendere conto dell'illuminazione effettiva generata dal feed, sfruttando un approccio a più onde piane (MPW, Multiple Plane Wave), che calcola quindi la risposta dello specchio a diversi angoli di incidenza, in base al diagramma di radiazione del feed che ne illumina la superficie. Quindi, questo metodo è stato sfruttato per studiare e ottimizzare la risposta angolare degli specchi selezionati, tenendo conto anche degli specifici vincoli meccanici e di produzione, come il raggio minimo dello strumento usato per l'eventuale fabbricazione e lo spessore minimo delle pareti metalliche tra le aperture. Successivamente all'ottimizzazione di questi due specchi è stato ottimizzato anche il layout ottico delle BWG, definendo la posizione ottimale dei feed e degli specchi, per ridurre al minimo l'errore angolare fra la direzione di puntamento dell'antenna e quella del fascio principale e massimizzare le prestazioni finali. In parallelo, sono stati realizzati due prototipi di questi due specchi e quindi è stata effettuata una campagna di misurazioni per valutarne le prestazioni e confermare la risposta in frequenza simulata. Nelle conclusioni vengono infine discussi i principali risultati ottenuti.

Summary

This thesis, developed in collaboration with the European Space Agency (ESA, Darmstadt, Germany), focuses on the study of main critical aspects related to the implementation and use of new frequency bands in ESA's ground stations, located in various parts of the planet. These frequencies, between 22 and 27 GHz, in the so-called K band, will be used in the near future to establish high-speed space-to-Earth (and vice versa) radio links. Thanks to them, it will be possible to guarantee a new communication channel able to provide an adequate data rate necessary to transmit, quickly and efficiently, toward Earth, the ever-increasing amount of data collected by future space missions. These missions mainly include Earth observation satellites (e.g. MetOP-SG, METeorological OPerations - Second Generation), probes sent through the solar system (e.g. Euclid) or even manned lunar missions. In particular, the Thesis describes the work carried out for two different projects: the SNOWBEAR project, and another one focused on the upgrade of Deep Space antennas (e.g. DSA), which are part of ESA's ESTRACK network.

SNOWBEAR (Svalbard grouNd Station for Wide Band Earth Observation Data Reception) was a study funded by the MetOp-SG mission, as part of ESA's Earth observation program. The main purpose of SNOWBEAR was to evaluate the reception performance of a high-speed radio link, exploiting microwave frequencies between 25.5 and 27 GHz, used for the payload data download from the satellite to a ground station installed in the Svalbard islands, in a polar environment.

At the state of the art, in the field of Earth Observation satellites, no data downlink channel is using these frequencies (the data channel of JPSS-1 satellite is in K band but no publications on the subject are available).

Specifically, one wants to study the impact of atmospheric phenomena, with particular emphasis on the attenuation induced by clouds, rain and snowfalls, on the performance of this receiving communication channel. Furthermore, it is also wanted to expand the know-how in the construction, integration and validation of ground stations capable of tracking fast satellites during all their daily orbits; or even test the operation of various subsystems that make up the station and which have been studied in recent years by ESA, such as the 6.4 meter diameter parabolic antenna, capable of working in S and K bands, its 3-axis pointing system, the multilayer radome which is mandatory to protect the antenna from the harsh environment, the cryogenically cooled low-noise amplifiers, S/K band tracking system etc... In order to obtain these results, an integration phase, ended in 2018, was followed by a data collection campaign, lasted for 2 years (December 2018 - December 2020), during which numerous parameters of interest were recorded meanwhile NASA's JPSS-1 satellite passes over the station.

In this thesis, after a general introduction of the project and on the strategies adopted to

achieve the objectives, is described all the different parts that come into play in the link budget model, from the satellite, through the estimation of propagation loss, up to the ground station with its different receiving chains. This model was implemented to estimate the receiving performance of the link which were then compared with real measurements and all other parameters, in particular atmospheric ones, to extract useful information in case of important signal attenuation and consequent performance deterioration. An overview of the data acquisition method and its problems is also offered, along with counter measurements taken in order not to alter the subsequent analyses. Then, general statistics on the data collected are shown, both from operational point of view (i.e. passes acquired correctly or lost and for what reason) and concerning attenuation or signal-to-noise ratio, divided by elevation range or time period. Finally, the conclusions discuss main results obtained, in particular regarding the impact that snow accumulated on the radome has on the general performance of the link, and some considerations concerning the ground station system design and some operating procedures aimed at maximizing the station efficiency. These considerations may eventually be taken into account by the agency or by anyone who wants to build this type of ground station in order to design it in the best possible way, having already dealt with a series of possible problems and solutions.

The second project addressed in this thesis is a feasibility study aimed at evaluating how to expand the capacity of DSAs, adding new frequency bands while having the least possible impact on the performance of those currently installed and operational. Indeed, at present ESA operates a network of three DSA antennas, installed in New Norcia (DSA1), Cebreros (DSA2) and Malargue (DSA3), all equipped with Beam Waveguide (BWG) optic that illuminate a 35 meter main reflector, and which can operate in the S, X, K and Ka bands. But, as for SNOWBEAR, given the ever-increasing need for high data rates and the new frequency allocation recommended by the International Telecommunication Union, for future missions it is necessary to move both the Telemetry, Tracking and control (TTC) channel and the data one, from the S/X bands currently used to the new X/K bands. Therefore, to ensure full-duplex communication in the X/K bands in all three DSAs, it is necessary to rethink the layout of each BWG to implement the new bands where they are missing. To do this, it is necessary to use frequency selective surfaces, known as dichroic mirrors. In the particular case of DSAs, only inductive dichroic mirrors are used which guarantee a high-pass response, designed as periodic openings in a metal screen. This is mainly due to the fact that these antennas work with very high transmission powers and in reception they require extremely low noise temperatures, thus excluding the use of any dielectric material.

In the Thesis, a general introduction of the project is initially made, describing all the current configurations of each BWG, together with their possible new implementations, specifying which ones were considered the best. An in-depth investigation of various dichroic mirrors is then presented, each with a different number of layers, shape and size of the apertures, as well as manufacturing techniques, in order to evaluate the frequency response in the bands of interest and identify the best compromise between performance, ease of implementation and costs. For a preliminary analysis, the author studied their response in terms of transmission, reflection and cross-polarization coefficients has been optimized for the nominal angle of incidence equal to 30 degrees, under the hypothesis of illumination with a single plane wave (SPW), allowing to obtain a general overview of each dichroic performance. Using a specific commercial software (GRASP) based on the physical optics (PO) method, the antenna performance in the various

cases was then simulated in terms of radiation patterns, G/T, side lobes and cross-polarization, to have an idea of which configuration is the best option. From this preliminary stage, two mirror models and one configuration for each antenna were selected. The hypothesis of a single plane wave considered in the preliminary phase is not entirely adequate for a system operating with a focused beam and/or when the illumination law is not ideal as in the BWG. In this case, it is important to take into account the actual illumination generated by the feed, using a Multiple Plane Wave (MPW) approach, which then calculates the mirror response at different angles of incidence. Therefore, this method was exploited to study and optimize the angular response of the selected mirrors, also taking into account the specific mechanical and production constraints, such as the minimum radius of the instrument used for the eventual fabrication and the minimum thickness of the metal walls between the openings. After the mirror optimization, the optical layout of the BWGs was also optimized, defining the optimal position of the feeds and dichroic to minimize the angular error between the pointing direction of the antenna and main beam to maximize final performance. In parallel, two prototypes of these two mirrors were made and then a measurement campaign was carried out to evaluate their performance and confirm the simulated frequency response. Main results obtained are discussed in the conclusions.

Contents

List of Figures

List of Tables

Acronyms

ACU	Antenna Control Unit
AOS	Acquisition Of Signal
AZ	Azimuth
BI-RME	Boundary Integral-Resonant Mode Expansion
BWG	Beam Waveguide
DC	Down Converter
DSA	Deep Space Antenna
DUT	Device Under Test
EESS	Earth Exploration-Satellite Service
EIRP	Effective Isotropic Radiated Power
EL	Elevation
ENR	Excess Noise Ratio
EO	Earth Observation
ESA	European Space Agency
ESTEC	European Space Research and Technology Centre
EUMETSAT	European Organisation for the Exploitation of Meteorological Satellites
FDS	Cross-elevation
FEP	Front End Processor
FER	Frame Error Rate
FSS	Frequency Selective Surfaces
FTP	File transfer Protocol
GO	Geometrical optics
HDR	High Datarate Receiver
HRDFEP	High Rate Demodulator Front-End Processor
ITU	International Telecommunication Union
JPSS	Joint Polar Satellite System

KSAT	Kongsberg Satellite Services
LEOP	Low Earth Orbit Phase
LEO	Low Earth orbit
LHCP	Left Hand Circular Polarisation
LNA	Low Noise Amplifier
M&C	Monitoring and Control
MetOP-SG	Meteorological Operational-Second Generation
MoM	Method of Moments
MPW	Multiple Plane Wave
NASA	National Aeronautics and Space Administration
ND	Noise Diode
NOAA	National Oceanic and Atmospheric Administration
NPI	Network/Partnering Initiative
NT	Noise Temperature
OMT	Orto Mode Transducer
POM	Power Meter
PO	Physical Optics
RHCP	Right Hand Circular Polarisation
RX	Receiving
SCU	Station Control Unit
SMD	Stored Mission Data
SNOWBEAR	Svalbard Ground Station for Wide Band Earth Observation Data Reception
SOS	Space Operations relay
SPW	Single Plane Wave
SRS	Space Research
SvalSat	Svalbard Satellite Station Facility
TE	Transverse Electrical
TKRX	Tracking Receiver
TLE	Two Line Element
TM	Transverse Magnetic
TTC	Telemetry Tracking and Control
TX	Transmitting
VNA	Vector Network Analyzer
WTS	Weather Station
XEL	Cross-elevation
XPD	Cross-polar Discrimination

Chapter 1

Introduction

Since immemorial time, mankind has always looked up to the night sky. According to recent discoveries, prehistoric populations up to 40000 years ago had a sophisticated knowledge of constellations. It is assumed that some ancient cave paintings are, in addition to classic hunting scenes and daily life, also symbols of animals representing stars constellations. They also appear to have used stars as a primitive calendar, keeping track of time by watching how their position changed over time.

Throughout history of civilization, from Babylonians, Greeks, ancient Americans societies until modern people, as humanity evolved developing new technologies and deepening its knowledge in arts and science, the Universe and even Earth itself have been unceasing sources of fascination, mystery and fundamental questions.

Where do we come from? What came before the Big Bang? How big is the Universe? Are there other habitable planets out there? What are dark matter and dark energy? How Earth's nature forces acts and how their interconnection sustain life? Where will a hurricane make landfall? What is the status of vegetated areas? What will the weather be like in the next days?

Despite some of these questions are likely to remain unanswered, while others will still require years of study and research, many have been answered, thanks primarily to the significant evolution of space science that took place in the last century.

As a matter of fact, space science and exploration are living a great era, from Sputnik, the world's first artificial satellite ever launched to the first human step on the moon and roving on Mars, not forgetting other missions like Cassini-Huygens, Hubble, Rosetta and planned new ones such as the James Webb Space Telescope, Euclid, Artemis and many others.

In addition to all those space missions aimed to investigate some of the fundamental aspects in the Universe nature, galaxies or our solar system by sending probes into interplanetary space, a lot of missions take also place very close to us, in Earth orbits. Over a thousand satellites are circling our planet providing pictures and information with greater precision than ever before. Indeed, in many cases, to gather information about all Earth's environments, such as land, sea and atmosphere, there is no better alternative to the constant global monitoring offered by Earth Observation (EO) satellites. They give governments, society and the private sector a unique perspective on our world, helping to take informed decisions to face all humanity today's challenges, forging new scientific discoveries and pioneering new services, stimulating

an industrial and economic growth.

It is easy to understand how all these missions, whether they aim to study aspects related to deep space or observe phenomena on Earth, are an immense source of data streams. Obviously, before any kind of processing and use, or even be saved in a dedicated database, they must be transmitted toward the ground in the most reliable way. Moreover, each mission is unique and extremely complex, even a small error can compromise the result. To achieve all their several exploration, science or technology milestones is thus extremely important to develop and deploy a reliable Telemetry, Tracking & Control (TTC) and high data rate communication services in order to collect all the precious collected payload data. A continuously support from ground stations, since the early stage of the launch until mission ending is also necessary and, to do so, ground stations are generally located all around the globe, in the best possible position, according to the type of mission, maximising the reciprocal visibility time.

The two broadest application families tackled by the projects described in this Thesis are Space Research (SRS) and Earth Exploration-Satellite Service (EESS). SRS includes all near-Earth and deep-space satellites, equipped with active or passive sensors and focused on research of outer space. EESS instead includes mostly EO satellites in polar orbits supporting of a very large range of applications. Just for completeness, other families are Satellite data relay (e.g. European Data Relay Satellite, EDRS), radionavigation (e.g. Galileo) and general Space Operations (SOS).

Up to now, missions have widely used S, X and Ka frequency bands for their TTC and payload data transmissions. For S and X bands in particular, atmospheric impairments are almost negligible and ITU models provide well-established information, which are used for link budget and availability calculations. Moreover a state of the art RF technology is also well proven and standardised.

Generally, S-band (2.025-2.3 GHz) is used mainly for TTC channel because of its limited data rate requirement; X-band (7.145-8.5 MHz) is used for both TTC and payload data downlink in SRS missions while only for data in EESS ones; Ka-band (31.8-34.7 GHz) is finally used only in SRS applications for both TTC and data channels for deep space missions requiring large data uplink and/or downlink capability.

Over the years, an ever-increasing demand of scientific data has pushed S and X bands to their limit. Nowadays, those bands are highly congested and they are no more able to completely satisfy the need of high downlink capacity. Indeed, incoming planned EO missions and beyond would require a communication channel with a significantly larger capacity than the ones normally used nowadays. Hence, the use of a higher and broader frequency band, identified in the so called K band (22.55-23.15 GHz uplink, 25.5-27 GHz downlink), has been scheduled and put forward to ensure next generation missions the necessary data rate. Notable examples are the Joint Polar Satellite System (JPSS) and MetOp-SG constellations[1], [2]. The former, developed by the National Aeronautics and Space Administration (NASA) for the National Oceanic and Atmospheric Administration (NOAA), had launched its first satellite, NOAA-20 (JPSS-1 before the launch and early orbit phase conclusion), in 2017. The latter, a collaboration between European Space Agency (ESA) and the European Organisation for the Exploitation of Meteorological Satellites (EUMETSAT) planned the launch of its first satellite in 2023.

This PhD. Thesis, written in collaboration with ESA through a NPI (Network/Partnering Initiative), is focused on two different topics: the SNOWBEAR project, described in Chapter 2,

and the ESA Deep Space Antennas (DSA) upgrade, described in Chapter 3. The evolution of ESA's ground stations to support future deep space and EO missions and the study of various aspects associated to the implementation of this new K-band is thus the common thread that link the projects in this work.

SNOWBEAR will be of outstanding importance for ESA and the whole space community in general because it will possibly shed some light into the effective operational impact of the weather on K-Band satellite links. The characterisation of atmospheric phenomena, in this band, and their impact on the ground station performance and operation is indeed the general goal of this project. Currently, due to the uncertainty of adopted models, huge margins are sometimes taken into account in the link budget analysis, bringing various possible unnecessary effects such as increase of design and maintenance costs, over-complication, over-dimensioning of the antennas, over-sizing of the network capability, etc. For most of EO missions, ground stations located at polar latitudes are mandatory to guarantee a full coverage of all satellite passes. Therefore antennas are often protected by radomes because of the cold temperature and strong winds [3]. The effects of snow accumulated on the radome surface (or directly on the reflector surface, for those cases where radome is missing) have been investigated in the past [4]–[7], with some preliminary works at frequencies slightly above the Ku band [8], [9]. While at lower frequencies these effects are not as severe as they can be in K band, the migration toward higher frequencies triggered further investigations [10], [11]. In literature, while some effects have been discussed (e.g. attenuation, de-pointing), a comprehensive analysis comprising numerical and experimental results, as well as extensive campaigns on a real ground station tracking an operative satellite according to different tracking systems (either program track or autotrack [12]), was missing. In this framework, a real case study, consisting in a K-Band receiving terminal located at Svalbard was set up, and a measurement campaign to provide operational and link propagation statistics, fundamental for the optimal design of forthcoming missions and sizing of the future terminals, has been carried out.

In parallel, the future exploitation of new frequency bands requires modification of the present optical and RF systems of the ESA's Deep Space Antennas [13]–[17]. The second project described in this Thesis is thus a trade-off of different alternative feed systems in order to add these new frequency bands (e.g. 22.55-23.15 GHz up and 25.5-27 GHz down) in order to implement simultaneous, full-duplex, X and K bands channels in all three ESA's Deep Space Antennas (Cebreros, Malargüe and New Norcia), mainly for supporting future ESA (and possibly third parties) deep space and Moon missions [18], [19]. In particular, this work was focused on the design of new dichroic mirrors and the consequent re-analysis of each associated antenna optical layout to determine the best possible solution in terms of feasibility, maintainability and cost.

Chapter 2

SNOWBEAR project

EO satellites are generally intended to monitor the Earth along Polar orbits in order to be able to see every portion of the surface while Earth rotates underneath them. Therefore, the receiving ground station on Earth is naturally placed at Polar latitudes in order to maximise the number of visible passes and the payload data dumping time. This type of installations practically always require a radome to protect the antenna against the harsh Polar environment, most notably strong winds, low temperatures and snow.

In this framework, the SNOWBEAR project, led by a broad European Consortium, was launched. It was financed by the MetOP-SG mission, from ESTEC, within the ESA Earth Observation program while, from the industrial side, the main contractor of the project was KSAT (Kongsberg Satellite Services).

The general purpose of SNOWBEAR was to de risk the introduction of this new high data-rate downlink channel [20], [21], from 25.5 to 27 GHz, for EO missions payload data downlink. More in depth, it was wanted firstly to improve the know-how in building, integrate and validate a new ground station at Polar latitudes able to track a LEO satellite during all its daily orbits and download the payload data by means of the K-band frequencies. Secondly, to better understand the theory involved in the analysis of K band link budgets and in particular improve the models currently used for estimation of the radome performance.

Thanks to SNOWBEAR one also wants to characterize the K-band receiving conditions, assessing the impact of propagation artefacts (i.e. clouds, rain and snow) on the mission data reception performance on a pre-operational scenario. All the work and results obtained with SNOWBEAR are indeed of fundamental importance to better design the forthcoming EO missions (i.e MetOP-SG), especially in terms of ground station telecommunication system technologies and operational procedures to be implemented.

To do so, a K-band receiving ground station prototype was built in the relevant location environment of Svalbard, Norway, implementing also several ground segment technologies that have been studied in the recent years by the ESA Ground Station division (i.e. a dual band S/K feed, radome, cryogenic LNA, K-band downconverter). Svalbard was chosen as an ideal location for K-band data reception due to its dry climate which minimizes radio signal attenuation.

The whole project consisted in two main phases. The first Ground Station integration and

Figure 2.1: SNOWBEAR ground station picture

validation phase was concluded in December 2018 and it was followed by a two years long measurement campaign [22]–[24], from December 2018 to December 2020 during which the link performance has been measured and all relevant antenna, receiver and weather parameters have been recorded for all the NOAA-20 passes successfully tracked. Some of these parameters are antenna pointing direction, received co-polar and cross-polar signals power, tracking errors, frames, temperatures, precipitations, humidity, etc. The information is collected in four separate raw data files:

- recordings from the Station Controller Unit (SCU)
- recordings from the High Rate Data Front End Processor (HRDFEP)
- recordings from the Weather Station (WTS)
- a checksum file

The SCU is the Monitoring and Control (M&C) system of the SNOWBEAR antenna. It provides the necessary remote M&C functionalities for all the RF devices as well as the Antenna Control Unit (ACU). It also permits configuration of the system and switching between the available operational modes (TLE track, S-Band Autotrack, Ka-Band Autotrack, Sun track, position track) and is fitted with a data logger, which enables recording of every monitored parameter of the system. The sampling rate of the SCU is 1 sample per second. The HRDFEP is composed of the High Datarate Receiver (HDR) and the FEP. It provides all necessary functionality to schedule and monitor data reception. In the case of SNOWBEAR, no payload data is stored by the equipment, only performance statistics (Signal level, Signal to Noise Ratio, frame recorded, corrected/uncorrectable frames). The Weather Station consist in a state of the art terminal, located ay few hundred meters from the SNOWBEAR antenna and near the main building facility, which records all relevant meteorological information at a rate of 1 sample every 5 seconds.

To achieve the aforementioned goals, the strategy of this work was to develop a link budget model able to take all the data as inputs and to post-processed them in order to get an estimation of each pass performance assuming clear sky conditions. Then, comparing the link estimated and measured performance against weather data, one wants to generate a detailed analysis for each single pass, or multiple passes altogether and estimate effects of atmospheric impairments on the signal reception, but also to improve the knowledge of the radome impact in K-band, in particular in presence of rain or snow accumulation on its top. It was wanted also to generate statistics on the ground station system operation to learn lessons on design, installation, testing and validation of such a system in order to better design future ones. The link budget model has been implemented and improved ad hoc for SNOWBEAR during these years considering the general link budget theory, radome model defined from previous studies, the on-site validation of the antenna and receiving chain.

2.1 Link budget model

This section describes all the different parts involved in the link budget model designed so far, starting from spacecraft till the ground station receiving chains.

The link budget is the first step to take in order to determine the feasibility and performance of any communication link system, before proceeding with its effective design and development. Feasibility in this case means to determine not only if the communication link between two points can be established but also if the level of power available at the receiver is enough for the transmitted information to be received in reliable way. Depending on the specific application, a minimum level of performance must be guaranteed at least for a period of time considered satisfactory. Another use of a link budget, is to compare different system design solutions, helping to understand which of the possible hardware implementation strategy is the most suitable one. Additionally, it must be noticed that a link budget is an essential study, not just for evaluating the minimum requirements of the system and each part of it, but also it is useful also in order to design the system without over dimension it. Indeed nowadays, due to the uncertainty of present atmospheric models, specially at high frequencies and at low elevation angles, huge margins are sometimes taken into account in the link budget analysis. This brings various possible unnecessary effects, in particular in the ground segment design, such as increase of system costs, over-complication, over-dimensioning of the antenna etc.

Another important aspect that must be considered is the fulfilment of law constraints on the maximum allowed transmitted power set by authorities [25]. In our case of study, the installed antenna is not intended to be used as a transmitting one, but just as a receiving antenna, therefore is necessary to asses the link budget only for the downlink channel.

2.1.1 NOAA-20 Spacecraft

NOAA-20 is the first polar-orbiting Earth Observation satellite using the 26 GHz band for the payload data downlink channel and it reflects the actual trend for this kind of link to move towards K-band to exploit its advantages. It is one of the fifth-constellation satellites being part of the JPSS program, a partnership between NOAA and NASA, which will contribute to a significant technological and scientific advance in environmental monitoring.

Figure 2.2: NOAA-20 spacecraft model

NOAA-20 has been placed in a polar Sun-synchronous orbit, with an inclination angle equal to 98.7° with respect to the equatorial plane, at a nominal altitude of 824 km. The satellite completes 14 orbits daily providing full global coverage twice a day.

The information on the satellite system and all parameters description explained hereafter is all that can be reported from a confidential document [26] that NOAA shared with ESA. Indeed, NOAA itself shared with ESA just limited information about the spacecraft behaviour. For this reason, ESA has no control on NOAA-20 components parameters, as instead it has on the Svalbard ground station ones, and they shall be taken as they are, without having the possibility of performing direct measurements to verify them.

A general overview of the satellite RF communication links is given in Figure 2.3. In yellow is highlighted the RF Stored Mission Data (SMD) K-band channel towards ground stations located at Svalbard (Norway), Fairbanks (Alaska), McMurdo and Troll (Antarctica). For this case, the transmission occurs at a nominal downlink frequency of 26.7034 GHz with a total bitrate of 300 or 150 Mbps and using Right Hand Circular Polarization (RHCP). In the latter case a convolutional code is used for the signal channel coding.

The key satellite related parameter considered in the link budget is the Effective Isotropic Radiated Power (EIRP) which is the figure of merit used to characterize the transmitting part of a link. It is defined as the total power that would have to be radiated by an isotropic antenna to produce the same power flux density as the actual antenna is radiating in the direction of its main beam. For NOAA-20 the EIRP is calculated considering the equation

$$EIRP = P_{TWTA} - L_{sc} + G_t \tag{2.1}$$

where P_{TWTA} is the K-band Travelling Wave Tube Amplifier (TWTA) output power, specified to be 13 dBW; L_{sc} are passive losses due to cables, switches and rotary joints between the TWTA and the antenna input, quantified as equal to 7 dB; finally G_t is the peak gain of the antenna, equal to 39 dBi. Therefore, the EIRP nominal value in the link budget is equal to 45 dBW.

For this link budget, no pointing loss from the spacecraft has been considered. This choice comes from the fact that the antenna installed on-board is mounted on gimbals and it can be steered to ensure a very accurate pointing with practically no loss.

Knowing the geographical position of the ground station, the orbital altitude of the satellite

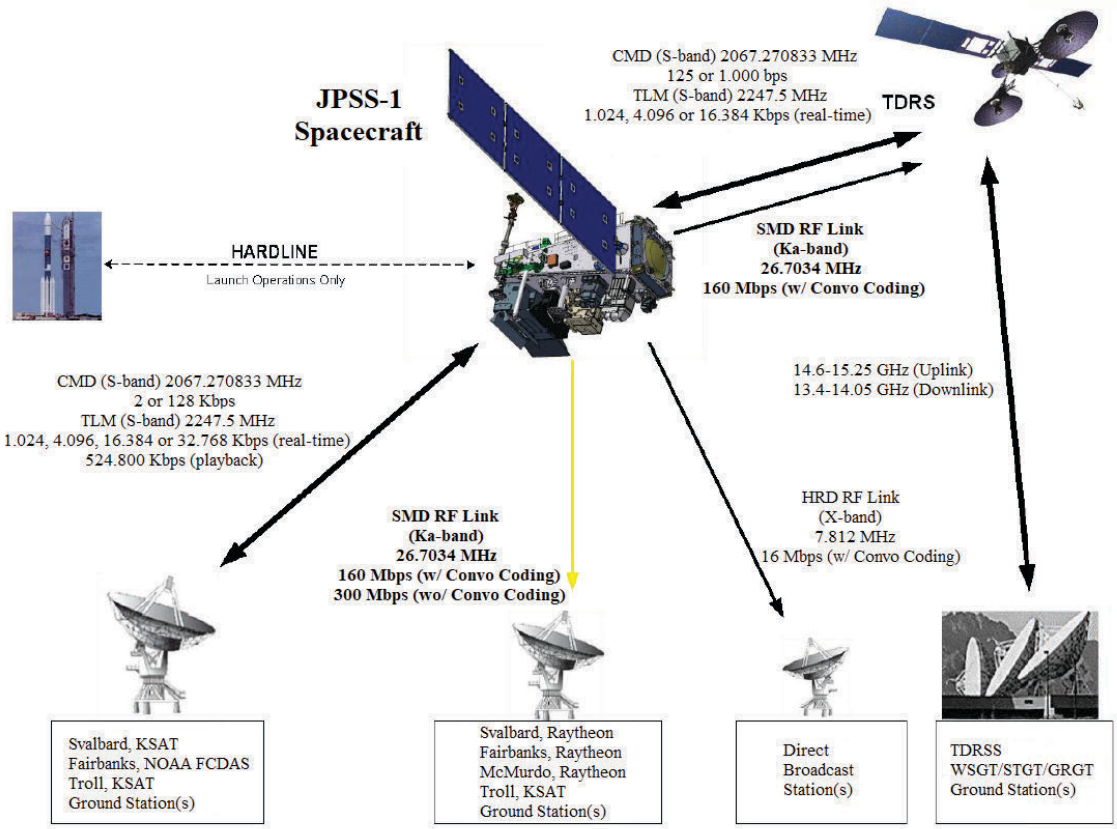

Figure 2.3: NOAA-20 communication links [26]

(a value of 824 km is reported as the nominal altitude) and its elevation over the horizon is possible to calculate their mutual distance, called slant range, for each instant of time during the flight over Svalbard. Determining this distance is important because one can directly derive the free space path loss value evolution during each pass.

In Figure 2.4 is shown the geometry scheme for the slant range D calculation. h is the nominal NOAA-20 altitude above the Earth surface, r_E is the Earth radius, θ is the satellite elevation angle relative to the ground station horizon (positive or negative), α is the angle between the satellite nadir and the ground station and γ is the geocentric angle between the ground station and the satellite.

Starting from the cosine's law

$$D^2 = r_E^2 + (r_E + h)^2 - 2(r_E + h)r_E \cos\gamma \tag{2.2}$$

by noticing that $\alpha + \theta + \gamma = \pi/2$ and substituting γ

$$D^2 = r_E^2 + (r_E + h)^2 - 2(r_E + h)r_E \cos(\pi/2 - (\alpha + \theta)) \tag{2.3}$$

$$= r_E^2 + (r_E + h)^2 - 2(r_E + h)r_E \sin(\alpha + \theta) \tag{2.4}$$

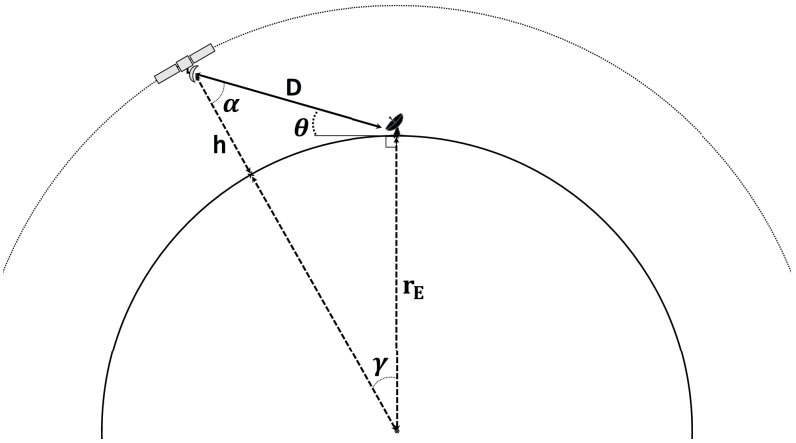

Figure 2.4: Slant range geometry

Now from the second and third term of the sine's law

$$\frac{\sin\gamma}{D} = \frac{\sin\alpha}{r_E} = \frac{\sin(\pi/2+\theta)}{r_E+h} \tag{2.5}$$

one can write

$$\frac{\sin\alpha}{r_E} = \frac{\sin(\pi/2+\theta)}{r_E+h} \tag{2.6}$$

$$\sin\alpha = \frac{r_E}{r_E+h}\cos\theta \tag{2.7}$$

$$\alpha = \arcsin(\frac{r_E}{r_E+h}\cos\theta) \tag{2.8}$$

Substituting the expression for α in Equation (2.3) one finally gets the formula for slant range distance calculation, depending on the elevation θ:

$$D = \sqrt{r_E^2 + (r_E+h)^2 - 2(r_E+h)r_E\sin[\theta + \arcsin(\frac{\cos\theta}{1+h/r_E})]} \tag{2.9}$$

Black line of Figure 2.5 shows the slant range distance calculated from the elevation angle.

2.1.2 Propagation

The overall propagation loss is made up of two main contributions: the free space path loss and losses due to the propagation of the radio wave through the atmosphere.

Free space path loss is the main contribution in the overall propagation losses and can be calculated with a very good accuracy because it relies on deterministic values. Indeed, it is defined in [27] as the ratio between received and transmitted power from two isotropic antennas, through free space. It depends just on the working frequency and the distance between

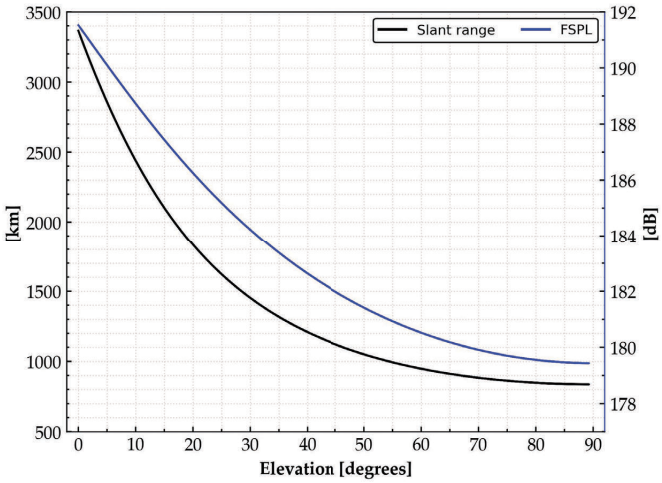

Figure 2.5: NOAA-20 Slant range and free space path loss vs. elevation

transmitting and receiving antennas. The formula for its calculation is:

$$L_{fspl} = 10\log(\frac{4\pi r f}{c})^2 \tag{2.10}$$

where r, in meters, is the slant range distance calculated as described in Section 2.1.1, f is the frequency in Hertz and c is the speed of light through vacuum in m/s

Blue line of Figure 2.5 represents the free space path losses calculated for the link budget corresponding to a certain elevation and slant range distance.

Atmospheric losses instead depends on several variables such as frequency, temperature, humidity and many others weather processes with a stochastic nature. Atmospheric attenuation prediction is therefore a challenging task, due to the randomness of its variables, but is very important in order to design a system with sufficient link margin for the communication to be reliable even in case of severe weather impairments.

For our particular case, the best scenario would have been to implement a radiometer, synchronized with the antenna, to follow the satellite along all its daily orbits while measuring the atmospheric parameters of interest from which one estimates the signal losses. Since the presence of a radiometer was not planned, it was impossible to know all these weather parameters profiles along the path followed by the signal through atmosphere and then to estimate, as accurately as possible, the attenuation during each pass.

Therefore, the atmospheric attenuation can only be estimated by using prediction models. In particular, in this link budget have been implemented those ones provided by the International Telecommunication Union (ITU), collected in its radiowave propagation Recommendations [28] and related to design of Earth-space systems [29].

A first distinction must be made between losses due to the ionosphere related effects and those related to the troposphere. Since ionosphere effects, such as Faraday rotation or propagation delay, are critical for low frequencies, below 1 GHz, but are completely negligible over 12 GHz [30], in this work just the tropospheric effects are considered.

These tropospheric effects include gaseous, clouds, rain and scintillation induced attenuations. All of them are addressed in specific ITU Recommendations, each of one gives a procedure to estimate its specific contribution to the total atmospheric attenuation.

For the present link budget, it was decided to implement, among all the contribution just introduced, only the model for the estimation of gaseous attenuation in clear sky condition. This was done, firstly, because with our actual means it was impossible to get a reasonable estimation of the cloud coverage or rain rate distribution along the signal path and consequently obtain a reliable cloud or rain attenuation value. Secondly, implementing only the clear sky contribution means that the comparison between theoretical performance, against the real one measured by the receiver, gives information about the excess atmospheric attenuation value, i.e. due to clouds, rain, snow, fog ... Since K-band frequencies are a novelty for this kind of applications, characterise excess atmospheric attenuation value in different weather condition is one of the desired project outcome.

The procedure followed for the estimation of the gaseous attenuation is hereafter described.

Attenuation due to atmospheric gases

When a RF signal passes through the atmosphere, it interacts with the different gas molecules, which in turn may absorb part of its energy. The absorption level is much higher as the frequency of the signal is closer to the molecular resonance of one of the considered element.

The main gases composing the atmosphere are Nitrogen (78%), Oxygen (21%), Argon (0.9%), (Carbon dioxide 0.1%), water vapour (0-2%) and many other in very small percentages. Most of them do not interact with the radio waves in the 26 GHz band, and so are completely negligible, except oxygen and water vapour, which in fact are the only two contributions taken into account for the estimation of the gaseous attenuation factor.

In Recommendation ITU-R P.676-12[31] two methods for the estimation of oxygen and water vapour gaseous attenuations are here briefly presented.

Annex 1 The procedure described in Annex 1 is more accurate since it follows a more rigorous approach and is valid for frequencies up to 1000 GHz and for all the elevation angles.

It is based on the evaluation of the resonance line profile of both oxygen and water vapour from specific combination of pressure, temperature and humidity values, from which is possible to estimate the total specific attenuation γ (in dB/km), defined as summation of γ_o and γ_w, respectively the specific attenuations due to dry air (oxygen) and water vapour.

The general formula for the slant path gaseous attenuation, as defined in [31], is:

$$A_{gas} = \int_{h_1}^{h_2} \frac{\gamma(h)}{\sqrt{1 - \cos^2 \varphi(h)}} dh \tag{2.11}$$

where

$$\cos \varphi(h) = \frac{(R_E + h_1) n(h_1)}{(R_E + h) n(h)} \cos \varphi_1 \tag{2.12}$$

$\gamma(h)$ is the specific attenuation at height h, R_E is the average Earth radius (6.371 km), φ_1 is the local apparent elevation angle at height h_1 and $n(h)$ is the refractive index at height h.

A good approximation to evaluate this integral consists in divide the atmosphere into many exponentially increasing layers, determine the specific attenuation γ_i and the path length a_i through each layer and summing their product.

$$A_{gas} = \sum_{i=1}^{imax} a_i \gamma_i \tag{2.13}$$

With this method is possible to get the most accurate results if the local profiles of temperature, pressure and humidity vs. height are available. If they are not, reference standard profiles from Recommendation ITU-R P.835-6 [32] can be used.

Annex 2 This Annex describes a less accurate but more simplified method with respect the previous one, valid just for frequencies in the range 1 - 350 GHz and for elevation greater than 5°.

As Annex 1, this procedure still exploits the line-by-line summation of the resonance lines profile for the oxygen and water vapour specific attenuation γ_o and γ_w.

To compute the overall gaseous attenuation for the desired slant paths through the atmosphere, temperature, pressure and water vapour density are used to define the equivalent heights h_o and h_w for both oxygen and water vapour components of slant path attenuation. These two values are then used to multiply the related specific attenuation to obtain the total zenith attenuation level as sum of the oxygen and water vapour contributions.

$$A_{gas\_zenith} = \gamma_o h_o + \gamma_w h_w \tag{2.14}$$

With respect to the procedure in Annex 1, for which pressure p, temperature T, and water vapour density ρ profiles are needed as input, the procedure in this Annex accepts the local data measured at the Earth surface. If local data is not available, the mean annual global reference atmosphere given in [32] can be used.

Finally, for Earth to space communication links and for elevation angles between 5 and 90 degrees, the total zenith attenuation obtained before is rescaled by using the cosecant law to obtain the desired gaseous attenuation level at a certain elevation angle.

$$A_{gas} = \frac{A_{gas\_zenith}}{\sin el} \tag{2.15}$$

Due to the division by a sin function, this formula gives huge values for very low elevations. To reduce this effect, the concept of slant range is applied to the equivalent heights h_o and h_w. They are therefore considered as altitudes in order to calculate the path length through the atmosphere depending on the elevation angle, in the same way followed for the slant range distance between the satellite and the ground station. To find the final value of the atmospheric attenuation, for each elevation angle the values of γ_o and γ_w are finally multiplied with their respective value of path length.

Brightness noise temperature

Noise affecting the signal transmission comes from many sources, especially in satellite to Earth communication link in which there are a lot of contributions to be taken into account. In the considered frequency band, noise is generated by thermal agitation of molecules, atoms or electrons depending on the considered media and its physical temperature.

To characterize the noise generated by an element, the equivalent noise temperature T_{eq} is introduced. It is a parameter defined as the physical temperature that a resistor connected to a matched load would have, to generate at its outputs the same amount of noise power density N_0 produced by the considered element. This type of noise is additive, white and Gaussian and its frequency spectrum maximum value depending only on the physical temperature.

To get the total noise power level N the noise power spectral density is then multiplied by the considered bandwidth, according to the Nyquist formula:

$$N = N_0 B = kT_{eq}B \tag{2.16}$$

where $k = 1.38 \times 10^{-23} J/K$ is the Boltzmann's constant.

The overall level of noise (see Section 2.1.4) is the result of summing external generated radio noise and internal thermal noise from passive or active devices. The external radio noise, defined through the brightness noise temperature T_{br}, is composed by the sum of sky and ground emissions. T_{sky} is, in turn, the contribution of cosmic background, whose value at the considered frequency is taken equal to 2.7 °K and weighted through the atmospheric loss L_{atm} and the atmospheric noise temperature, T_{atm}, which is the parameter from atmospheric absorption effects.

$$T_{sky} = T_{bkg}10^{-L_{atm}/10} + T_{atm_{ph}}(1 - 10^{-L_{atm}/10}) \tag{2.17}$$

As an approximation to model the impact of ground temperature contributions, for elevations very close to the terrain profile, the study reported in an ESA's internal document[33] has been used. It exploits a closed form approximations for the gain pattern of the antenna to compute the total temperature sensed when the pointing direction is close to the terrain profile. By comparison between different approximation models with a simulated pattern of several ESA's antennas, it figures out that the best results have been obtained by using a single sidelobe Gaussian approximation.

From this Gaussian approximation, a multiplicative coefficient expressing the % of temperature picked up from the ground has been formulated as:

$$k = \alpha\left[erfc\left(\frac{1.851x}{HPBW}\right) + 10^{-A_{dB}/10}\left(erfc\left(\frac{1.851(x+\mu)}{HPBW}\right) + erfc\left(\frac{1.851(x-\mu)}{HPBW}\right)\right)\right] \tag{2.18}$$

where:

$$\alpha = \frac{1}{2}\frac{1}{1 + 2 \cdot 10^{-A_{dB}/10}}$$

Values μ and A_{dB} coincide respectively with position and amplitude (in dB) of the first sidelobes and x is the angular distance between the terrain profile and the boresight pointing of the antenna.

Thus the total brightness temperature just before the radome is determined as

$$T_{br} = kT_{gnd} + (1 - k)T_{sky} \tag{2.19}$$

2.1.3 Ground Station

The SNOWBEAR ground station is part of Svalbard Satellite Station facility (SvalSat), located on the Plataberget plateau near the small town of Longyearbyen, in the Svalbard archipelago (Norway). It is the world's largest commercial ground station complex, with more than 31 state of the art multi-mission and customer dedicated antenna systems working from C to K bands. Thanks to its geographical position, located at a latitude of 78° N, it has been recognized as an optimally position for satellite control [34]. Indeed the extreme northern location gives SvalSat the ability to provide support to all the possible orbits travelled each day by low Earth polar orbiting satellites. The almost flat terrain profile guarantee also a wide range of elevations for which the antenna has a free line of sight to the satellite, thus it is able to be tracked early during its pass, maximizing the available time for the data download.

The terrain profile around the SNOWBEAR antenna is shown in Figure 2.7. In the north direction there is the Isfjorden, so the altitude profile is very low. Proceedings eastward there are some low mountains and few radomes profile, till the south direction where the highest point, slightly more than 6° tall, is due to the presence of a mountain quite near to the plateau. From south-west to north, the terrain profile become again very low, except along those directions where other radomes are installed, but in any case it is always below 4°. The very tall thin line around 240° is due to the presence of a tall dipole antenna.

Figure 2.6: Svalbard Satellite Station facility. Credit:[KSAT]

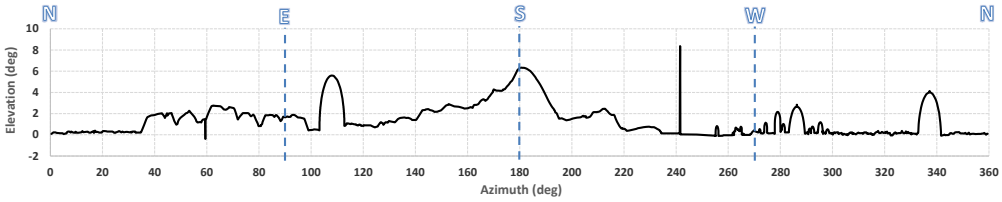

Figure 2.7: Elevation profile seen from the antenna

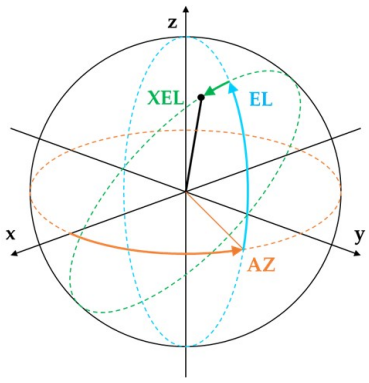

Figure 2.8: Representation of Azimuth, Elevation and Cross-elevation axis

Antenna

The installed antenna (Figure 2.9), fabricated by MTM mechatronics [35], is a ring focus dual reflector Cassegrain antenna composed by a 0.8 m sub reflector with a rotational ellipse shape, designed to reduce the coupling effects, and a 6.4 m parabolic main reflector.

The feed (Figure 2.10a) is placed in the sub-reflector focus (i.e. the system focus) and it is characterized by two circular corrugated horns where the K-band feed is coaxial to the S-band one.

The antenna is design to work in S and K bands (i.e. 2.2 - 2.3 and 25.5 - 27 GHz) and it is equipped with a 3-axis control movement: the Azimuth (AZ) axis to rotate the antenna structure along a vertical axis in the plane tangential to the ground, the Elevation (EL) axis to rotate the reflector along a horizontal axis, and the Cross-Elevation (XEL) axis to tilt the reflector perpendicularly to the elevation direction.

Simulations have been made both by University of Pavia (Unipv) [36] and FDS Italy s.r.l. using the feed and antenna models provided by MTM, for the radiation pattern estimation, shown in Figure 2.10b. Simulations made by Unipv were done with GRASP while the ones made by FDS with a full-wave software.

In order to take into account the near-field effect due to the close proximity of the feed and sub-reflector, these two components have been simulated as a whole using Ticra CHAMP© software. The output of CHAMP is indeed a field spherical wave expansion that was then imported in GRASP and simulated together with the main reflector.

The values related to the antenna used in the link budget are the following: a diameter of

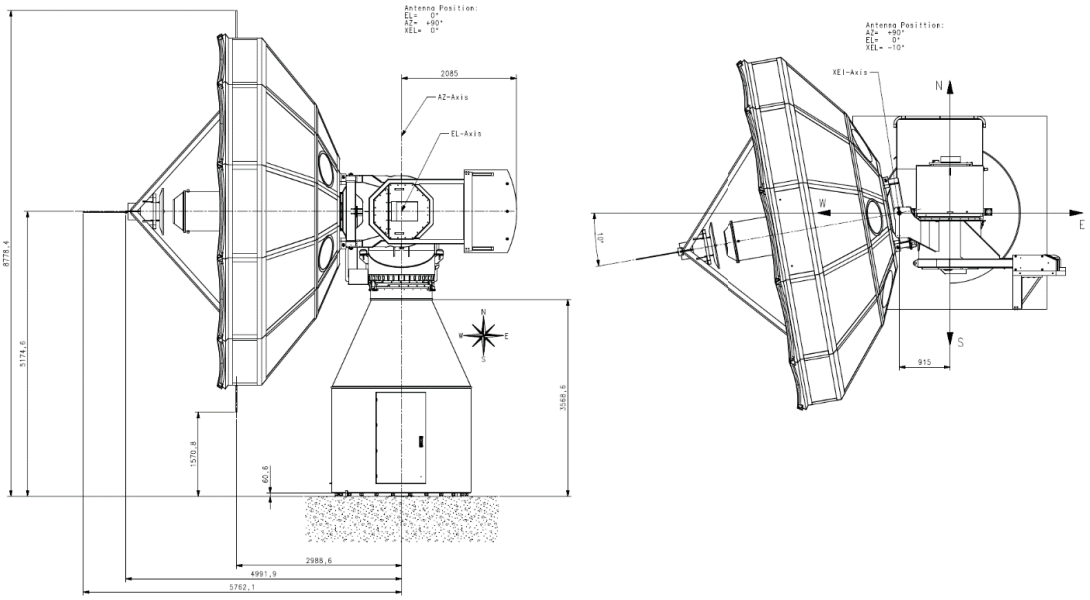

Figure 2.9: SNOWBEAR mechanical drawing of the antenna

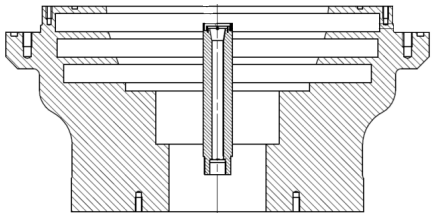

(a)

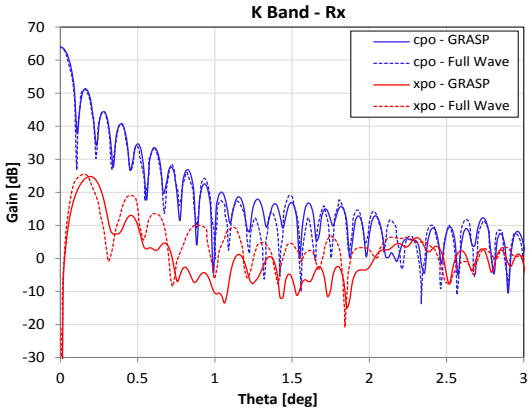

(b)

Figure 2.10: a) Sketch of the S/K band feed b) Antenna simulated radiation pattern

6.4 meters, maximum calculated gain along the boresight direction equal to 63.4 dBi, half power beamwidth equal to 99 mdeg, first sidelobe level and offset with respect to the main lobe are respectively equal to -12.6 dB and 165 mdeg.

Radome

To protect the antenna from the harsh polar environment it was covered by self-supporting Multi-Layer Radome (MLR), characterized by a spherical truncated structure, with a diameter equal to 11.8 m and truncation of 87%. Designed and produced by University of Pavia and

FDS s.r.l. Italy [37], it is made up of many dielectric pentagonal and hexagonal shape multi-layer panels, joined together by overlapping joints and metallic bolds, providing outstanding RF transparency at both 26 GHz and S-Band frequencies.

For multi layers radomes, the stratification is generally realized just with 3 different dielectric layers (A-layers), but at higher frequencies and for bigger radomes, the resulting panel would be just too thin to ensure the structure tightness. Therefore, the followed solution was to work with a larger number of layers, realizing thicknesses at multiples of the half-wavelength. In particular, a stratification based on the layout shown in Figure 2.11 has been designed. In this case, two half-wavelength stratifications are separated by an inner low dielectric-constant layer, achieving the best performance for both mechanical and electromagnetic aspects, with minimum compromise. Foam was used to realize the low dielectric constant layers, whereas fiberglass, due to its good compromise between mechanical and electromagnetic properties in addition to its reasonable costs, is adopted to realize the high dielectric constant ones.

Figure 2.11: Panels stratification

This typology, i.e. panels composed by a seven layer configuration, has been chosen because it ensures the best trade off between mechanical and electromagnetic performance. Indeed, the radome mechanical robustness depends mainly on the central layer width and using a low loss material (i.e. polyurethane) is possible to design the core depending on mechanical specifications with a limited impact on the electromagnetic performance. Moreover, the outer A-layers, made in sequence by Fiberglass - Foam - Fiberglass, act together as an impedance matching for the inner one, minimizing reflections and giving even more robustness to the radome. These matching layers are necessary also to protect the inner core from the external environment, at the cost of introducing more losses. Among these seven layers, one more composed of gelcoat is added on the external surface. This is done in order to increase the radome hydrophobicity and thus reducing the accumulation of rain on its surface.

The dimensions and electromagnetic parameters of each layer are property of FDS Italy srl.

The overall transmission loss of the radome is made up of two contributions: the loss due to the panels, derived from the scattering parameters of the multilayer, and the loss due to the panel interconnections (i.e. joints), which represent indeed a discontinuity for the electromagnetic wave penetrating the radome surface. Their effect is expressed via the so called Induced Field Ratio (IFR) of the joint, which is a measure of the scattering efficiency of the joint normalised with respect to its optical shadow area. Both of these values have been studied in the previous years, by FDS and Microwave laboratory of the University of Pavia [20]. Many panel prototypes were built, each one with different material characteristics and productive technology in order to find the best trade off between performance and costs. The IFR of the joints

were simulated and measured as well. Once the optimum panel configuration and technology has been chosen, simulations of the antenna covered by the radome were made in order to estimate its effect on the antenna gain. Moreover a simulation of the antenna covered by just the radome framework were made too, in order to estimate the effect of the framework alone.

The numerical results obtained by the simulation of the antenna system with and without the radome showed that the radome impact is very limited and the worst case degradation achieved in K-Band is around 0.88 dB [20].

Antenna noise temperature

The antenna noise temperature T_{ant} is defined as the noise power seen at the output terminals of the antenna, which is calculated as the sum of all the radio noise collected by the antenna from every direction and weighted by the its gain.

$$T_{ant} = \frac{1}{4\pi} \int_0^{\pi} \int_0^{2\pi} G(\theta, \phi) T_{ext}(\theta, \phi) \sin\theta d\theta d\phi \tag{2.20}$$

where $G(\theta, \phi)$ is the antenna gain and $T_{ext}(\theta, \phi)$ is the sum of brightness and radome noise temperatures in Kelvin where:

$$T_{rdm} = T_{rdm_{ph}}(1 - 10^{-(L_{rdm}/10)}) \tag{2.21}$$

and

$$T_{ext} = T_{brg} 10^{-L_{rdm}/10} + T_{rdm} \tag{2.22}$$

2.1.4 Receiving chain

A block diagram of the SNOWBEAR ground station receiving chain is reported in Figure 2.12. A description of each component in term of its nominal gain, losses or bandwidth is hereafter given.

The S-band chain (i.e. the lower part) is reported just for sake of completeness, since it is not considered for this study but it is anyway an important part of the system. Indeed, it is used to track the satellite during the early phase of each pass before a stable K-band tracking acquisition and also as a backup when it is lost for any reason.

Each device or connection between elements has been tested with on-field measurements to check if it was compliant with its nominal specifications.

Feed to LNA path

Focussing just on the K-band chain, immediately after the feed horn, the signal passes through a waveguide OrtoMode Transducer (OMT) and a polariser, which are used to separate the two orthogonal circular polarization. For NOAA-20 the Copolar (Cpol) and Cross-polar (Xpol) signals correspond respectively to the RHCP and LHCP polarisations.

Then, along each path, there is a coupler used eventually to inject a signal for calibration or test purposes.

After a band-pass filter are installed the LNAs, preceded by switches for routing the signals correctly. They consist in four LNAs, two cryogenic cooled LNAs and two additional ambient

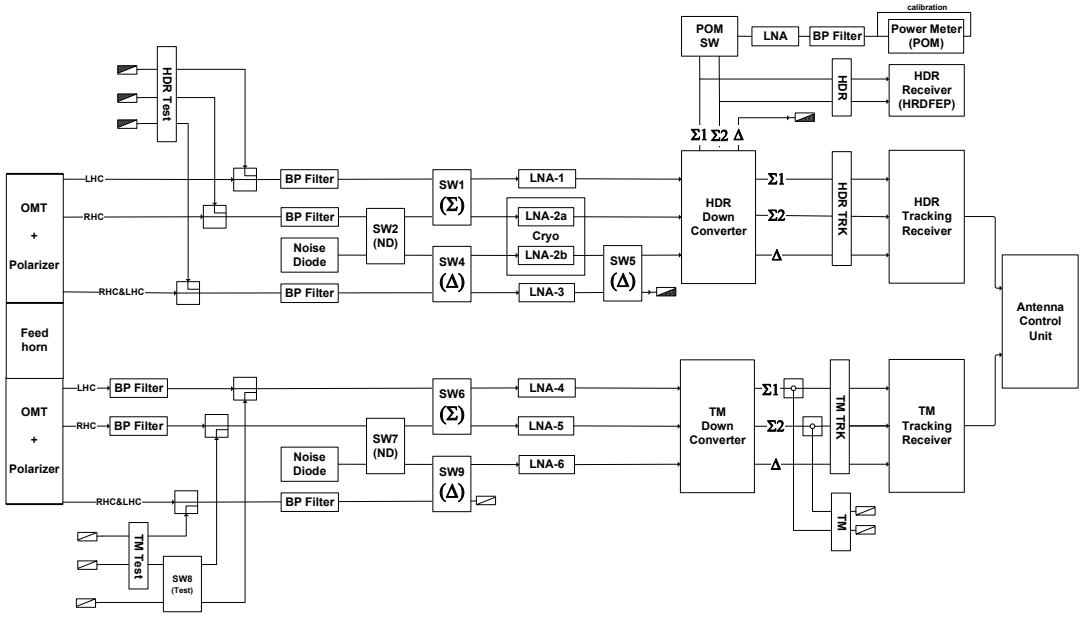

Figure 2.12: SNOWBEAR receiving chain Upper part, K-band. Lower part, S-band

temperature ones. Each LNA was characterized in terms of its nominal gain, noise figure and bandwidth. It must be highlighted that LNA should be designed with the highest possible gain and the lowest possible noise figure in order to cut down all the further contributions and add the smallest level of noise to the signal. During normal operations, the Cpol signal is routed towards the LNA-2a while Xpol and the delta signal for the satellite tracking respectively towards LNA-1 and LNA-2b.

All the connection between the OMT/polariser, filters and switches to the LNAs are made in waveguide to ensure the lowest possible loss.

In the link budget, thanks to the logged switch position, is possible to know where each signal is routed to and therefore choose the corresponding feed to LNA loss $L_{feed-LNA}$ to calculate the copolar or cross-polar signal level at the input of the correspondent LNA with the formula:

$$S_{LNA} = EIRP - L_{prop} - L_{rdm} + G_{ant} - L_{feed-LNA} \qquad (dB) \tag{2.23}$$

A noise diode is also installed and used as a reference noise source for the receiver calibration and to evaluate its contribution to the overall system noise temperature. In particular, a calibrated noise is injected in both chains prior and after each pass to calibrate their gains to be used in the link budget model. Indeed, one has seen variations of DC gain vs temperature, as shown in Figure 2.13.

As it is clearly visible, the gain variation is inversely proportional to the temperature within the antenna hub. The peak to peak variation is of about 2.5 dB over the whole year and for some cases up to 0.5 dB between beginning and end of a pass (in average less than 0.1 dB).

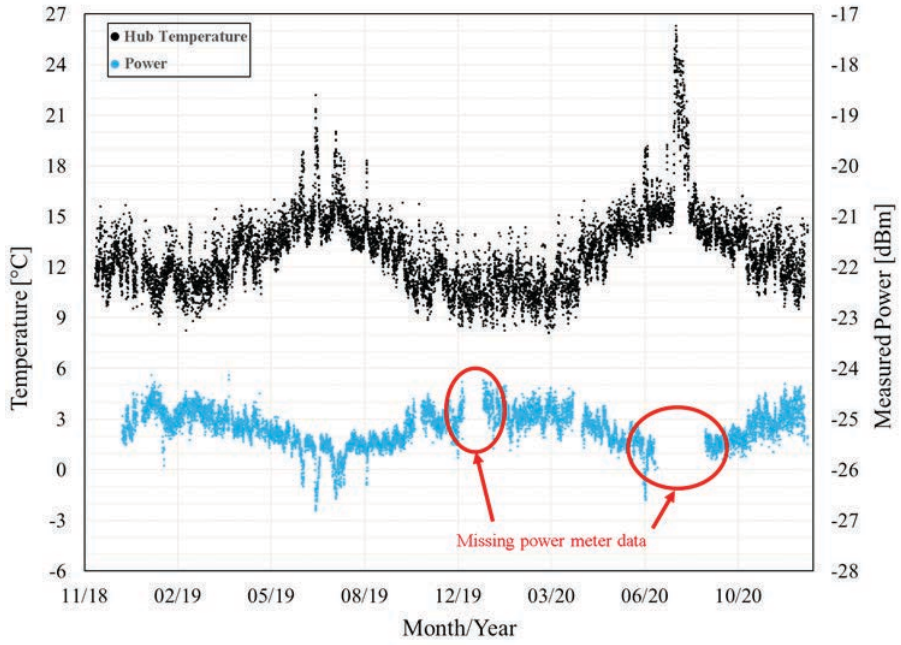

Figure 2.13: Gain variation vs. hub temperature

LNA to tracking receiver

After the LNAs each output signal is routed, through coaxial cables, to the inputs of the down converter (DC), introducing the loss L_{LNA-DC}.

Attenuators are used both between the LNA-2a and the DC, and along the connection marked as Σ_2, which is the path followed by the Cpol signal, in order to lower its power level to avoid DC and tracking receiver (TKRX) saturation. The path marked as Σ_1 is instead the one followed by Xpol signal and due to the lower gain of LNA-1 no attenuator is needed.

The down converter is used to shift down in frequency the RF signal to an intermediate one (IF) for the further processing. In particular, the input signal in the 26 GHz band is shifted around 1200 MHz for the path toward the High Rate Demodulator Front-End Processor (HRD-FRP) and around 70 MHz for the one toward the tracking receiver.

Coaxial cables are used for the connections between DC and TKRX, introducing losses $L_{DC-TKRX}$.

Then, the signal is filtered by the tracking receiver input filter, centred at 70 MHz with a nominal bandwidth of 5 MHz, and the tracking errors generated considering the sum and delta signals are used by the Antenna Control Unit (ACU) in order to command the antenna pointing mechanism.

The formula

$$S_{TKRX} = S_{LNA} - L_{LNA-DC} + G_{DC} - L_{DC-TKRX} \qquad (dB) \tag{2.24}$$

is used to calculate copolar or cross-polar signal level at the input of the tracking receiver.

Down Converter to HRDFEP

The DC IF outputs, around 1200 MHz, are connected to the HRDFEP interface panel with coaxial cables. Σ_1 and Σ_2 are respectively the path followed by Xpol and Cpol signals.

This system receives the 1200 MHz IF from the downconverter, demodulates the signal and decodes the received data. For each satellite pass, a number of status parameters from the demodulation and decoding processes are stored but, due to the scope of this project, the desired output of the HRDFEP is the demodulation and processing performance, not the payload data content. Hence, the data itself is neither used nor stored. The formula

$$S_{HDR} = S_{LNA} - L_{LNA-DC} - G_{DC} - L_{DC-IFP} - L_{IFP-HDR} \qquad (dB) \tag{2.25}$$

is used to calculate copolar or cross-polar signal level at the input of the HDR. The formula

$$N_{HDR} = T_{sys} + G_{LNA} - L_{LNA-DC} - G_{DC} - L_{DC-IFP} - L_{IFP-HDR} + k + BW_{HDR} \qquad (dB) \tag{2.26}$$

is instead used to calculate the noise power level at the input of the HDR and consequently the SNR_{HDR}.

Down Converter to Power Meter

DC output channels are connected also to a switch able to select which of them send to the power meter input.

With this parallel measurement chain it was wanted to try an alternative method for the noise measurement, from which then possibly make an estimation of the noise temperatures, in particular the system and external brightness ones.

To do so, the Power Meter (POM) record the Xpol channel a few MHz away from the payload signal frequency spectrum. The Xpol is considered because of its lower power level with respect to the Cpol (i.e around 18 dB less). This is done to allow the noise to be detected instead of the signal, but on the other side one cannot go too far in frequency with the filter pass band because components gain and losses at frequencies far from the signal ones are not characterized.

The POM IF and bandwidth are equals to 1535 and 24 MHz.

Table 2.1 shows the nominal values of most relevant Ground Station parameters used in the link budget. The formula

$$S_{POM} = S_{LNA} - L_{LNA-DC} - G_{DC} - L_{DC-IFP} - L_{IFP-POM} \qquad (dB) \tag{2.27}$$

is used to calculate copolar or cross-polar signal level at the input of the HDR.

System noise temperature

The system noise temperature T_{sys} is a figure of merit used to characterize the noise level of a receiver. It is generally referred to the input of the LNA because this is the point where noise has the strongest impact on the signal level and where the various noise contributions, referred to that point, are easy to relate with their physical meaning. T_{sys} is thus the summation of many

contributions, estimated in our case by using the formula:

$$T_{sys} = T_{ant_{LNA}} + T_{feed} + T_{rec} \tag{2.28}$$

where:

$\mathbf{T_{ant_{LNA}}}$ is the radio noise collected by the antenna T_{ant}, scaled by the attenuation $L_{feed-LNA}$ associated to the considered feed to LNA path. T_{ant} is, in turn, the sum of T_{brg}, the brightness temperature encountered in Section 2.1.2, reduced by the radome losses L_{rdm}, and the radome noise temperature T_{rdm} itself.

$$\begin{aligned} T_{ant_{LNA}} &= T_{ant} 10^{-(L_{feed-LNA}/10)} \\ &= (T_{brg} 10^{-(L_{rdm}/10)} + T_{rdm}) 10^{-(L_{feed-LNA}/10)} \end{aligned} \tag{2.29}$$

$\mathbf{T_{feed}}$ is the noise added by the ohmic losses between the feed and the LNA. $T_{feed_{ph}}$ is the physical temperature of the feed system.

$$T_{feed} = T_{feed_{ph}} (1 - 10^{-(L_{feed-LNA}/10)}) \tag{2.30}$$

$\mathbf{T_{rec}}$ is the sum of all the equivalent temperatures from active components and ohmic losses placed after the LNA, referred to its input. Due to the very high gain of the LNA, generally just the first two or three components after it are sufficient in the calculation.

$$\begin{aligned} T_{rec} &= T_{LNA} + T_{LNA-DC} + T_{DC} \\ &= T_{LNA_{ph}} (10^{(NF_{LNA}/10)} - 1) + \frac{T_{LNA-DC_{ph}} (10^{(L_{LNA-DC}/10)} - 1)}{G_{LNA}} \\ &\quad + \frac{T_{DC_{ph}} (10^{(NF_{DC}/10)} - 1) L_{LNA-DC}}{G_{LNA}} + \dots \end{aligned} \tag{2.31}$$

$T_{LNA_{ph}}, T_{LNA-DC_{ph}}$ and $T_{DC_{ph}}$ are the physical temperature of the specified element, in Kelvins, while gains, losses and noise figures are expressed in dB.

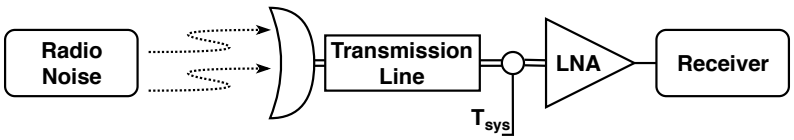

Figure 2.14: Reference point for the system noise temperature

From T_{sys} is then possible to calculate the noise power spectral density N_0 and, knowing the bandwidth B, also the noise power N at the input of the receiver.

$$N = N_0 B = k T_{sys} B \tag{2.32}$$

Theoretical vs. estimated T_{sky},T_{rec} and T_{sys}

Equations (2.17), (2.28) and (2.31) are used to calculate a "theoretical" value of T_{sky}, T_{sys} and T_{rec} from nominal values (at most experimentally verified in the building phase) of all the components that come into play into the equations. Later in this Thesis will be introduced an "estimated" or "measured" version of them (Section 2.2, single pass analysis). T_{sys} and T_{rec} in particular are estimated from a real measurement of noise power level at the POM input performed exploiting the noise diode and the procedures described hereafter. Once T_{sys} and T_{rec} are known, T_{sky} can be estimated by inverting all the equations till Equation (2.17) considering by force the theoretical value of elements between the radome and the input of the LNA (there is no way to measure those values in real-time).

To determine the receiving chain noise contribution T_{rec}, referenced at the input of the considered ambient or cryogenic LNAs, a calibrated noise diode has been integrated into the receiving chain. This diode is characterized by an Exceed Noise Ratio (ENR) of 15.2 dB, defined as the ratio between its ON and OFF state output power when the diode has a reference physical temperature of 290 °K. Considering the noise temperatures instead of powers, the ENR is expressed as[38]:

$$ENR = \frac{T_{on} - T_{off}}{T_0} \tag{2.33}$$

where T_{on}, T_{off} and T_0 are respectively the noise temperatures of the diode in its ON state, OFF state, and the standard temperature of 290 °K. If the diode temperature is different than 290 °K, the ENR must be corrected with the formula:

$$ENR_{corr} = 10 \log \left(10^{\left(ENR_{ref}/10\right)} + \frac{T_0 - T_d}{T_0} \right) \tag{2.34}$$

where T_d is the diode physical temperature and ENR_{ref}, in decibels, is the reference ENR value calculated at 290 °K. This correction is in the order of 0.02 dB, for a temperature of -20 °C (253 °K) so basically negligible.

For T_{sys} and T_{rec} estimation the Y-factor method has been exploited. It is widely used to measure the noise figure or the effective input noise temperature of a Device Under Test (DUT), by using a noise source and measuring DUT output power either when the noise source is ON and OFF. The DUT in our case is the whole receiving chain.

For T_{rec} at the input of each LNA, the noise power level at the input of the POM has been measured either before and after the pass recording, for both the cryogenic and ambient receiving chains and for both diode ON and OFF states (P_{on} and P_{off},for 10 seconds in each case). The values in the middle of the pass are obtained by linear interpolation of starting and ending values.

When performing such measurements, thanks to the way the switches are positioned, all the devices between the feed and the considered LNA are completely excluded from the measurement. Moreover, the measure is independent from the receiver bandwidth. The Y-factor is therefore:

$$Y = \frac{P_{on}}{P_{off}} = \frac{kBT_{sys_{on}}}{kBT_{sys_{off}}} = \frac{T_{rec} + T_{on}}{T_{rec} + T_{off}} \tag{2.35}$$

where T_{rec} is the noise temperatures of the receiving chain while T_{on} and T_{off} are the ones generated by the noise diode in the ON and OFF states, all of the three referred at the input of the LNA. Considering the noise diode physical temperature T_d, the difference between the ON and OFF temperature at its output T_δ and the losses due to the connection between the diode and each LNA L_{ND-LNA} (linear, comprised between 0 and 1, whose physical temperature is assumed equal to T_d), T_{off} and T_{on} can be found by using the following formulas:

$$T_{off} = T_d 10^{-(L_{ND-LNA}/10)} + T_d\left(1 - 10^{-(L_{ND-LNA}/10)}\right) \tag{2.36}$$

$$T_{on} = (T_d + T_\delta)\, 10^{-(L_{ND-LNA}/10)} + T_d\left(1 - 10^{-(L_{ND-LNA}/10)}\right) \tag{2.37}$$

And finally:

$$T_{rec} = \frac{T_{off}P_{on} - T_{on}P_{off}}{P_{off} - P_{on}} \tag{2.38}$$

The accuracy of this calculation relies on the accuracy of T_{on} and T_{off}, thus on the physical temperature of the diode (recorded), the loss L_{ND-LNA} and the diode ENR (verified before the installation).

For the system noise temperature estimation, the procedure involving the Y factor is a bit different. The two measurements of the noise power level at the POM, with the noise diode ON and OFF from the previous paragraph, are related to the real measurement of the background noise, P_{POM}, recorded by means of the POM.

Indeed, the POM input passband filter is centred just outside the spacecraft signal bandwidth in order to kill the signal itself and let only the noise be measured. It is worth to mention that while data are normally recorded by the HDR on the cryogenic channel, the receiver architecture constrains the POM to measure the signal on the ambient channel (i.e. the crosspolar signal). Therefore, T_{sys} estimated is the one related the the ambient channel and to retrieve the cryogenic one is necessary to subtract and then add again the related T_{rec}.

Starting from the formula:

$$T_{sys} = \frac{T_{pom}}{G_{pom}} = T_{pom}\frac{T_{\delta_{LNA}}}{T_{\delta_{pom}}} \tag{2.39}$$

G_{pom} is the overall gain from the LNA to the POM itself, which is calculated as the ratio between $T_{\delta_{pom}}$ and $T_{\delta_{LNA}}$, where $T_{\delta_{pom}}$ and $T_{\delta_{LNA}}$ are the difference between measured noise temperature with the diode ON and OFF respectively at the POM and LNA inputs. T_{sys} then can be expressed as:

$$T_{sys} = T_{\delta_{LNA}}\frac{T_{pom}}{T_{on} - T_{off}} = T_{\delta_{LNA}}\frac{P_{pom}}{P_{on} - P_{off}} \tag{2.40}$$

where

$$T_{\delta_{LNA}} = T_\delta 10^{-(L_{ND-LNA}/10)} \tag{2.41}$$

and P_{on}, P_{off} were already defined. This equation is applied for every value of P_{pom} measured during the pass.

Table 2.1: Nominal values of most relevant Ground Station parameters

Parameter		**Value**	**Parameter**		**Value**
Frequency	GHz	26.7034	DC ch1 Gain (to TKRX)	dB	20.5
Latitude	deg	78.227	DC ch2 Gain (to TKRX)	dB	20.45
Longitude	deg	15.434	DC ch1 Gain (to HDR)	dB	8.96
Height	km	0.4695	DC ch2 Gain (to HDR)	dB	9.11
Antenna Gain	dBi	63.4	DC ch1 Noise Figure	dB	13
Antenna Diameter	m	6.4	DC ch2 Noise Figure	dB	12
Antenna Efficiency	%	68.2	DC to TKRX ch1 Gain	dB	22.66
1° Sidelobe Delta	dB	12.6	DC to TKRX ch2 Gain	dB	22.66
1° Sidelobe Offset	deg	0.165	DC to IFP ch1 Loss	dB	8.75
K band HPBW	deg	0.099	DC to IFP ch2 Loss	dB	8.49
S band HPBW	deg	1.2	IFP to HDR ch1 Loss	dB	4.8
HDR IF	MHz	1200	IFP to HDR ch2 Loss	dB	4.7
POM IF	MHz	1535	IFP to POM ch1 Gain	dB	26.81
TKRX IF	MHz	70	IFP to POM ch2 Gain	dB	26.53
Feed to LNA1 Loss	dB	1.2	ND - LNA1 cable Loss @27.05	dB	1.83
Feed to LNA2 Loss	dB	1.27	ND - LNA2 cable Loss @27.05	dB	1.92
LNA1 Gain	dB	41.2	TKRX bandwidth	MHz	5
LNA1 Noise Figure	dB	1.68	HDR bandwidth	MHz	1200
LNA2 Gain	dB	48.96	POM bandwidth	MHz	24
LNA2 Noise Figure	dB	0.68	POM filter roll-off @27.05	dB	38
LNA1 to DC ch1 Loss	dB	8.72	I channel bitrate	Mbit/s	150-300
LNA2 to DC ch2 Loss	dB	16.65	Q channel bitrate	Mbit/s	150-300

2.2 Measurement campaign and Data processing descriptions

This chapter is intended to describe how data were collected during the measurement campaign and how the were post-processed and analysed to extract all the desired information and performance statistics about the communication link during the operational phase of the SNOWBEAR project, from December 2018 until the end of November 2020. Major outcomes and lessons learned, both from the station design and operative procedures points of view, will be finally discussed as results.

2.2.1 Operational strategy

First of all, Figure 2.15 gives an overview of the sky covered by all the possible NOAA-20 orbit trajectories. It performs 14 orbits per day and it has a repetition cycle of 227 passes, meaning that every 16 days each pass is repeated identically.

Passes coloured in yellow-red are those ones having a maximum elevation lower than 81 degrees and thus tracked in the AZ/EL configuration, while green-blue ones have a maximum elevation greater than 81 degrees and they were tracked in the AZ/EL/XEL configuration. Yellow-red and green-blue are used to identify also each orbit travel direction, from start to end.

The black region at low elevation is the masking profile that is the terrain elevation profile as seen from the antenna position.

The strategy followed by the NOAA-20 mission is to download all the data collected since the last data dumping completely at the beginning of each pass, starting around 5 degrees of elevation. As soon as the stream of useful data is completed, idle frames started to be transmitted until the last part of the pass when the data collected during the pass over Svalbard is again

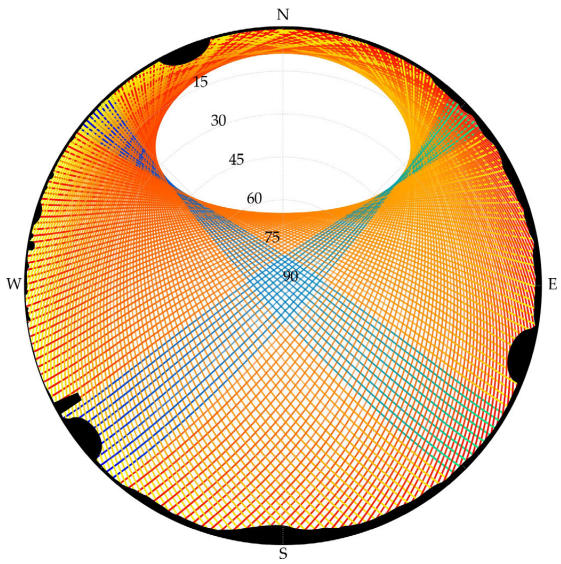

Figure 2.15: NOAA-20 orbits trajectories

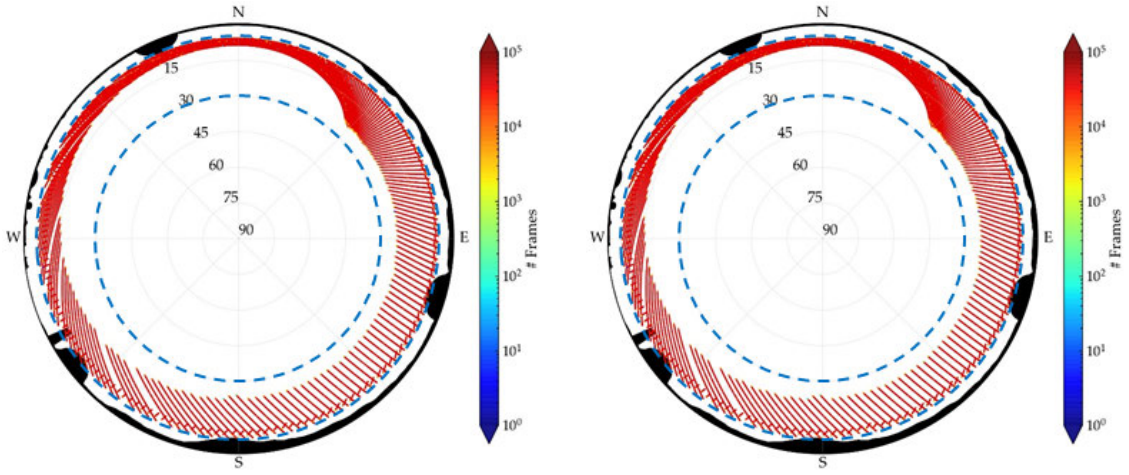

Figure 2.16: Distribution of NOAA-20 dumped frames

dumped.

Figure 2.16a and Figure 2.16b are a polar representation of the dumped frame rate during two different cycles from which is possible to see that data dumps occur between 5 and 30 degrees (the two dashed blue circles) despite very few exceptions probably because of problems in other stations.

As already mentioned, pass recordings were nominally performed using the autotrack mode, whose locking strategy is explained hereafter.

No masking profile was implemented inside the ACU, so the antenna is pre-steered based on the program track information (i.e TLE) towards the Aquisition of Signal (AOS) position. At the elevation of 2 degrees the autotrack mode is enabled for both S and K bands. It becomes active when the tracking error signal is stable for at least 3 seconds. Proceeding in this way, the S-Band autotrack lock the signal around 2 deg or as soon as horizon mask allows if it is higher. A stable condition for the K-Band autorack is instead typically reached 1 or 2 deg above the S-band one therefore there is always a transition phase, at the beginning of each pass, when the S-band is engaged and then the K-band one comes into play. For instance in the worst case, i.e. the mountain towards south, which is 5 deg high, the S-Band tracking is activated at around 5 deg and the K-band at 7 deg.

2.2.2 Data collection

Each pass is uniquely identified with its orbit number from the end of NOAA20's Low Earth Orbit Phase (LEOP). Table 2.2 shows the starting date and the orbit intervals for each cycle collected during the measurements campaign. As from orbit 13603, due to a failure of the polarisation switch, the system was forced to operate in program track mode. Since in this configuration the antenna pointing comes out to be not properly aligned to the main RF beam, considerable pointing losses affected the signal reception especially for cross-elevation passes at high elevations. It was therefore decided not to consider recordings from orbit 13604 onwards

for most of the performance statistics. The total number of passes for the period 1st December 2018 – 30th November 2020 is 10370 (8244 discarding passes from 13603).

The data retrieved by the SNOWBEAR system was collected after each satellite pass by Kongsberg Satellite Services (KSAT), the Svalbard Ground Station operator, and made available to the users on a restricted FTP server. The information consists in 4 separate raw data files: first one contains the Station Controller Unit (SCU) log, the second the one from the High Rate Data Front End Processor (HRDFEP), the third the Weather Station (WTS, placed in the proximity of the main building on the plateau) log, while the fourth is a checksum file.

The SCU is the Monitoring and Control (M&C) system of the SNOWBEAR antenna. It provides the necessary remote M&C functionalities for all the RF devices as well as the Antenna Control Unit (ACU). It also permits configuration of the system and switching between the available operational modes (TLE track, S-Band Autotrack, K-Band Autotrack) and is fitted with a data logger, which enables recording of every monitored parameter of the system. They includes: antenna physical pointing position from the encoders readings or from the TLE prediction and antenna azimuth, elevation and cross-elevation deviation between the two; both S and K band tracking errors; speed of the antenna axes; power levels readings from the tracking receiver (both S and K bands, only copolar polarisation), HRDFEP (K-band only, both copolar and crosspolar polarisations) and power meter inputs; the currently active or enabled tracking mode, that is K band, S band autotrack or program track. Then are also recorded various settings from other components such as the position of switches used to route the co-polar and cross-polar signals to the LNAs; temperatures inside the radome; noise power measured by the power meter; status of noise diode (on/off)... The sampling rate of the SCU is 1 sample per second.

The HRDFEP provides all necessary functionality to schedule and monitor data reception. The High Datarate Receiver (HRDFEP) is a sub-system of the HRDFEP. In the case of SNOWBEAR, no payload data is stored by the equipment, only performance statistics such as the input power levels, both co-polar and cross-polar; signal to noise ratio (SNR, both co-polar and cross-polar) and received, corrected and lost frames. Conversely to other parameters, the SNR level is not measured directly but it is estimated from the demodulated signal constellation. Sampling rate is also 1 sample/s.

Finally, the Weather Station consist in a state of the art terminal, located any few hundred meters from the SNOWBEAR antenna, which records all relevant meteorological information at a rate of 1 sample every 5 seconds. These variables include temperature, pressure, humidity, precipitation, snow thickness, wind ...

The checksum file, called "delivery report" is generated automatically at each pass by the KSAT Network Operation System (KNOS). It consist in a simple check on the size of the SCU, HRDFEP and Weather Station files.

Table 2.2: Orbit cycle starting date and related orbit number interval

Cycle	Starting date	Orbit interval	Cycle	Starting date	Orbit interval
23	01/12/18	5359-5447	**47**	10/12/19	10669-10895
24	07/12/18	5448-5674	**48**	26/12/19	10896-11122
25	23/12/18	5675-5901	**49**	11/01/20	11123-11349
26	08/01/19	5902-6128	**50**	27/01/20	11350-11576
27	24/01/19	6129-6355	**51**	12/02/20	11577-11803
28	09/02/19	6356-6582	**52**	28/02/20	11804-12030
29	25/02/19	6583-6809	**53**	15/03/20	12031-12257
30	13/03/19	6810-7036	**54**	31/03/20	12258-12484
31	29/03/19	7037-7263	**55**	16/04/20	12485-12711
32	14/04/19	7264-7490	**56**	02/05/20	12712-12917
33	30/04/19	7491-7717	**57**	18/05/20	12918-13165
34	16/05/19	7718-7944	**58**	03/06/20	13166-13392
35	01/06/19	7945-8171	**59**	19/06/20	13393-13619
36	17/06/19	8172-8398	**60**	05/07/20	13620-13846
37	03/07/19	8399-8625	**61**	21/07/20	13847-14076
38	19/07/19	8626-8852	**62**	06/08/20	14077-14300
39	04/08/19	8853-9079	**63**	22/08/20	14301-14527
40	20/08/19	9081-9306	**64**	07/09/20	14528-14754
41	05/09/19	9307-9533	**65**	23/09/20	14755-14981
42	21/09/19	9534-9760	**66**	09/10/20	14982-15208
43	07/10/19	9761-9987	**67**	25/10/20	15209-15435
44	23/10/19	9988-10214	**68**	10/11/20	15436-15662
45	08/11/19	10215-10441	**69**	26/11/20	15663-15729
46	24/11/19	10442-10668	**TOT**		10370 / 8244

2.2.3 Data Processing

As a first step the information from these three streams are synchronised and merged together, by means of ad-hoc created Python routines, into a single ”aggregated” file containing all information regarding a pass and needed for the following steps. With a sampling rate of one sample per second, the information from HRDFEP and weather station are interpolated based on the SCU timestamp.

Passes may be lost for different reasons such as system issues or even for no information from one of the sources. Anyway, these lost passes are useful to understand the cause of failure and think about system improvements.

Furthermore, every Wednesday, routine maintenance tests of the Fairbanks Ground Station are performed, dumping the payload data over Alaska instead of Svalbard. This means for SNOWBEAR that the four passes of the afternoon do not feature payload data dump in the 26 GHz band and only background noise is recorded.

Correctly aggregated files were then checked one at a time, performing a single pass analysis, in order to discriminate between passes with and without problems and to classify them. These issues may be an initial lock on a sidelobe, partial or bad recorded information, loss of tracking for whatever reason and so on.

The second step consist in the so-called ”Single pass Analysis”. From this processing, correctly aggregated files were checked one at a time, in order to visually identify other issues on the pass and therefore classify them. These issues may be an initial lock on a sidelobe, servo system failures, problems with the HRDFEP, the SCU or RF switches, etc.

This discrimination is mandatory to not misrepresent the following analyses, which are performed on the set of usable passes after a filtering process of each individual pass, depending on the pass classification. Some of these ”exceptional” passes are flagged and excluded from the final analyses (e.g. in case of receiver failures there is no data), but others are instead only partially considered. This is the case in particular for those passes that exhibit issues only in a limited and recognizable time frame during the fly over Svalbard.

Different filtering algorithms have been therefore implemented for each possible issue, in order to get rid of bad samples and make each pass usable, because they are not directly related to propagation through the atmosphere and thus they would spoil the statistics.

The last step includes the so called ”cycle analysis” and ”statistical analysis”. The cycle analysis consists in aggregating the passes by repetition cycles. In this way the recorded samples can be used to draw a polar map, which covers almost the full range of possible combinations of antenna azimuth and elevation positions. This is very useful as different phenomena are impacting the propagation link in different ways depending on the antenna elevation and thus filtering the data based on the elevation can help isolating the specific effect of interest. For instance it was possible to identify a fictitious threshold at 30 deg elevation to separate attenuation effects due to snow or rain accumulation on the radome, which are affecting only elevations above 30 deg from purely atmospheric effects, which are on the contrary more evident below 30 deg of elevation. The statistical analyses were performed on the complete dataset and were useful to characterise the overall performance over different months of the year or in different elevation ranges.

Figure 2.17 summarize the overall processing scheme.

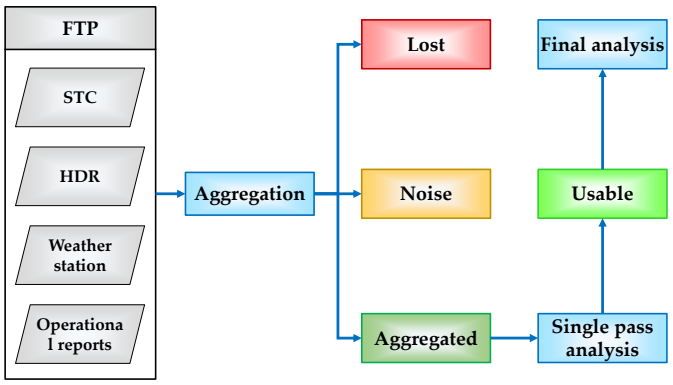

Figure 2.17: Processing scheme

The pass classification comprises seven different macro-categories, with the following meanings:

Usable AT and TLE nominal, these are the correctly recorded (or mostly) passes possibly available for the analysis.
No K-band no data dumped on Svalbard, thus, even if correctly acquired, these passes record essentially background noise. Not used for the analysis
Maintenance lost passes because of system maintenance
Servo lost passes because of problems related to the antenna moving mechanisms
M&C lost passes because of problems related to the ACU or SCU
Receiver lost passes because of problems related to the HDR or HRDFEP
Switch lost passes because of problems related to the routing switches

The most common occurring issues, presented hereafter in figs. 2.18 to 2.20, were: a lock on a sidelobe, the azimuthal axis wrap and the orbit trajectory near the horizon terrain profile. In these figures the co-polar (blue) and cross-polarisation (red) signal levels are shown superimposed on a dashed line (black) which represents the calculated theoretical copolar signal strength in case of clear sky. The instantaneous antenna elevation is also reported as reference (grey dashed line).

The lock on a sidelobe, occuring during the satellite rising over the horizon, might happen if autotrack was enabled when elevation was still below the mask or in its close proximity. Instead of being locked on the main delta null, whose direction corresponds to the main lobe (for the sum signal), the system lock on a side local null, generally corresponding to the angular direction of the first sidelobe of the sum radiation pattern. The time duration of this issue is random and depends upon what time the K-band becomes unstable enough to force the system to switch to S-Band autotrack and then relock correctly on K-band main lobe.

The azimuthal axis wrap occured just during one particular pass that systematically lose the pointing for a short time at very high elevation due to a servo-mechanic issue. This issue is self-explanatory by looking at Figure 2.19.

Finally, when the orbit trajectory is very close or even cut other radomes profile, both autotrack and signal reception are spoiled.

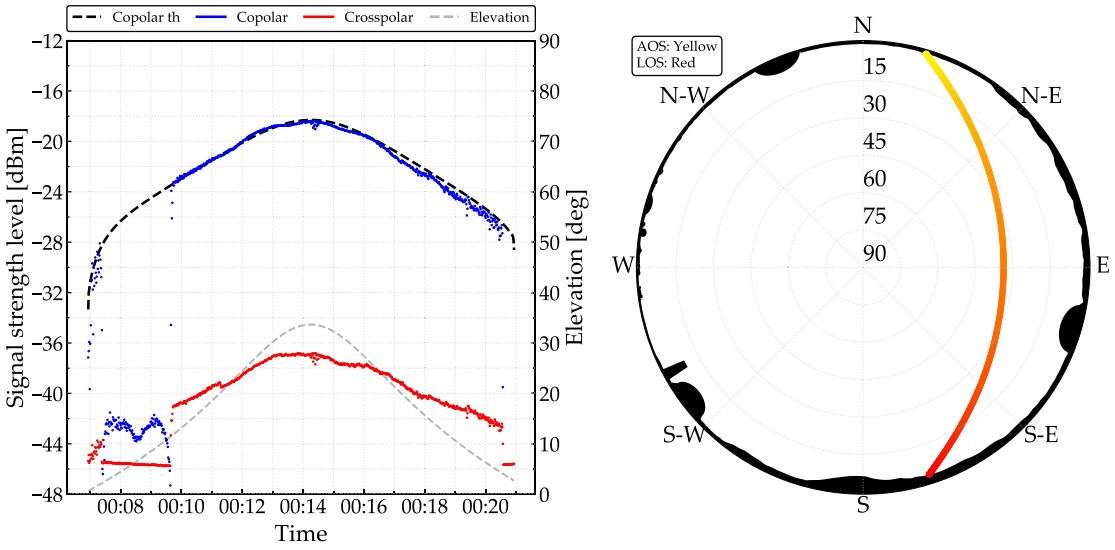

Figure 2.18: AOS on a sidelobe issue

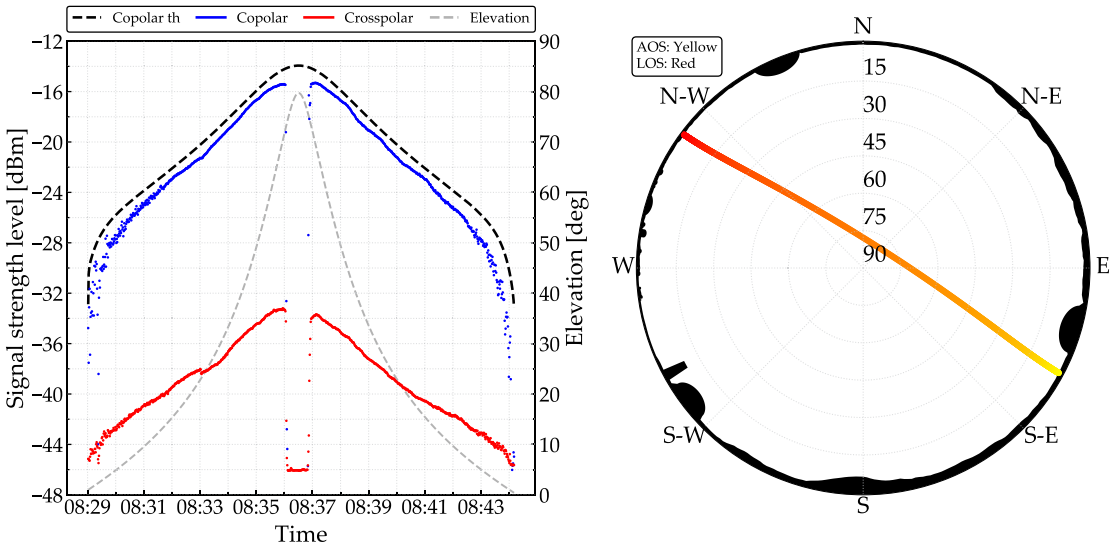

Figure 2.19: Azimuthal wrap issue

In addition to generating the single pass plots, this first analysis step produces a summary file, which collects some reference information for each pass, such as: Orbit number, cycle number, pass number within the cycle, Acquisition of Signal (AOS), Loss of Signal (LOS), maximum elevation reached, average outside and inside temperature, accumulated snow, noise diode calibration, TLE predictions validity, etc.

Based on this information some preliminary statistical evaluation can be performed on the pass recordings proficiency and the major causes of disruption. This is depicted in Figure 2.21

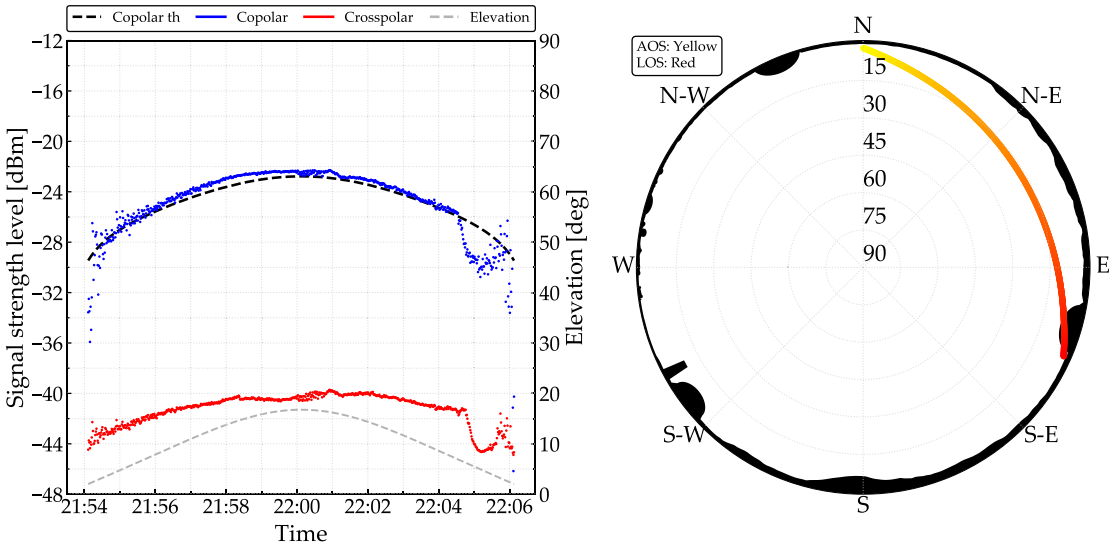

Figure 2.20: Orbit trajectory in proximity of other radomes profile

which shows the percentages of passes classified in each category, grouped by orbit cycle. As it can be appreciated the overall percentage of usable passes (autotrack nominal in light green, TLE nominal in emerald green) is in the order of 90%. The TLE nominal category represent passes taken after the 4th of July 2020, when a failure of the main polarisation switch occurred preventing the use of the autotrack functionality. The passes were therefore taken in the backup program track (open loop) mode, based on TLE but not used for the most of the performance statistics.

Figure 2.22 shows the same information considering the whole dataset.

The average sample distribution per cycle over the elevation is represented in Figure 2.23 while Figure 2.24 represent the recorded samples percentage distribution for the whole dataset. Is clearly visible that the vast majority of samples are recorded at low elevation. More in depth, 75% of the samples are collected at elevations <30 degrees, 19% at elevations between 30 and 60 degrees and only 6% for above 60 degrees. The total number of usable samples for the analysis is roughly 5 million, corresponding to 14 hundreds of hours.

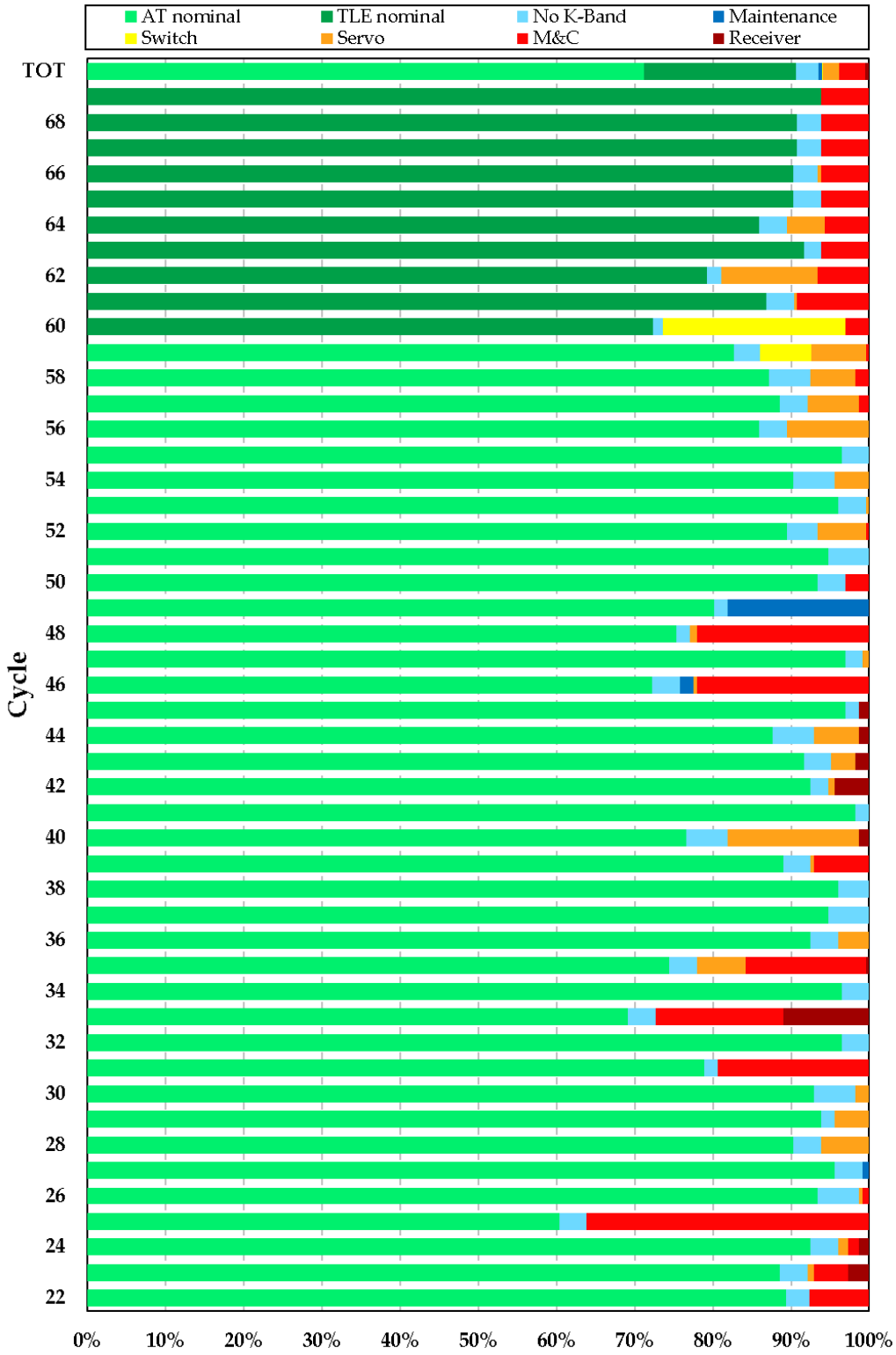

Figure 2.21: Passes classification percentages

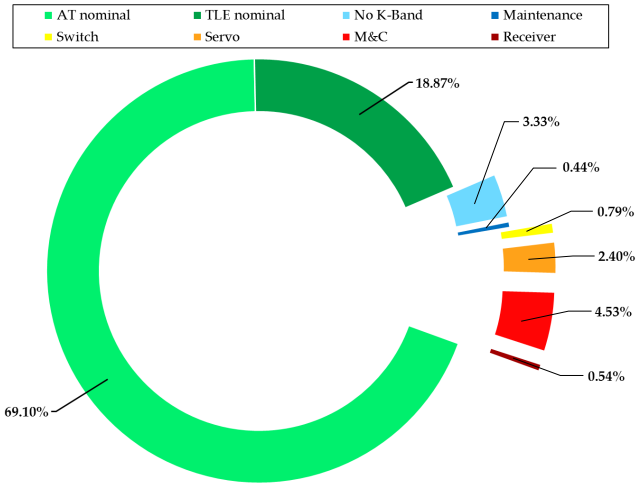

Figure 2.22: Passes classification percentages, whole dataset

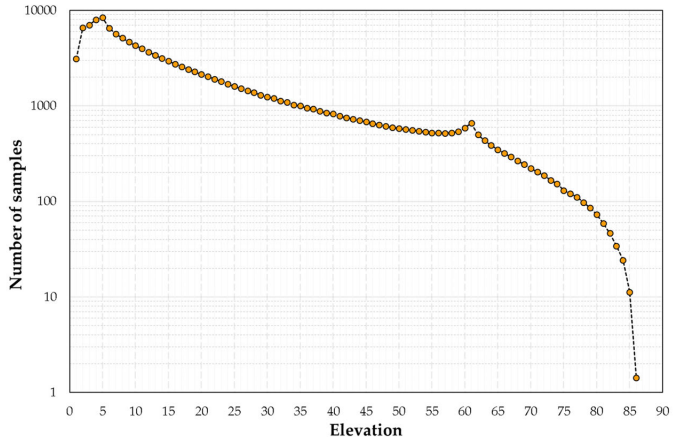

Figure 2.23: Cycle average number of recorded points vs elevation

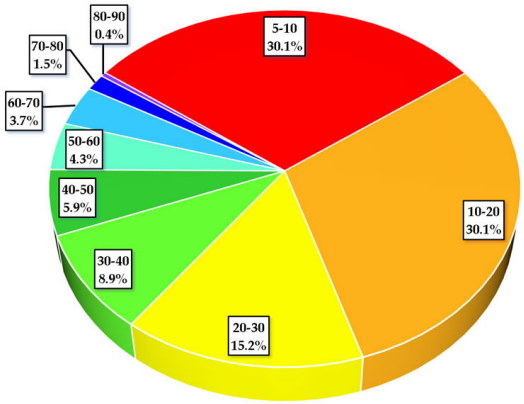

Figure 2.24: Percentage distribution of recorded samples vs elevation

Single pass analysis

This first post-processing step consist in displaying the evolution of some of the most relevant system parameters over the pass duration and comparing them against theoretical predictions. This step permits to visualise the performance of each single pass and identify all passes with issues that prevent them to be used for statistical evaluations. Six plots were generated for each pass, hereafter described.

Receiver signal strength The first plot generated by the python script displays the recorded signal strength at the HRDFEP over time. Both co-polar (RHCP, blue) and cross-polarisation (LHCP, red) levels are shown and they are superimposed on a dashed line (black), which represents the calculated theoretical signal strength (from Equation (2.25)) in case of clear sky. The instantaneous antenna elevation is also reported as reference (grey dashed line). This is the case for all plots versus time. The theoretical signal strength is calculated by the already described Link Budget in Section 2.1, implemented in a Python project, combining nominal spacecraft EIRP, path losses (clear sky atmospheric loss), modelled radome, antenna performances and level plan. Variation of LNA and converter gain due to temperature are accounted via a model derived from the pre- and post-pass calibrations performed with an integrated noise diode, which showed that the power recorded with both noise diode on and off showed a mirrored trend with respect to the hub temperature (Section 2.1.3).

Pointing and tracking error This plot displays the so called pointing error and tracking error evolution versus time.

The first is defined, in the frame of this project, as the deviation between the antenna axes positions as calculated from the TLE orbital predictions and the ones recorded by the antenna encoders (after non idealities, RF refraction and systematic errors correction).

The tracking errors are the angular misalignment with respect to the spacecraft position calculated by means of the monopulse autotrack system. The X is the cross-elevation axes, while Y is the elevation.

The plot shows also, with different background colours, which tracking mode was active in the different phases of the pass. White background means open loop program track based on TLE predictions; grey background means monopulse autotrack using the 26 GHz band signal and eventually orange background means monopulse autotrack using the 2 GHz band one.

Two additional Cartesian plots show the same errors in cross-elevation versus elevation representation. On these plots, two dotted circles represent the size of the antenna main lobe HPBW and the position of the first sidelobe, as visual reference to evaluate the misplacements entity. On the pointing error graph a text box reports how old were the TLE used for the calculation of the reference orbit.

Polar trajectory plot This polar graph shows the trajectory of the spacecraft through the sky as seen from the antenna location. The start of the pass is indicated in yellow and the end in red. The plot shows in black also the masking profile helping to identify graphically if a pass is crossing some masking object such as radomes, wire antenna (see SW direction) or mountains (mostly South and NE direction).

Residuals, Pointing and Tracking Loss This plot displays the so-called *residuals* from the comparison between the theoretical and recorded signal strength. They are called this way as they represent the "residual" signal attenuation along the Satellite-Ground Station link after removing the path loss. The residuals are then the combination of all other impairments such as absorption loss from snow or water accumulation on the radome, pointing loss, etc ... Mathematically speaking it is just the difference between the theoretical and measured copolar signal level at the input of the HDR. Since the reference theoretical signal strength is calculated assuming clear sky conditions, the residuals are also accounting for the excess atmospheric attenuation due to the actual weather conditions (high humidity, clouds, rain). The graph shows also the pointing loss calculated correlating the modulo of the pointing and tracking errors shown in the previous graph and the antenna radiation pattern. This is particularly useful to discriminate how much from the overall loss comes from antenna de-pointing and how much is due to atmosphere/absorption.

Noise Temperature This plot displays the noise temperature estimated by means of the SNOWBEAR noise calibration system and formulas described in Section 2.1.4. Just to recall, the procedure consists in measuring the background noise within a frequency band just outside the spacecraft signal bandwidth, by means of a parallel measurement chain (on the crosspolar chain) composed by a passband filter that cancels the spacecraft signal and a power meter that records the noise power. Measurements are calibrated at each spacecraft pass by injecting a known level of noise by an integrated noised diode. In this way one can estimate not only the overall System Noise temperature of both the ambient and cryogenic temperature LNAs chains, but also isolate the contribution from receiver electronics and sky (including radome). The plot reports then the ambient (red) and cryogenic (blue) system noise temperatures and the noise temperature from the sky (cyan). A dashed black curve shows as reference the sky temperature calculated by the theoretical model.

As showed from the plots this method works for low elevations, because at middle elevations and above, the crosspolar is simply too strong with respect to the background noise. Therefore, the noise temperature statistics are limited to elevations under 30 degrees.

Signal to Noise Ratio This plot displays the signal to noise ratio (SNR) as calculated by the HRDFEP from the demodulator output scatterplot (blue curve). This is affected by saturation (at 29 or 33 dB depending whether payload or idle data is transmitted) due to the on board generated noise. In order to get a saturation-free representation (cyan) the SNR is also calculated combining the measured signal strength at the receiver and the measured system noise temperature. Once again the SNR calculated using the theoretical model is reported with a dashed black curve. A red dashed line represents the reference for "good reception", i.e. corresponds to the SNR needed to guarantee a Frame Error Rate (FER) of at least 10^{-7}. The background is coloured in grey when the spacecraft is dumping payload data (and white when is dumping idle data).

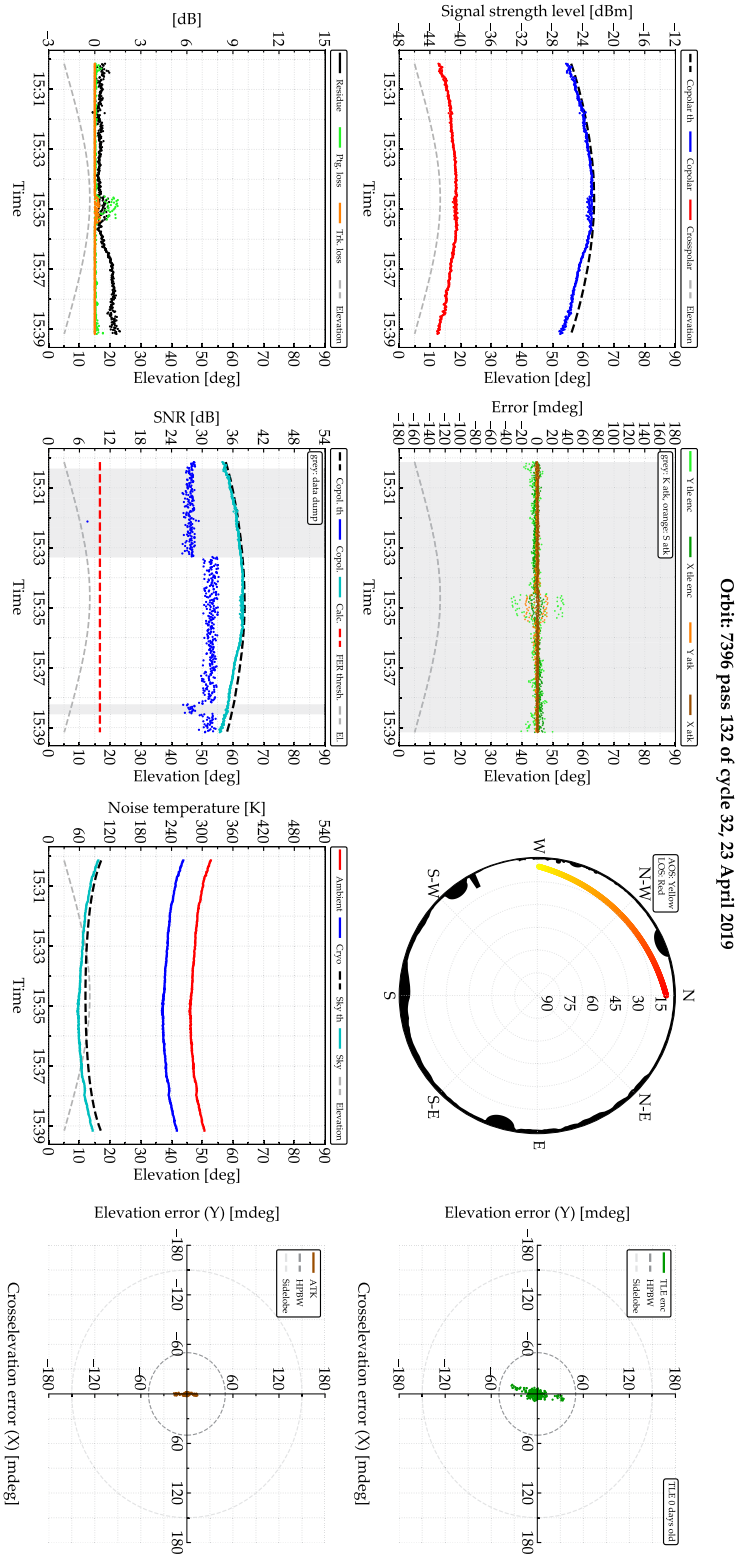

Figure 2.25: Example of single pass analysis (1)

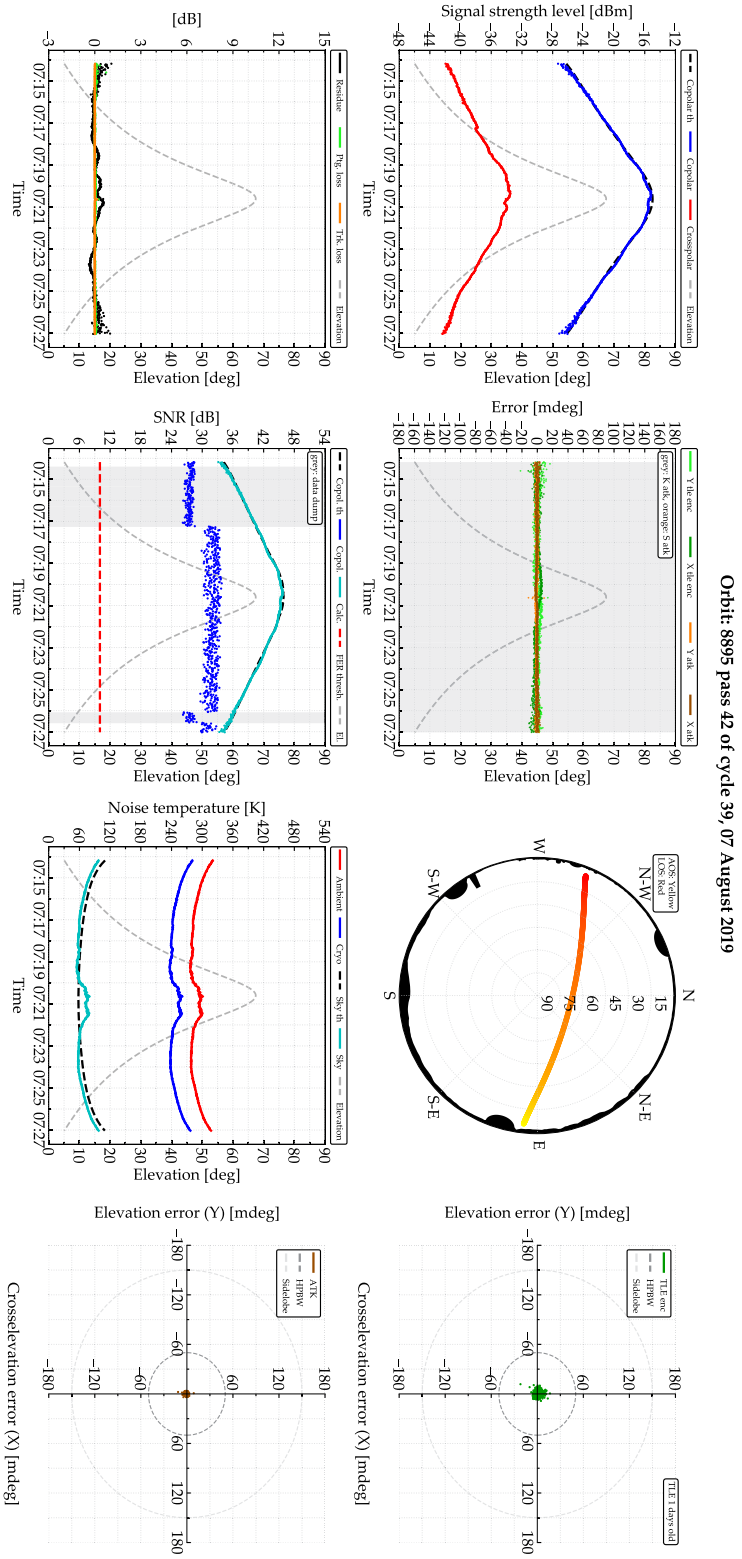

Figure 2.26: Example of single pass analysis (2)

Cycle analysis

This post-processing stage groups and analyise the recorded passes in cycles of 227 orbits, covering 16 days each. This particular grouping was selected because in this way the polar graphs generated by plotting certain parameters of interest versus azimuth and elevation position could cover the full hemisphere with no overlap between orbits.

Received signal power The power level of the co-polar component of the received signal at the ground station receiver, in dBm, plotted versus elevation and in polar coordinates. In the square plot are shown both the instantaneous values measured during satellite passes and the mean (estimated considering the linear values, converted than back in logarithmic) for each elevation step (resolution is 1 degree).

Crosspolar discrimination The cross-polar discrimination, i.e. the difference between the signal strength of the copolar and crosspolar components of the signal at the ground station receiver is plotted vs. elevation and in polar coordinates. In the square plot are shown both the instantaneous values measured during satellite passes and the mean (estimated considering the linear values, converted than back in logarithmic) for each elevation step (resolution is 1 degree). Note that the dotted line indicates the nominal cross-polar level, around 18 dB, calculated from spacecraft and ground station antenna nominal axial ratio specifications, that are respectively equal to 2 and 0.5 dB.

Pointing Errors and corresponding loss The angular deviation direction between the predicted position of the spacecraft in the sky and the actual pointing of the antenna is plotted in its two cross-elevation and elevation components in polar coordinates, beside the estimated pointing loss calculated from the antenna gain pattern and considering the two angular error. For passes recorded in autotrack mode the errors and consequently the pointing loss represent the difference between the TLE trajectory prediction and the antenna pointing position, while if recorded in TLE tracking mode they represent the tracking voltage error recorded by the tracking receiver converted in degree.

Frames The value of received, corrected and uncorrectable (lost) frame rate is plotted in polar coordinates.

Residuals The residual errors between the measured and theoretically estimated signal strength at the receiver are plotted vs. elevation and in polar coordinates. In the square plot are shown both the instantaneous values measured during satellite passes and the mean (estimated considering the linear values, converted than back in logarithmic) for each elevation step (resolution is 1 degree). Please note that in the polar plot the colour scale saturates at 8 dB. This was chosen as best compromise in order to identify the angular areas affected by degradations, even if small.

Another useful representation of the residuals is vs. time in order to have the possibility to correlate their variations against weather events. In such composite representation, the two upper graphs represent the maximum (red track), minimum (green track) and average (black)

residual errors for each pass. The upper part of the graph is dedicated to the residuals and pointing loss: the upper graph show the calculated value for elevations above 30 deg, the second for elevations below 30 deg, the third graph show with the same colour code the estimated pointing loss. The lower part of the graph is dedicated to the weather effects: the upper graph shows the mean precipitation (i.e. drizzle, rain, snow, hail etc.) intensity in mm/h, the middle one is the accumulated snow on the ground, in centimetres, and the lowest one is the mean external temperature in Celsius for each pass.

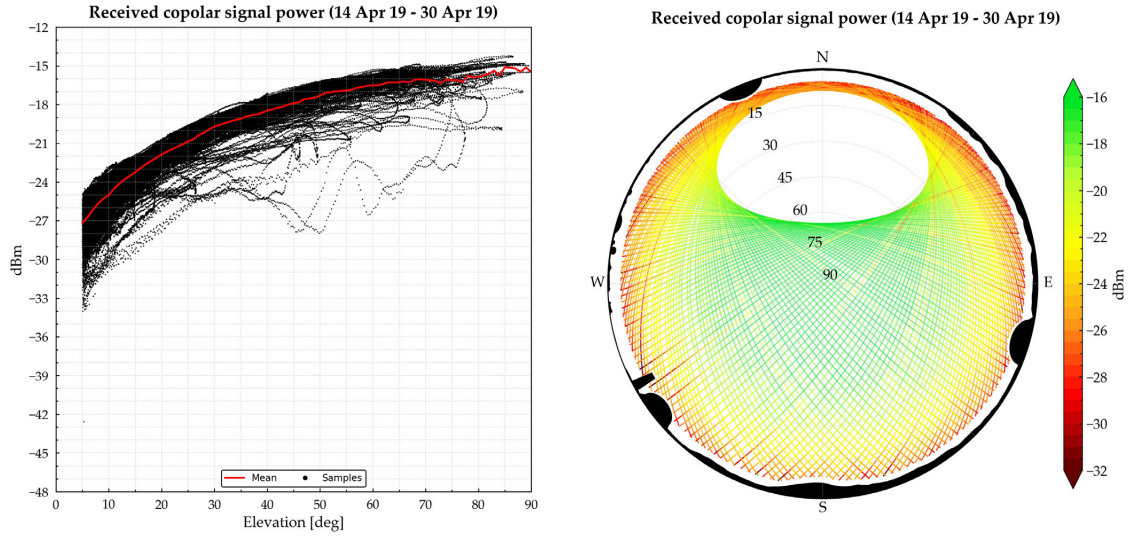

(a) (b)

Figure 2.27: Example of received signal level (a) vs. elevation, b) in polar plot

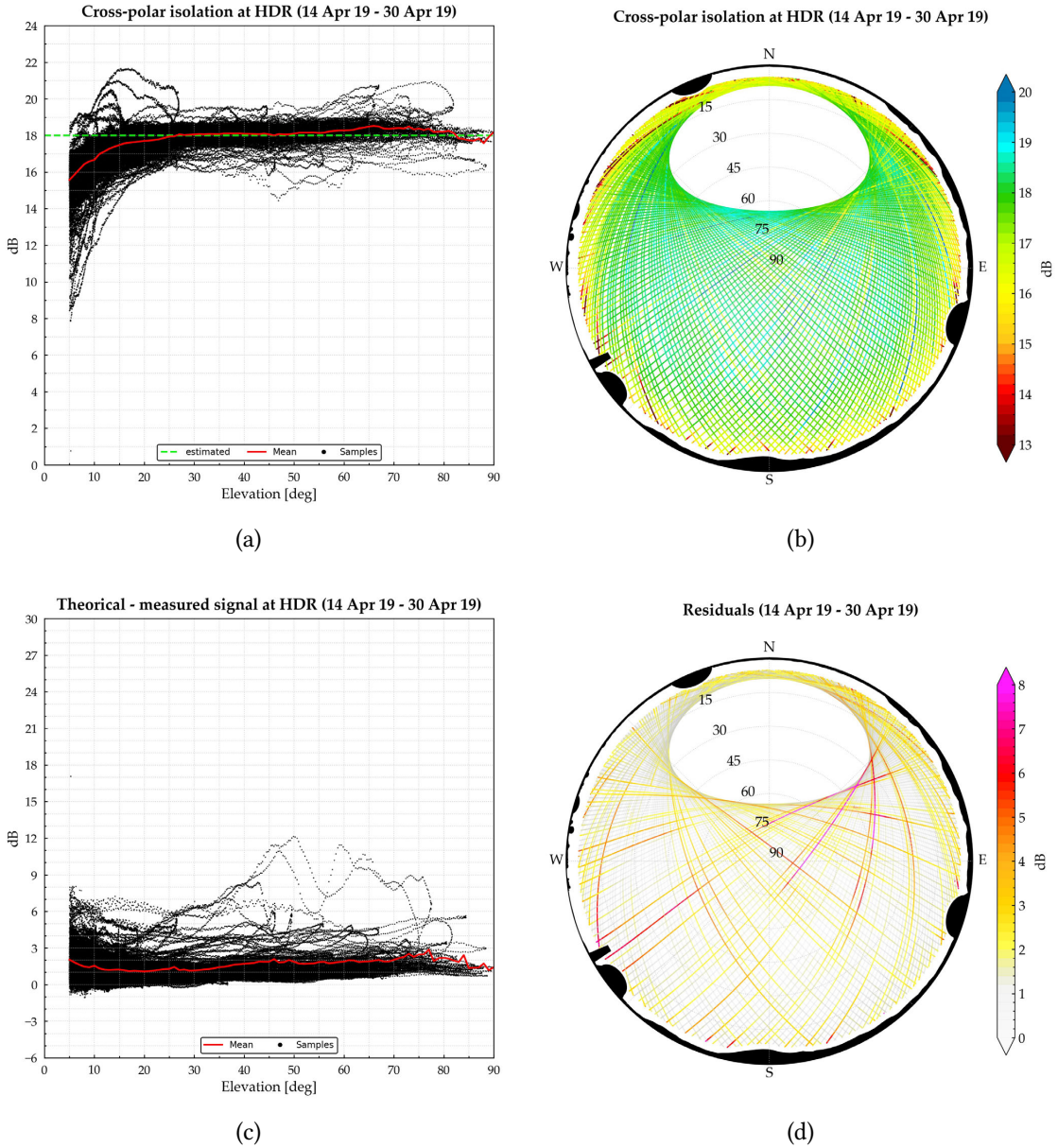

Figure 2.28: Example of crosspolar isolation level (a) vs. elevation, b) in polar plot; residuals (c) vs. elevation, (d) in polar plot

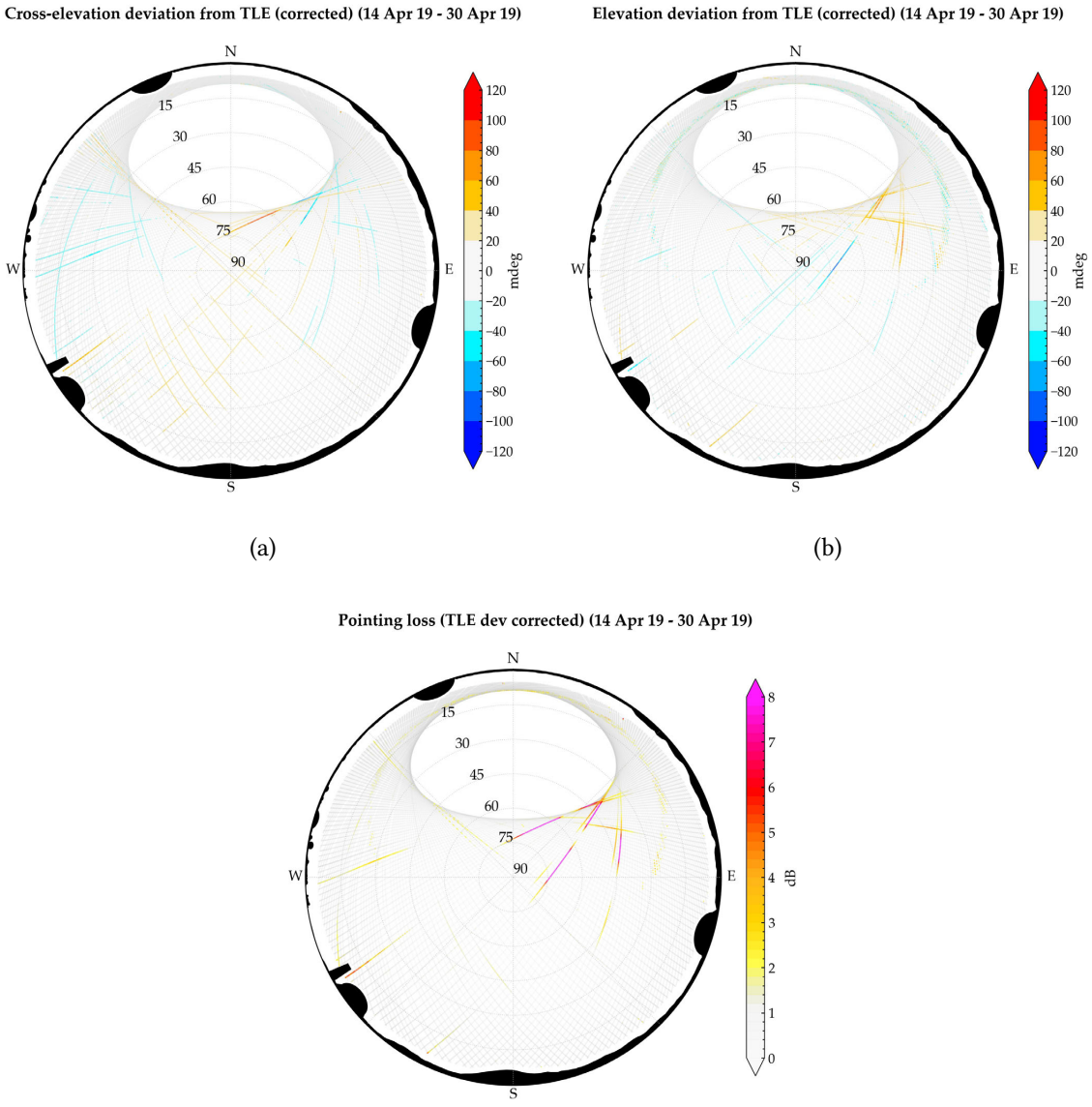

Figure 2.29: Cycle analysis example: a) Cross-elevation, b) Elevation components of the Pointing error, c) Pointing loss

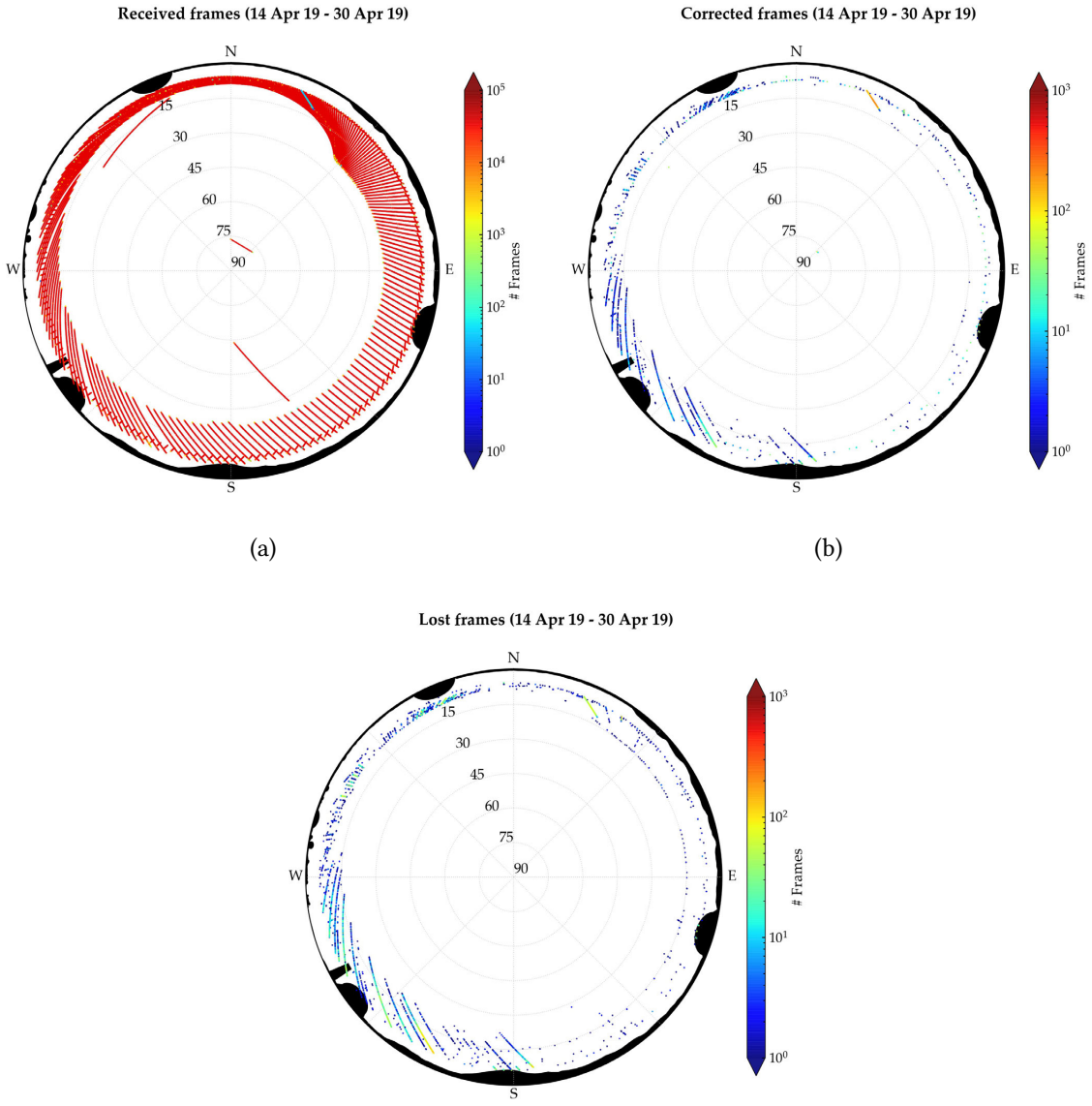

(a) (b)

(c)

Figure 2.30: Cycle analysis example: a) Received frames, b) Corrected frames, c) Lost frames

2.3 Snow on radome

Being Svalbard a rather deserted environment with very few precipitations all around the year it was deemed sufficient to use for the SNOWBEAR radome the same snow removal technique used so far for all other radomes at SVALSAT. This consists in cleaning the surface using a rope, which is attached at the radome's summit and is manually swept around the semi-sphere after each snowfall. Unfortunately, since the very beginning of the operational phase, it became quite clear that the tiny layer of snow mixed with ice that remained attached to the radome surface after the cleaning, although very thin, was still causing severe losses on the K-band link. At the same time it became quite clear that the very rare occurrences of rainy episodes in Svalbard could not be used to collect statistically useful data on the effect of the rain on the radome on the link budget, which was one of the original goals of the project. Therefore, it was decided to steer the analysis effort from the observation of rain effects to the more severe and statistically meaningful snow and ice effects.

As first step the single pass and full cycle analysis were used for a qualitative evaluation of the snow/ice impairments, i.e. at which elevation the effect was noticeable, when was it mostly happening, which correlations with the weather events could be observed and last but not least to try to identify its root cause.

First of all it was recognised that the highest concentration of impairments (residuals and pointing loss) were recorded in the months of March/April and October/November, with another peak during the Christmas holidays. It was demonstrated that this latter was most likely due to the fact that in that period no maintenance activity (snow removal) was performed. In the same period high winds were recorded in the very same direction of the attenuation peaks,

Figure 2.31: Example of snow on radome

so it was concluded that the snow was pushed on the radome by the wind and stayed until the end of the holidays when the maintenance activities restarted.

The higher occurrence of signal loss in the spring and late-autumns months seems to be related to the composition of the snow cumulating on the radome. While during the extremely cold winter months the snow is very dry and uniform, in these other months the sun illuminates the radome and melts the snow during the day, then during the night it freezes again. The radome surface is therefore covered with a composite irregular layer made by wet snow, ice and water, which has higher dielectric constant and loss tangent than the dry snow. This causes, as expected, higher signal absorption, while the non-homogeneous distribution seems to have the even more detrimental effect of squinting the RF beam. It was in fact calculated that the absorption component could account only for a relatively small portion of the overall signal loss (in the order of 4-6 dB), while residuals up to 20 dB were recorded.

De-pointing Problem Description

At the frequencies of interest, snow accumulation on a radome can provide different effects on the link, most important are reflection, absorption, scattering, and de-pointing of the main beam.

Reflection occurs because of the impedance mismatch between air, the snow layer on top of the radome, and the radome itself. Even at those frequencies where, ideally, radome is perfectly transparent when dry, snow introduces an extra condition not account for during the design phase of the panel layers, causing mismatch.

The absorption effect comes naturally from the fact that the signal travels through a lossy dielectric medium. For snow, this normally happens when the liquid water content (LWC) of the snow itself is larger than zero, i.e., when snow can be defined as wet. This can be the case in certain periods of the year because of increased temperatures and/or direct sunlight incidence. Scattering of the incoming electromagnetic wave occurs when signal wavelength is comparable with the dimension of snow crystals.

Finally, de-pointing is induced when the wave front is unevenly distorted because of the snow on top of the radome, for example because the snow accumulation shape and thickness vary along the radome. All effects are more significant when the antenna is moving at elevations higher than around 30 degrees, where the presence of snow is more probable because the radome above is less steep, and snow can accumulate easier. While the final outcome of all these effects is a reduction of the signal magnitude, de-pointing is particularly critical because it is responsible for the generation of a misalignment between the antenna pointing and the satellite position. The modelling can be complex, as well as the possibility to correct for it in real time, as a number of parameters, for example the dielectric and geometrical properties of the snow accumulation, are difficult to predict and/or to sense.

As an example, Figure 2.32 presents the effects caused on the antenna pointing by two snow layers, apparently similar, for an entire orbital cycle. More in details, Section 2.3 and Section 2.3 show the modulo of pointing error, while Section 2.3 and Section 2.3 show its direction, on a polar map in the elevation/cross-elevation domain, which represent the entire sky as seen from the ground station. In particular, the pointing error is calculated as the angular deviation between the antenna axes positions as recorded by the antenna encoders and during a reference

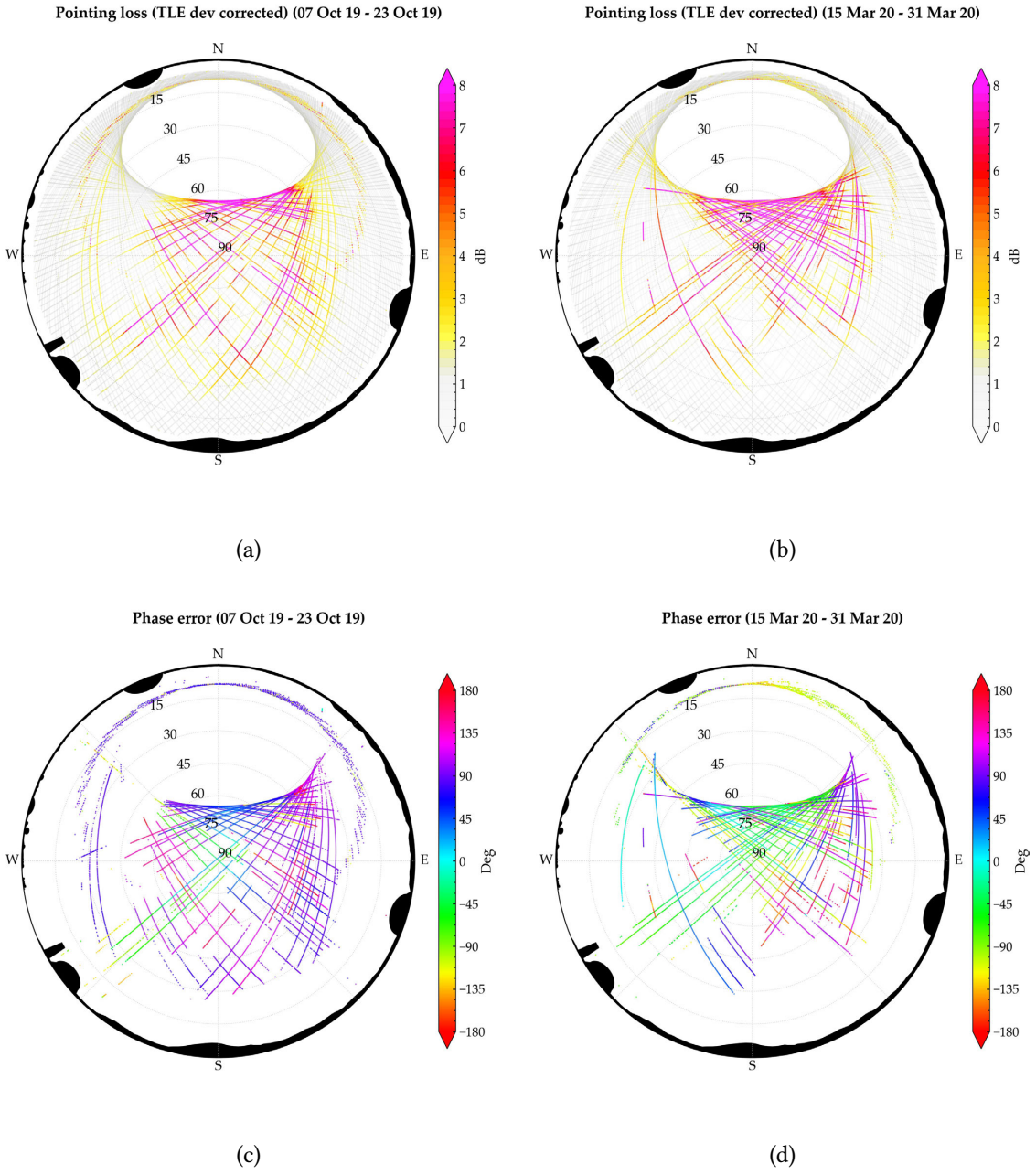

Figure 2.32: Distributions of the pointing loss modulo (a-b) and phase (c-d) for two cycles with similar snow layer on the radome

case, identified considering the same pass recorded in autotrack during summer and under ideal sky conditions (this is taken instead of the orbital predictions in order to a-posteriori correct a systematic error of the SNOWBEAR pointing system). As one can see (Section 2.3 and Section 2.3), pointing errors distributions are very similar in terms of magnitude (it can be observed that magnitudes exceeding 100 mdeg are recorded, as large as the width of antenna main beam,

shown in Figure 2.10b, thus potentially causing large impairments) but the phase distribution, corresponding to the de-pointing direction (Section 2.3 and Section 2.3), is considerably different between the two cases. Therefore, it is impossible to determine whether snow tends to squint the beam towards a certain direction, for instance depending on the antenna elevation angle (and thus amount of beam intercepted by the snow cap).

Since the system normally works in autotrack mode and the antenna pointing direction is driven by the tracking error (e.g. the null of the delta channel radiation pattern) one could think to limit the induced pointing loss by setting the system in program track mode and follow the predicted satellite trajectory. But a more in depth analyses of each pass performance showed that both autotrack and program track modes are affected by the snow cap in a similar way.

To better understand, Figure 2.33 to Figure 2.36 show a set of key parameters recorded during the same pass , using both autotrack (Figure 2.33 and Figure 2.35) or program track (Figure 2.34 and Figure 2.36), in presence of snow/ice on top of the radome. More in detail, Figure 2.33 and Figure 2.34 show the recorded signal strength over time at the receiver. Both co-polar (right-hand circular polarization, RHCP, blue) and cross-polarization (left-hand circular polarization, LHCP, red) levels are shown and they are superimposed on a dashed line (black) which represents the calculated theoretical co-polar signal strength in the ideal case (no snow and clear sky). Finally, the elevation angle (dashed grey) of the antenna along over time is shown. Instead, Figure 2.35 and Figure 2.36 show the so-called residual (black line), which is the difference between the theoretical and recorded co-polar signal strength (i.e. the difference between the black dashed line and the blue line in Figure 2.33 and Figure 2.34).

Figure 2.34 and Figure 2.36 show also the pointing loss (green line) and the tracking loss (orange line). These are not measured, but calculated, and useful to understand the origin of the residual. In particular, pointing loss is simply calculated from the pointing errors (as already stated, calculated from the angular deviation between the antenna axes positions as recorded by the antenna encoders and as recorded during a reference pass in summer and under ideal sky conditions) mapping it on the radiation pattern of the antenna. Tracking loss is calculated from tracking errors, which are calculated as the angular deviation between the direction of the delta signal null and the direction of antenna axes positions as recorded by the encoders. Again, once the tracking errors are known, tracking loss is calculated mapping the tracking error on the radiation pattern of the antenna.

First, comparing the residuals, it is possible to see that similar losses occur for both operational procedures. This means that both program track and autotrack are not able to compensate for the de-pointing. In particular, for autotrack mode, observing Figure 2.33 it can be seen that tracking losses are practically zero for almost the entire pass, confirming that the antenna followed the deflected delta null, as expected for the autotrack mode. Instead, pointing losses are large, indicating that the pointing of the antenna is not in line with the reference pass recorded during summer with clear sky. Conversely, in program track, Figure 2.34, the situation is practically the opposite, with minimal pointing losses (as expected, as in program track the predicted pointing is supposed to be in line with the reference summer pass) and large tracking losses, as the signal and delta beams are distorted by the presence of snow on top of the radome.

Overall, a key point emerged, regardless of the tracking mode, auto or program. In presence of snow/ice on top of the radome, pointing errors were extremely high both in autotrack mode

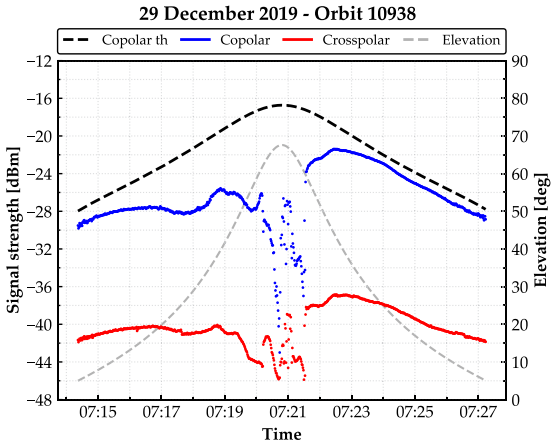

Figure 2.33: Example of a winter pass recorded in autotrack. Measured co-polar (blue) and cross-polar (red) signals at the receiver, theoretical co-polar (dashed black) and elevation angle (dashed grey)

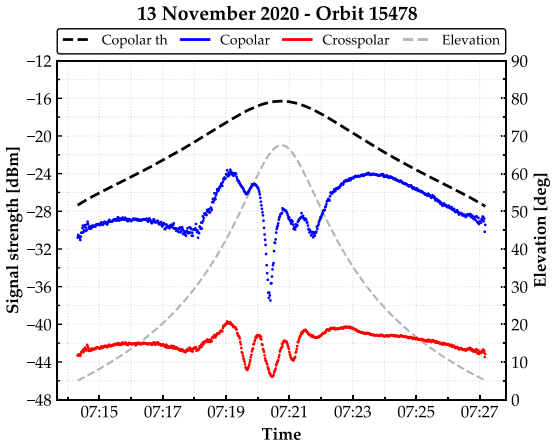

Figure 2.34: Example of a winter pass recorded in program track. Measured co-polar (blue) and cross-polar (red) signals at the receiver, theoretical co-polar (dashed black) and elevation angle (dashed grey)

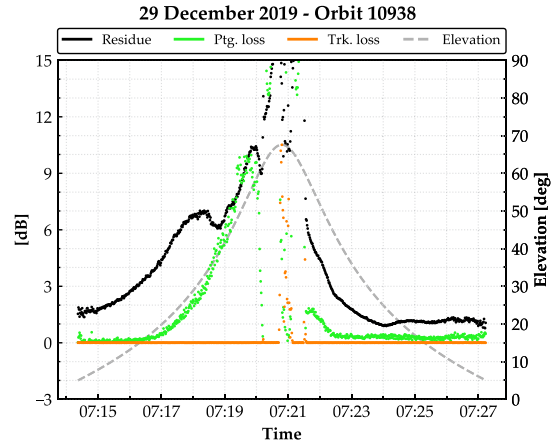

Figure 2.35: Measured residual (black), calculated pointing loss (green) and tracking loss (orange) for the case reported in Figure 2.33

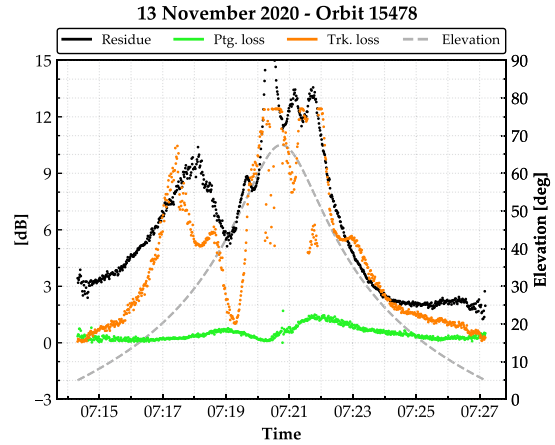

Figure 2.36: Measured residual (black), calculated pointing loss (green) and tracking loss (orange) for the case reported in Figure 2.34

(closed loop) as in program track (open loop). This led to the conclusion that the beam squint imposed by the snow affects differently the sum (data channel, TE11) and delta mode (tracking channel, TM01) of the antenna. In autotrack, this can be inferred by the fact that residuals are present, despite the lack of tracking errors for most of the pass. Indeed, if the squint of the sum mode was identical to the delta mode one, the latter correctly compensated, as tracking errors are negligible, then residuals would be also negligible. In program track, an identical squint for sum and delta mode would have imposed practically identical values for tracking errors and residuals, but this is not the case. However, this assumption requires further investigations,

presented in the next section.

Simulations

In order to verify our measurements and confirm assumptions made about the antenna depointing caused by the snow and in particular for what concerns the different deflection undergone by the sum and delta channels, a set of simulations were carried out, with the aim of exemplifying notable cases. To maintain a tolerable computational effort and preserving a general validity, instead of simulating the entire reflector antenna with its own radome, a cylindrical horn was modelled in HFSS (a commercial full-wave 3D EM simulation software [39]) and simulations were run at 27 GHz, considering different scenarios, shown in Figure 2.37.

To keep the simulations as consistent as possible with the real SNOWBEAR case, the sum channel was generated exciting the two degenerate TE11 modes, 90 degrees out of phase one to the other to obtain the circular polarisation. Conversely, the delta channel was generated exciting the TM01 mode.

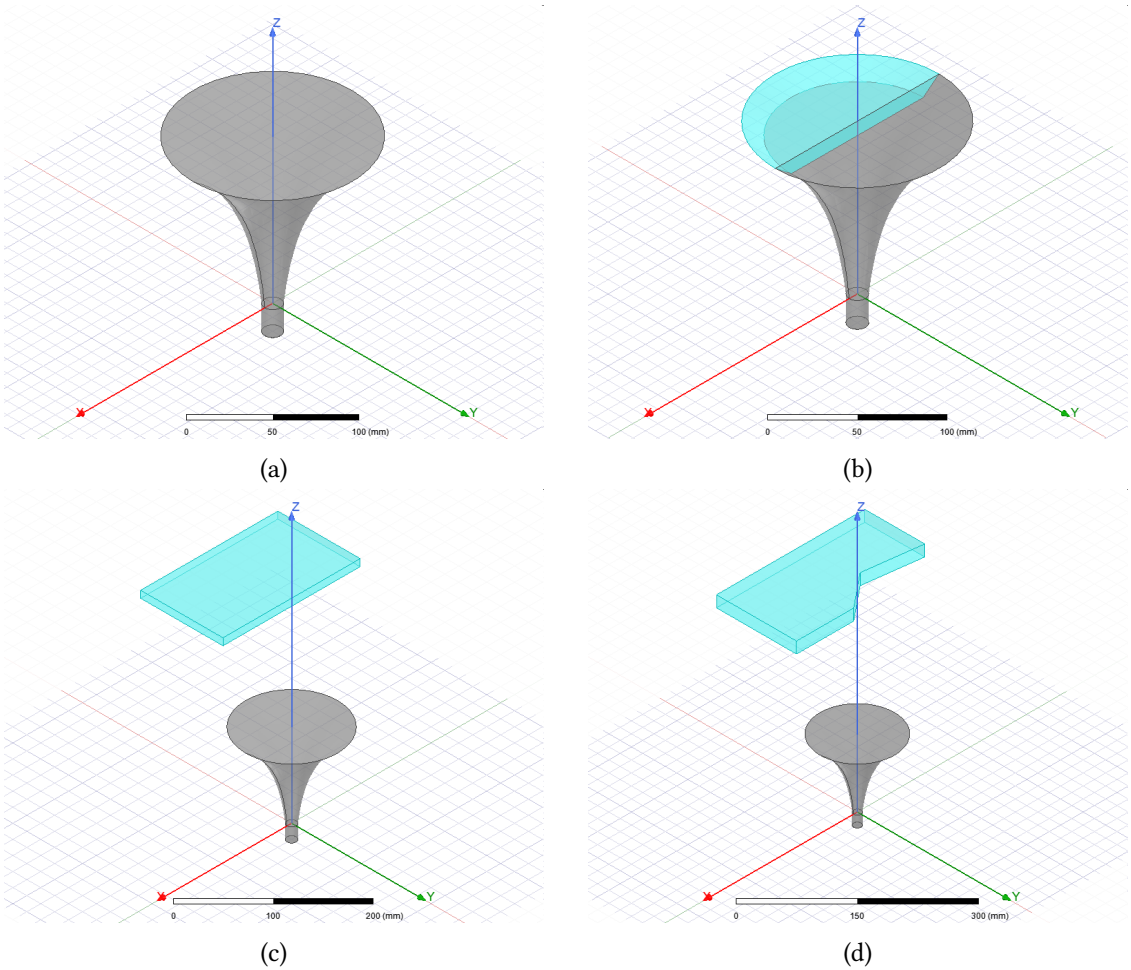

Figure 2.37: Circular horn antenna and snow layer simulation schemes

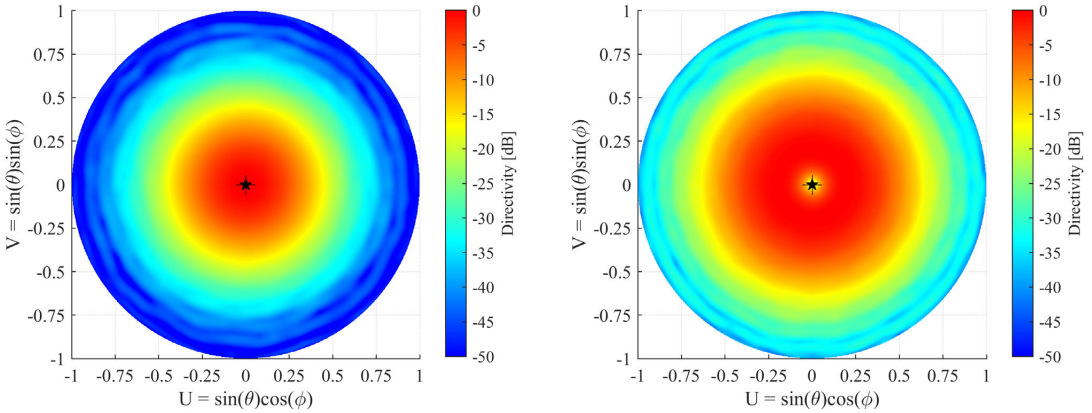

Figure 2.38: TE11 (a) and TM01 (b) modes for case A (Figure 2.37a)

First of all, the horn was simulated standalone to have a reference case to be compared against the others (case A). Computed sum and delta radiation patterns for this ideal case are shown in the UV-domain in Figure 2.38a and Figure 2.38b, respectively. All results are normalised to maximum directivity value. Black and white stars in the graphs indicate respectively the position of the maximum directivity and the tracking null.

Then, a layer of dry snow (density equal to $300kg/m^3$, corresponding to a dielectric constant $\epsilon_r = 1.549$ [40]) was modelled and inserted in the horn immediately above the aperture (case B). The thickness of this layer is 1 cm and it is placed in order to cover half of the horn aperture. Computed sum and delta radiation patterns for this case are shown in the UV-domain in Figure 2.39a and Figure 2.39b, respectively.

As a third case, a uniform layer of dry snow, modelled as a parallelepiped with a thickness of 1 cm was placed in front of the feed, at a distance of 15 cm (more than 10 free-space wavelengths) from the horn aperture (case C). The snow is displaced with respect to the antenna Z-axis so that the propagation direction is half covered by it. Computed sum and delta radiation patterns for this case are shown in the UV-domain in Figure 2.40a and Figure 2.40b, respectively.

The fourth case (case D) is similar to the previous one except from the snow thickness, orientation and shape. The thickness is 2 cm and the snow shape is not regular but is designed to be conformal with a region of the radome where two or more panels are joint together thus resuming the profile of the radome panels junctions. This because it was observed that sometimes the snow tends to stick on the radome following the joint profile creating a region with an important discontinuity between the presence of snow, at higher elevations, and without snow, at lower elevations, which may be considered as a worst case. Computed sum and delta radiation patterns for this case are shown in the UV-domain in Figure 2.41a and Figure 2.41b, respectively.

Finally, the setup of the last case (case E) is identical to the one of case D, but with wet snow (dry density equal to $400kg/m^3$ and $LWC = 3\%$, corresponding to $\epsilon_r = 1.824$, $tg\delta = 0.05094$ [40]). Computed sum and delta radiation patterns for this case are shown in the UV-domain in

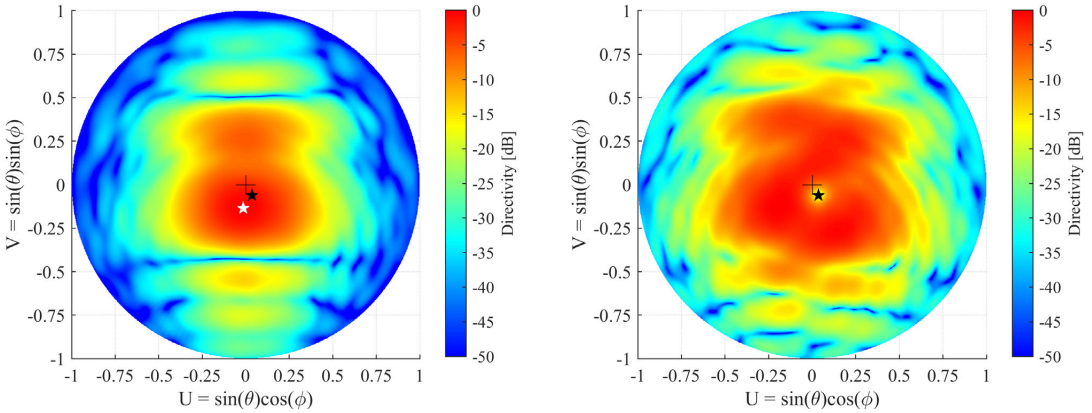

Figure 2.39: TE11 (a) and TM01 (b) modes for case B (Figure 2.37b)

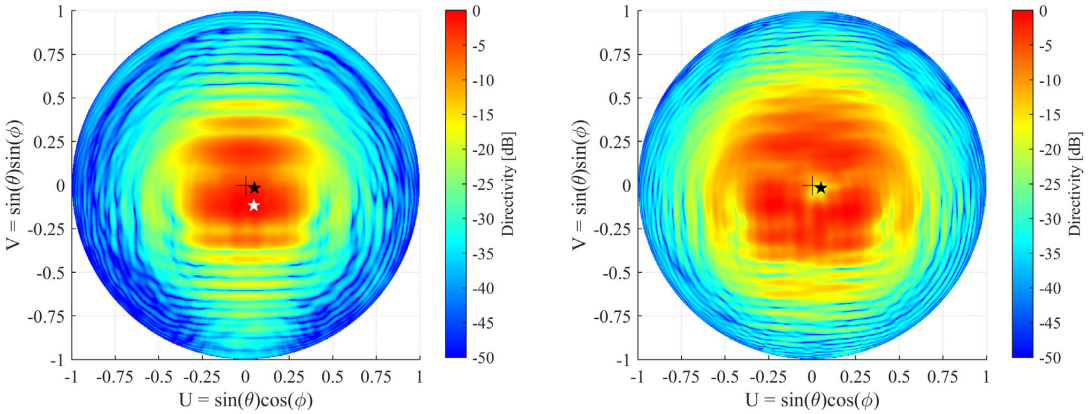

Figure 2.40: TE11 (a) and TM01 (b) modes for case C (Figure 2.37c)

Figure 2.42a and Figure 2.42b, respectively.

For all the simulations, the angular squint for the Σ-channel main lobe and Δ-channel null are summarised in Table 2.3. Considering the horn HPBW, which is approximately 20.5 degrees, in presence of snow it is possible to observe a significant misalignment between both channels and the Z-axis direction. In particular, for case D and E, the irregular contour of the simulated layer greatly changes their shape. The only significant change observed in the radiation patterns between case D (dry snow) and case E (wet snow) is a different position for both max directivity and tracking null caused by the different attenuation of that portion of the wave that travels inside the snow. Looking at the Δ-channel diagrams it can also be observed that the mode null identification can be misinterpreted by the presence of many local nulls, and more in general by the pattern degradation, further worsening the performance in autotrack mode.

Overall, Table 2.3 confirms that the de-pointing effect is relevant, and in general not equal for

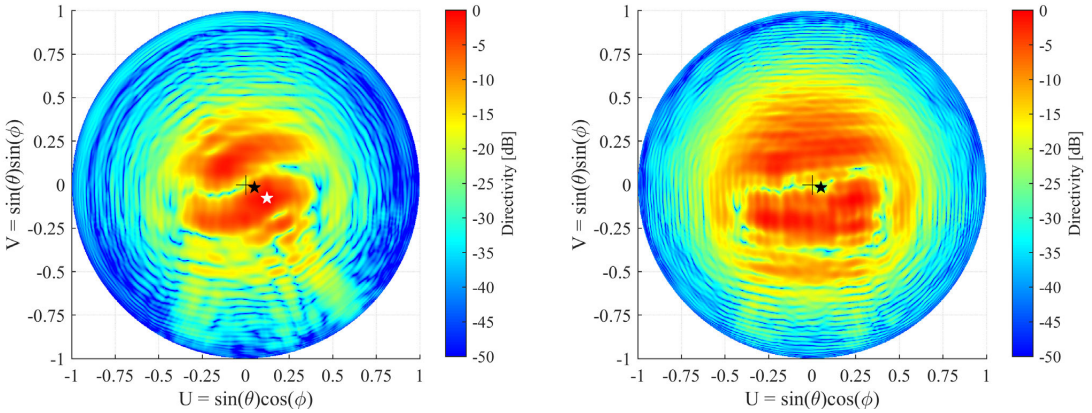

Figure 2.41: TE11 (a) and TM01 (b) modes for case D (Figure 2.37d)

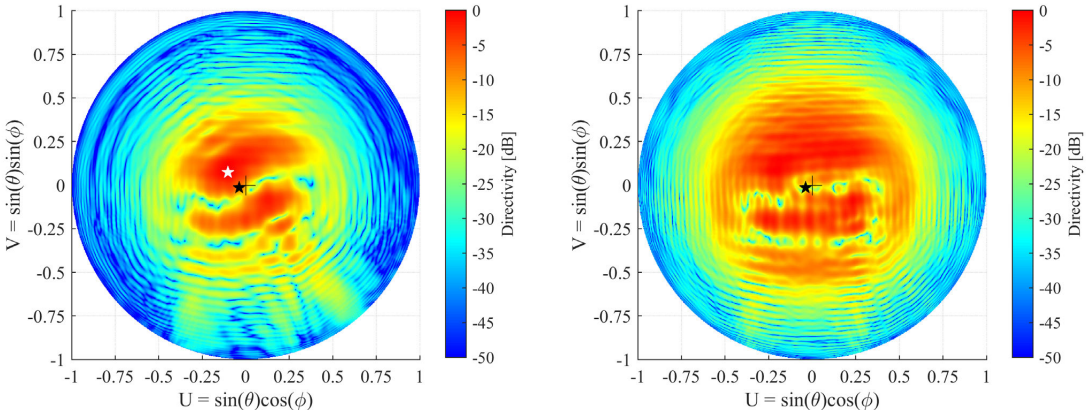

Figure 2.42: TE11 (a) and TM01 (b) modes for case E (Figure 2.37d)

the sum and delta modes, even if the particular case where the de-pointing effect is practically equal can happen, as demonstrated with the experimental passes reported in Fig. 21 to 24, collected using autotrack. In particular, analysing Figure 2.43 and Figure 2.44, related to a pass recorded during the night of 9 December 2018, thus with conditions that strongly suggest the presence of dry snow (i.e. no sunlight and freezing temperatures), it is possible to see huge residuals, overlapped almost perfectly with the pointing loss estimation trend (apart from the central part when the autotrack was lost). This means that, even if the snow accumulated on the radome was affecting the antenna pointing, the snow distribution was as such as the de-pointing effect is similar for the sum and the delta mode. Another example where the de-pointing effect is similar for the sum and the delta mode is presented in Figure 2.45 and Figure 2.46. This pass was recorded on 24 March 2019, during a clear sky day, as shown in Figure 2.47 (the photo is unfortunately over-exposed because of the snow albedo). Thus, even if the external

temperature was still below 0 degrees, the snow was irradiated by direct sunlight, and this may cause an initial, mild, melting of the snow accumulated on the radome. In this case, not only the de-pointing effect is similar for the sum and delta modes, but practically no pointing errors were recorded and consequently no loss contribution was estimated. This can be the case when snow accumulated on the radome is distributed uniformly along the antenna axis. However, residuals are as high as 3 dB, thus suggesting that this estimated loss can reasonably be attributed to effects others that de-pointing, mainly to snow absorption.

Table 2.3: Squint values (deg, elevation θ and azimuth ϕ) for cases of Figures 2.38 to 2.42 for sum (Σ) and delta (Δ) modes. Horn HPBW approx. 20.5 deg.

	B	C	D	E
Σ, θ	7.807	7.281	8.335	7.212
Σ, ϕ	-96.340	-67.989	-32.320	144.728
Δ, θ	4.108	3.037	3.037	2.315
Δ, ϕ	-60.751	-19.29	-19.29	-158.199

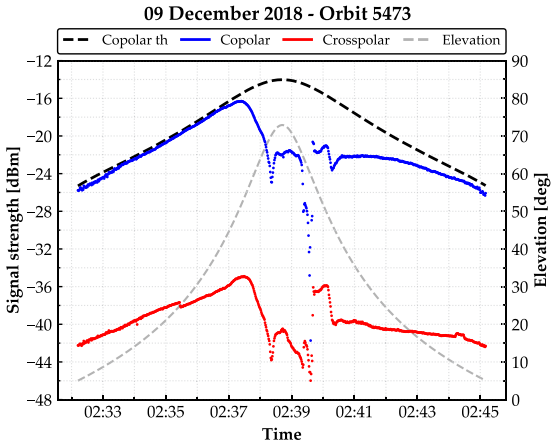

Figure 2.43: Orbit 5473, 9 December 2018, recorded in autotrack. Measured co-polar (blue) and cross-polar (red) signals at the receiver, theoretical co-polar (dashed black) and elevation angle (dashed grey)

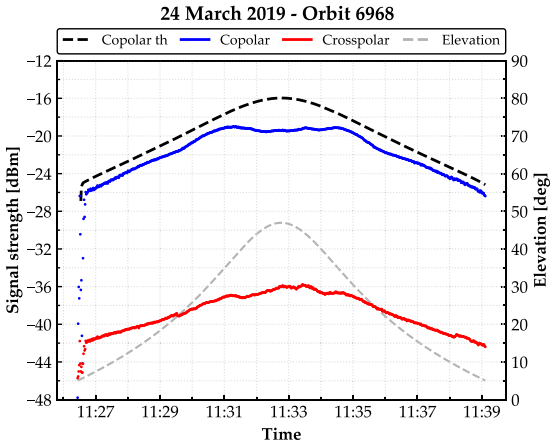

Figure 2.44: Orbit 6968, 24th March 2019, recorded in autotrack. Measured co-polar (blue) and cross-polar (red) signals at the receiver, theoretical co-polar (dashed black) and elevation angle (dashed grey)

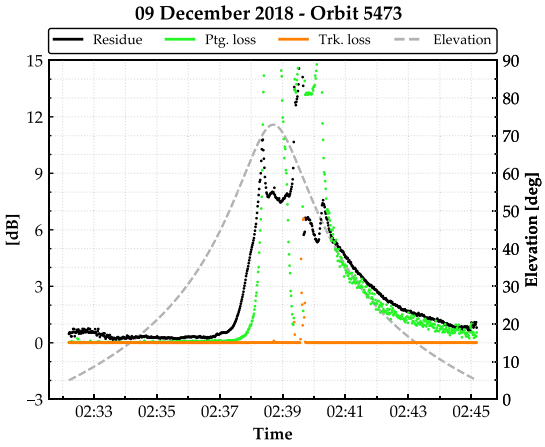

Figure 2.45: Orbit 5473, 9 December 2018. Measured residual (black), calculated pointing loss (green) and tracking loss (orange) for the case reported in Figure 2.43

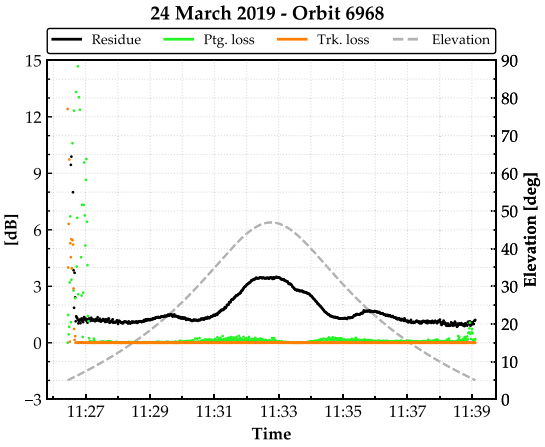

Figure 2.46: Orbit 6968, 24th March 2019. Measured residual (black), calculated pointing loss (green) and tracking loss (orange) for the case reported in Figure 2.44

Figure 2.47: Photo from the webcam taken on 24 March 2019 at 12:00, each one span 90 degree from east (top) to north (bottom)

2.4 Final assessment of key parameters

As a final post-processing step all recorded samples were merged in a single data frame in order to derive statistical analyses of each link performance. This chapter provides the final statistics for the key link parameters: residuals and SNR cumulative distributions together with cross-polar isolation and brightness noise temperature levels. All the various parameter statistics, derived and described hereafter, were obtained considering the set of pass recordings from cycle 23 to cycle 59 (i.e only passes recorded in autotrack mode). This because of the systematic error loss induced in TLE mode.

2.4.1 Residuals (exceeded attenuation)

The first analysis concern the residuals distribution for the considered dataset at different elevation ranges, compared against the statistics of exceeded attenuation obtained via specific tools (Propa [41]) implementing the ITU models. This latter (see Figure 2.49) estimated the probability that a certain atmospheric attenuation is exceeded for a given percentage of time, while the residuals statistics account for the probability that overall attenuation (atmospheric + other effects, e.g. snow/ice, de-pointing) is exceeded.

The comparison between the two graphs show clearly that in the case of residuals the trend vs. elevation (higher loss at higher elevations) is inverted with respect to the one expected in presence of mere atmospheric effects (lower loss at higher elevations). Firstly, this is due to the fact that ITU prediction at low elevation are overestimated with respect to formulas used in our processing. Secondly, the effect of snow on the radome is not obviously implemented in ITU and it induces a strong signal loss at higher elevations.

Presented also on a monthly basis, the cumulative distribution of residuals was calculated for different elevation steps in order to separate and distinguish the effect of snow, mainly above 30 degrees, from the standard atmospheric propagation. Figure 2.50 to Figure 2.58 show a marked variability in residuals. In particular, the monthly variability is more pronounced as the elevation increases. At very low elevation, i.e. where there is little or no impact from the snow accumulation on the radome, greatest attenuations were registered in summer, consistently with a general increase in humidity and more frequent atmospheric phenomena such as clouds and rain with respect to other months. It is worth to mention that in the elevation range below 10 degrees other phenomena like scintillation and multipath effects may dominate with respect to gaseous attenuation.

In Figure 2.51 and Figure 2.52 severe losses were recorded, as it is clear looking at the blue curves corresponding to December and January. These losses are related to a thick cumulated snow layer on the radome, due to Christmas and New Year's holidays, when no one was on-site to regularly clean the radome. Looking at elevations above 30 degrees, estimated attenuation is generally greater in the period from September to January and March. In March and September-October the attenuation is probably due to the simultaneous accumulation of wet snow and ice, difficult to be removed with the installed rope on the radome, which melts and freezes cyclically over the day. These months are indeed in the transition period between midnight sun and polar nights. From November to January, the snow is reasonably dry and thus more volatile. This helps the cleaning process or makes the snow easier to be moved away by the wind.

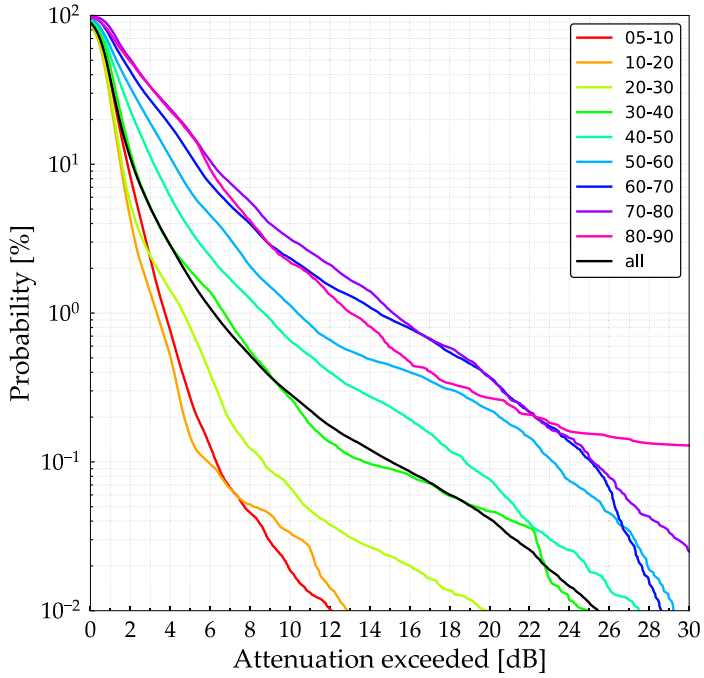

Figure 2.48: Residuals cumulative distribution for different elevation ranges [deg]

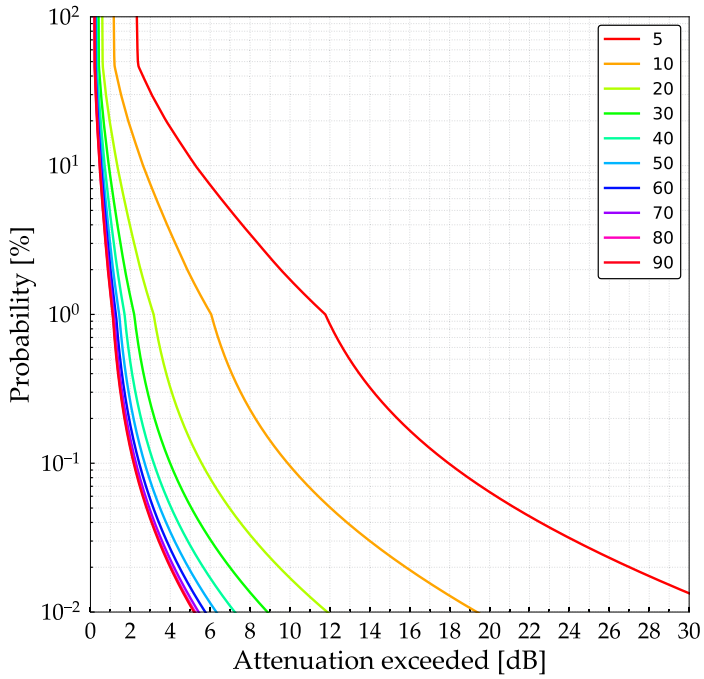

Figure 2.49: Exceeded attenuation from ITU models at different elevations [deg]

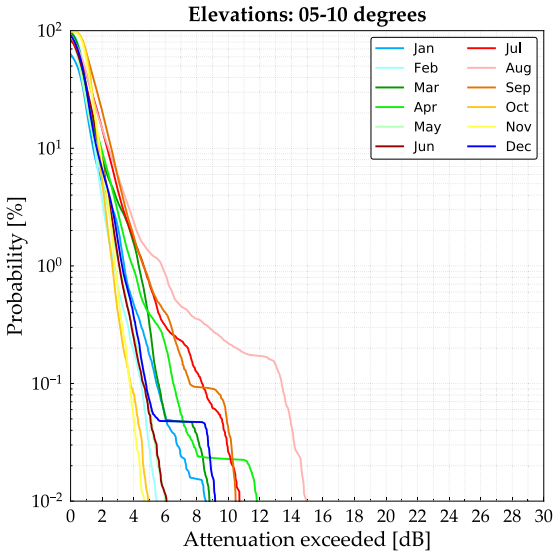

Figure 2.50: Residuals CD per month. 5 to 10 degrees

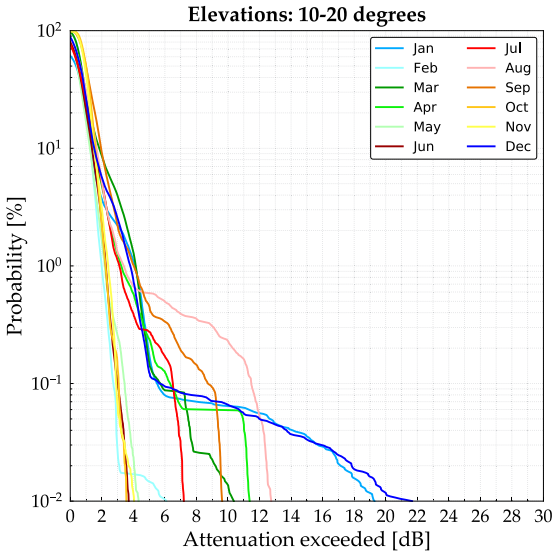

Figure 2.51: Residuals CD per month. 10 to 20 degrees

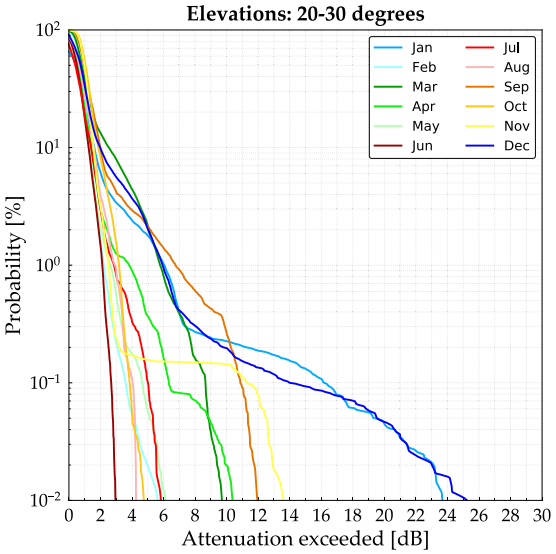

Figure 2.52: Residuals CD per month. 20 to 30 degrees

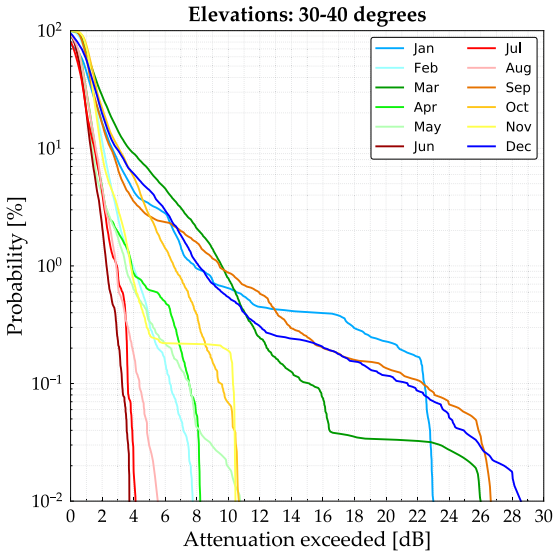

Figure 2.53: Residuals CD per month. 30 to 40 degrees

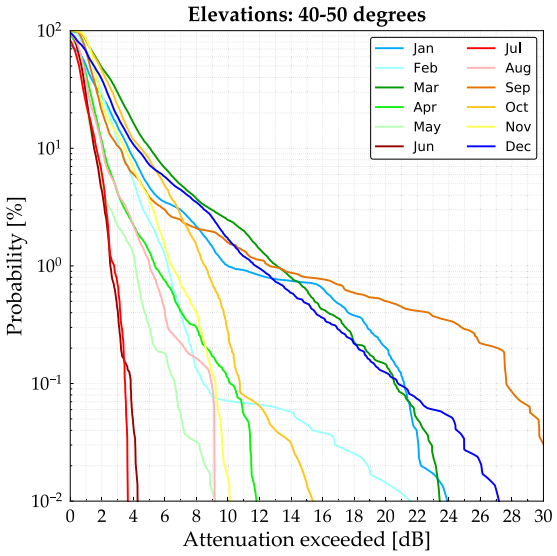

Figure 2.54: Residuals CD per month. 40 to 50 degrees

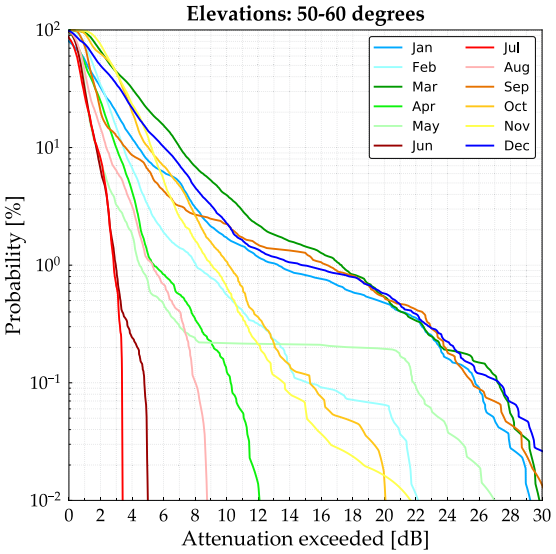

Figure 2.55: Residuals CD per month. 50 to 60 degrees

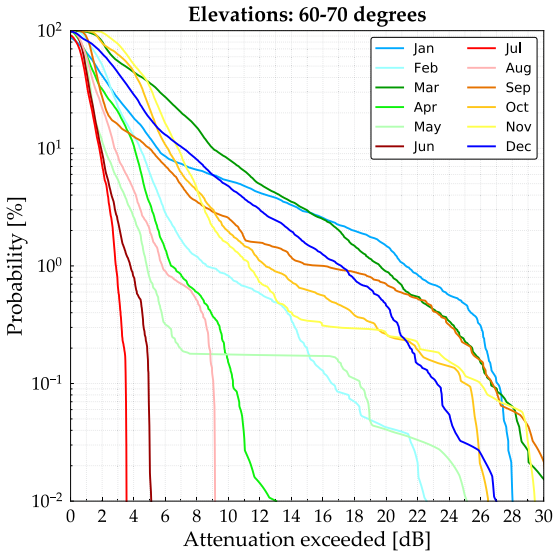

Figure 2.56: Residuals CD per month. 60 to 70 degrees

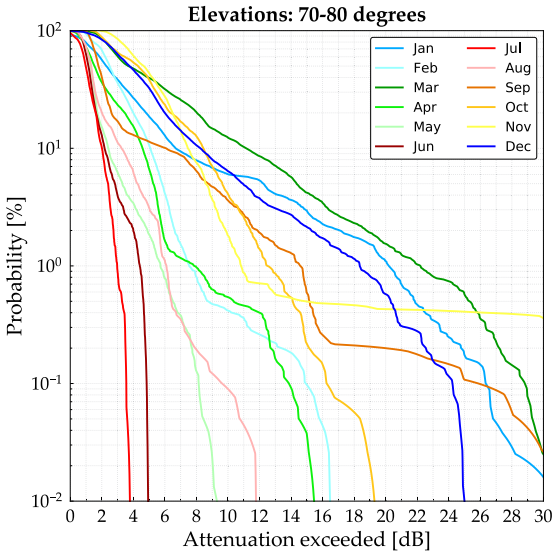

Figure 2.57: Residuals CD per month. 70 to 80 degrees

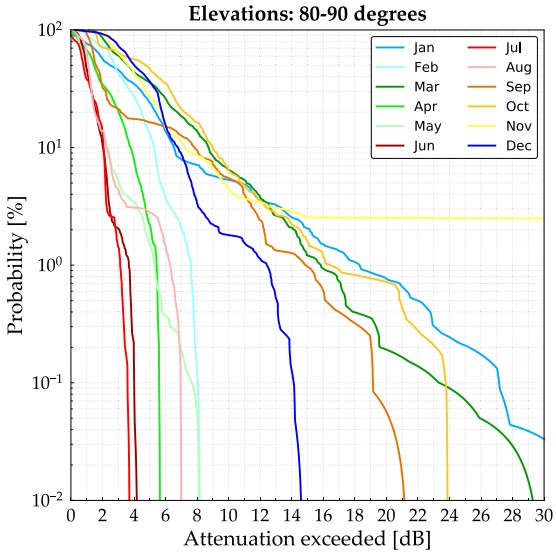

Figure 2.58: Residuals CD per month. 80 to 90 degrees

2.4.2 Signal to Noise

In the same way as for the residuals also the SNR statistics for various elevations were analysed. The two graphs of Figure 2.60 and Figure 2.60 represent respectively the SNR measured by the receiver and the one estimated from the comparison of the input signal strength and noise temperature.

Therefore the first graphs is clearly affected by the already mentioned ”saturation” effect at 29 dB, (black dotted line) when payload data is transmitted, and 33 dB (blue dotted line), when only idle data is transmitted, while the second is more representative of the ideal behaviour. Investigations with the receiver manufacturer have demonstrated that the saturation is due to on board generated noise, which masks the ground station contribution for high signal levels. Due to these phenomena the only statistically relevant samples are the ones recorded when the signal level is low enough to make the on board contribution negligible with respect to the ground one.

The green dotted lines on the graphs represent the measurement sensitivity, while the red one shows the SNR level needed to guarantee a FER of at least 10^{-7}.

Although the two graphs show similar trends in the region not affected by saturation, it has to be noted a major discrepancy in the statistics for elevations in the range of 5 to 10 deg elevation (and consequently also for the overall ones, being this range the most statistically relevant in terms of samples). This discrepancy seems to be due to the fact that the HRDFEP estimates the SNR from the scatterplot and this might be affected by other detrimental effects such as depolarisation, loss of demodulator lock, unstable autotrack or less accurate one (S-Band), that are less affecting the mere signal power recordings from which the SNR is estimated in the second graph. This could explain the (less evident) differences between the two graphs also for other elevation ranges.

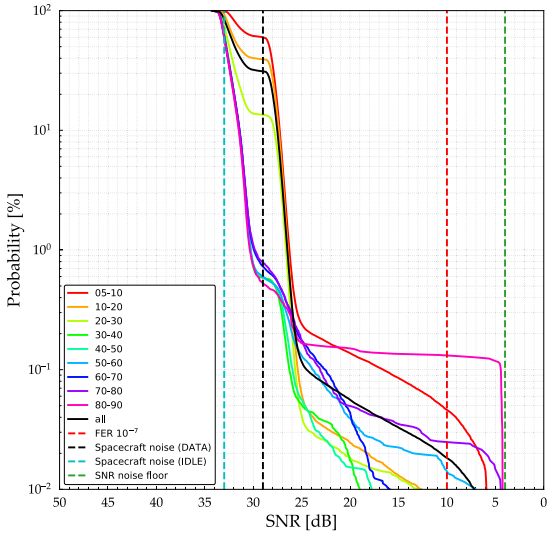

Figure 2.59: Measured SNR probability for different elevation ranges

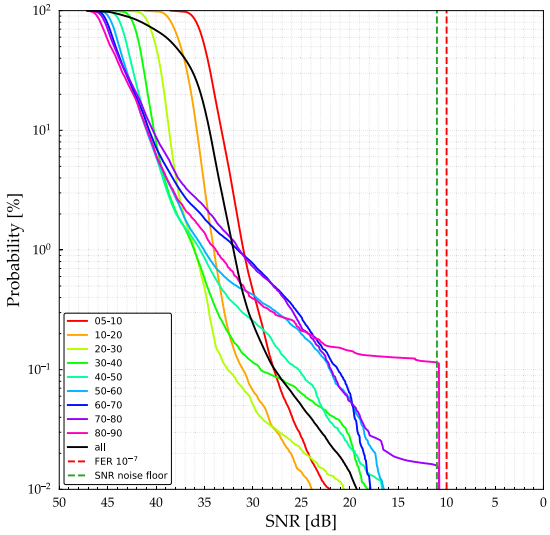

Figure 2.60: Estimated SNR probability for different elevation ranges

2.4.3 Cross-polarisation

Figure 2.61 shows the mean value for the cross-polar isolation at the HDR presented on a monthly basis and for elevations between 5 and 30 degrees because at higher elevations they become almost flat stabilizing around the nominal value, estimated around 18 dB.

The curves confirm the expected behaviour, i.e. during the winter months, where humidity and atmospheric effects are less significant the amount of signal coupled on the cross-polarisation (depolarisation effect) is lower, while in summer it is exactly the opposite. Furthermore the depolarisation effect is higher at lower elevations due to the longer path through the atmosphere.

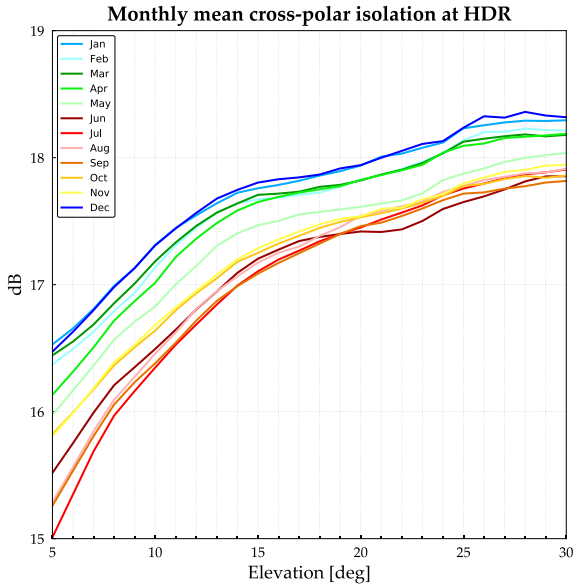

Figure 2.61: Monthly average cross-polar isolation

2.4.4 Brightness temperature

Figure 2.62 and Figure 2.63 show respectively the mean theoretical and calculated brightness noise temperature, presented on a monthly basis and for elevations between 5 and 30 degrees. The behaviour is similar to the one observed also for the XPD and above 30 degrees the variation with elevation is negligible.

Brightness temperature includes all the external noise temperature contributions, from the cosmic background to the clean radome. Theoretical values are defined using weather station parameters together with the ITU formulae for atmospheric attenuation. Calculated values are estimated considering the system noise temperature, computed by means of the Y-factor method and noise diode measurements, level plan and Power Meter recordings of the background noise during each pass.

The comparison between the estimated curves, based on measured temperature and humidity and ITU models, and the ones based on direct measurements of the background noise shows

in this case a good matching (lower temperature for winter months, higher for summer).

Our model appears to be pessimistic for the estimation of brightness temperature in winter and optimistic in summer, but this increased spreading could also be due to the intrinsic measurement accuracy.

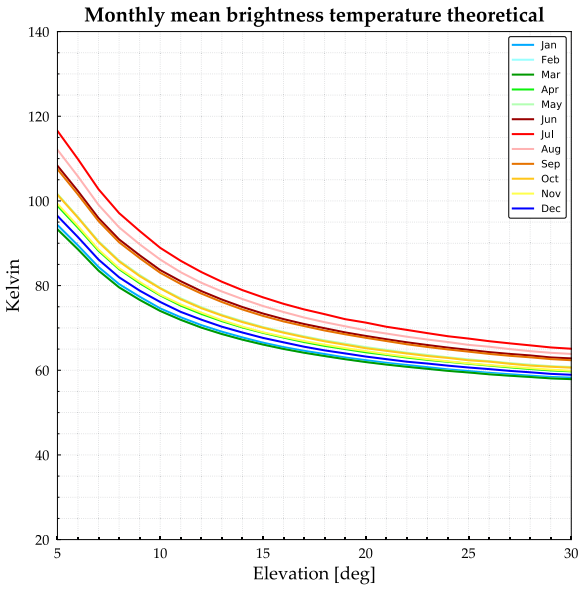

Figure 2.62: Mean theoretical brightness temperature values

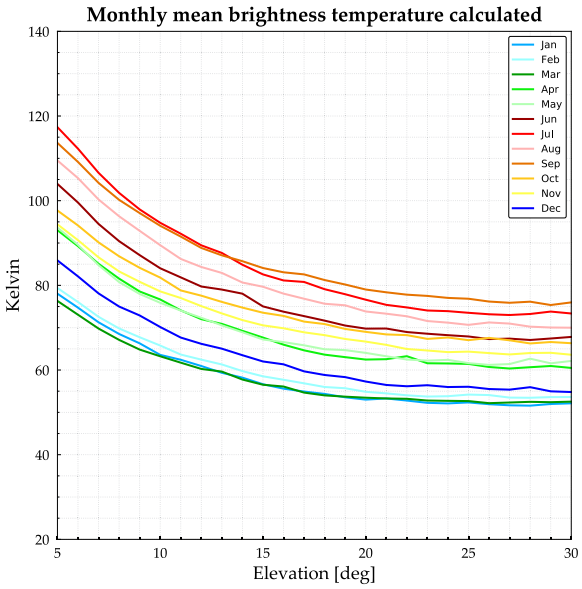

Figure 2.63: Mean calculated brightness temperature values

Chapter 3

Deep Space Antennas upgrade

Currently, the European Space Agency (ESA) is running a network of three Deep Space Antennas, installed in New Norcia (Australia, DSA1), Cebreros (Spain, DSA2) and Malargue (Argentina, DSA3) [13], [14].

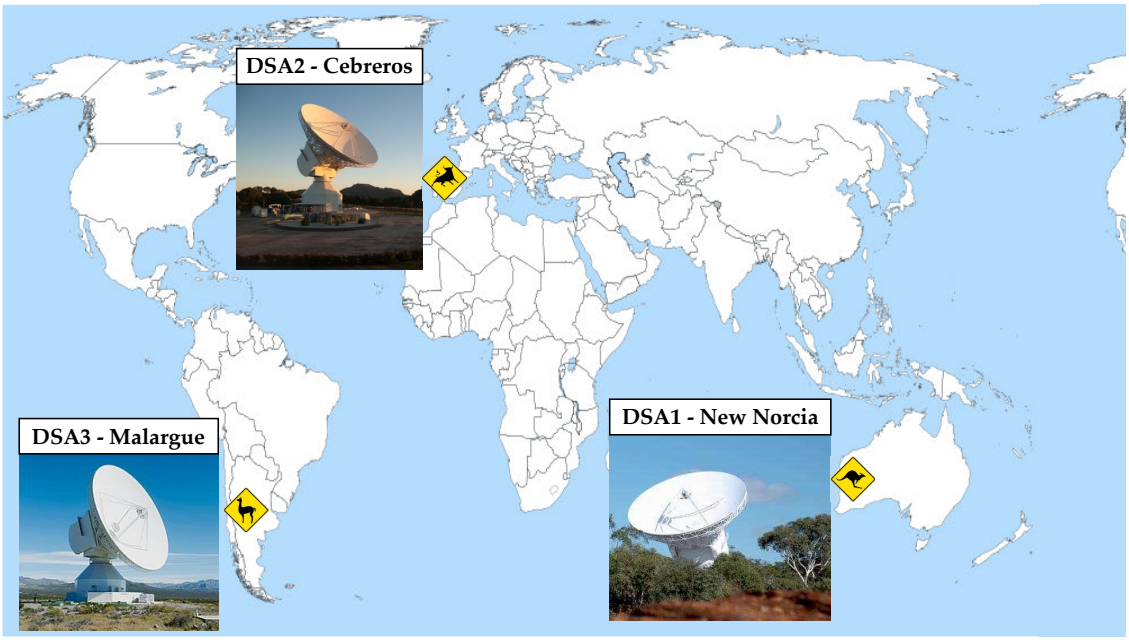

Figure 3.1: DSAs geographical positions

They are all provided with a Beam Waveguide (BWG) optics which illuminates a 35-meter shaped Cassegrain main reflector. The shaping of such a Cassegrain dual reflector system was studied in order to optimize effects such as aperture amplitude distribution, subreflector shadowing and spillover [42], [43]. The BWG system, allows for decoupling the feed from antenna elevation and azimuth movements and, through the aid of dichroic mirrors, permits simultaneous operation in multiple frequency bands. Indeed they can operate in the following S, X, K and Ka bands.

DSA 1: S-band TX (2025-2120 MHz); S-band RX (2200-2300 MHz);
X-band TX (7145-7235 MHz); X-band RX (8400-8500 MHz);
DSA 2: X-band TX (7145-7235 MHz); X-band RX (8400-8500 MHz);
K-band RX (25500-27000 MHz);
Ka-band TX (34200-34700 MHz); Ka-band RX (31800-32300 MHz).
DSA 3: X-band TX (7145-7235 MHz); X-band RX (8400-8500 MHz);
K-band RX (25500-27000 MHz);
Ka-band TX (34200-34700 MHz); Ka-band RX (31800-32300 MHz).

Therefore, they integrate X band capability but still lack a complete K band one. To guarantee a simultaneous X and K band full-duplex (i.e both uplink and downlink) channels in all three ESA's DSAs, the actual layout of each antenna has to be upgraded to implement the new bands where they are missing.

In order to fit all these multiple frequency bands into the BWG is necessary to use a Frequency Selective Surface, also known as dichroic mirror . These devices are ideally transparent for given bands and at the same time opaque for others. Countless typologies of FSSs can be designed, tailoring their behaviour for each one needs but, in the particular case of the DSAs, only high-pass i.e. inductive dichroic mirrors, designed as periodic apertures in a metal screen, are employed. The principal reason for the aforementioned limitation is that, for DSA applications, very high transmitting powers and extremely low noise temperatures (NT) are mandatory. Therefore the use of any dielectric material is excluded and the only possibility is to realize periodic apertures in a metal screen, limiting the frequency behaviour of such devices to exhibit a high-pass (inductive) response, where the mirror is opaque at lower frequencies and transparent for higher ones. This, in turn, limits the layout possibilities for the BWG optics and may create difficulties when a large number of dichroic mirrors are put in place to separate/combine a high number of different frequency bands.

3.1 BWG possible configurations

The first step of this study was the identification of the most suitable option for the lower part of each BWG.

The current optical layout schemes of the three DSAs are shown in figure 3.2a and 3.2b.

DSA1 is operating in S and X band (both uplink and downlink channels) thanks to the dichroic mirrors M6, able to separate between these two bands, and the flat mirror M7.

Instead, DSA2 and DSA3 operate in X (uplink and downlink channels), K (downlink channel) and Ka bands (uplink and downlink channels). In these two BWG the elliptic mirror M5 is movable, allowing to select between two different paths: with M5 is in position 1 (upper circle of figure 3.2b), X and Ka band capabilities are selected, while with M5 is in position 2 (lower circle of figure 3.2b), are selected X and K ones. All solutions proposed for the presented study concerning DSA2 and DSA3 refer to M5 in position 2, therefore the layout related to M5 in position 1 is assumed to remain unaltered.

In addition, all the mechanical modifications required to accommodate the new frequency bands shall be compatible with the already existing infrastructure of DSA antenna systems and the new frequency band shall be accommodated by limiting the interference to the existing

ones. To cope with these requirements different possible layouts, described in the following sections, have been investigated. From this trade-off analysis, layouts DSA1-A and DSA23-B were finally selected as the best ones, in terms of cost and ease of construction, because they need the fabrication of the same dichroic mirror and a new double S/X feed. Solution DSA23-A was also kept into account and not discarded a-priori because it offers the possibility to investigate a new kind of all-metal dichroic mirror exhibiting a low-pass frequency response.

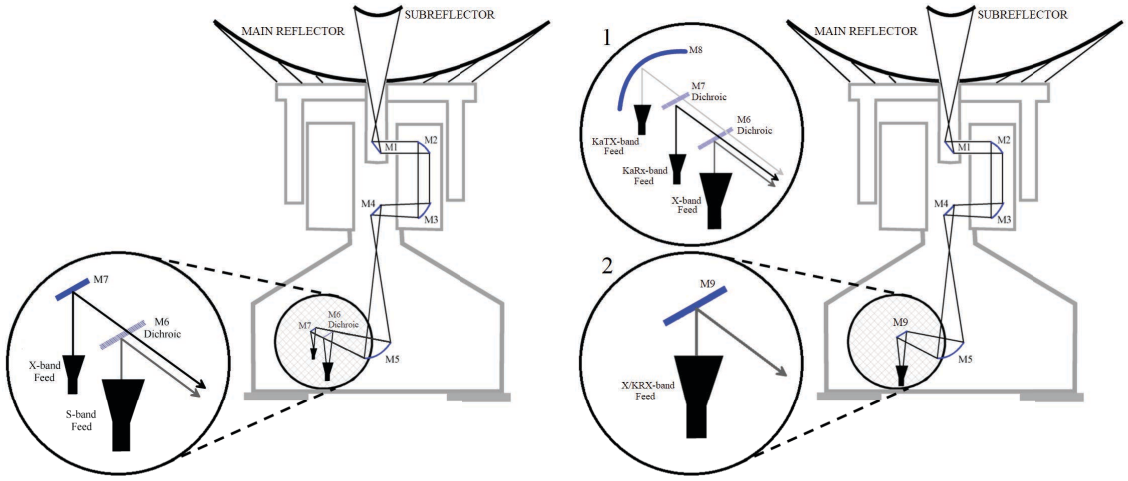

(a) Schematic of the current DSA1 optical layout (b) Schematic of the current DSA2/3 optical layout

Figure 3.2: Current configurations

3.1.1 DSA1 possible layouts

For the upgrade of the DSA1, a simultaneous operation in S/X or X/K bands shall be kept, thus two options were examined.

First option (DSA1-A) is shown in figure 3.3a and it is based on the replacement of the actual dichroic mirror M6 with a new one able to reflect both S and X bands and transmit K band. This solution also requires the installation of a new solid mirror M7, the development of a new K band feed and a dual band feed, able to generate an optimum beam in both S and X bands. The main advantage of this option is the relatively easy design for the new dichroic mirror M6. Instead, a significant challenge is provided by the dual-band S/X feed, whose design and fabrication could result very problematic.

The second option (DSA1-B), shown in figure 3.3b, is based on relatively standard components. A new dichroic mirror M7 able to reflect the X band and transmit the K band shall be designed. Regarding the feeds, only the new K band feed need to be designed because S and X feeds are already installed. However, the main drawback of this solution is that it needs a major mechanical modification of the DSA1 arrangement in order to make the current dichroic M6 movable, thus able to provide two positions: S/X (dichroic inserted) and X/K (dichroic retracted). This is considered a significant limitation in terms of costs, installation uncertainties and station downtime.

3.1.2 DSA2 and DSA3 possible layouts

For the upgrade of the DSA2 and DSA3 three options were investigated.

First option (DSA23-A), shown in figure 3.4a, requires the installation of a new solid mirror M10 and a relatively easy design of a new feed able to operate only for the K band uplink channel, because the feed working in X band and for the K band downlink channel is already installed. On the contrary, it needs to replace the solid mirror M9 with a dichroic mirror able to reflect the X band and the K band downlink channel, but to transmit the K band uplink channel. This solution is very attractive because it represent a straightforward approach for the implementation of the 22 GHz band in the BWG, but it requires the design, fabrication and testing of an extremely challenging dichroic mirror, which is expected to be completely different from the current ones, in terms of design and manufacturing techniques.

The second option (DSA23-B) is shown in figure 3.4b and it is similar to the solution A for the DSA1, with the only difference that S band is not implemented neither in DSA2 nor in DSA3. For this solution the actual feed working in X band and for the K band downlink channel can be kept exploiting just X band capability and a new K band feed shall be designed. A new solid mirror M10 shall be installed to extend the BWG and the actual mirror M9 shall be replaced with a new dichroic able to reflect the X band and transmit the K band. This alternative permits the independence of X and K bands which may help to improve the beam generation and the global performance of the feeding section. Moreover, the main advantage is that all devices designs are within the expected feasibility.

Last considered option (DSA23-C) is shown in figure 3.4a. For this solution it is needed to develop a new feed able to operate both in X and K band simultaneously. As per solution DSA23-A, this one is very attractive but it requires the design, fabrication and testing of an extremely challenging feed.

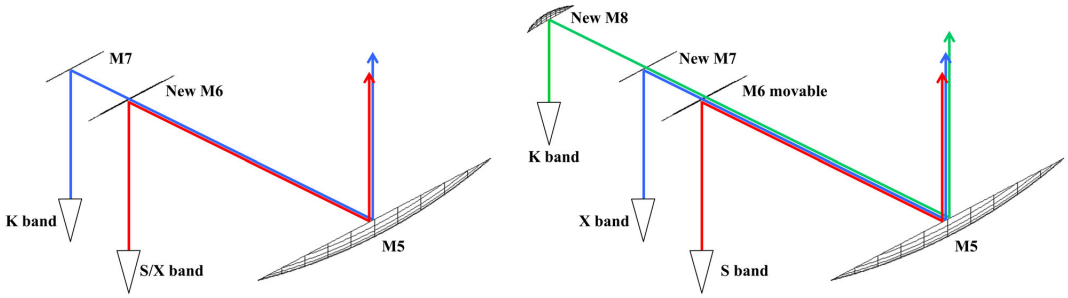

(a) Configuration DSA1-A (b) Configuration DSA1-B

Figure 3.3: DSA1 possible configurations

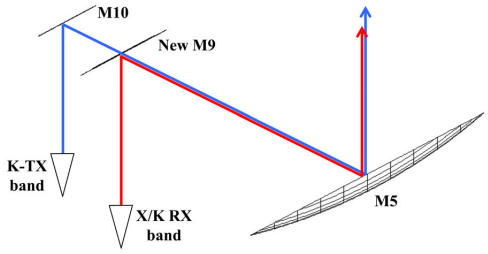

(a) Configuration DSA23-A

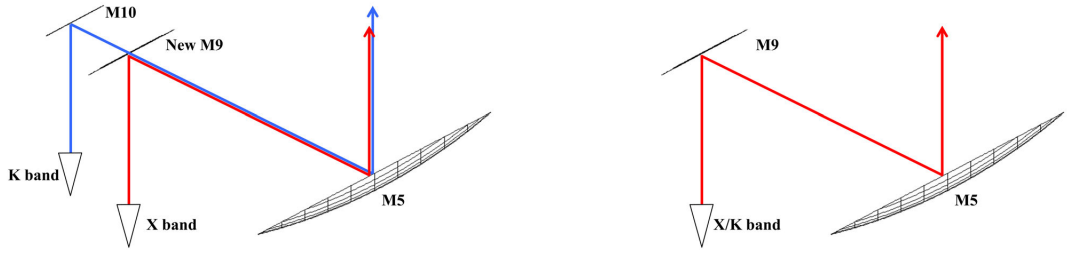

(b) Configuration DSA23-B (c) Configuration DSA23-C

Figure 3.4: DSA23 possible configurations

3.2 Dichroic mirrors designs

This section describes all the dichroic mirrors designs investigated for the DSAs upgrade. In view of the selected layouts from section 3.1, this design step shall focus its attention on a dichroic mirror able to reflect both S and X bands while transmitting the entire K band.

Each dichroic mirror has been studied by means of the MoM/BI-RME method [44], [45], which implements the Method of Moments (MoM) with entire domain basis functions calculated numerically by the Boundary Integral-Resonant Mode Expansion (BI-RME). The code permits to model inductive dichroic mirrors with arbitrary shape apertures. Additionally it allows for considering apertures rounding radii in order to account for dichroic manufacturing. The MoM/BI-RME code is currently employed by ESA and several leading companies. Among the others, the MoM/BI-RME code has been adopted to design and analyse the S/X dichroic mirror M6 installed in the DSA1 [46], dichroic mirror M6 and M7 installed in the DSA2 and DSA3 [47].

A thorough investigation of many designs (table 3.1) with different number of layers, aperture shapes and also fabrication techniques was performed to completely assess their frequency response and to define the best compromise between performance, ease of construction and costs.

For a preliminary analysis, their response in terms of transmission, reflection coefficients and cross-polarization discrimination has been optimized for nominal incidence angle of 30deg, under single plane-wave illumination.

The single plane wave analysis provides a preliminary understanding of the dichroic performance, however, this hypothesis may not be fully adequate for a dichroic mirror operating in a focused beam waveguide system, and/or when the illumination law is not ideal. In this case, it is important to take into account the actual illumination generated by the feed horn. For this reason, the University of Pavia has also developed a novel design approach [48], the Multiple Plane Wave (MPW) method, which computes the response of the dichroic mirrors for several different incident angles, according to the radiation pattern impinging on the surface of the dichroic mirror.

Hence, this method has been exploited to study the angular response of each mirror, which have been also optimised accounting for specific mechanical and manufacturing constraints, such as the rounding radius and the minimal metal walls thickness between the apertures. The goal was to obtain the best possible frequency response over a set of incident angles, from 25deg to 35deg [49]. K band feed radiation patter tapering is approximately 5.4 dB at 5deg from the nominal incidence angle therefore most of the impinging power is in fact confined within this angular range.

The two manufacturing techniques considered for the fabrication of the mirror test samples are respectively milling and wire erosion.

Milling is a consolidated approach for the manufacturing of such large dichroic mirrors (approx. $1m^2$), able to provide a good manufacturing accuracy and surface roughness compatible with K-band operations at a moderate manufacturing cost. As an example, a mirror currently in use in the ESA DSAs up to the Ka-band (34 GHz), was realized with tolerances better than 15 μm and a surface roughness in the order of 1.6 μm. On the other hand, milling imposes important constraints about the minimum radius of the tool used to fabricate the mirror and even more important on the maximum ratio between the mirror thickness and radius of the tool. Indeed,

a ratio of approximately 10 is considered as limit for the mirror designs in order to maintain within acceptable limits the tool oscillations during manufacturing process.

On the other hand, wire erosion technique, compared to milling, has a higher fabrication costs, provides greater accuracy, but the achievable surface roughness is slightly worse. Moreover, it offers the possibility to reduce significantly the minimum rounding radius, creating sharper apertures.

Once the design of dichroic mirrors have been completed, the overall BWG analysis has been performed (see Section 3.2.11).

In each of the following sections, mechanical structure and performance results of each mirror design are reported. All cross-polarization diagrams refer to circular polarization and XPD was computed accounting for the transmitted TE and TM modes phase delay and relative amplitude, as described in [50].

Please note that in this section are presented all the mirrors studied during the preliminary phase (PDR) of the study that were thus optimized and then simulated together with all the BWG, except for D1 and D6. In fact, from this first phase it was seen how their preliminary designs guaranteed the best performance among all the mirrors and therefore they were chosen for the next phase of the project (CDR) during which further analyses and optimizations have been carried out (ohmic losses and sensitivity analyses). Therefore, only for these two designs, preliminary results are not shown and values reported in this section come from their final design.

Table 3.1: Dichroic mirrors reference table

Dichroic	**Transmission band**	**Reflection band**	**Aperture shape**	**# layers**	**Manufacturing technique**
D1	K	S/X	Rectangular	1	Milling
D2	K	S/X	Rectangular	1	Wire erosion
D3	K	S/X	Rectangular	2	Milling
D4	K	S/X	Hexagonal	1	Milling
D5	K	S/X	Hexagonal	2	Milling
D6	K	S/X	Cross	1	Milling
D7	K	S/X	Cross	2	Milling / Wire erosion
D8	K-TX	X/K-RX	Cross	2	Milling / Wire erosion

3.2.1 D1 - Rectangular holes, single layer

Dichroic mirror D1 is a single layer inductive FSS based on rounded rectangular apertures designed to transmit both the K-RX and K-TX channels; in addition, it was designed to reflect S and X bands.

Rectangular apertures are a natural choice for this kind of application because they exhibit good performance both in terms of reflection coefficient and polarization purity in the transmitted band. Moreover they are relatively small thus they can be closely packed together to mitigate the problems related to grating lobes onset. Finally, they are relatively easy to be manufactured in an all-metal screen.

This dichroic mirror was designed with a thickness of 9.2 mm and a rounding radius of 0.9 mm. Therefore, the maximum ratio between the mirror thickness and the rounding radius is around 10 (9.2/0.9), compatible with a milling technique. A minimal metal walls thickness between apertures of 0.5 mm is imposed to provide a sufficient stiffness to the mirror against its own weight.

Figure 3.5 show the dichroic mirror lattice drawing and specify all relevant dimensions.

The simulated performance reflection and transmission coefficients for TE and TM linear polarisations of D1 at the nominal incidence angle (i.e. 30deg) is shown in Figures 3.6a and 3.6c. XPD for the circular polarisation at 30deg is shown in Figure 3.6e. Performance of TX and RX channels for both S and X bands are practically ideal, with a reflection coefficient better than -0.002 dB and a XPD better than -30.01 dB. It can be appreciated that the reflection coefficient is lower than -10 dB in the bands of interest, while the XPD is lower than -25 dB, apart from the highest K-RX band.

A more comprehensive overview of D1, in terms of maximum transmission coefficient and XPD against incidence angle, is given by Figures 3.6b, 3.6d and 3.6f, for the edge and centre frequencies of both K-TX and K-RX channels. The overall mirror response is good, at the cost of worsening a bit the frequency response around 22.55 GHz where the transmission coefficient drop to -0.6 dB. It is also possible to see a rapid degradation of the performance with the angle especially at 27 GHz.

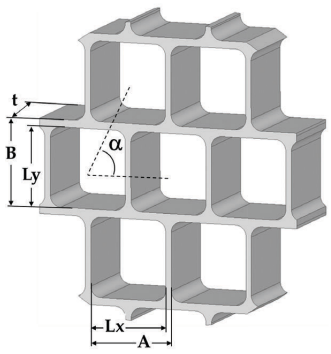

Figure 3.5: Lattice D1. Parameters (in mm): A=7.89, B=7.99, Lx=7.39, Ly=7.49, T=9.2, α=63.72 deg

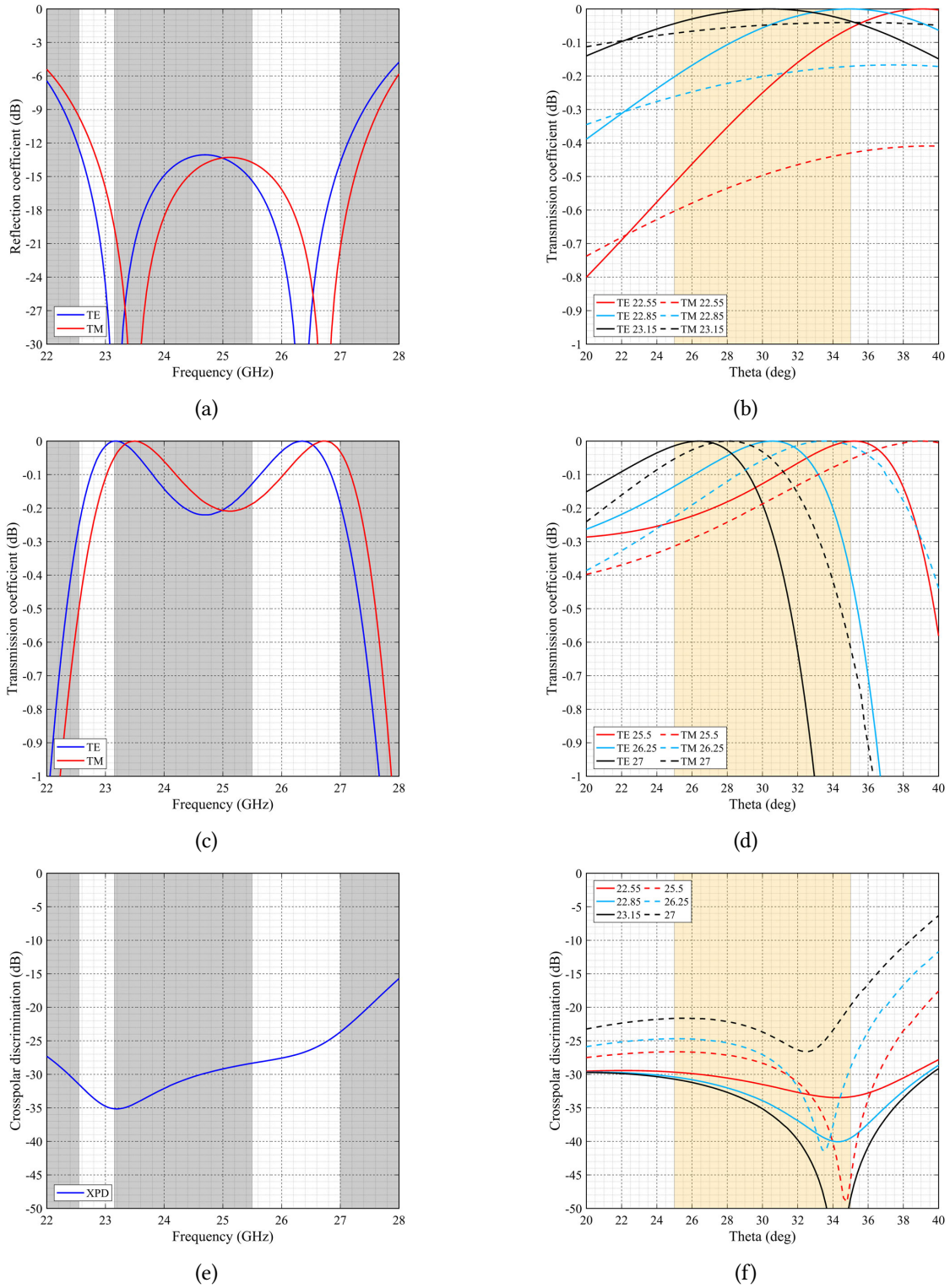

Figure 3.6: D1 performance: Reflection, Transmission coefficients and XPD at 30 deg (a,c,e); same for the 20 to 40 deg angular range (b,d,f)

3.2.2 D1a - Rectangular holes, double layer

Dichroic mirror D1a is a double-layer version of the former one. While the manufacturing complexity is greatly increased, the double-layer design provides additional degrees of freedom to possibly improve the frequency response.

Figure 3.7 show the dichroic mirror lattice drawing and specify all relevant dimensions. This mirror was designed with a thickness of 9.8 mm and a rounding radius of 1 mm.

The simulated performance reflection and transmission coefficients for TE and TM linear polarisations of D1a at the nominal incidence angle (i.e. 30deg) is shown in Figures 3.8a and 3.8c. XPD for the circular polarisation at 30deg is shown in Figure 3.8e. Performance of TX and RX channels for both S and X bands are practically ideal, with a reflection coefficient better than -0.001 dB and a XPD better than -31.46 dB.

A more comprehensive overview of D1a, in terms of maximum transmission coefficient and XPD against incidence angle, is given by Figures 3.8b, 3.8d and 3.8f, for the edge and centre frequencies of both K-TX and K-RX channels.

Considering just the 30deg angle response it can be appreciated an improvement with respect to the single-layer design for both reflection coefficient and XPD. The transmission coefficient is greater than -0.2 dB in the bands of interest, while the XPD is lower than -30 dB. But, looking at the angular response it can be seen that a clear improvement has been achieved only for XPD and K-TX band while, for the K-RX band, performance are comparable or even worse than those of mirror D1.

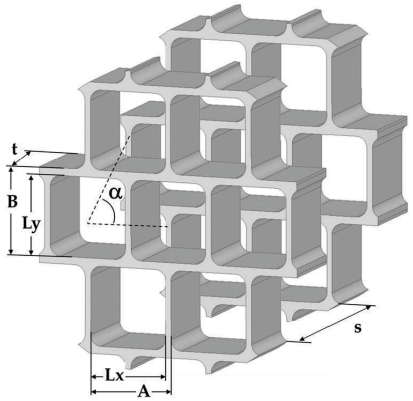

Figure 3.7: D1 lattice. Parameters (in mm):: A=8.18, B=8.21, Lx=7.22, Ly=7.29, s=8.34, α=63.52 deg

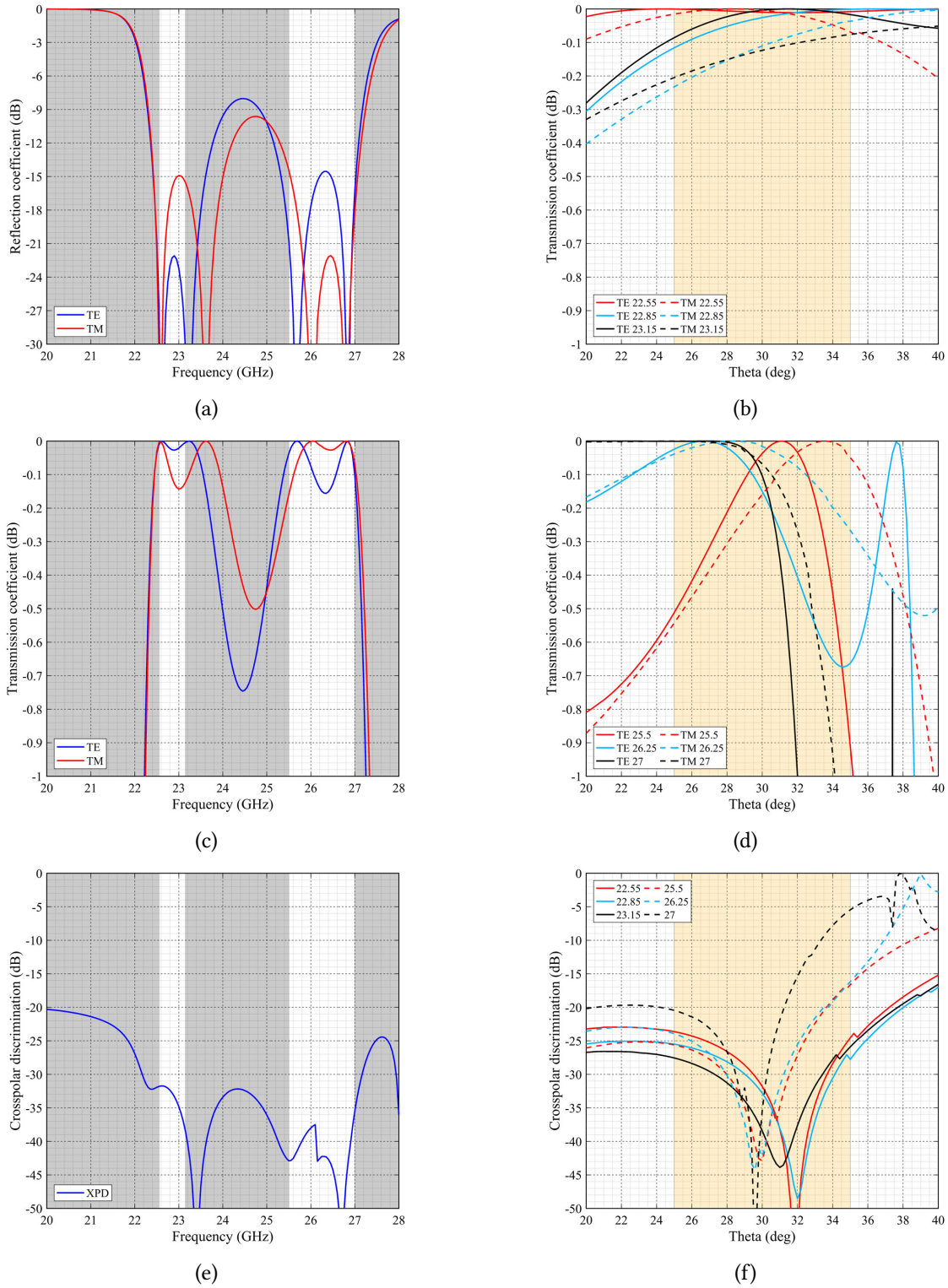

Figure 3.8: D1a performance: Reflection, Transmission coefficients and XPD at 30 deg (a,c,e); same for the 20 to 40 deg angular range (b,d,f)

3.2.3 D2 - Hexagonal holes, single layer

Another possible FSS layout is based on rounded hexagonal holes. The use of hexagonal shapes allows for tightly packing the holes and provides a large number of degrees of freedom. This permits to improve the electrical performance of the dichroic mirror and to increase its mechanical stiffness [51]. This solution was investigated also to provide an useful benchmark to evaluate the potential of an aperture other than rectangular.

Figure 3.9 show the dichroic mirror lattice drawing and specify all relevant dimensions. This dichroic mirror was designed with a thickness of 9.1 mm and a rounding radius of 1 mm.

The simulated performance reflection and transmission coefficients for TE and TM linear polarisations of D2 at the nominal incidence angle (i.e. 30deg) is shown in Figures 3.10a and 3.10c. XPD for the circular polarisation at 30deg is shown in Figure 3.10e. Performance of TX and RX channels for both S and X bands are practically ideal, with a reflection coefficient better than -0.002 dB and a XPD better than -29.48 dB.

A more comprehensive overview of D2, in terms of maximum transmission coefficient and XPD against incidence angle, is given by Figures 3.10b, 3.10d and 3.10f, for the edge and centre frequencies of both K-TX and K-RX channels.

It can be appreciated that the frequency response is in general similar to that of D1, with a worse XPD for the K-TX band.

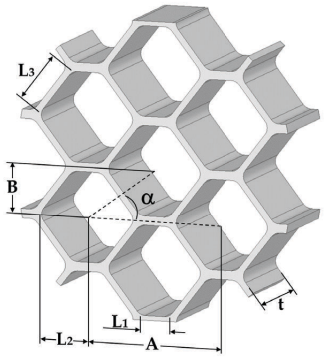

Figure 3.9: D2 lattice. Parameters (in mm): A=13.93, B=4.92, L1=3.03, L2=5, L3=5.67, α=35.25

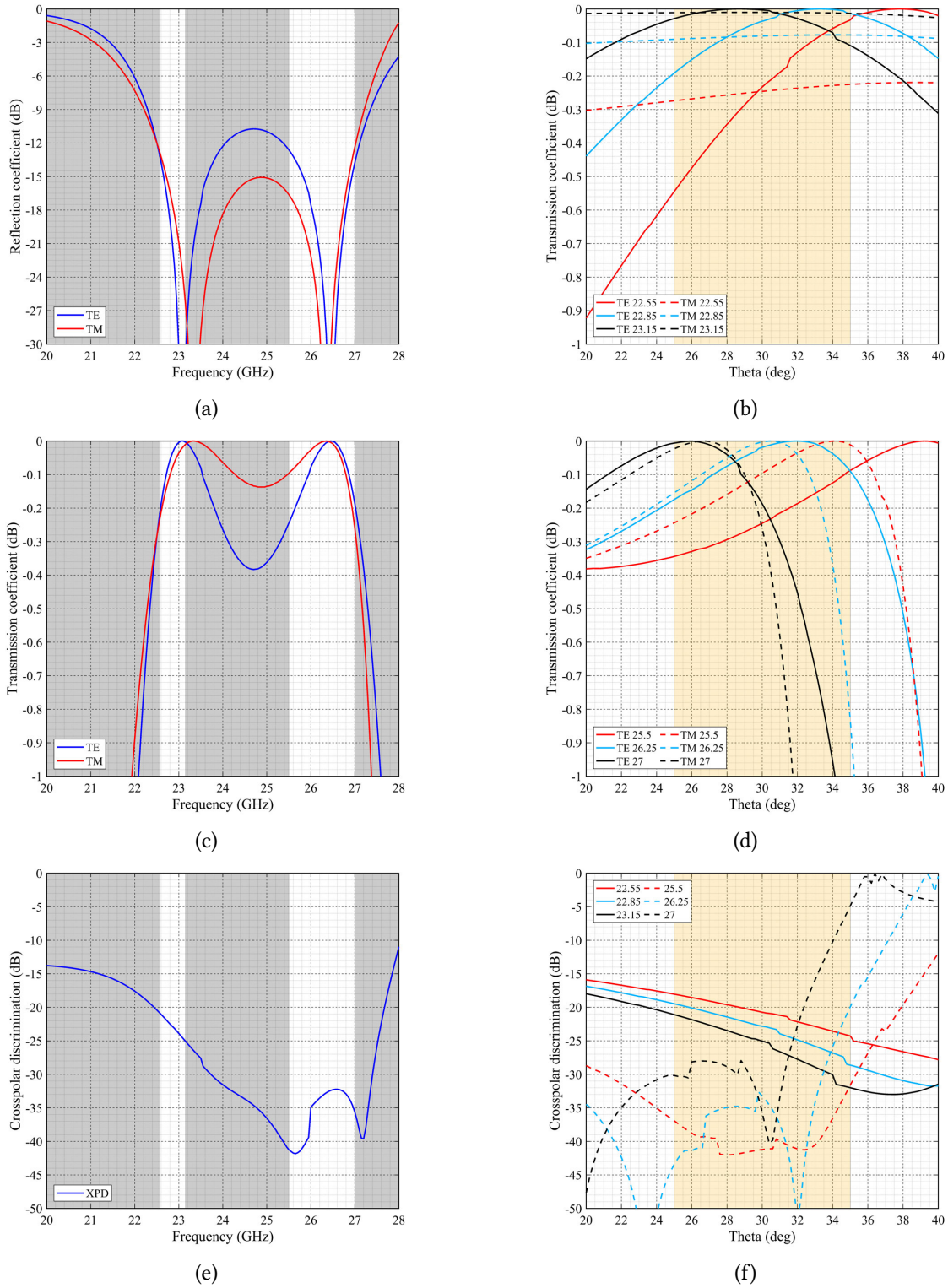

Figure 3.10: D2 performance: Reflection, Transmission coefficients and XPD at 30 deg (a,c,e); same for the 20 to 40 deg angular range (b,d,f)

3.2.4 D2a - Hexagonal holes, double layer

Dichroic mirror D2a is a double-layer version of D2, with hexagonal aperture oriented 90 degrees clockwise. As for mirror D1a, the manufacturing complexity is increased but the double-layer design could provide additional degrees of freedom to possibly improve the frequency response.

Figure 3.11 show the dichroic mirror lattice drawing and specify all relevant dimensions. This mirror was designed with a thickness of 10.4 mm and a rounding radius of 1.05 mm.

The simulated performance reflection and transmission coefficients for TE and TM linear polarisations of D2a at the nominal incidence angle (i.e. 30deg) is shown in Figures 3.12a and 3.12c. XPD for the circular polarisation at 30deg is shown in Figure 3.12e. Performance of TX and RX channels for both S and X bands are practically ideal, with a reflection coefficient better than -0.001 dB and a XPD better than -30.95 dB.

A more comprehensive overview of D2a, in terms of maximum transmission coefficient and XPD against incidence angle, is given by Figures 3.12b, 3.12d and 3.12f, for the edge and centre frequencies of both K-TX and K-RX channels.

Considering just the 30deg angle response it can be appreciated an improvement of the performance, with respect to previous mirrors. Transmission coefficient is greater than -0.08 dB for both TE and TM modes, while XPD is good for K-TX band and less than -30 dB for K-RX one.

But, looking at the angular response it can be seen that a significant improvement has been achieved only for the K-TX band transmission coefficient (always greater than -0.2 dB), while for the K-RX band and XPD performance are comparable or even worse than those of previous mirrors.

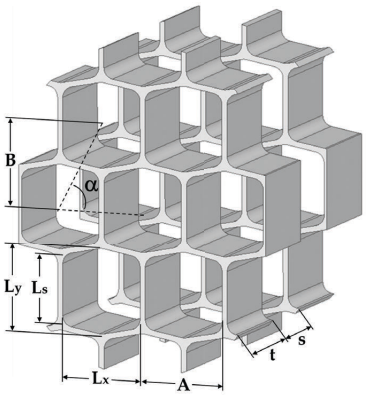

Figure 3.11: D2a lattice. Parameters (in mm): Lx=7.65, Ly=8.2, Ls=6.7, A=8.2, B=7.95, s=7.9

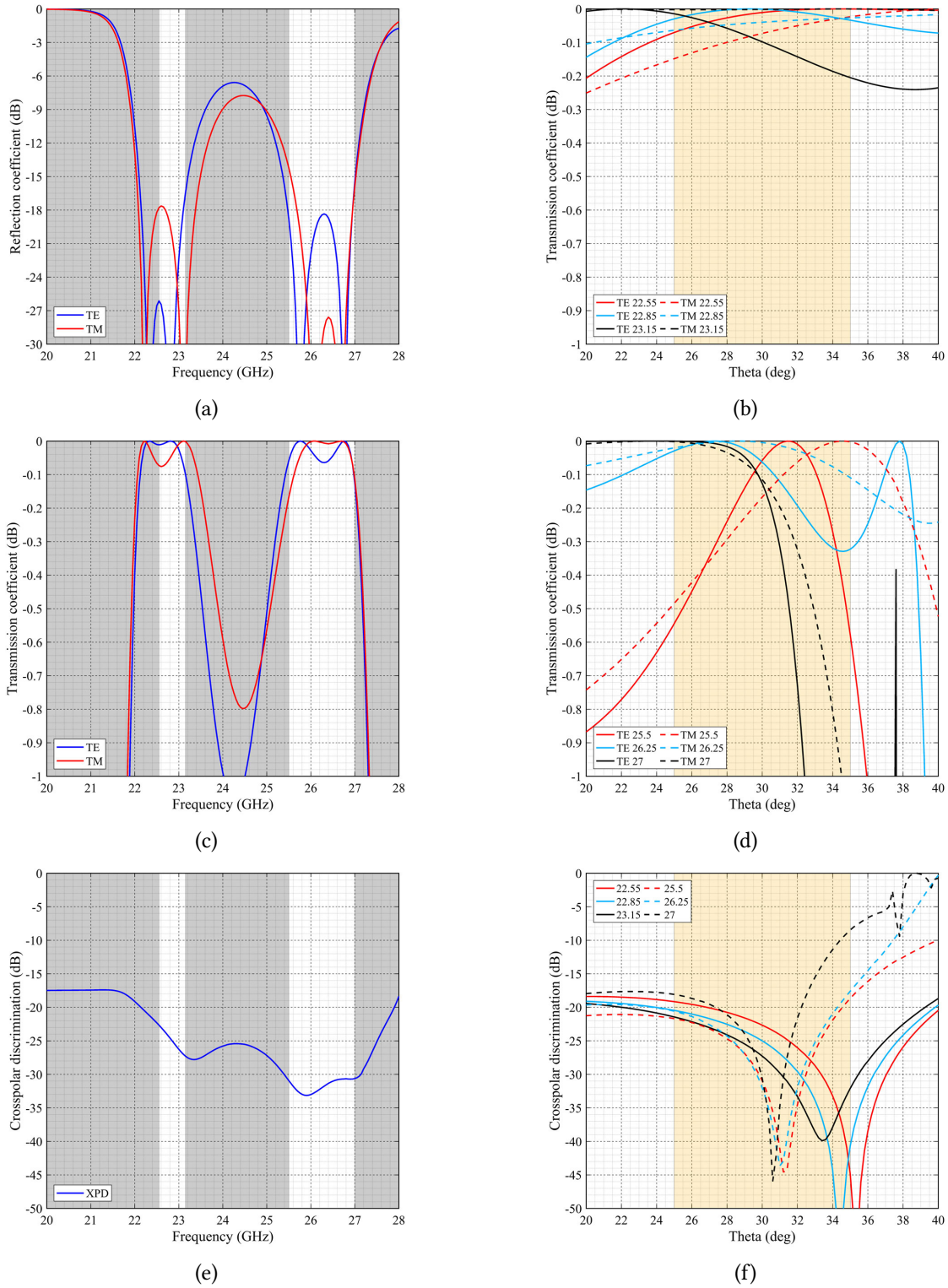

Figure 3.12: D2a performance: Reflection, Transmission coefficients and XPD at 30 deg (a,c,e); same for the 20 to 40 deg angular range (b,d,f)

3.2.5 D3 - Cross-shaped holes, single layer

Dichroic mirror D3 is a single layer inductive FSS based on cross-shaped apertures. Like rectangular holes, cross apertures are a natural choice because they can be closely packed together to avoid an early excitation of grating lobes onset. This dichroic mirror was designed with a thickness of 9 mm and a rounding radius of 0.2 mm. Therefore, the maximum ratio between the mirror thickness and the rounding radius is not compatible with milling technique and this mirror shall be fabricated with wire erosion. A minimal metal walls thickness between apertures greater than 0.5 mm is imposed to provide a sufficient stiffness to the mirror against its own weight.

Figure 3.13 show the dichroic mirror lattice drawing and specify all relevant dimensions.

The simulated performance reflection and transmission coefficients for TE and TM linear polarisations of D3 at the nominal incidence angle (i.e. 30deg) is shown in Figures 3.14a and 3.14c. XPD for the circular polarisation at 30deg is shown in Figure 3.14e. Performance of TX and RX channels for both S and X bands are practically ideal, with a reflection coefficient better than -0.002 dB and a XPD better than -28.07 dB.

A more comprehensive overview of D1, in terms of maximum transmission coefficient and XPD against incidence angle, is given by Figures 3.14b, 3.14d and 3.14f, for the edge and centre frequencies of both K-TX and K-RX channels. The overall mirror response is comparable with those of D1 with a worsened XPD and higher fabrication costs.

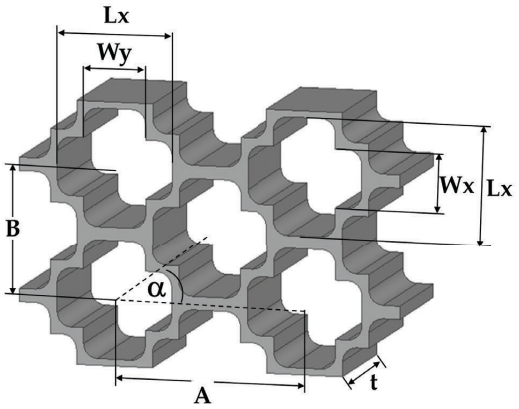

Figure 3.13: D3 lattice. Parameters (in mm): Lx=8.12, Ly=8.28, Wx=4.1, Wy=4.38, A=13.51 , B=4.60

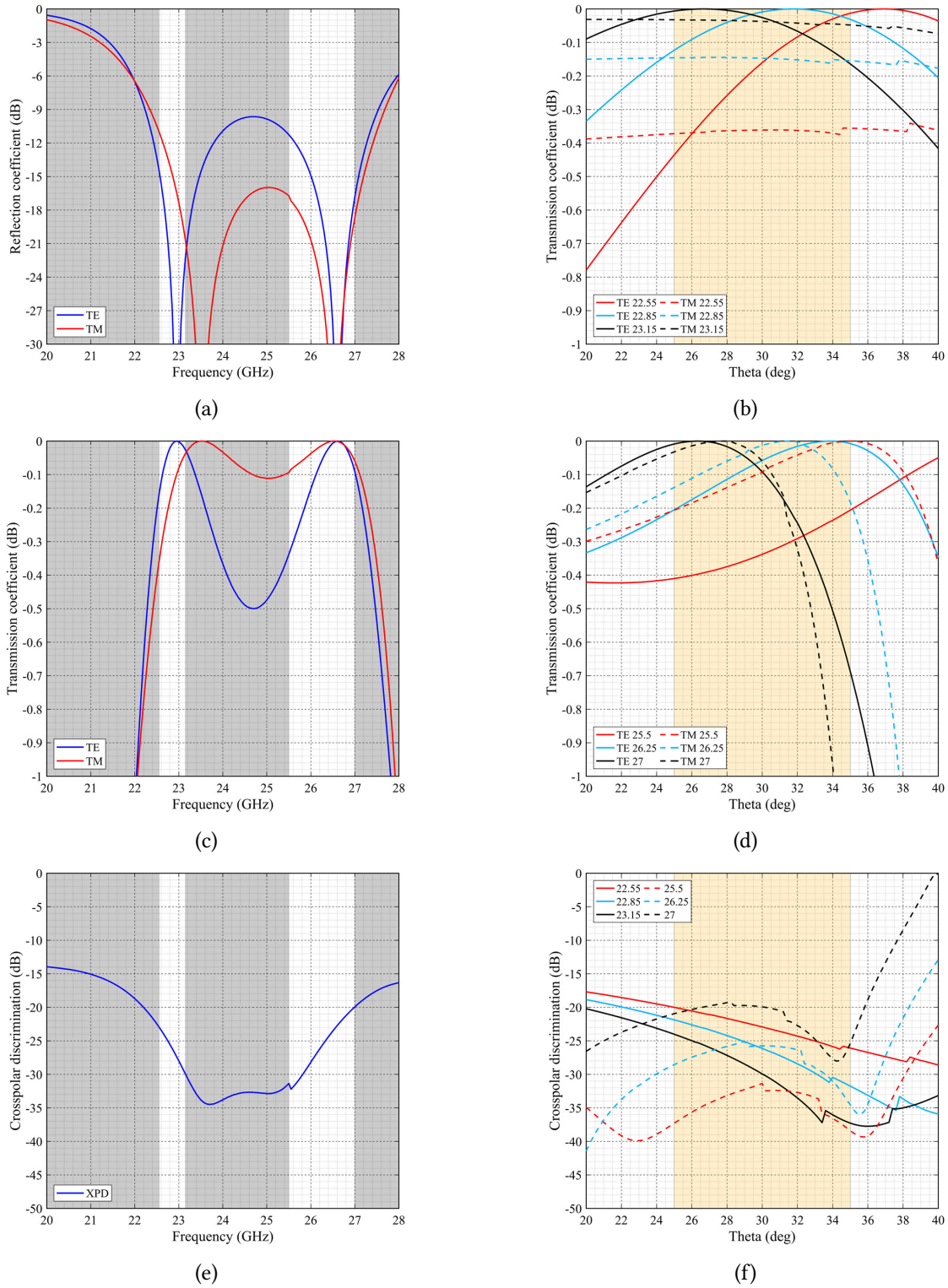

Figure 3.14: D3 performance: Reflection, Transmission coefficients and XPD at 30 deg (a,c,e); same for the 20 to 40 deg angular range (b,d,f)

3.2.6 D4 - Cross-shaped holes, double layer

Dichroic mirror D4 is a double layer inductive FSS based on cross shaped apertures. As for previous multilayer design, the manufacturing complexity and costs are increased but it provides additional degrees of freedom to possibly improve the frequency response.

This dichroic mirror was designed with a thickness of 1.34 mm and a rounding radius of 0.3 mm. Therefore, the maximum ratio between the mirror thickness and the rounding radius is compatible with a milling technique. The minimal metal walls thickness between apertures is greater than 0.5 mm.

Figure 3.15 show the dichroic mirror lattice drawing and specify all relevant dimensions.

The simulated performance reflection and transmission coefficients for TE and TM linear polarisations of D4 at the nominal incidence angle (i.e. 30deg) is shown in Figures 3.16a and 3.16c. XPD for the circular polarisation at 30deg is shown in Figure 3.16e. Performance of TX and RX channels for both S and X bands are practically ideal, with a reflection coefficient better than -0.003 dB and a XPD better than -34.37 dB.

A more comprehensive overview of D1, in terms of maximum transmission coefficient and XPD against incidence angle, is given by Figures 3.16b, 3.16d and 3.16f, for the edge and centre frequencies of both K-TX and K-RX channels.

The combination of a multilayer design with cross-shaped apertures allowed to obtain the best response among all the dichroics analysed. In fact, the simulated transmission coefficient is below -0.1 dB for all considered frequencies and angles of incidence. The worst case, close to -0.2 dB, is the TM polarisation at 25.5 GHz and 25 deg of incidence. XPD is rather good with respect to other designs, constantly below -25 dB apart from 23.15 and 25.5 GHz at highest incidence angles.

Even thought it is by far the best designed dichroic, it is too thin to guarantee a self-supporting structure. In fact, the final dichroic will be around one square meter in diameter, so it would be too thin to support its own weight avoiding an excessive and significant bending.

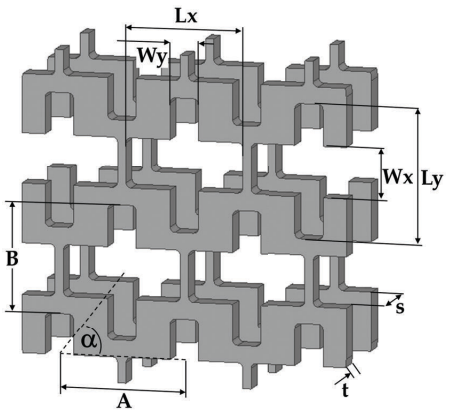

Figure 3.15: D4 lattice. Parameters (in mm): Lx=8.12, Ly=8.28, Wx=4.1, Wy=4.38, A=13.51, B=4.60

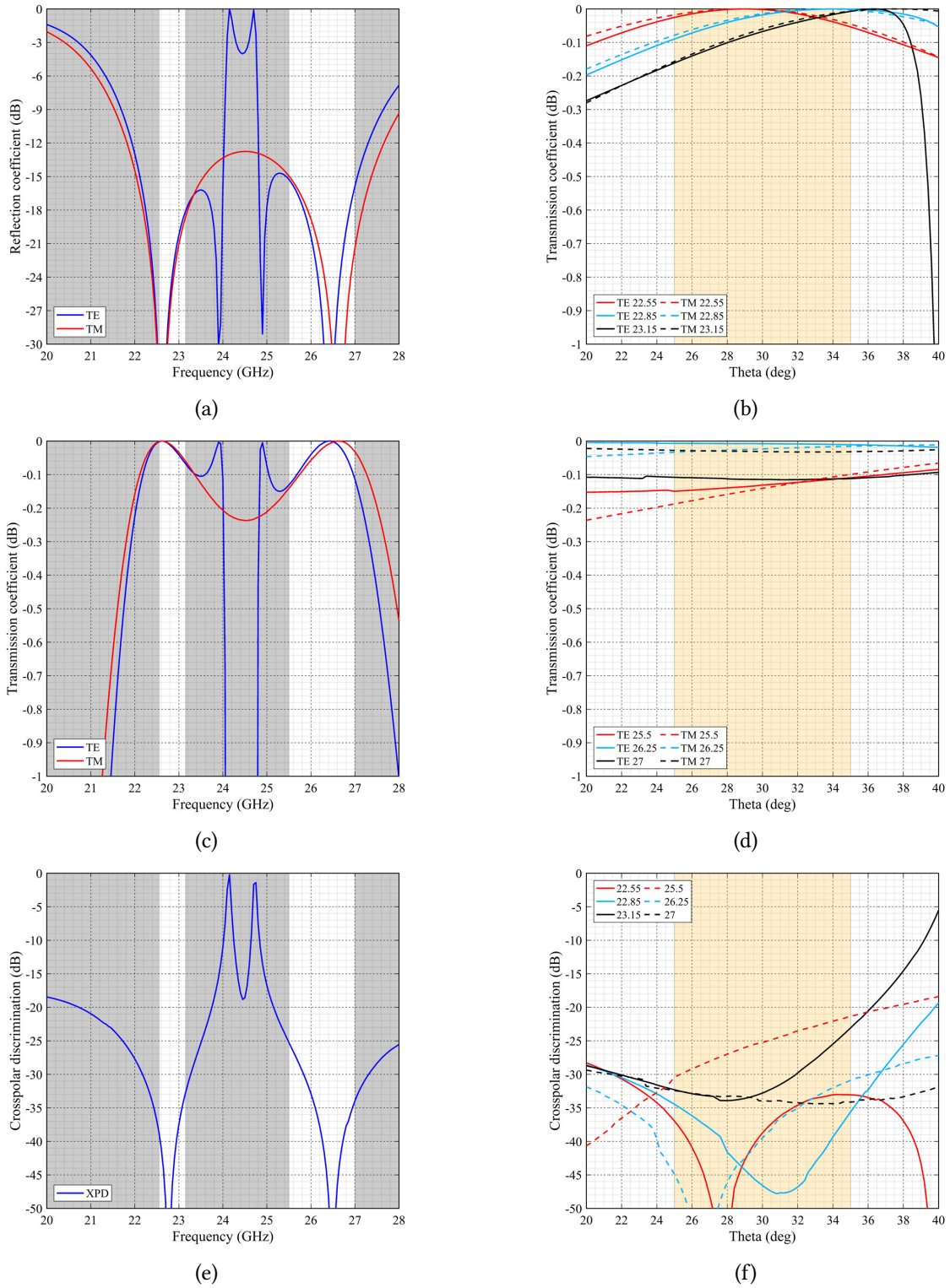

Figure 3.16: D4 performance: Reflection, Transmission coefficients and XPD at 30 deg (a,c,e); same for the 20 to 40 deg angular range (b,d,f)

3.2.7 D5 - Cross-shaped holes, double layer

Dichroic mirror D5 is a double layer inductive FSS based on cross shaped apertures. The design is similar to that of mirror D4 but, in contrast to it and all other mirrors, D5 was designed for the configuration DSA23-A analysed in Section 3.1. Although it is a configuration that has been discarded, one still wanted to study such a mirror design to verify that it was possible to obtain an all-metal design with a frequency response that is not purely inductive (i.e. high pass filter). Starting from D4 response, the cross-shaped hole width and mirror lattice have been defined through parametric simulations and optimization, in order to design the mirror to be capable of transmit the K-TX band, which is at a lower frequency than the K-RX one, which is instead reflected.

This dichroic mirror was designed with a thickness of 2.6 mm and a rounding radius of 0.3 mm. Therefore, the maximum ratio between the mirror thickness and the rounding radius is compatible with a milling technique. The minimal metal walls thickness between apertures is greater than 0.5 mm.

Figure 3.17 show the dichroic mirror lattice drawing and specify all relevant dimensions. Geometric parameters are the same of mirror D4 so they are not indicated for simplicity.

The simulated performance reflection and transmission coefficients for TE and TM linear polarisations of D5 at the nominal incidence angle (i.e. 30deg) is shown in Figures 3.18a and 3.18c. XPD for the circular polarisation at 30deg is shown in Figure 3.18e. Performance of TX and RX channels for both S and X bands are practically ideal, with a reflection coefficient better than -0.001 dB and a XPD better than -50 dB.

A more comprehensive overview of D5, in terms of transmission (K-TX band, Figure 3.18b), reflection coefficients (K-RX band, Figure 3.18d) and XPD (K-RX band, Figure 3.18f) against incidence angle is also given for the edge and centre frequencies of both K-TX and K-RX channels.

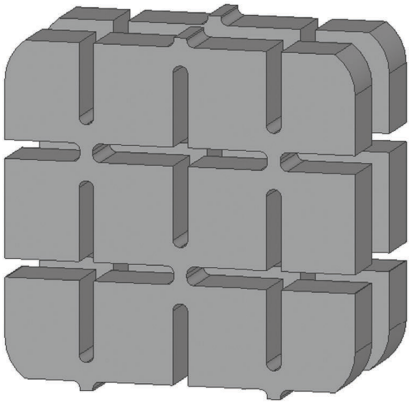

Figure 3.17: D5 lattice. Parameters (in mm): Lx=7.2, Ly=7.36, Wx=0.76, Wy=0.61, A=7.73, B=4.81, s=2.65

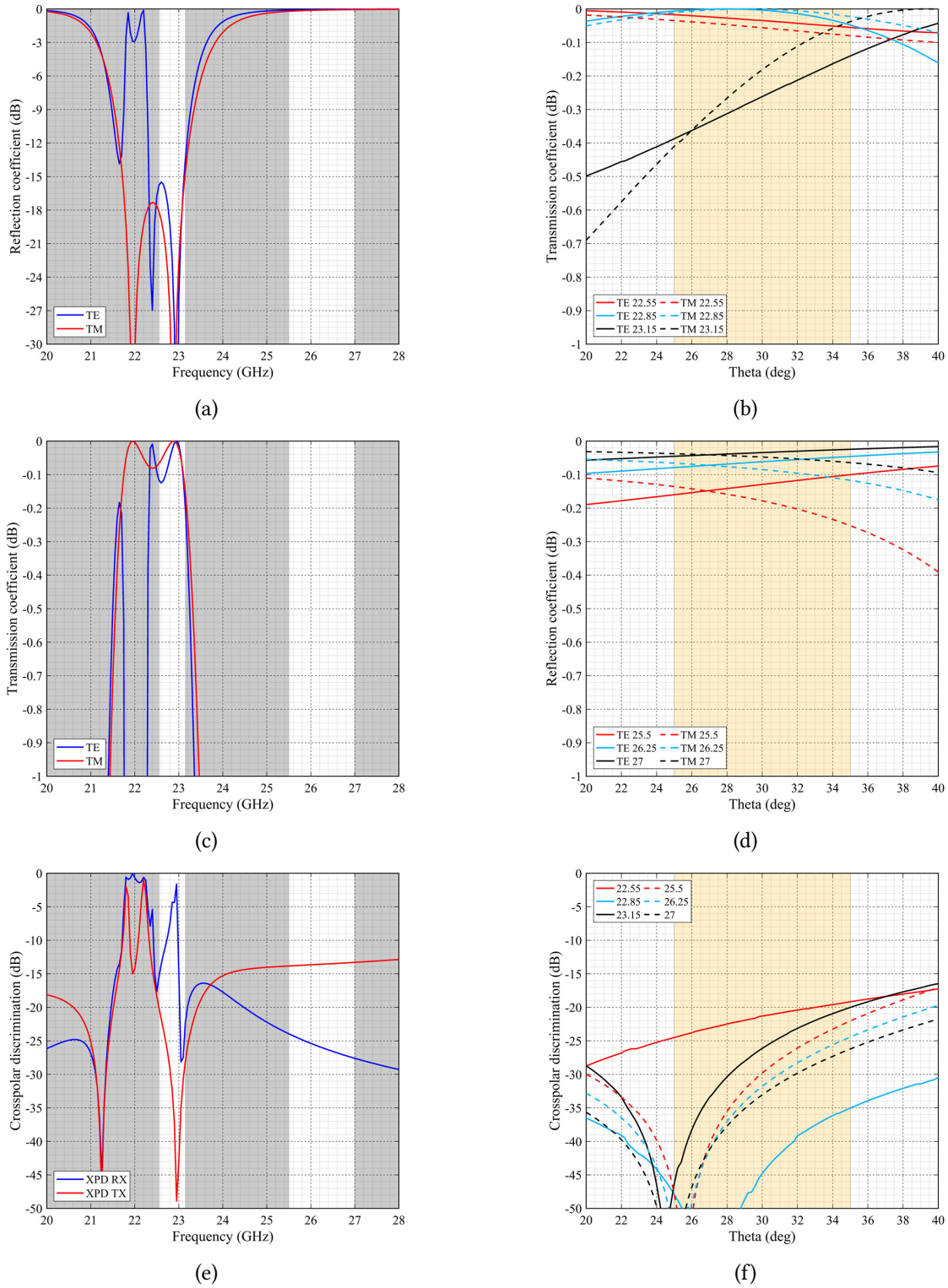

Figure 3.18: D5 performance: Reflection, Transmission coefficients and XPD at 30 deg (a,c,e); same for the 20 to 40 deg angular range (b,d,f)

3.2.8 D6 - Rectangular holes, single layer, thicker

Dichroic mirror D6 is to some extent an advanced case of mirror D1, that is a single layer inductive structure with rectangular apertures designed to transmit both the K-RX and K-TX channels

Its lattice is the same as D1 (Figure 3.5), but the relevant dimensions are different: (in mm) Lx=6.95, Ly=6.98, A=7.55, B=7.58. A minimal metal walls thickness between apertures of 0.5 mm is imposed to provide a sufficient stiffness to the mirror against its own weight. Compared to the previous mirror D1, the thickness of D6 is now much larger and equals to 17.16 mm, while the rounding radius is 0.2 mm, making manufacturing by wire erosion technique mandatory.

While such a large thickness is expected to deteriorate the angular response and XPD of the mirror, because of the complex relationship (mutual coupling) between the inner and outer faces of the mirror, in reality this is (partially, totally, or even over-) compensated for by smaller aperture dimensions, which in turn allows for shrinking the inter-element spacing, improving the bandwidth.

The simulated performance reflection and transmission coefficients for TE and TM linear polarisations of D6 at the nominal incidence angle (i.e. 30deg) is shown in Figures 3.19a and 3.19c. XPD for the circular polarisation at 30deg is shown in Figure 3.19e. Performance of TX and RX channels for both S and X bands are practically ideal, with a reflection coefficient better than -0.001 dB and a XPD better than -31.18 dB.

K-TX frequency response is quite good but also quite narrow, while K-RX band one is broader than others with a transmission coefficient values up to -0.22 dB in the middle band but lower at the edges. XPD is lower than -30 dB.

A more comprehensive overview of D6, in terms of maximum transmission coefficient and XPD against incidence angle, is given by Figures 3.19b, 3.19d and 3.19f, for the edge and centre frequencies of both K-TX and K-RX channels.

This design shows an improved angular response with respect to the others. The K-RX indeed exhibits a quite flat transmission coefficient response and the XPD is constantly close or lower than -30dB over the 25-35 degrees range.

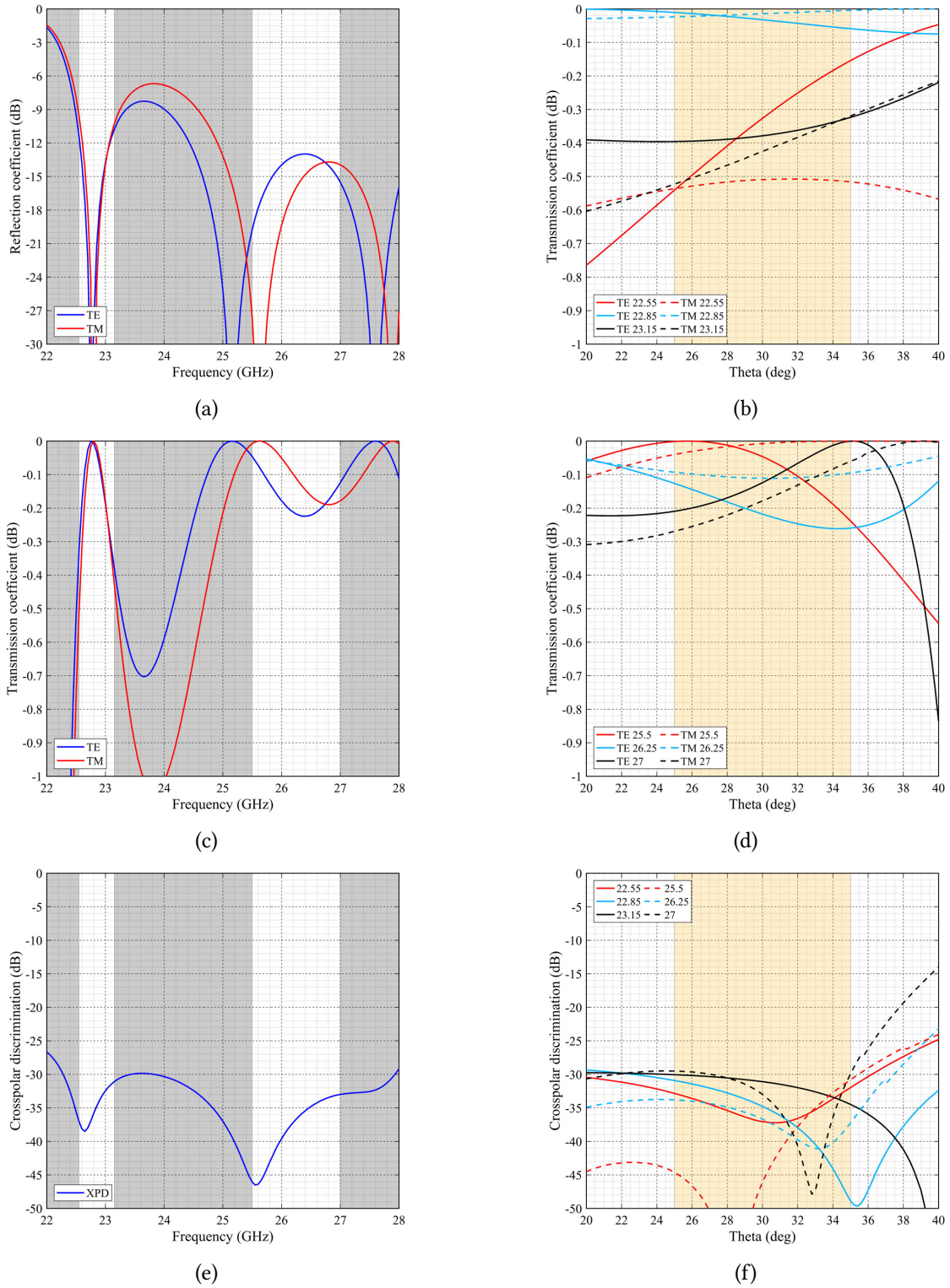

Figure 3.19: D6 performance: Reflection, Transmission coefficients and XPD at 30 deg (a,c,e); same for the 20 to 40 deg angular range (b,d,f)

3.2.9 Sensitivity analysis

Being the two designs elected as best cases, a sensitivity analysis of mirrors D1 and D6 has been performed for testing the designs robustness in the presence of uncertainty. Transmission coefficients for TE, TM modes and XPD values have been computed considering each of the mirror parameter as a random variable characterized by a Gaussian probability function with mean μ and standard deviation σ shown in 3.2. These values have been chosen because they are compatible, on the basis of previous experiences, with the respective construction techniques [47]. Moreover, the metrology measurement campaign, discussed in Section 3.2.11, done after this analysis, found values of μ and σ in line with the hypothesis for this sensitivity analysis.

Three different angles of incidence (e.g. 25, 30 and 35) were considered for both mirrors. 1000 simulations were run for D1 and 2000 for D6 because of the uncertainties related to the wire erosion technique, expressed also by considering a greater value of σ. Results are provided in term of graphs and tables reporting the average value of the transmission coefficient and XPD along the 90, 99 and 99.9 percentiles (i.e. 90 percentile means that 90% of the results are better than the specified value) for a set of frequencies.

Table 3.2: Mean and standard deviation values for the mirrors sensitivity analysis inputs

	D1		**D6**	
Input	μ	σ	μ	σ
Lx	7.39	0.005	6.95	0.012
Ly	7.57	0.005	6.99	0.012
A	7.89	0.005	7.55	0.012
B	8.07	0.005	7.59	0.012
thick	9.60	0.012	17.16	0.012
R	1.00	0.005	0.20	0.010

Mirror D1

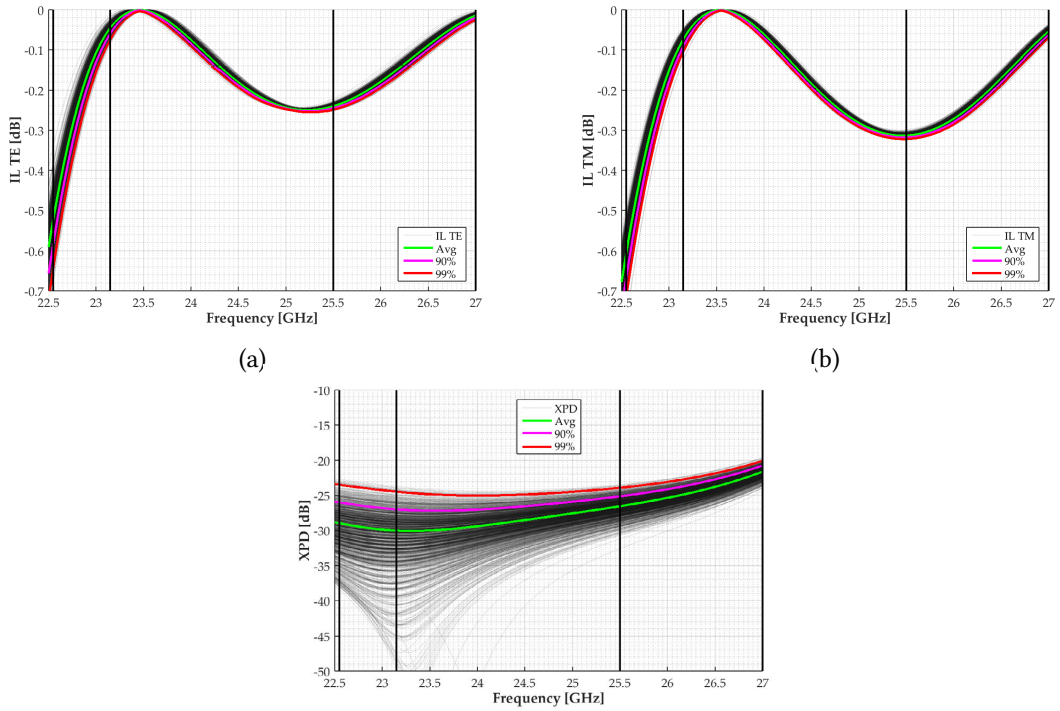

Figure 3.20: D1 sensitivity analysis graphs for TE (a), TM (b) transmission coefficients and XPD (c) at 25 degrees of incidence

Table 3.3: D1 sensitivity analysis results at 25 degrees of incidence

	TX coeff. TE [dB]				TX coeff. TM [dB]			
GHz	**avg**	**90.0%**	**99.0%**	**99.9%**	**avg**	**90.0%**	**99.0%**	**99.9%**
22.55	-0.521	-0.581	-0.641	-0.679	-0.604	-0.666	-0.712	-0.772
22.85	-0.203	-0.238	-0.273	-0.295	-0.262	-0.300	-0.328	-0.366
23.15	-0.045	-0.059	-0.075	-0.085	-0.073	-0.091	-0.104	-0.125
25.50	-0.240	-0.245	-0.249	-0.252	-0.314	-0.318	-0.322	-0.324
26.25	-0.135	-0.145	-0.153	-0.159	-0.226	-0.236	-0.243	-0.249
27.00	-0.014	-0.020	-0.025	-0.029	-0.053	-0.062	-0.070	-0.077

	XPD [dB]			
GHz	**avg**	**90.0%**	**99.0%**	**99.9%**
22.55	-28.950	-26.009	-23.498	-22.824
22.85	-29.644	-26.581	-24.023	-23.355
23.15	-30.018	-26.991	-24.474	-23.828
25.50	-26.541	-25.135	-23.917	-23.514
26.25	-24.628	-23.485	-22.522	-22.132
27.00	-21.626	-20.762	-20.089	-19.659

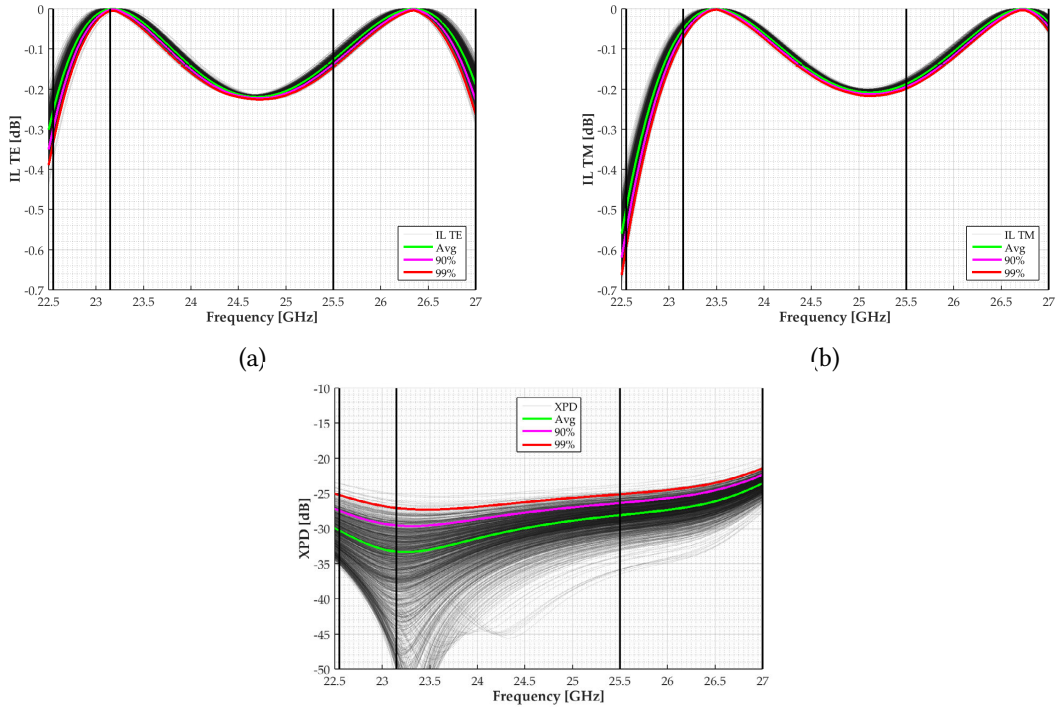

Figure 3.21: D1 sensitivity analysis graphs for TE (a), TM (b) transmission coefficients and XPD (c) at 30 degrees of incidence

Table 3.4: D1 sensitivity analysis results at 30 degrees of incidence

	TX coeff. TE [dB]				TX coeff. TM [dB]			
GHz	**avg**	**90.0%**	**99.0%**	**99.9%**	**avg**	**90.0%**	**99.0%**	**99.9%**
22.55	-0.252	-0.296	-0.332	-0.374	-0.496	-0.551	-0.592	-0.611
22.85	-0.057	-0.075	-0.092	-0.112	-0.201	-0.233	-0.257	-0.270
23.15	-0.001	-0.002	-0.005	-0.010	-0.049	-0.062	-0.073	-0.080
25.50	-0.127	-0.138	-0.146	-0.151	-0.187	-0.194	-0.199	-0.202
26.25	-0.003	-0.007	-0.011	-0.013	-0.057	-0.066	-0.073	-0.076
27.00	-0.189	-0.228	-0.263	-0.289	-0.033	-0.045	-0.056	-0.063

	XPD [dB]			
GHz	**avg**	**90.0%**	**99.0%**	**99.9%**
22.55	-30.309	-27.471	-25.240	-23.602
22.85	-32.241	-28.834	-26.352	-24.519
23.15	-33.294	-29.557	-27.087	-25.157
25.50	-28.100	-26.357	-25.121	-23.935
26.25	-26.866	-25.229	-24.097	-22.891
27.00	-23.558	-22.342	-21.457	-20.421

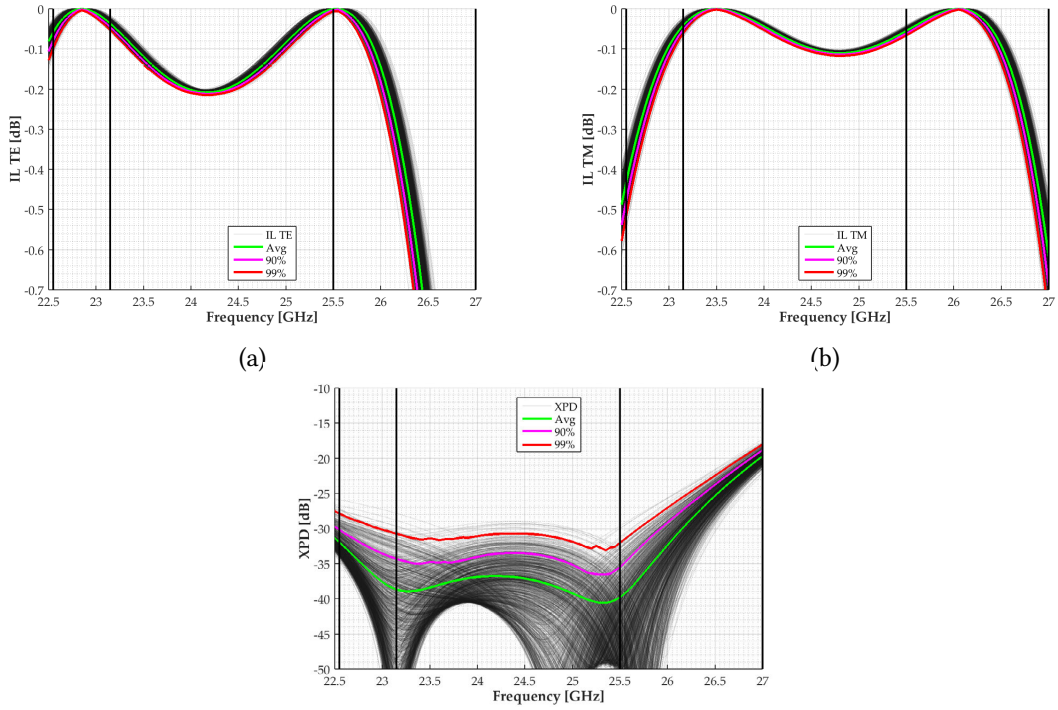

Figure 3.22: D1 sensitivity analysis graphs for TE (a), TM (b) transmission coefficients and XPD (c) at 35 degrees of incidence

Table 3.5: D1 sensitivity analysis results at 35 degrees of incidence

	TX coeff. TE [dB]				TX coeff. TM [dB]			
GHz	**avg**	**90.0%**	**99.0%**	**99.9%**	**avg**	**90.0%**	**99.0%**	**99.9%**
22.55	-0.058	-0.078	-0.097	-0.113	-0.430	-0.477	-0.514	-0.548
22.85	-0.001	-0.002	-0.004	-0.006	-0.171	-0.198	-0.219	-0.239
23.15	-0.037	-0.046	-0.054	-0.058	-0.041	-0.052	-0.061	-0.071
25.50	-0.001	-0.003	-0.006	-0.011	-0.055	-0.062	-0.066	-0.069
26.25	-0.396	-0.470	-0.531	-0.585	-0.014	-0.021	-0.029	-0.036
27.00	-2.370	-2.612	-2.817	-2.976	-0.616	-0.690	-0.768	-0.813

	XPD [dB]			
GHz	**avg**	**90.0%**	**99.0%**	**99.9%**
22.55	-31.965	-30.169	-27.889	-26.307
22.85	-35.874	-32.597	-29.486	-27.254
23.15	-38.696	-34.340	-30.767	-28.343
25.50	-39.778	-35.509	-32.042	-29.792
26.25	-28.655	-26.383	-24.714	-23.651
27.00	-19.697	-18.839	-18.019	-17.504

Mirror D6

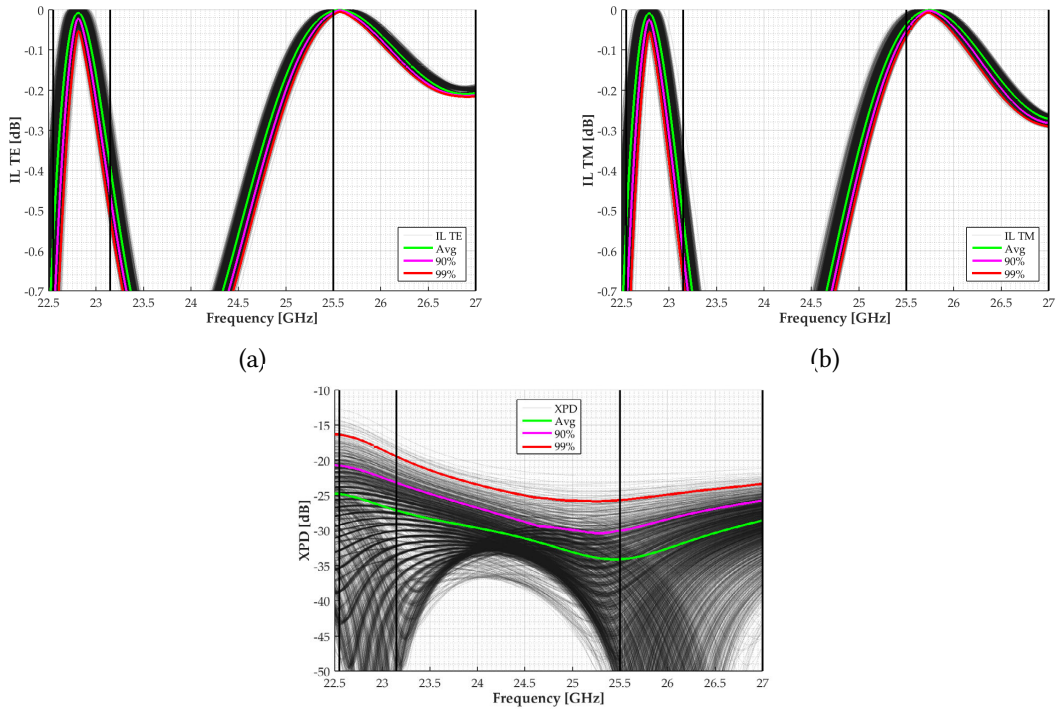

Figure 3.23: D6 sensitivity analysis graphs for TE (a), TM (b) transmission coefficients and XPD (c) at 25 degrees of incidence

Table 3.6: D6 sensitivity analysis results at 25 degrees of incidence

	TX coeff. TE [dB]				TX coeff. TM [dB]			
GHz	**avg**	**90.0%**	**99.0%**	**99.9%**	**avg**	**90.0%**	**99.0%**	**99.9%**
22.55	-0.562	-0.810	-1.046	-1.236	-0.530	-0.766	-0.987	-1.137
22.85	-0.016	-0.039	-0.076	-0.100	-0.032	-0.071	-0.116	-0.153
23.15	-0.392	-0.463	-0.520	-0.546	-0.523	-0.610	-0.674	-0.721
25.50	-0.003	-0.007	-0.013	-0.017	-0.036	-0.052	-0.066	-0.076
26.25	-0.123	-0.136	-0.145	-0.150	-0.098	-0.117	-0.137	-0.149
27.00	-0.207	-0.213	-0.216	-0.217	-0.272	-0.282	-0.291	-0.294

	XPD [dB]			
GHz	**avg**	**90.0%**	**99.0%**	**99.9%**
22.55	-24.804	-20.765	-16.368	-14.087
22.85	-25.837	-21.742	-17.561	-15.557
23.15	-27.143	-23.194	-19.460	-17.638
25.50	-34.094	-30.048	-25.681	-23.181
26.25	-31.415	-27.593	-24.483	-22.625
27.00	-28.587	-25.731	-23.365	-21.837

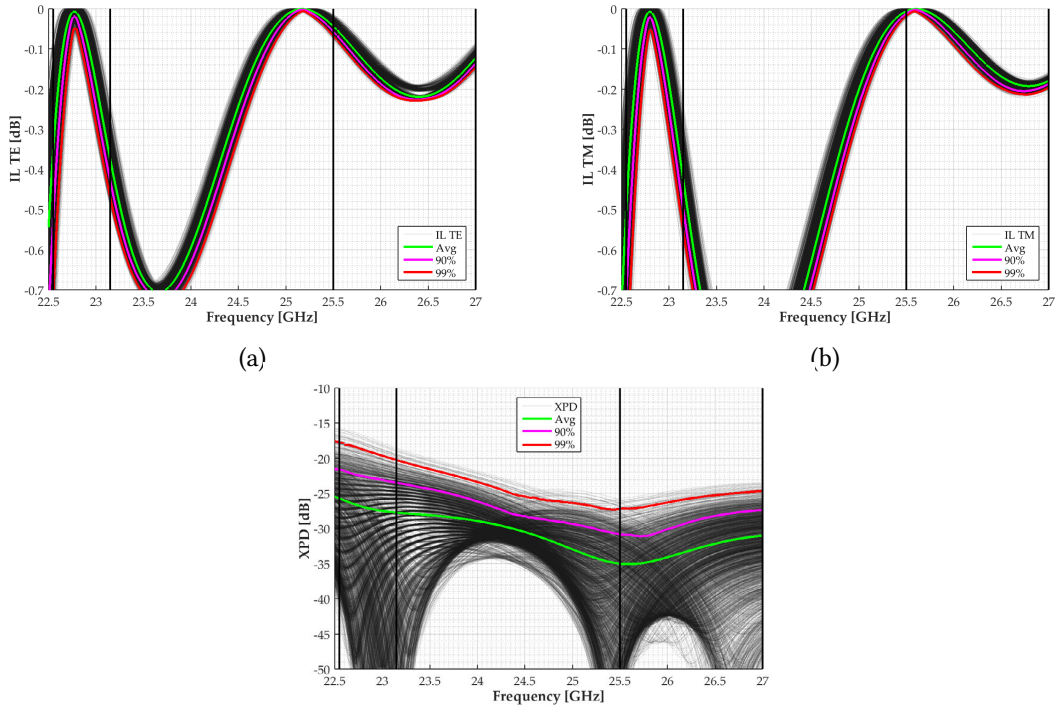

Figure 3.24: D6 sensitivity analysis graphs for TE (a), TM (b) transmission coefficients and XPD (c) at 30 degrees of incidence

Table 3.7: D6 sensitivity analysis results at 30 degrees of incidence

	TX coeff. TE [dB]				TX coeff. TM [dB]			
GHz	**avg**	**90.0%**	**99.0%**	**99.9%**	**avg**	**90.0%**	**99.0%**	**99.9%**
22.55	-0.345	-0.514	-0.714	-0.889	-0.495	-0.709	-0.931	-1.092
22.85	-0.035	-0.068	-0.104	-0.131	-0.022	-0.052	-0.092	-0.127
23.15	-0.376	-0.430	-0.471	-0.491	-0.427	-0.500	-0.554	-0.606
25.50	-0.044	-0.057	-0.068	-0.076	-0.006	-0.012	-0.018	-0.025
26.25	-0.212	-0.222	-0.226	-0.228	-0.117	-0.139	-0.155	-0.161
27.00	-0.122	-0.136	-0.146	-0.156	-0.179	-0.188	-0.196	-0.202

	XPD [dB]			
GHz	**avg**	**90.0%**	**99.0%**	**99.9%**
22.55	-25.730	-21.637	-17.758	-15.942
22.85	-27.115	-22.701	-18.996	-17.292
23.15	-27.728	-23.498	-20.264	-18.811
25.50	-34.994	-30.834	-27.221	-25.953
26.25	-33.083	-29.025	-25.705	-24.461
27.00	-31.012	-27.346	-24.645	-23.565

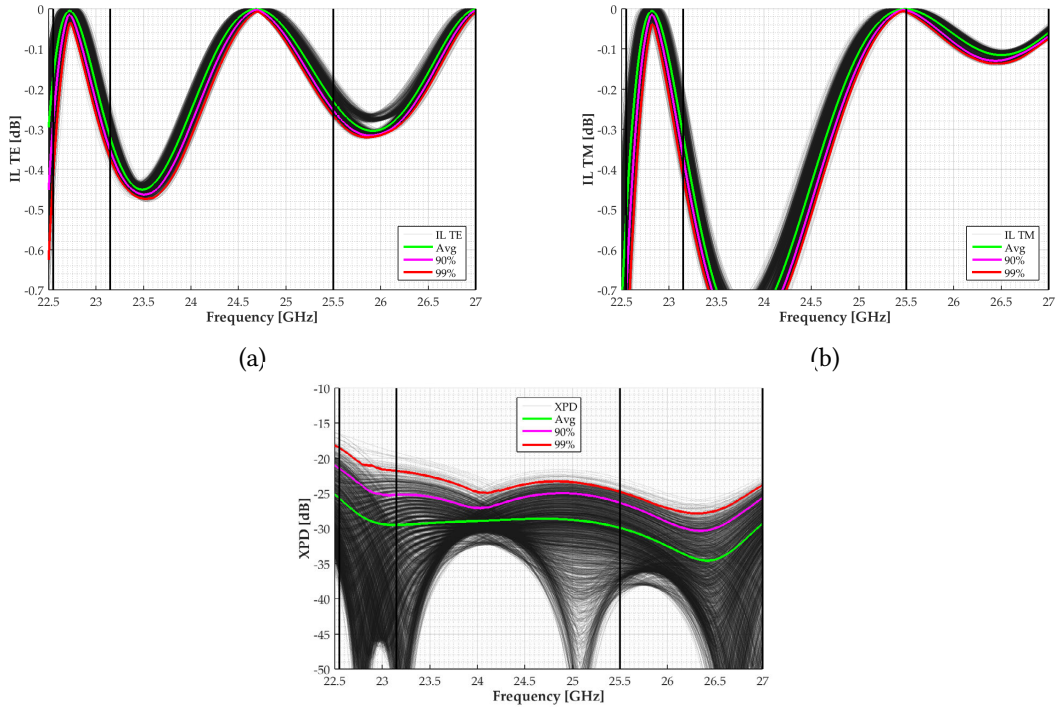

Figure 3.25: D6 sensitivity analysis graphs for TE (a), TM (b) transmission coefficients and XPD (c) at 35 degrees of incidence

Table 3.8: D6 sensitivity analysis results at 35 degrees of incidence

	TX coeff. TE [dB]				TX coeff. TM [dB]			
GHz	**avg**	**90.0%**	**99.0%**	**99.9%**	**avg**	**90.0%**	**99.0%**	**99.9%**
22.55	-0.167	-0.277	-0.410	-0.509	-0.507	-0.699	-0.898	-1.028
22.85	-0.060	-0.095	-0.126	-0.146	-0.010	-0.025	-0.050	-0.080
23.15	-0.321	-0.353	-0.374	-0.393	-0.318	-0.372	-0.420	-0.452
25.50	-0.231	-0.253	-0.267	-0.274	-0.001	-0.004	-0.008	-0.013
26.25	-0.252	-0.270	-0.278	-0.286	-0.100	-0.120	-0.128	-0.133
27.00	-0.002	-0.004	-0.011	-0.018	-0.059	-0.068	-0.075	-0.079

	XPD [dB]			
GHz	**avg**	**90.0%**	**99.0%**	**99.9%**
22.55	-25.725	-21.489	-18.546	-16.654
22.85	-28.760	-24.544	-21.006	-18.813
23.15	-29.485	-25.172	-21.794	-19.761
25.50	-29.914	-26.334	-24.775	-23.364
26.25	-34.080	-30.199	-27.818	-26.267
27.00	-29.268	-25.635	-23.842	-22.949

3.2.10 Ohmic losses

Dichroic mirror designs D1 and D6 have been verified against ohmic losses by simulation using full-wave simulation tools, setting a finite value for the metal conductivity (a bit higher than the real value to take into account also the surface roughness effect) and comparing results with the case of a perfect, infinite, conductivity.

Ohmic losses are calculated taking into account aluminium as bulk material.

Mirror D1

In this case, using milling technique, a finite value for the metal conductivity of $1.7x10^7$ S/m, that is roughly half of the pure aluminium conductivity, is expected to be achieved. According to experience this is a reasonable number for milling machining passivated by coatings [47]. A maximum loss around 0.02 dB for the K-TX band and a noise temperature contribution for the K-RX channel, assuming a physical temperature for the mirror equal to 300 K, around 1.5 K were calculated.

Mirror D6

Since this mirror is intended to be fabricated using wire erosion, a conservative finite value for the metal conductivity around $0.9x10^7$ (roughly a quarter of the conductivity of pure aluminium) is imposed. A maximum loss around 0.08 dB for the K-TX band and 0.035 dB for the K-RX band, correspondent to a noise temperature contribution for the K-RX channel around 2.75 K were calculated. This value is slightly worse compared to D1 because of D6 lower conductivity and higher thickness.

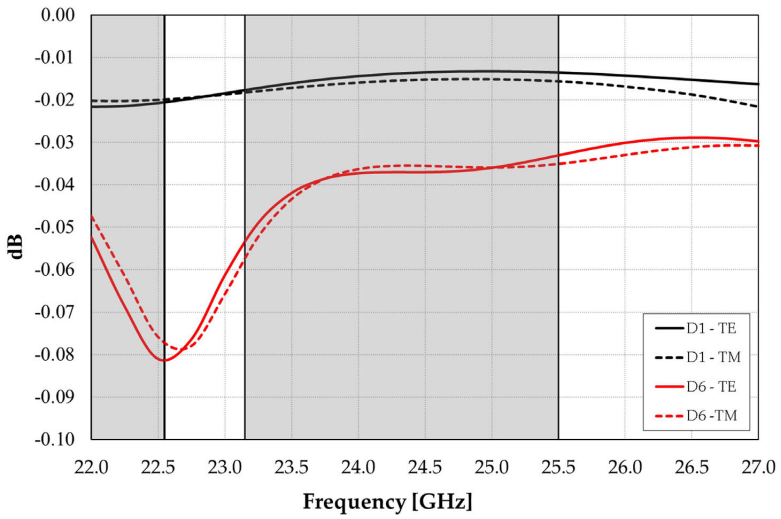

Figure 3.26: D1 & D6 ohmic loss

3.2.11 Measurements

In this section is described the technical aspects related to the manufacturing and testing of the two breadboard items based on mirrors D1 and D6 (Figures 3.27a, 3.27b, 3.28a and 3.28b). Both metrology and electromagnetic measurements campaigns, described in the following sections, have been carried out.

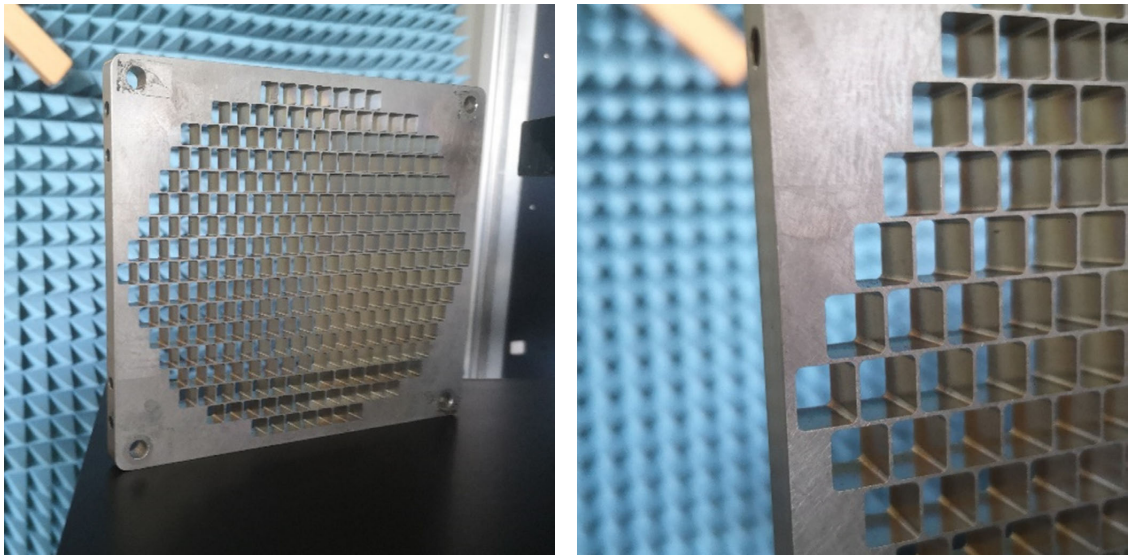

(a) (b)

Figure 3.27: Photographs of D1: (a) general view; (b) enlarged view

Dimension of both breadboard items, except for the thickness, are identical and equals to 168 x 145 mm^2, with 269 apertures. The ratio between 168 and 145 is approximately equal to 1.159, which is in line with $\cos 30^{-1} = 1.155$, where 30 is the nominal incidence angle in degrees of the radiation beam impinging on the mirror. In this way, the cross section exhibited to the beam is practically identical along the two directions. The slight difference is due to the need of allocating a finite number of apertures, which in addition are placed in such a way they can be roughly inscribed within an ellipse. Thus, the footprint exhibited by the aperture will be the one of a circle along the beam propagation direction, and this is in line with typical illuminations generated by test horns, in case they will be adopted for testing.

In terms of wavelengths, the breadboard is approximately 10.9 x 10.9 at 22.5 GHz, and 13.1 x 13.1 at 27 GHz, respectively the lower and upper frequency limit. This provides a unit in line with common standards for measurements in K band.

At X and S bands, the mirror is considered to provide a sub-optimum setup for testing, but taking into account the almost ideal performance in these bands, which are reflected by the mirror (for these frequencies, no less than 2.5 times lower than the K band, the effect of apertures is almost vanished) no testing is deemed necessary.

The breadboards, fabricated in aluminium, are completed with an edges rounding of 5 mm and 4 holes, one in each corner, useful for fixing itself to the support during testing.

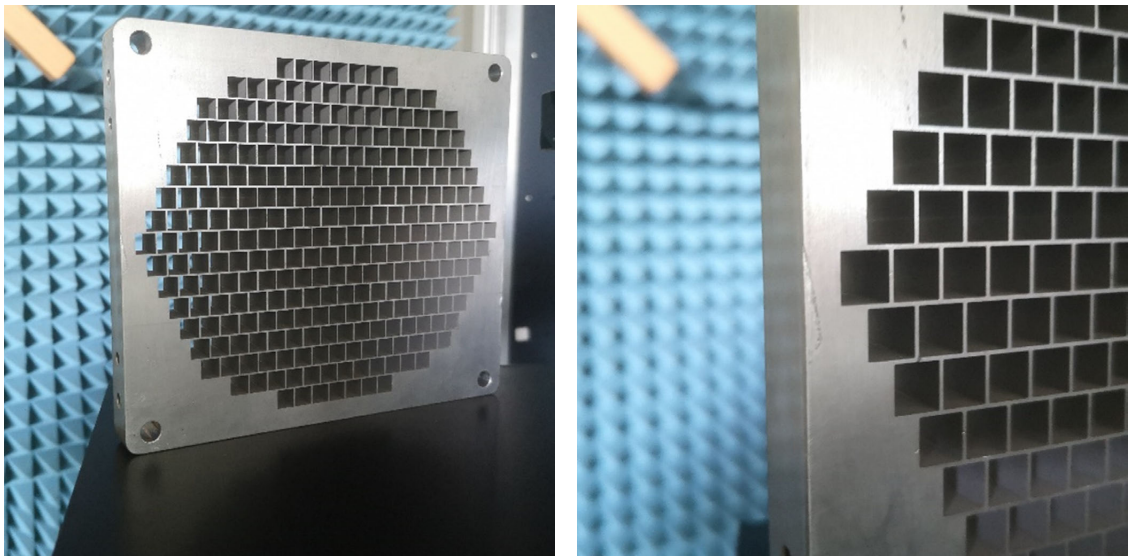

(a) (b)

Figure 3.28: Photographs of D6: (a) general view; (b) enlarged view

Metrology

The first metrology analysis consisted in randomly picking up different apertures along the mirror surface and test their dimensions. The results are reported in the following tables and figures.

For D1, 20 different apertures were measured, horizontally and vertically. It can be appreciated that, on average, the aperture is 3 μm and 4 μm smaller for the horizontal and vertical dimension, respectively. In addition, the variation at $\pm 3\sigma$, where approx. 99% of the cases are expected, is 6 μm and 33 μm for the horizontal and vertical dimension, respectively.

Concerning the lattice distances, three different pairs were measured. It can be appreciated that, on average, the aperture separation is no more than 6 μm larger than expected. In addition, the variation at $\pm 3\sigma$, where approx. 99% of the cases are expected, is 6 μm and 18 μm for the horizontal and vertical separation, respectively.

For D6, 15 different apertures were measured, horizontally and vertically. It can be appreciated that, on average, the aperture is 12 μm and 15 μm smaller for the horizontal and vertical dimension, respectively. In addition, the variation at $\pm 3\sigma$, where approx. 99% of the cases are expected, is 12 μm and 30 μm for the horizontal and vertical dimension, respectively.

Concerning the lattice distances, also in this case three different pairs were measured. It can be appreciated that, on average, the aperture separation is no more than 5 μm smaller than expected. In addition, the variation at $\pm 3\sigma$, where approx. 99% of the cases are expected, is 6 μm and 12 μm or the horizontal and vertical separation, respectively.

Finally, the RMS for the surface roughness was also measured, both for D1 and D6, measuring the inner wall of different apertures, also in this case using a dedicated metrology machine.

For D1, realized by milling, an average value of 0.3 μm was measured (the theoretical value supposed for D1 and used for simulations was 1.6 μm). For D6, realized by wire erosion, an

average value of 4.13 μm was measured (the theoretical value supposed for D1 and used for simulations was 3.2 μm). New simulations were therefore run, updating the models with values for the surface roughness measured experimentally. It is shown that losses are practically the same, as the variation for the RMS value with respect to the original value is minimal (D6) or in any case close to the floor (D1).

The important aspect remains the difference between milling and wire erosion. The value for the RMS for the latter can be as large as 10 times compared to the former. However, simulations indicate that losses do not scale linearly, moving from approx. 0.02 dB maximum for milling to approx. 0.08 dB maximum for wire erosion.

Table 3.9: Metrology results for D1, aperture dimensions

#	Horizontal [mm]	Vertical [mm]	#	Horizontal [mm]	Vertical [mm]
1	7.388	7.476	11	7.382	7.490
2	7.385	7.488	12	7.388	7.487
3	7.389	7.487	13	7.388	7.491
4	7.388	7.493	14	7.389	7.489
5	7.389	7.491	15	7.387	7.486
6	7.388	7.443	16	7.388	7.489
7	7.386	7.486	17	7.388	7.489
8	7.386	7.486	18	7.387	7.487
9	7.390	7.489	19	7.387	7.490
10	7.387	7.489	20	7.388	7.491

Table 3.10: Metrology results for D1, lattice distances

#	Horizontal [mm]	Vertical [mm]
1	7.889	8.000
2	7.889	7.989
3	7.893	8.000

Table 3.11: Metrology results for D6, aperture dimensions

#	Horizontal [mm]	Vertical [mm]	#	Horizontal [mm]	Vertical [mm]
1	6.939	6.970	9	6.942	6.967
2	6.934	6.971	10	6.935	6.967
3	6.932	6.961	11	6.933	6.964
4	6.936	6.936	12	6.937	6.972
5	6.941	6.967	13	6.947	6.972
6	6.934	6.960	14	6.938	6.967
7	6.937	6.969	15	6.939	6.978
8	6.940	6.958			

Table 3.12: Metrology results for D6, lattice distances

#	Horizontal [mm]	Vertical [mm]
1	7.549	7.578
2	7.549	7.571
3	7.546	7.575

Table 3.13: Summary of the metrology results for D1, aperture dimensions. Difference is measured with respect to the nominal value

	Horizontal [mm]	Vertical [mm]	Difference [mm]	Difference [mm]
Avg.	7.387	7.486	-0.003	-0.004
Max	7.390	7.493	0.000	0.003
Min	7.382	7.443	-0.008	-0.047
St.Dev	0.002	0.011		

Table 3.14: Summary of the metrology results for D1, lattice distances. Difference is measured with respect to the nominal value

	Horizontal [mm]	Vertical [mm]	Difference [mm]	Difference [mm]
Avg.	7.890	7.996	0.000	0.006
Max	7.893	8.000	0.003	0.010
Min	7.889	7.989	-0.001	-0.001
St.Dev	0.002	0.006		

Table 3.15: Summary of the metrology results for D6, aperture dimensions. Difference is measured with respect to the nominal value

	Horizontal [mm]	Vertical [mm]	Difference [mm]	Difference [mm]
Avg.	6.938	6.965	-0.012	-0.015
Max	6.947	6.978	-0.003	-0.002
Min	6.932	6.936	-0.018	-0.044
St.Dev	0.004	0.010		

Table 3.16: Summary of the metrology results for D6, lattice distances. Difference is measured with respect to the nominal value

	Horizontal [mm]	Vertical [mm]	Difference [mm]	Difference [mm]
Avg.	7.548	7.575	-0.002	-0.005
Max	7.549	7.578	-0.001	-0.002
Min	7.546	7.571	-0.004	-0.009
St.Dev	0.002	0.004		

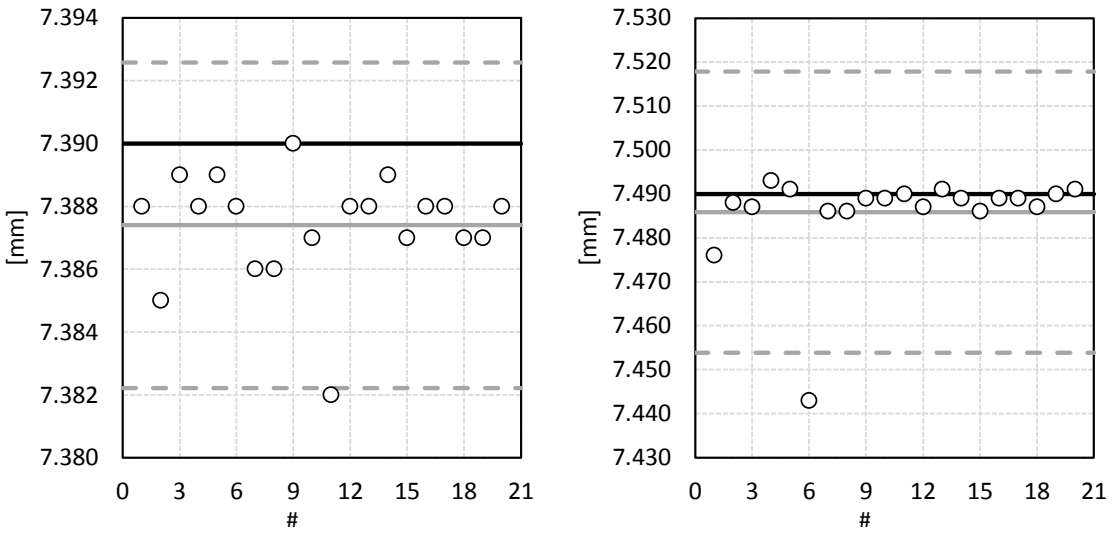

(a) (b)

Figure 3.29: D1 aperture metrology results: (a) horizontal, (b) vertical dimension of the apertures. Measurement values: white dots, nominal value: black line, average of the measurement: solid grey line, $\pm 3\sigma$: dashed grey lines

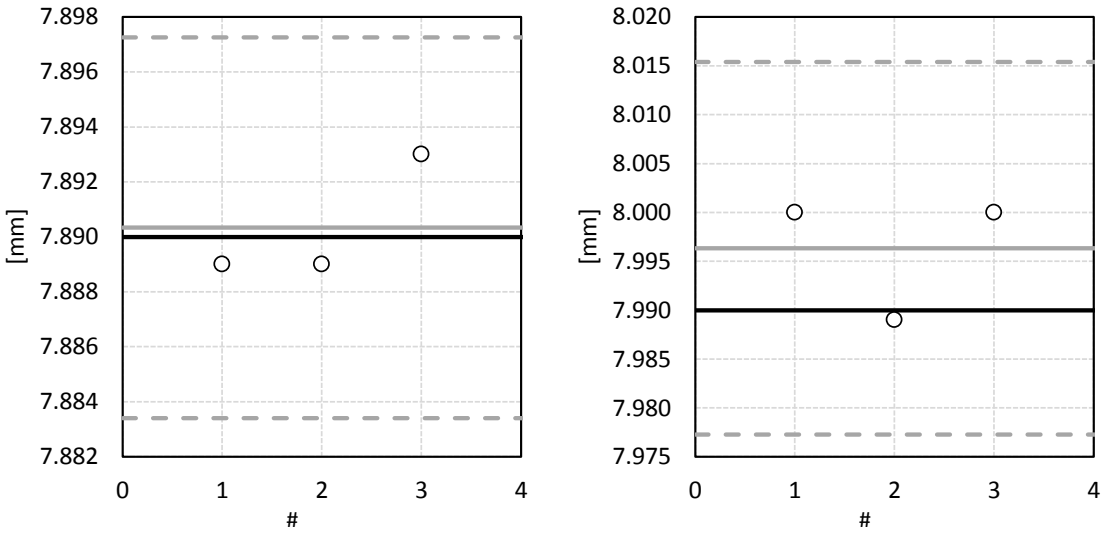

(a) (b)

Figure 3.30: D1 lattice metrology results: (a) horizontal, (b) vertical dimension of the apertures distances. Measurement values: white dots, nominal value: black line, average of the measurement: solid grey line, $\pm 3\sigma$: dashed grey lines

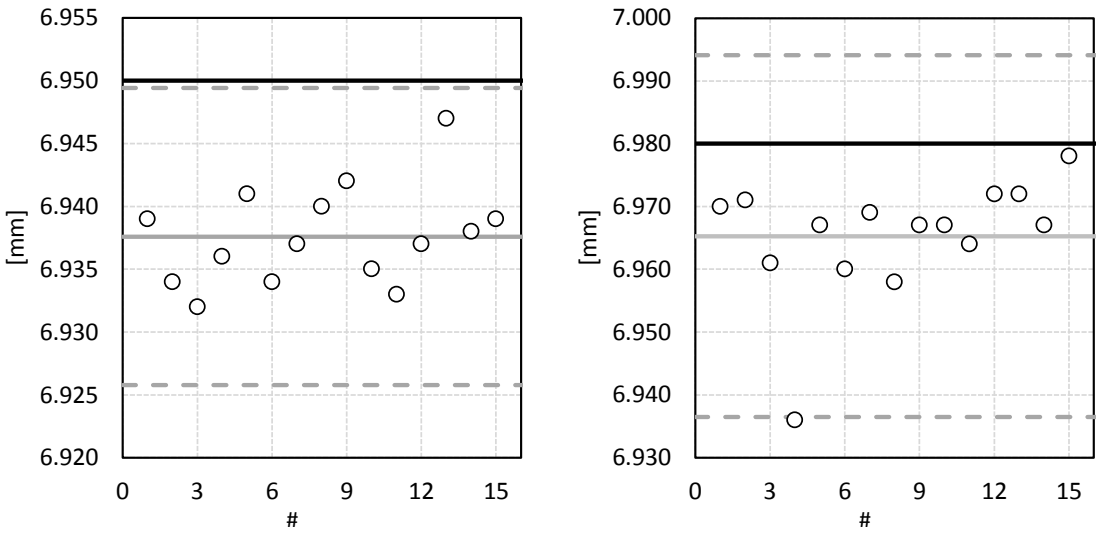

Figure 3.31: D6 aperture metrology results: (a) horizontal, (b) vertical dimension of the apertures. Measurement values: white dots, nominal value: black line, average of the measurement: solid grey line, $\pm 3\sigma$: dashed grey lines

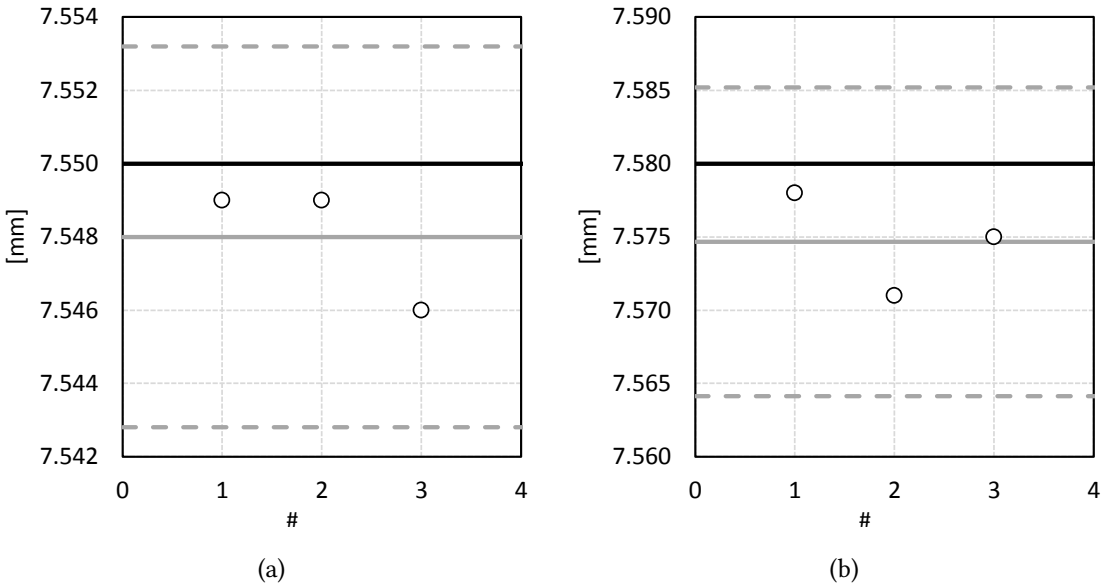

Figure 3.32: D6 lattice metrology results: (a) horizontal, (b) vertical dimension of the apertures distances. Measurement values: white dots, nominal value: black line, average of the measurement: solid grey line, $\pm 3\sigma$: dashed grey lines

Electromagnetic performance

The breadboard testing setup is identical for both D1 and D6. The original plan was to firstly test them using a setup based on two horns and then another one based on a Compact Antenna Test Range (CATR), potentially providing interesting comparisons (Figure 3.33). However, the results achieved with both setups were not as expected, despite the time and efforts spent to optimally calibrate them.

Figure 3.33: Original measurement setup

Instead, a further measurement session was undertaken, implementing a different setup at the University of Pavia (Figure 3.34 and Figure 3.35), using a dedicated frame.

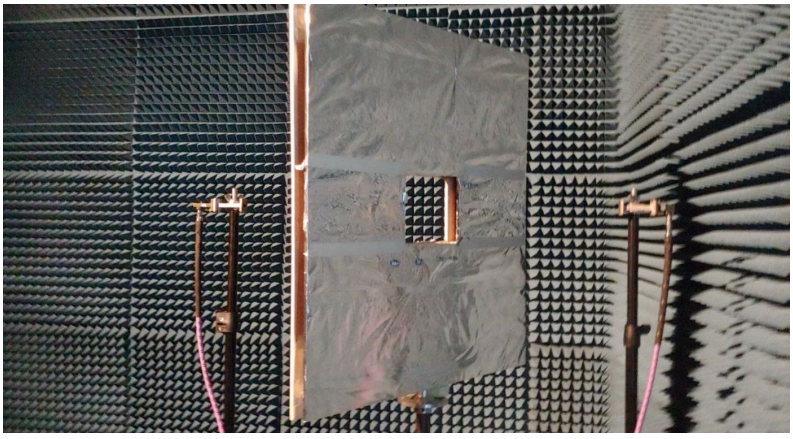

Figure 3.34: Measurement setup for transmission coefficient

Two open-ended WR42 waveguides were used as transmitting and receiving radiators, providing a coverage for all frequencies of interest, from 22 GHz to 28 GHz. Considering the far-field distance around 15 cm, the mirrors were placed at 20 cm from both radiators, aiming at a compromise between the wave front uniformity and the illumination tapering.

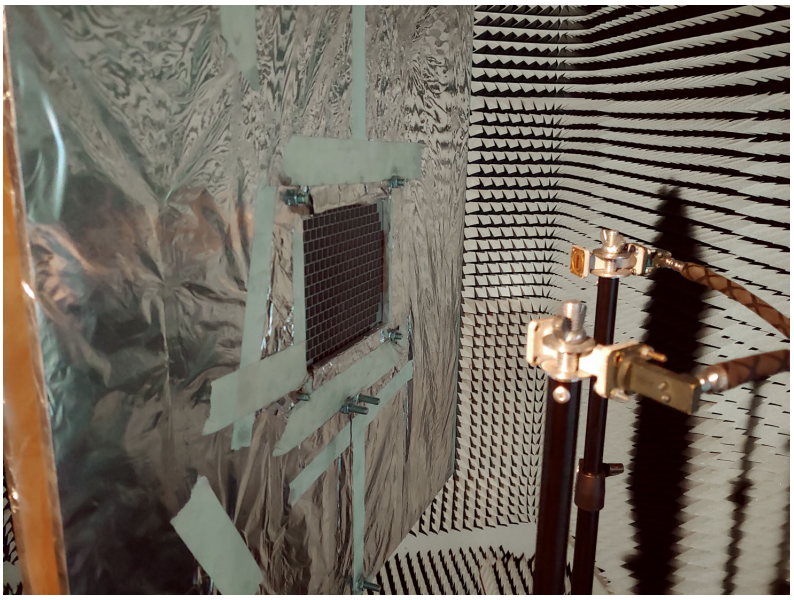

Figure 3.35: Measurement setup for reflection coefficient

Measurement took place in an anechoic chamber and two major key points were exploited. Firstly, time-domain transform and gating, provided by the Vector Network Analyzer (VNA) used to carry out the measurements, allowed to identify and isolate as much as possible the main contribution, reducing the spurious effects such as multiple reflections. Secondly, a large frame was fabricated and used. This was approximately 60 x 60 cm^2, with an hole in the centre to accommodate the mirror and allowed to work with a large metal screen in between the transmitting and receiving radiators, thus minimizing the edge effects, as the illumination taper at the frame edge is minimized.

The electric performance of the mirror is derived from a differential measurement. For transmission coefficient evaluation, the scattering parameter S21 was measured firstly with the mirror inside the frame and then without. For reflection measurements, the scattering parameter S21 is measured firstly with the mirror inside and secondly with a metal screen in front of it. Basically, in this latter case, a full metal screen were created.

However, two potential inaccuracies were identified: the operation of inserting/extracting the mirror into/from the frame is quite delicate; the edge effects caused by the inner borders of the frame are present during the measurement without the mirror, but not during the measurement with, thus causing an unbalance between the two cases.

Measurement took place as it follows:

- Frequencies: 22-28 GHz (thus covering 22.55-23.15 GHz and 25.5-27 GHz);
- Polarization: dual linear (HH and VV);
- Scattering parameters: transmission and reflection coefficient;
- Incidence angle: nominal, θ = 30 deg, ϕ = 0 deg.

Considering D1, the reflection measurements (Figure 3.36a) for the vertical polarization show a frequency shift in the order of 1.5 GHz for the first resonance and approximately 0.2

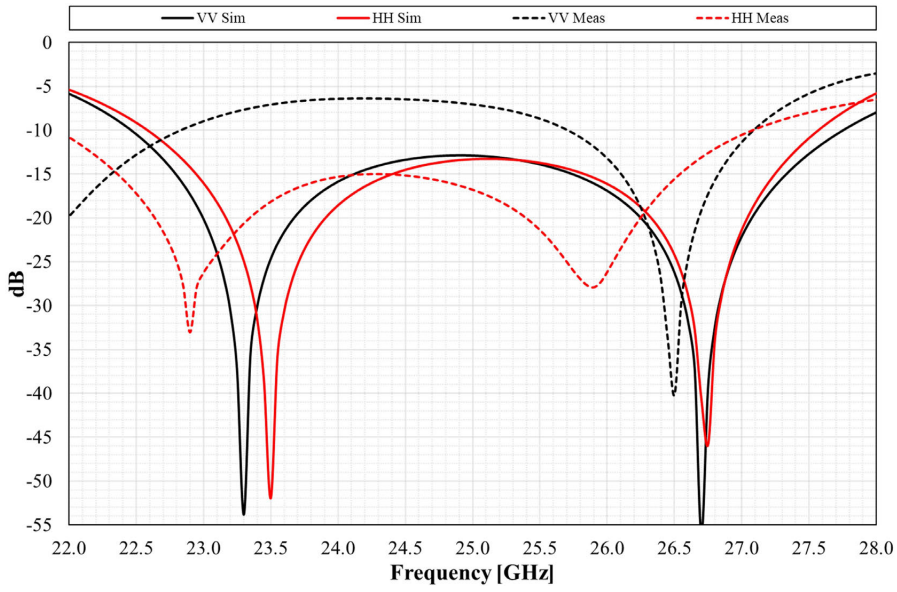

(a)

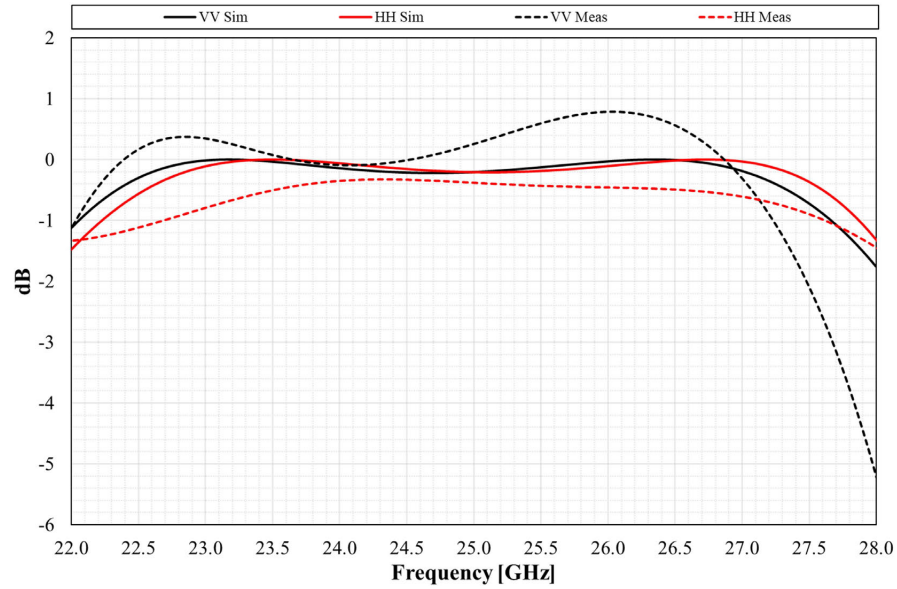

(b)

Figure 3.36: D1 measurements: (a) reflection and (b) transmission coefficients

GHz for the higher one, thus a difference of approx. 6% and 0.7%. For the horizontal polarization the frequency shift is no more than 1 GHz for both resonances (approx. 4%). The results about vertical polarization also exhibits a shoulder, in between the two K-band channel, higher than expected, approx. at -6 dB. However, this is not shown for the horizontal polarization. Therefore, it is supposed to be a spurious effect, not intrinsically related to the mirror. Transmission measurements (Figure 3.36b) basically confirm these trends. For vertical polarization,

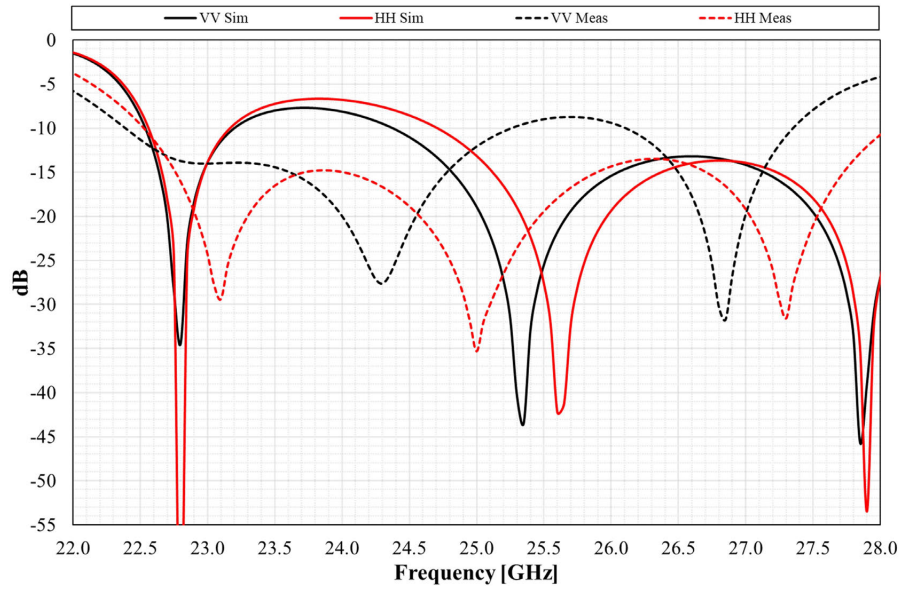

(a)

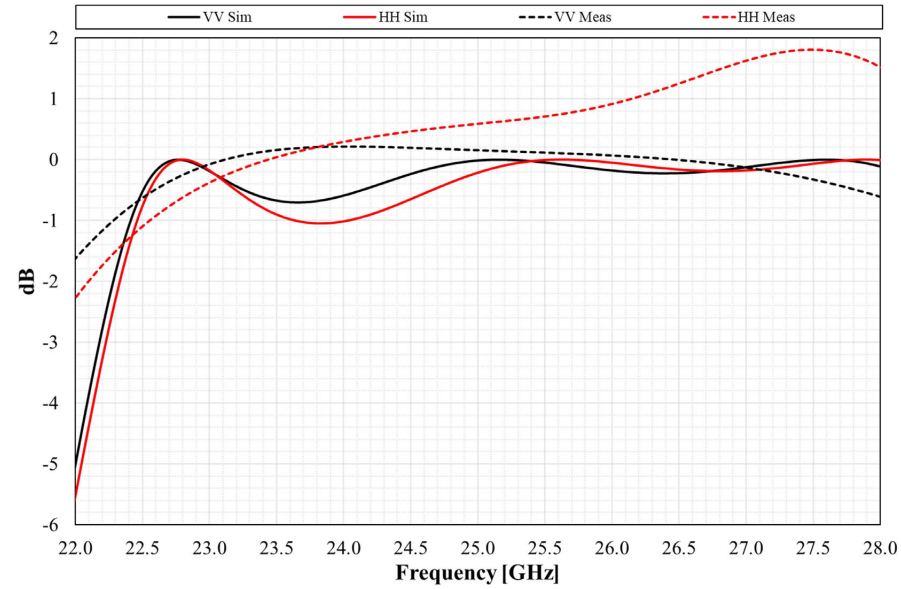

(b)

Figure 3.37: D1 measurements: (a) reflection and (b) transmission coefficients

the frequency shift is no more than 1 GHz (approx. 4%), but with positive values as high as 0.7/0.8 dB, which is clearly not physical. Again, this is a clear indication of a spurious effect, not intrinsically related to the mirror. As it was the case for reflection measurements, also for the transmission ones these effects are not in place, and measurements are well in line with simulations.

For D6, the reflection measurements (Figure 3.37a) for the vertical polarization show a frequency shift again in the order of 1.5 GHz, thus a difference of approx. 6%. For the horizontal polarization this frequency shift is lower. If compared with D1, the response shift is not rigid but, for the horizontal polarization, the first dip is shifted upward, while the second and third dips are shifted downward. Transmission measurements (Figure 3.37b) for the vertical polarization are basically in line with simulations. Instead, for the horizontal polarization, values exceeding the 0 dB threshold are reported. Again, this is a clear indication of a spurious effect, not intrinsically related to the mirror.

A further set of measurements was attempted with a different setup and VNA, employing two horns and putting the sample very close to them (Figure 3.38). Only the transmission coefficient was measured (Figures 3.39b and 3.40b) for both mirrors D1 and D6.

In general, the measured curves are more in line with the simulations, especially for the lower frequencies. In particular, poles of the frequency response seems more aligned with the theoretical ones, but there is still a problem of band reduction at the upper band limit. This might be a problem related to our setup with such a small device under test, in addition to the fact that the sample is placed in the near field of the two horns. Besides, the setup precision in terms of angles between the dichroic and the wave propagation direction can be further improved.

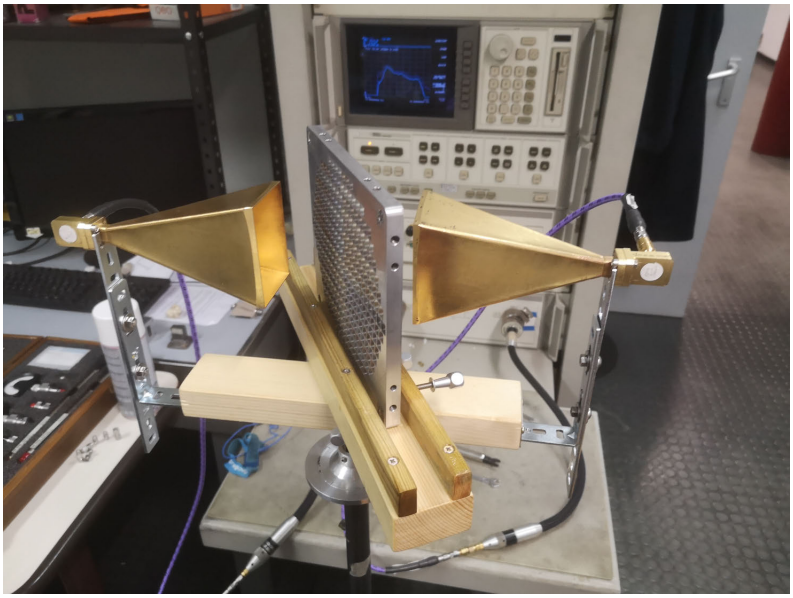

Figure 3.38: Second measurement setup with horn

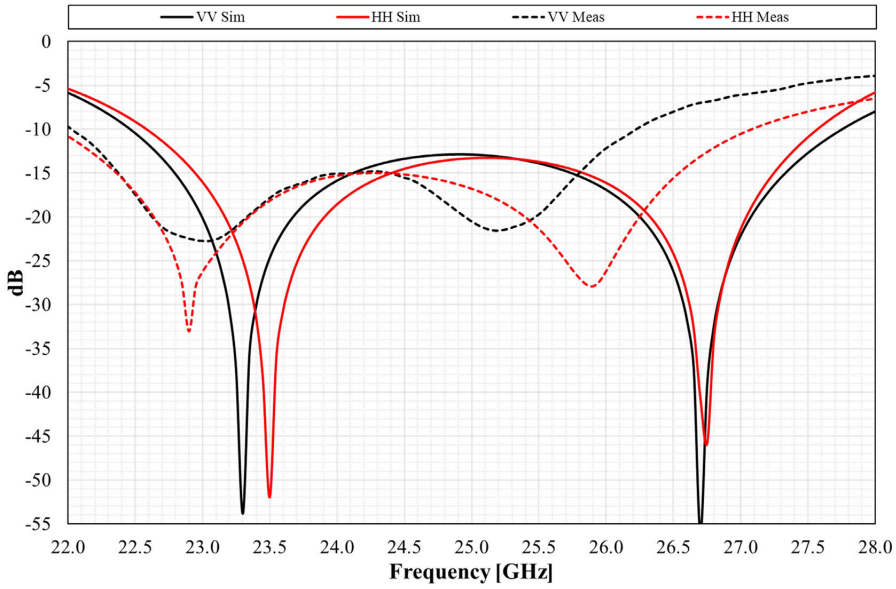

(a)

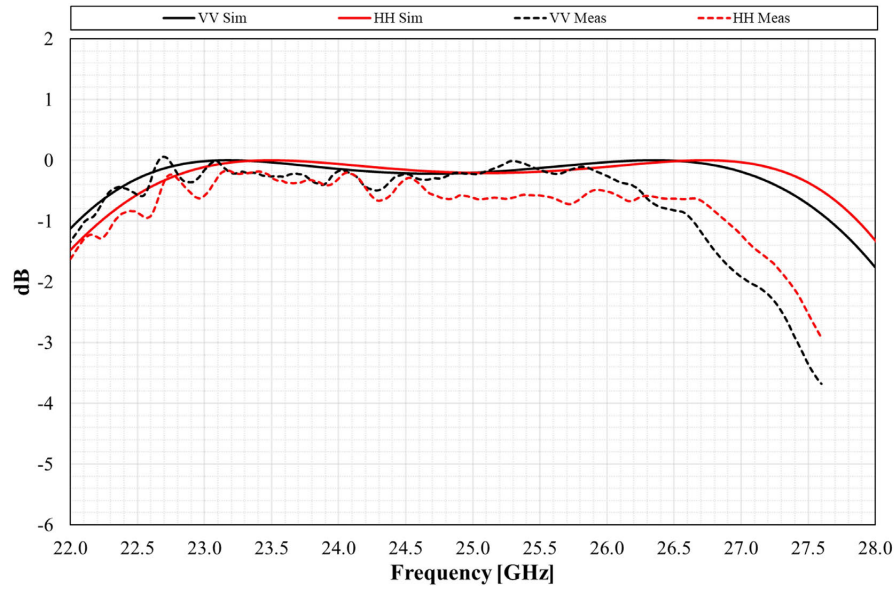

(b)

Figure 3.39: D1 measurements with horn: (a) reflection and (b) transmission coefficients

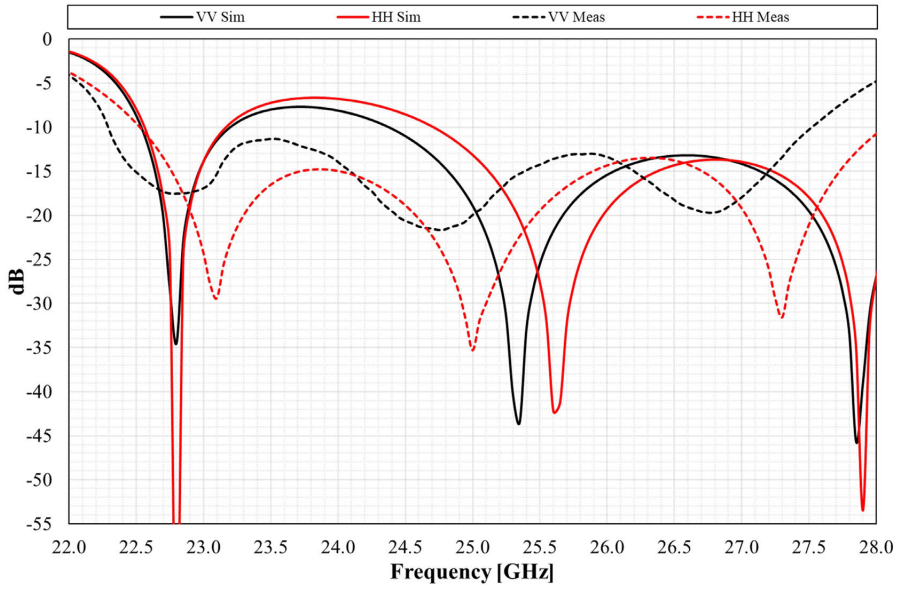

(a)

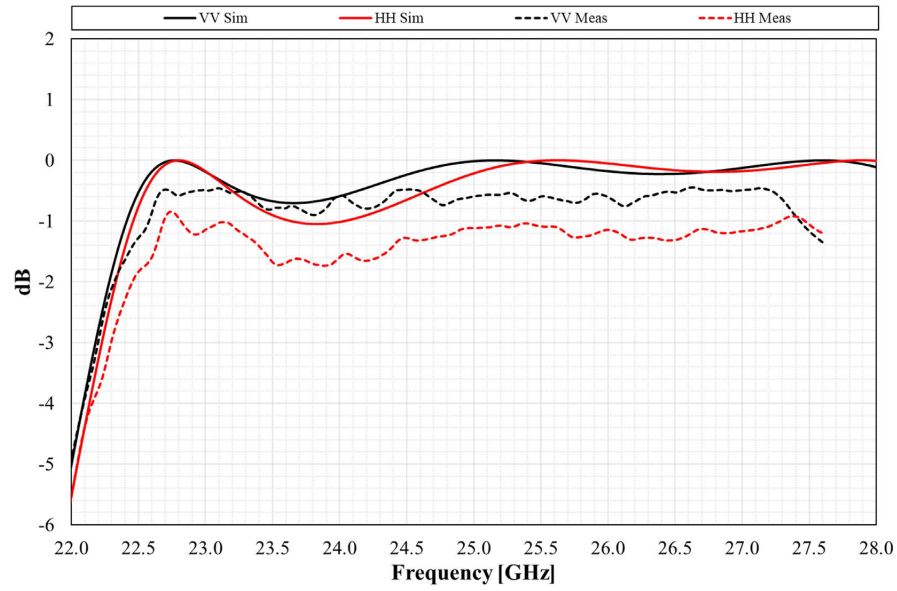

(b)

Figure 3.40: D6 measurements with horn: (a) reflection and (b) transmission coefficients

3.3 Antenna simulations

While the previous results are fundamental to understand the response of each mirror, antenna analysis is mandatory to determine their overall impact on the antenna performance and define the optimum solution. To this aim, the electromagnetic response of each mirror, as well as the entire antenna optics, were modelled and simulated using TICRA's GRASP software, a widely-adopted commercial tool based on the physical optics (PO) method.

The most commonly used techniques for large reflector antennas analyses are Geometrical Optics (GO), Physical Optics (PO), GTD (Geometrical Theory of Diffraction), PTD (Physical Theory of Diffraction) and Gaussian Beam Theory.

Geometrical Optics (GO) assumes that the electromagnetic field propagates, as a plane wave, in terms of "rays" defined as straight directions perpendicular to the wave fronts. The beam generated by the feed is thus represented as a conical flux tube, where the beam power is concentrated. At radio frequencies, however, GO is considered a reasonable approximation as long as the operational wavelength is negligible if compared to the reflector radius of curvature and the electromagnetic field varies slowly along small distances similar to wavelength.

Physical Optics approximation, in brief, evaluates the surface current density on a reflector induced by an electromagnetic field impinging on it. It is assumed that the surface current in a specific point on a curved, but perfectly conducting scatterer is the same as the surface current on an infinite planar surface which is tangent to the scattering surface at this point. Moreover, at points on the scatterer which are not directly illuminated by the incident field the surface currents are approximated with zero. The resulting scattered field from the reflector is then obtained by integrating the current density on the considered surface and it is used together with the incident field to compute the total one. This approach is more accurate and precise than the Geometrical Optics but it is more time consuming for reflectors with large electrical dimensions since field solutions shall be calculated using numerical methods.

Geometrical and Physical Theory of Diffraction (GTD and PTD) methods are respectively related to GO and PO and they are an extension of such techniques in order to account for diffraction.

For each considered antenna configuration and for each studied mirror, results from GRASP simulations are summarised in a table which reports the most important parameters, that are: maximum co-polar gain, antenna efficiency, first side-lobes level, maximum circular polarisation XPD and co-polar beam squint.

Maximum co-polar gain is the value obtained from the PO simulations; antenna efficiency is the ratio between the maximum PO gain and the maximum one achievable from uniform illumination of the main reflector; XPD is the maximum difference between the co-polar gain and the cross-polar level within the directions where the co-polar level is at most -1 dB less than the maximum gain.

As well as evaluate the impact of each mirror on the antenna and trade-off the actual configuration performance with new ones, each case was compared against its ideal case to get an insight of the best-case scenario obtainable. Therefore, simulations for the **ideal case** were run considering *perfect mirror* when the beam is reflected and *no mirror* when it is transmitted.

These results concern the HE11 mode of the antenna and for each simulated frequency a set of radiation pattern plots and a summary table of main antenna performance are generated. As

an example of how the above mentioned information is obtained, a couple of plots are shown hereafter in Figure 3.41. Figure 3.41a shows a representation of the co-polar and cross-polar radiation pattern plots for four cuts in the phi axis. The ITU mask (red dashed line) is also reported and maximum gain along first sidelobe peak are indicated. Figure 3.41b is a plot of the same radiation patterns in the U-V domain from which XPD and the beam squint error are evaluated.

Please note that in this section are presented antenna simulation results from all the mirrors described in Section 3.2 but, as stated for the mirror designs at the beginning of Section 3.2, all the results but those for D1 and D6 refers to the PDR phase of the project. Therefore, showed antenna performances considering D1 and D6 are simulations results obtained with optimized designs from the CDR phase.

Furthermore, position of the feeds and mirror following the dichroic one must be optimized to reduce the main beam squint angle.

Dichroic mirror finite thickness indeed induces an upward shift (d_m, purple continuous line of Figure 3.42) in the propagation direction of the electromagnetic signal coming from M5 and travelling through it (downward, if it is propagating towards M5). Because of this shift the feed no longer appears in the right place, hence the beam squint is increased and the antenna performance deteriorated. To compensate for it one has to adjust the position of subsequent flat mirror (M7 for DSA1 and M10 for DSA2/3). Thus, its position (D and d_m in Figure 3.42) with respect to mirror M5 was optimized and the best distance of the feed phase centre from the mirror (d_f Figure 3.42) was calculated in such a way to minimize the main beam squint angle while maximizing the performance by placing the phase centre of the feed in the best position. Optimization process was run at 26.25 Ghz.

Only antenna performances values obtained considering D1 and D6 take the results of this optimization into account, because such a task is strongly time-consuming and therefore it was faced during the CDR phase of the project, after the identification of D1 and D6 as best solutions.

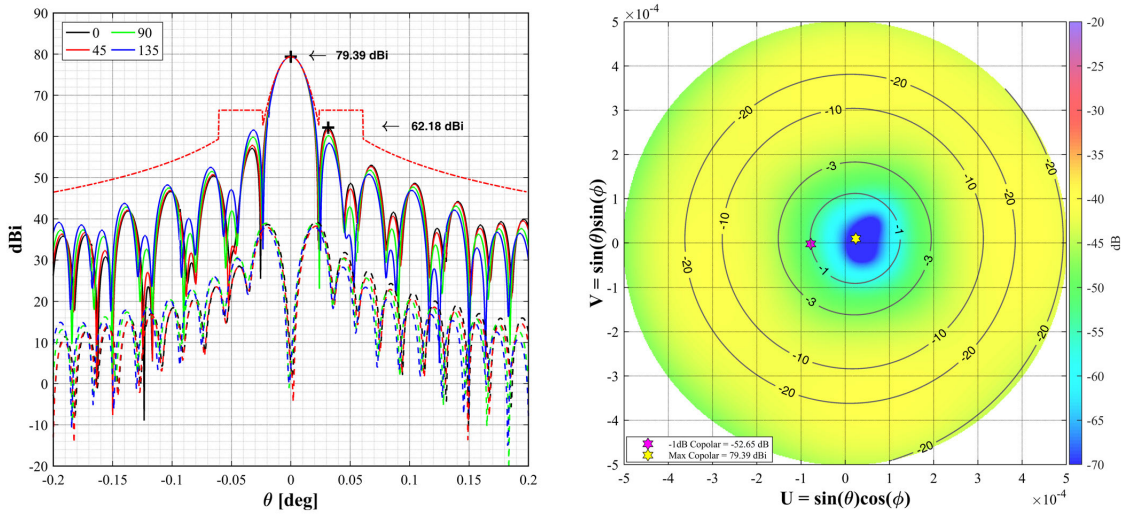

(a) (b)

Figure 3.41: Example of radiation patterns vs (a) theta for given cuts, (b) U-V domain

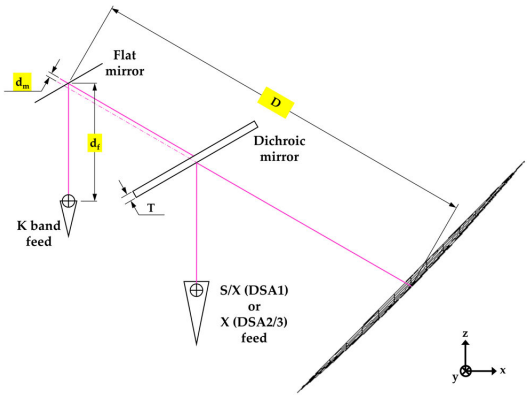

Figure 3.42: Scheme for flat mirror and feed optimization. D, distance between mirror centre and mirror M5; d_m, mirror centre shift (perpendicular with respect to direction D); d_f, distance between mirror centre (optimized) and feed phase centre

3.3.1 DSA 1

This section shows the results of all GRASP simulations performed for DSA1. In particular, they all refer to the DSA1-A configuration, described in Figure 3.3a. For each case are shown all the relevant lower beam-waveguide distances up to M5 and a table reporting the main parameters from the analysis. All distances are in meters.

Please note that the poor value exhibited in the actual case at 7.19 GHz for the cross-polarization is already presented in the current antenna design and it is due the dichroic mirror M6. Indeed, in order to compensate for that, a phase shifter was installed.

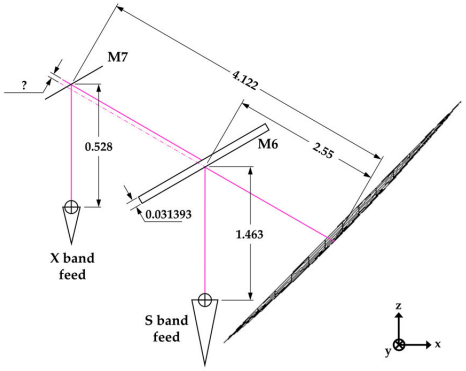

Figure 3.43: Currently low BWG optical layout implemented in DSA1

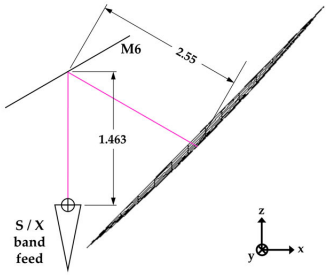

Figure 3.44: DSA1-A, low BWG optical layout for the S/X-band ideal case

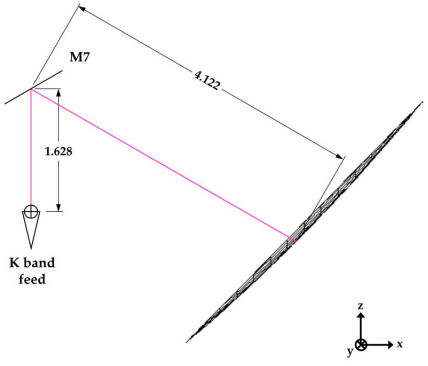

Figure 3.45: DSA1-A, low BWG optical layout for the K-band ideal case

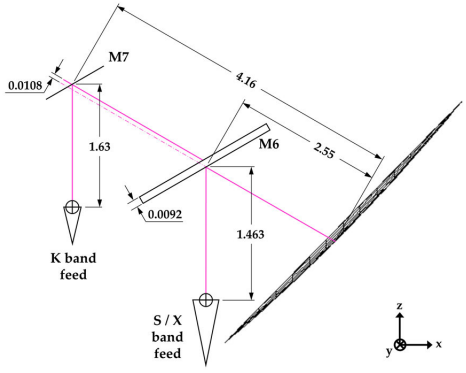

Figure 3.46: DSA1-A, low BWG optical layout for D1 case

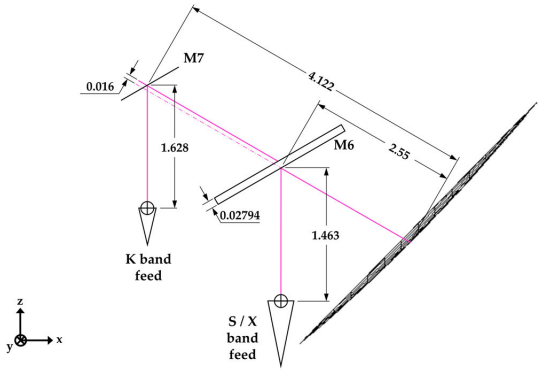

Figure 3.47: DSA1-A, low BWG optical layout for D1a case

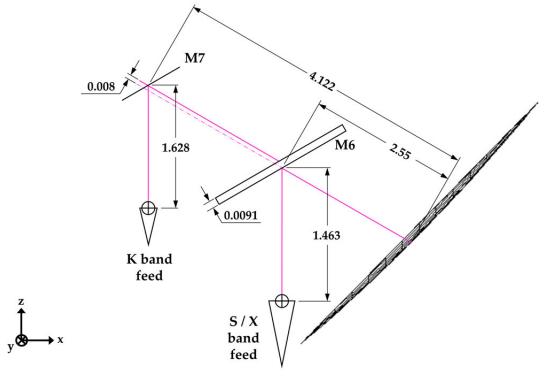

Figure 3.48: DSA1-A, low BWG optical layout for D2 case

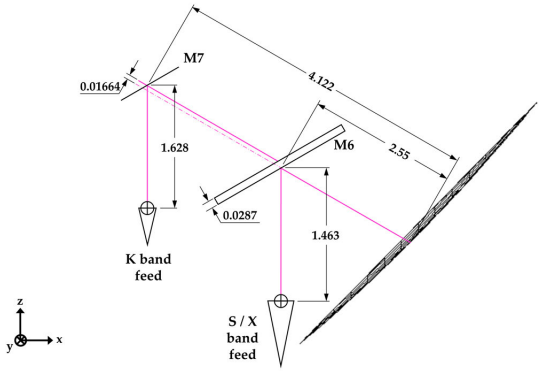

Figure 3.49: DSA1-A, low BWG optical layout for D2a case

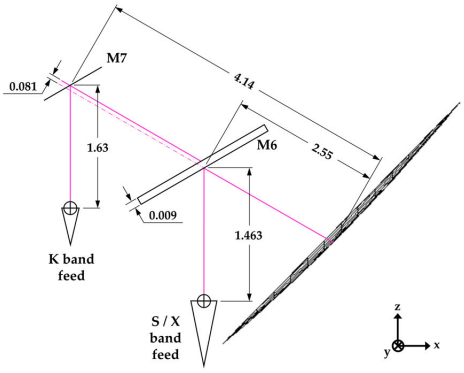

Figure 3.50: DSA1-A, low BWG optical layout for D3 case

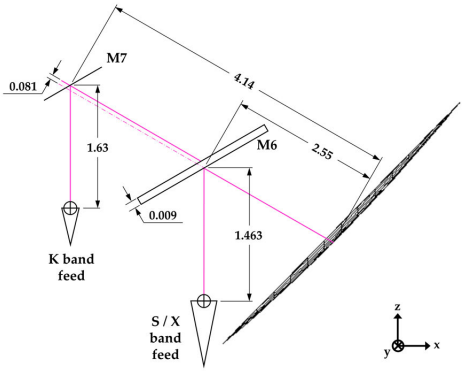

Figure 3.51: DSA1-A, low BWG optical layout for D4 case

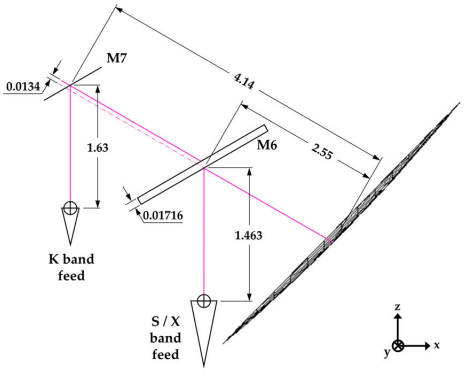

Figure 3.52: DSA1-A, low BWG optical layout for D6 case

Table 3.17: DSA1-A simulation results: Efficiency (%)

	Frequency [GHz]								
	2.025	**2.2**	**7.145**	**8.40**	**22.55**	**23.15**	**25.5**	**26.25**	**27**
Actual	78.05	79.87	75.89	84.26	n.a.	n.a.	n.a.	n.a.	n.a.
Ideal	76.80	80.23	85.15	82.73	87.28	87.52	87.93	88.09	88.00
D1	76.80	80.23	85.15	82.73	80.34	87.12	84.75	85.89	78.97
D1a	77.15	80.79	85.35	82.92	86.68	85.53	80.19	80.90	62.88
D2	77.33	80.79	85.35	82.92	81.64	86.52	84.75	83.36	66.45
D2a	77.33	80.79	85.55	82.92	85.69	85.72	81.31	82.78	65.84
D3	77.33	80.79	89.78	79.92	81.45	86.32	83.97	86.29	79.89
D4	76.98	80.42	89.17	79.37	87.08	85.72	84.75	87.29	85.60
D6	77.33	80.79	89.78	79.55	79.42	80.00	87.12	85.10	85.21

Table 3.18: DSA1-A simulation results: Directivity (dBi)

	Frequency [GHz]								
	2.025	**2.2**	**7.145**	**8.40**	**22.55**	**23.15**	**25.5**	**26.25**	**27**
Actual	56.34	57.16	67.17	69.03	n.a.	n.a.	n.a.	n.a.	n.a.
Ideal	56.27	57.18	67.67	68.95	77.76	78.00	78.86	79.12	79.36
D1	56.27	57.18	67.67	68.95	77.40	77.98	78.70	79.01	78.89
D1a	56.29	57.21	67.68	68.96	77.73	77.90	78.46	78.75	77.90
D2	56.30	57.21	67.68	68.96	77.47	77.95	78.70	78.88	78.14
D2a	56.30	57.21	67.69	68.96	77.68	77.91	78.52	78.85	78.10
D3	56.30	57.21	67.90	68.80	77.46	77.94	78.66	79.03	78.94
D4	56.28	57.19	67.87	68.77	77.75	77.91	78.70	79.08	79.24
D6	56.30	57.21	67.90	68.78	77.35	77.61	78.82	78.97	79.22

Table 3.19: DSA1-A simulation results: max XPD (dBi)

	Frequency [GHz]								
	2.025	**2.2**	**7.145**	**8.40**	**22.55**	**23.15**	**25.5**	**26.25**	**27**
Actual	-28.41	-27.09	-10.79	-33.60	n.a.	n.a.	n.a.	n.a.	n.a.
Ideal	-36.29	-44.48	-41.42	-40.56	-64.32	-62.79	-63.39	-69.92	-55.46
D1	-36.29	-44.48	-41.42	-40.56	-31.28	-34.64	-28.42	-25.88	-20.93
D1a	-36.55	-37.76	-31.22	-30.15	-31.44	-35.39	-26.56	-23.08	-17.98
D2	-36.27	-37.34	-30.15	-28.60	-21.47	-26.10	-33.43	-25.24	-21.16
D2a	-36.36	-37.53	-30.80	-29.55	-22.71	-26.76	-23.72	-20.72	-15.84
D3	-38.24	-38.93	-27.92	-38.14	-23.41	-30.62	-31.26	-24.00	-18.54
D4	-36.27	-45.16	-39.54	-37.38	-31.43	-31.74	-26.90	-27.35	-23.22
D6	-38.74	-40.56	-30.51	-29.62	-35.58	-31.18	-39.86	-35.70	-31.96

Table 3.20: DSA1-A simulation results: θ squint (mdeg)

	Frequency [GHz]								
	2.025	**2.2**	**7.145**	**8.40**	**22.55**	**23.15**	**25.5**	**26.25**	**27**
Actual	7.03	6.27	9.75	10.79	n.a.	n.a.	n.a.	n.a.	n.a.
Ideal	4.50	4.88	1.47	1.45	0.93	0.91	0.83	0.81	0.81
D1	4.50	4.88	1.47	1.45	1.02	1.03	0.79	0.83	1.42
D1a	5.27	5.46	1.56	1.56	1.09	1.15	2.42	3.41	5.54
D2	5.38	5.53	1.58	1.57	0.88	0.84	1.16	1.78	2.20
D2a	5.39	5.54	1.58	1.57	1.02	1.01	2.02	2.94	4.85
D3	6.84	4.47	1.85	1.63	0.81	0.77	0.85	1.18	1.66
D4	6.05	4.14	1.74	1.49	0.66	0.90	0.61	0.64	0.69
D6	6.85	4.50	1.83	1.60	0.94	0.99	0.85	0.82	0.89

Table 3.21: DSA1-A simulation results: First sidelobe (dB)

	Frequency [GHz]								
	2.025	**2.2**	**7.145**	**8.40**	**22.55**	**23.15**	**25.5**	**26.25**	**27**
Actual	-15.39	-16.11	-16.95	-16.69	n.a.	n.a.	n.a.	n.a.	n.a.
Ideal	-15.24	-16.08	-13.33	-15.40	-16.10	-16.28	-16.97	-17.02	-17.25
D1	-15.24	-16.08	-13.33	-15.40	-16.22	-16.46	-16.91	-17.07	-17.14
D1a	-15.28	-16.10	-13.34	-15.46	-16.01	-16.22	-16.58	-16.22	-14.28
D2	-15.30	-16.10	-13.34	-15.46	-16.06	-16.38	-16.84	-16.77	-17.89
D2a	-15.30	-16.10	-13.35	-15.46	-16.07	-16.31	-16.60	-16.05	-16.76
D3	-15.19	-15.97	-15.02	-15.61	-16.09	-16.37	-16.82	-16.97	-17.29
D4	-15.16	-15.93	-14.96	-15.31	-16.10	-16.12	-16.94	-17.02	-17.17
D6	-15.42	-16.08	-15.09	-15.83	-16.11	-16.36	-16.99	-17.03	-17.09

3.3.2 DSA 2 & DSA 3

This section shows the results of all GRASP simulations performed for DSA2/3. In particular, all but D5 case refer to the DSA23-B configuration, described in Figure 3.4b. D5 case refers instead to configuration DSA23-A, described in Figure 3.4a. For each case are shown all the relevant lower beam-waveguide distances up to M5 and a table reporting the main parameters from the analysis. All distances are in meters.

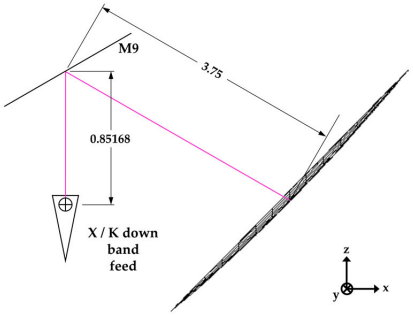

Figure 3.53: Currently low BWG optical layout implemented in DSA2/3

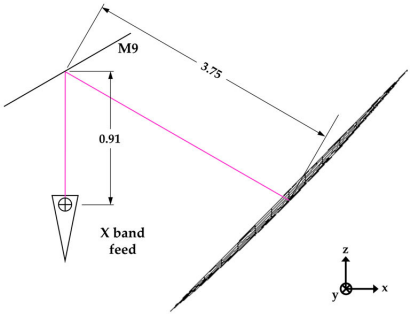

Figure 3.54: DSA23-B, low BWG optical layout for the X-band ideal case

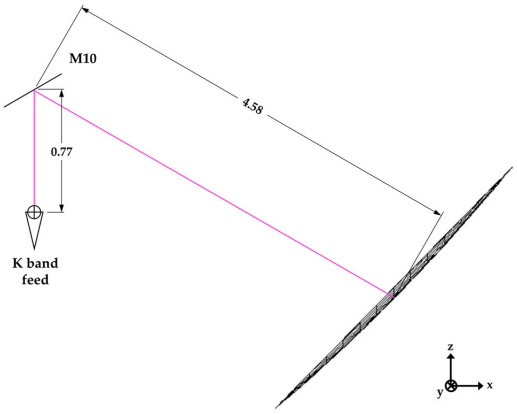

Figure 3.55: DSA23-B, low BWG optical layout for the K-band ideal case

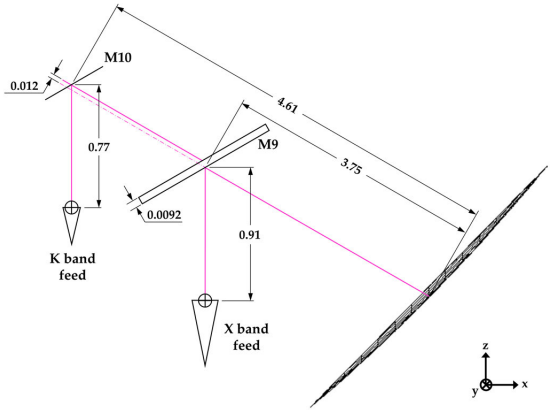

Figure 3.56: DSA2/3-B, low BWG optical layout for D1 case

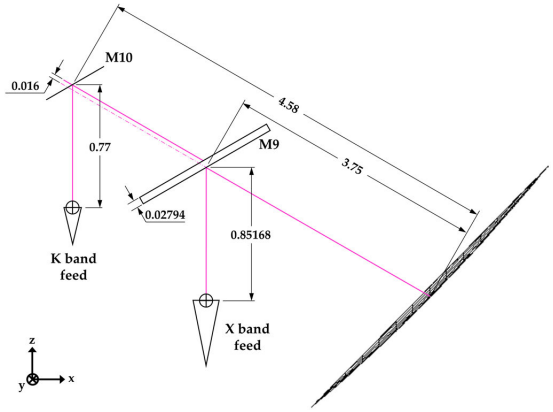

Figure 3.57: DSA2/3-B, low BWG optical layout for D1a case

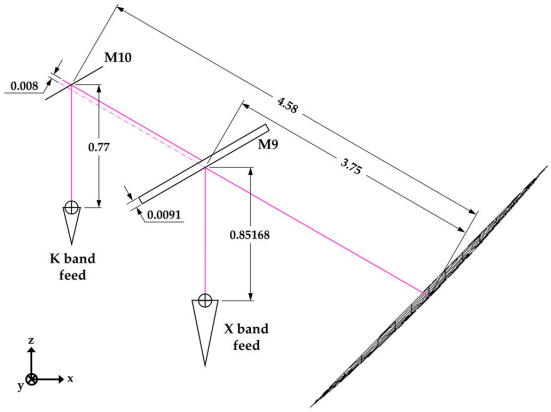

Figure 3.58: DSA2/3-B, low BWG optical layout for D2 case

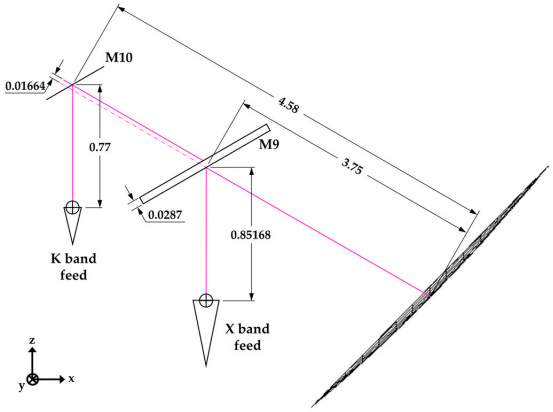

Figure 3.59: DSA2/3-B, low BWG optical layout for D2a case

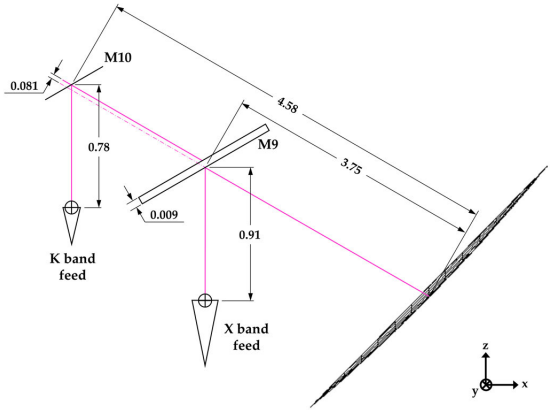

Figure 3.60: DSA2/3-B, low BWG optical layout for D3 case

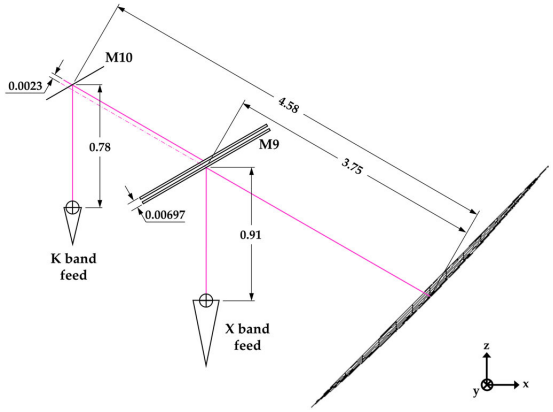

Figure 3.61: DSA2/3-B, low BWG optical layout for D4 case

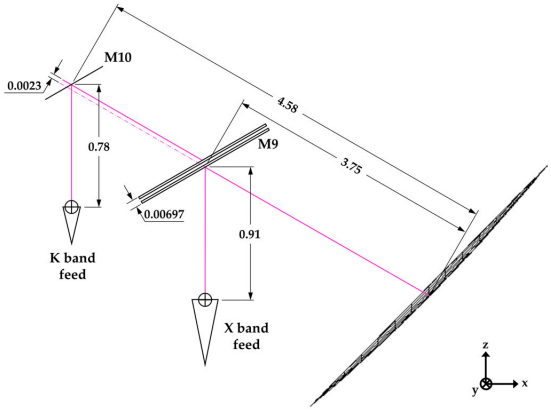

Figure 3.62: DSA2/3-A, low BWG optical layout for D5 case

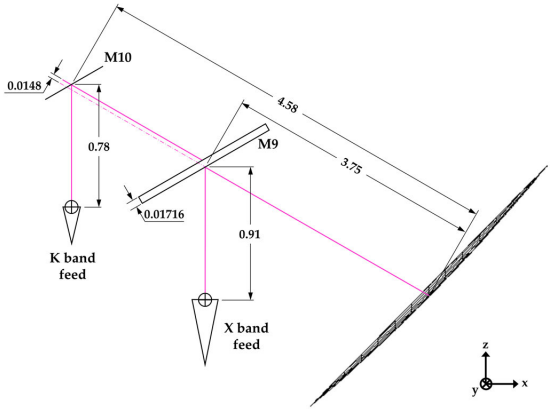

Figure 3.63: DSA2/3-B, low BWG optical layout for D6 case

Table 3.22: DSA23 simulation results: Efficiency (%)

	Frequency [GHz]						
	7.19	**8.45**	**22.55**	**23.15**	**25.5**	**26.25**	**27**
Actual	88.66	90.68	n.a.	n.a.	86.32	87.69	89.22
Ideal	88.66	90.68	89.11	88.74	88.54	88.50	88.61
D1	89.07	91.09	81.83	88.13	85.14	85.69	78.43
D1a	88.66	90.68	87.68	86.12	79.64	79.97	61.59
D2	88.66	90.68	82.97	87.52	84.94	65.46	67.37
D2a	88.66	90.68	86.68	86.52	80.75	81.65	64.49
D3	88.66	90.68	82.78	87.32	84.55	86.09	79.15
D4	88.66	83.08	88.49	88.13	85.14	88.09	88.20
D5	88.66	83.27	86.88	83.20	83.01	85.50	86.79
D6	89.28	91.09	80.52	80.93	87.52	85.30	85.40

Table 3.23: DSA23 simulation results: Directivity (dBi)

	Frequency [GHz]						
	7.19	**8.45**	**22.55**	**23.15**	**25.5**	**26.25**	**27**
Actual	67.90	69.40	n.a.	n.a.	78.78	79.10	79.42
Ideal	67.90	69.40	77.85	78.06	78.89	79.14	79.39
D1	67.92	69.42	77.48	78.03	78.72	79.00	78.86
D1a	67.90	69.40	77.78	77.93	78.43	78.70	77.81
D2	67.90	69.40	77.54	78.00	78.71	77.83	78.20
D2a	67.90	69.40	77.73	77.95	78.49	78.79	78.01
D3	67.90	69.40	77.53	77.99	78.69	79.02	78.90
D4	67.90	69.02	77.82	78.03	78.72	79.12	79.37
D5	67.90	69.03	77.74	77.78	78.61	78.99	79.30
D6	67.93	69.42	77.41	77.66	78.84	78.98	79.23

Table 3.24: DSA23 simulation results: max XPD (dBi)

	Frequency [GHz]						
	7.19	**8.45**	**22.55**	**23.15**	**25.5**	**26.25**	**27**
Actual	-51.93	-60.09	n.a.	n.a.	-38.86	-44.00	-50.40
Ideal	-51.93	-60.09	-61.07	-58.52	-61.48	-66.26	-52.65
D1	-31.51	-30.03	-31.59	-34.99	-28.37	-25.63	-20.69
D1a	-32.85	-31.38	-31.46	-35.14	-26.40	-22.91	-17.72
D2	-31.12	-29.55	-21.41	-25.75	-36.86	-28.91	-23.48
D2a	-32.15	-30.65	-22.68	-26.75	-23.44	-20.43	-15.61
D3	-29.37	-27.82	-23.53	-30.75	-31.05	-23.78	-18.38
D4	-34.03	-32.71	-30.97	-30.97	-28.33	-31.40	-31.01
D5	-42.34	-40.91	-23.88	-20.99	-25.87	-27.33	-28.33
D6	-32.45	-31.01	-35.48	-31.34	-38.85	-35.52	-31.82

Table 3.25: DSA23 simulation results: θ squint (mdeg)

	Frequency [GHz]						
	7.19	**8.45**	**22.55**	**23.15**	**25.5**	**26.25**	**27**
Actual	2.61	2.24	n.a.	n.a.	1.35	1.39	1.39
Ideal	2.61	2.24	1.60	1.57	1.50	1.49	1.47
D1	2.71	2.28	1.36	1.33	1.14	1.30	1.83
D1a	2.74	2.32	1.97	2.05	3.45	4.51	6.82
D2	2.73	2.29	1.51	1.46	1.86	3.12	3.08
D2a	2.73	2.29	1.71	1.77	3.02	4.01	6.05
D3	2.75	2.32	1.41	1.35	1.52	1.96	2.51
D4	2.77	2.55	1.00	0.97	1.01	0.85	0.82
D5	2.80	2.58	0.91	0.90	1.33	1.37	1.38
D6	2.72	2.30	1.48	1.46	1.36	1.32	1.41

Table 3.26: DSA23 simulation results: First sidelobe (dB)

	Frequency [GHz]						
	7.19	**8.45**	**22.55**	**23.15**	**25.5**	**26.25**	**27**
Actual	-17.34	-16.85	n.a.	n.a.	-15.54	-13.93	-14.04
Ideal	-17.34	-16.85	-16.23	-16.45	-16.96	-17.12	-17.22
D1	-17.42	-16.81	-16.43	-16.68	-17.07	-17.29	-17.43
D1a	-17.39	-16.88	-16.08	-16.29	-16.98	-16.43	-14.53
D2	-17.39	-16.90	-16.26	-16.50	-16.90	-16.91	-17.85
D2a	-17.39	-16.89	-16.17	-16.38	-16.95	-16.33	-15.20
D3	-17.40	-16.89	-16.29	-16.50	-16.99	-17.00	-17.14
D4	-17.38	-18.80	-16.35	-16.54	-17.18	-17.27	-17.44
D5	-17.37	-18.77	-16.37	-16.54	-15.43	-15.62	-15.84
D6	-17.43	-16.81	-16.31	-16.57	-17.20	-17.28	-17.20

3.3.3 Simulations summary and G/T

Main simulation results for what concerns efficiency and XPD are showed in the following Figure 3.64 to Figure 3.67. In general, the best performances have been obtained with mirror D4, exhibiting an antenna efficiency and XPD values respectively greater than 84.5% and lower then -23 dB for DSA1-A, while greater than 85% and lower then -28 dB for DSA23-B. But, as already discussed in Section 3.2.6, this mirror presents some manufacturing problems due to its thickness. Performances with mirror D5 (only for DSA23-B) are also good in terms of efficiency, above 83%, but not optimal in terms of XPD at the K-TX band edges. Furthermore, this mirror also has the same manufacturing problems as D4.

All the other cases, apart from D1 and D6, exhibit quite satisfactory performances in the K band, except for the highest frequencies above 26.5 GHz, where their behaviour rapidly degrade due to a not optimal angular response of the correspondent dichroic at higher frequencies.

Overall, as already seen in Section 3.2 for each singular mirror response, antenna simulations with D1 and D6 designs shown the best performance and compromises for all the bands.

Since these two cases were selected for the final phase of the project, the contribution to the overall antenna G/T was estimated for the K receiving band at 25.5, 26.25 and 27 GHz. In particular, the differential contribution of mirror D6 with respect to D1 is specified in Table 3.27 (Delta G/T, in red) for an antenna elevation of 90 degrees.

Antenna gains and dichroic-related parameters were obtained respectively from GRASP, HFSS and MoM-BiRME simulations. Because is quite complicated to obtain a very accurate estimate of noise temperatures for these applications, it was decided to consider the actual T_{sys}, extrapolated from an ESA internal technical note[52], and then calculate a best and worst case scenarios for the G/T degradation between the two mirrors when they are put in place. Therefore, the real value is reasonably in between the two and one could select the best one.

The procedure followed in [52] for T_{sys} is based on formulas and contribution described in [53], hereafter summarised.

The system noise temperature at the feed aperture can be calculated as the combination of the following components:

$$T_{sys} = T_{sky} + T_{refl} + T_{feed} + T_{rec} \tag{3.1}$$

T_{sky} is the sky noise contribution, which is the combination of cosmic background and atmospheric noise temperatures. The former is practically constant for this purpose while atmospheric noise depends on the geographical position, weather condition (through a statistical parameter which express the weather effects as a Cumulative Distribution of probability, CD) and antenna elevation angle.

The second one, T_{refl}, is the combination of all the noise contributions due to reflectors and gaps spill-over, struts diffraction, reflectors conductivity and dichroics effects. It can be calculated as the combination of elevation dependant and elevation-independent components.

The former is mainly due to the main reflector, sub-reflector and struts spillovers towards the ground. Sub-reflector spillover was calculated depending on the sky temperature at the working elevation angle. Same for the main reflector spillover, whose value is a weighted sum between sky and ground temperatures. Depending from the elevation angle, the antenna picks up noise also from the ground through the gap between its main reflector panels. Moreover, the quadrupole structure used to support the subreflector induces scattering of the wave and

thus a certain amount of noise depending on the elevation angle.

Conversely, the elevation independent contribution is due to the finite conductivity and spillover from all the other BWG mirrors.

For what concerns the dichroic mirror, its spillover loss contribution is negligible, due to the fact that its dichroic area is much larger than K-band beam impinging on that mirror. An ohmic loss is also present because of the propagation inside it, together with a non ohmic one caused by the beam reflection.

T_{feed} is the contribution from the feed system and due to the insertion loss of each component and its physical temperature.

Finally, T_{rec} is the temperature contribution of the receiver system referred to the feed aperture. For DSA application the noise temperature of the LNAs is the only contribution to the receiver noise, thanks to their very high gain.

To calculate the NT contribution of the dichroic mirror, comparing the two cases, the following formulas were used:

- Ohmic
  $NT = (1 - 10^{L_{ohm}/10}) \cdot T_{ref}$
- Reflection
  $NT = \left(1 - 10^{IL/10}\right) \cdot T_{ref}$ (best)
  $NT = 10^{\Gamma/10} \cdot T_{ref}$ (worst)

In the best case, IL is the simulated total antenna gain difference between the ideal case (i.e. no mirror) and the one with the dichroic mirror. This delta gain value is in fact formally equivalent to an insertion loss and therefore attributable to the power lost due to the signal reflection on the dichroic mirror.

For the worst case instead, Γ was taken as the reflection coefficient of the dichroic mirror at 30 degrees of incidence, obtained from the MoM-BiRME simulations. This case therefore overestimates a bit the contribution of D6 because it considers only one angle of incidence and not the entire angular response of each mirror, which is overall better for D6 than D1. The reflection coefficient selected in both cases was then used together with a reference temperature of 280 Kelvin to estimate the mirror noise temperature reflection contribution. Instead, the ohmic losses contribution was calculated using a reference value of 300 Kelvin. This difference occurs because the mirror sees an equivalent temperature of the surrounding environment while for dissipation losses the physical temperature of the mirror is considered. A positive value for Delta G/T means that D6 is better than D1.

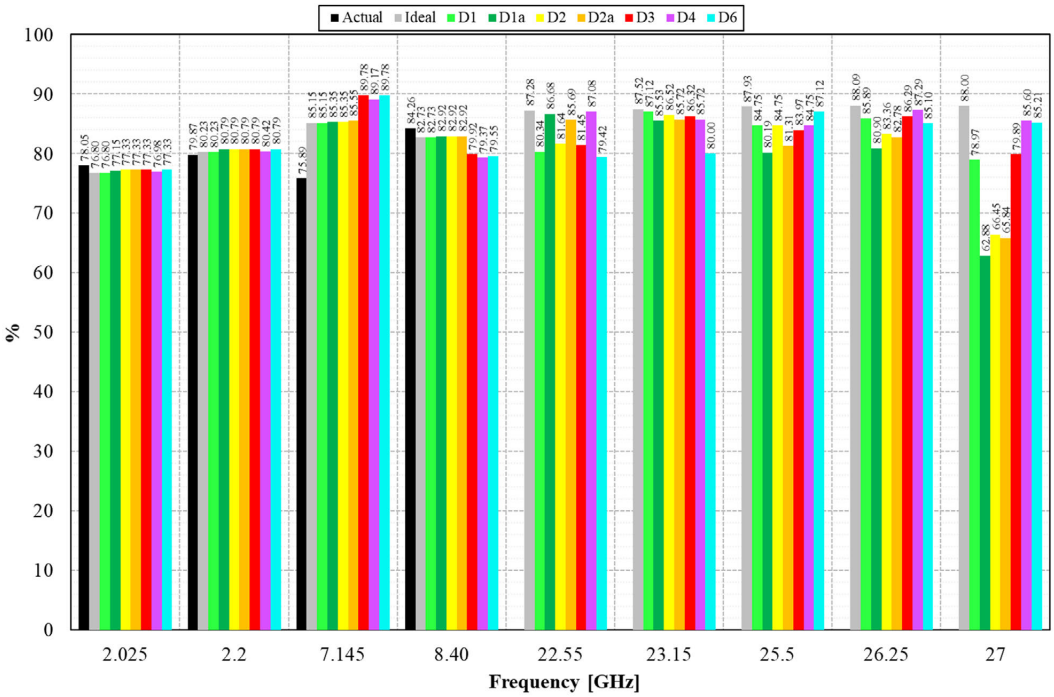

Figure 3.64: DSA1-A, PO efficiency summary

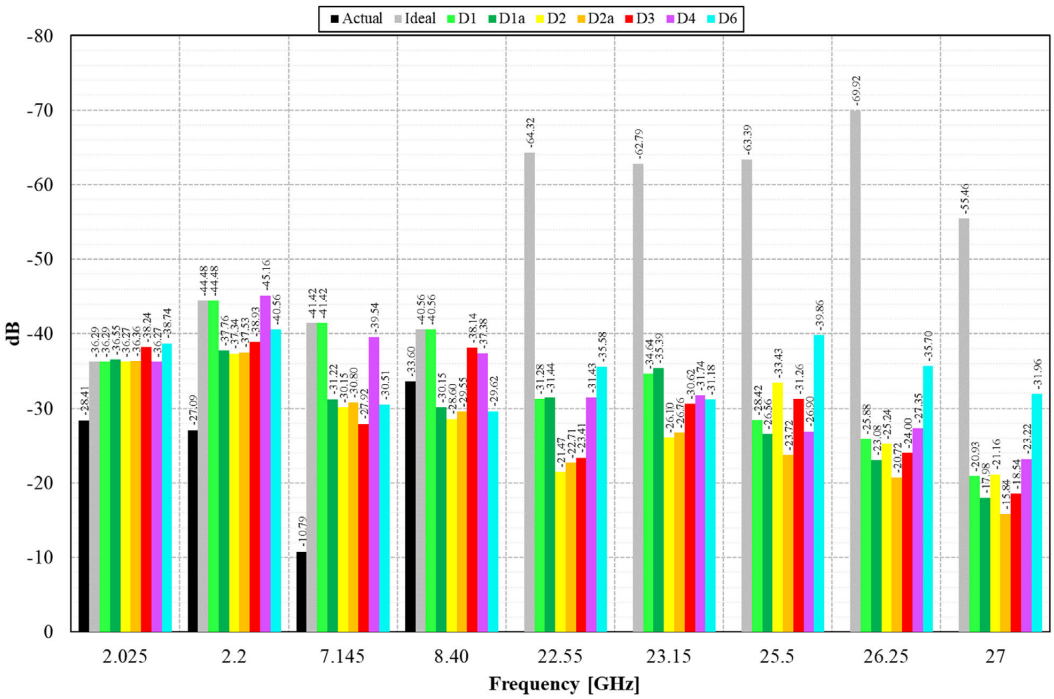

Figure 3.65: DSA1-A, max XPD summary

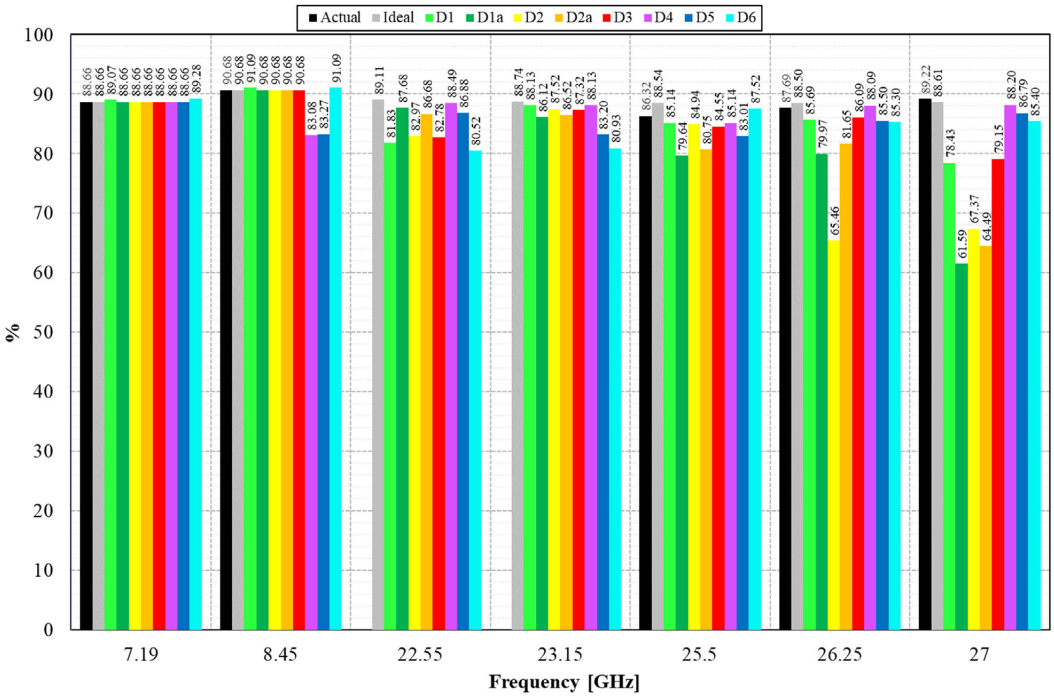

Figure 3.66: DSA23-B, PO efficiency summary

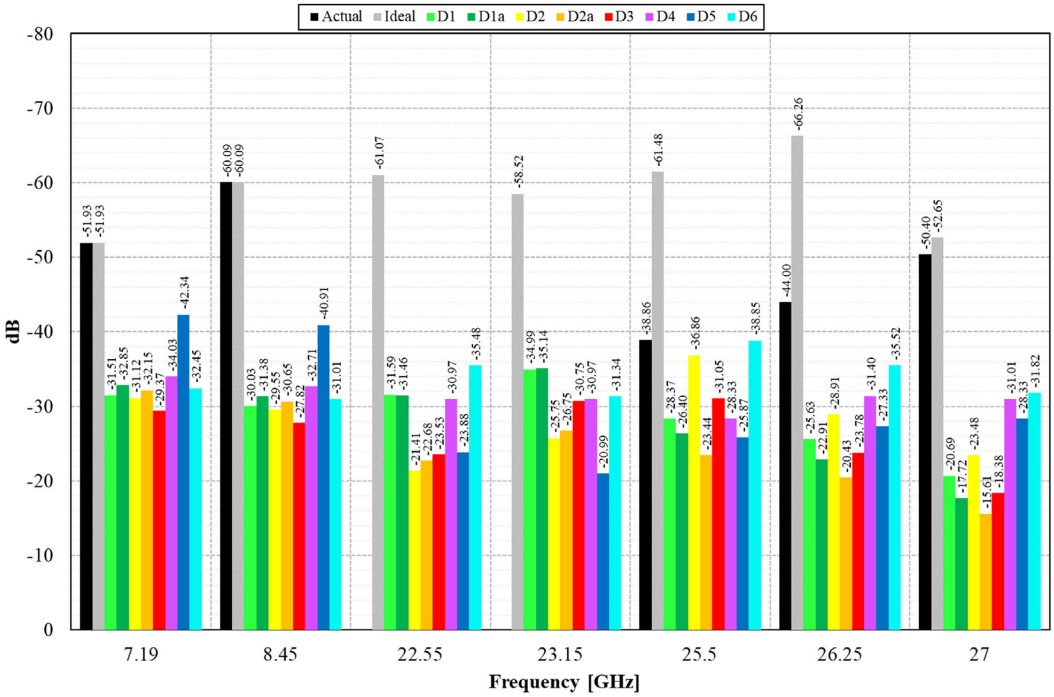

Figure 3.67: DSA23-B, max XPD summary

Table 3.27: G/T contribution between mirror D6 and D1, best and worst cases.

		DSA1			DSA2			DSA3		
Frequency	[GHz]	**25.5**	**26.25**	**27**	**25.5**	**26.25**	**27**	**25.5**	**26.25**	**27**
Ideal Antenna gain	[dBi]	78.86	79.12	79.36	78.89	79.14	79.39	78.89	79.14	79.39
T sys	[K]	59.10	59.10	59.10	56.20	56.20	56.20	52.70	52.70	52.70
D1 - Antenna gain	[dBi]	78.70	79.01	78.89	78.72	79.00	78.86	78.72	79.00	78.86
D1 - Ohmic loss	[dB]	-0.016	-0.018	-0.022	-0.016	-0.018	-0.022	-0.016	-0.018	-0.022
D1 - Refl. Coeff	[dB]	-13.95	-19.88	-13.59	-13.95	-19.88	-13.59	-13.95	-19.88	-13.59
D1 - Delta gain	[dB]	-0.16	-0.11	-0.47	-0.17	-0.14	-0.53	-0.17	-0.14	-0.53
D1 - NT ohmic	[K]	1.07	1.22	1.49	1.07	1.22	1.49	1.07	1.22	1.49
D1 - NT refl. worst	[K]	11.28	2.88	12.26	11.28	2.88	12.26	11.28	2.88	12.26
D1 - NT refl. best	[K]	10.13	7.00	28.72	10.75	8.88	32.17	10.75	8.88	32.17
D1 - NT total worst	[dBK]	18.54	18.01	18.62	18.36	17.80	18.45	18.13	17.54	18.22
D1 - NT total best	[dBK]	18.47	18.28	19.51	18.33	18.22	19.54	18.10	17.98	19.36
D6 - Antenna gain	[dBi]	78.82	78.97	79.22	78.84	78.98	79.23	78.84	78.98	79.23
D6 - Ohmic loss	[dB]	-0.035	-0.032	-0.031	-0.035	-0.032	-0.031	-0.035	-0.032	-0.031
D6 - Refl. Coeff	[dB]	-19.79	-13.15	-13.88	-19.79	-13.15	-13.88	-19.79	-13.15	-13.88
D6 - Delta gain	[dB]	-0.04	-0.15	-0.14	-0.05	-0.16	-0.16	-0.05	-0.16	-0.16
D6 - NT ohmic	[K]	2.41	2.19	2.12	2.41	2.19	2.12	2.41	2.19	2.12
D6 - NT refl. worst	[K]	2.94	13.56	11.46	2.94	13.56	11.46	2.94	13.56	11.46
D6 - NT refl. best	[K]	2.57	9.51	8.88	3.21	10.13	10.13	3.21	10.13	10.13
D6 - NT total worst	[dBK]	18.09	18.74	18.61	17.89	18.57	18.44	17.64	18.35	18.21
D6 - NT total best	[dBK]	18.07	18.50	18.46	17.91	18.36	18.35	17.66	18.13	18.13
Delta Gain	**[dB]**	**0.10**	**-0.05**	**0.32**	**0.10**	**-0.03**	**0.36**	**0.10**	**-0.03**	**0.36**
Delta NT worst	**[dB]**	**-0.45**	**0.74**	**-0.01**	**-0.47**	**0.77**	**-0.01**	**-0.49**	**0.81**	**-0.01**
Delta NT best	**[dB]**	**-0.40**	**0.22**	**-1.05**	**-0.42**	**0.14**	**-1.18**	**-0.44**	**0.15**	**-1.24**
Delta G/T worst	**[dB/K]**	**0.55**	**-0.79**	**0.33**	**0.57**	**-0.80**	**0.37**	**0.60**	**-0.85**	**0.37**
Delta G/T best	**[dB/K]**	**0.50**	**-0.27**	**1.37**	**0.52**	**-0.18**	**1.54**	**0.54**	**-0.19**	**1.60**

Chapter 4

Conclusions

This PhD. Thesis was written in collaboration with ESA following two different topics: the *SNOWBEAR project*, described in Chapter 2, and the *ESA Deep Space Antennas upgrade*, described in Chapter 3. The evolution of ESA's ground stations to support future deep space and EO missions and the study of various aspects associated to the implementation of this new K-band for such applications is thus the common thread of this work.

Indeed, over the last decades, an ever-increasing demand of scientific data has pushed S and X bands to their limit. Nowadays, those bands are highly congested and they are no more able to completely satisfy the need of high downlink capacity. In parallel, technological improvements pushed data acquisition rate of incoming planned EO missions and beyond. Therefore they would require a communication channel with a significantly larger capacity than the ones normally used nowadays. Hence, the use of a higher and broader frequency band, identified in the so called K band (22.55-23.15 GHz uplink, 25.5-27 GHz downlink), has been scheduled and put forward to ensure next generation missions the necessary data transmission rate.

Initial part of Chapter 2 gave an introduction on the SNOWBEAR project, highlighting its main goals and describing how to achieve them. To summarise, SNOWBEAR consisted in setting up a K-band receiving ground station in the Svalbard archipelago, and run a two years test campaign to characterize the K-band receiving conditions in a Polar environment. Major outcomes of SNOWBEAR were: study the impact of atmospheric impairments on the mission data reception performance, gain experience in the the ground station design process by assessing the validity and possibly improve the current antenna and radome electromagnetic model in both dry and wet conditions, gain experience also in its validation in this new frequency band, prove the reliability of present ITU models used for the atmospheric effects predictions.

Section 2.1 (*Link budget model*) presented the link budget model developed and used to predict the receiving performance during each recorded NOAA-20 pass, starting from NOAA-20, explaining how propagation losses are estimated and finally discussing the main features of the ground station e.g. radome, antenna and receiving chains.

Section 2.2 (*Measurement campaign and Data processing*) was then devoted to describe how data were collected and post-processed during the measurement campaign. Final data analyses and performance statistics about the communication link during the operational phase of the SNOWBEAR project, from December 2018 until the end of November 2020 were presented and

discussed.

In conclusion, SNOWBEAR project has recorded overall more than 10000 passes of the NOAA 20 satellite over Svalbard. The recorded data has been aggregated, post-processed and analysed in order to evaluate the performance of the K-band high data rate downlink and to investigate other several generic challenges of implementing K-band data reception in terms of system installation, validation, operation and data processing.

The most significant result, discussed in Sections 2.3 and 2.4 (*Snow on radome* and *Final assessment of key parameters*) is that impact of clouds and rain on the link performances are statistically and quantitatively in line with expectations and that the accumulation of snow on the radome was an underestimated threat that can cause severe disruption of the received signal especially during the periods of the year when the snow melts and gets a combined snow/ice/water composition. This degradation is mostly caused by deflection of the RF beam, which is currently impossible to be modelled and predicted accurately in real time. A crucial aspect is that it impacts differently the fundamental and high order modes causing huge losses independently from using system autotrack or program track mode to keep the antenna pointed. To solve or anyhow limit this problem one could improve radome design, considering a low-friction coating as outermost panel layer in order to prevent the snow accumulation. Secondly it is also possible to improve the snow removal techniques. The method currently adopted to clean the radome is simply a rope, attached to the radome top and moved by a technician to mechanically detach the snow from the radome surface. However, this procedure does not guarantee a complete cleaning, especially if there is a layer of ice or damp and compact snow. One could study other techniques to better remove the snow, such as spraying antifreeze liquid or blowing air, at the drawback of colliding with the daily operational problems that such an installation in a polar environment has. In these frame ESA/ESOC has already launched a study for tri-band (S, X and Ka-Band) radomes promoting advanced snow-phobic and snow removal solutions.

Because of this de-pointing problem, operatively speaking, precise and accurate antenna pointing capabilities are mandatory. SNOWBEAR's cross-elevation/elevation configuration showed bad pointing performance in particular for recording high elevation passes. The lesson learned for this point is that one should perform a very accurate characterisation during the on-site testing phase, especially for cross-elevation/elevation passes, in this way it would be possible to spot errors, investigate the root cause and then implement a better pointing model.

A secondary lesson learned about the tracking aid with the S-band is that when the antenna is above 90 deg elevation, in XEL/EL mode, if K-band autotrack is lost for any reason, the system is not able to recover and stays in S-Band autotrack until the end of the pass. This problem is due to the offset between the S-Band and K-Band autotrack nulls when the antenna is flipped over. Improve the feed design and axes alignment could minimise this nulls offset.

Given the risk of sidelobe acquisition al low elevations, cut through other antenna radomes one could also think to implement antenna masking profile in the ACU (keeping it up-to-date), such that autotrack is enabled at X deg above mask and not at fixed elevation

In parallel some effort shall be dedicated to develop more robust autotrack techniques that would allow to at least maintain the pointing within the main antenna beam (possibly half power beamwidth). If none of this will be successful the design of the future EO missions will have to take the snow issue into careful account. This is true especially for advanced techniques

such as VCM (Variable Code Modulation) and ACM (Adaptive Code Modulation), which make use of the additional link margin for higher elevations and might be jeopardised, bringing no added value in some periods of the year.

Regarding the Deep Space Antenna Upgrade, Chapter 3 started with a brief introduction on the ESA's Deep Space Network with all the frequency bands currently implemented in each antenna. The goal of this trade-off study was to analyse different alternative BWG layout and dichroic mirrors in order to guarantee a simultaneous X and K band full-duplex channels in all of the three ESA's Deep Space Antennas (Cebreros, Malargüe and New Norcia) mainly for supporting future solar system probes and Moon missions.

Then, in Section 3.1 (*BWG possible configurations*) the architecture of each DSA was described in detail, together with the discussion on each possible BWG layout modification.

After the identification of a best configuration for each DSA and the consequent dichroic to be installed, Section 3.1 (*Dichroic mirrors designs*) was focused on the study of such a mirror response.

Starting from the know-how on this subject from the design of the currently installed mirror done few years ago by UNIPV, a thorough investigation of many designs with different number of layers, aperture shapes and also fabrication techniques was performed to completely assess their frequency response and to define the best compromise between performance, ease of construction and costs.

Each mirror response in terms of transmission, reflection coefficients and cross-polarization discrimination has been designed considering a set of incident angles around the nominal one (i.e. 30 degrees) and also accounting for specific mechanical and manufacturing constraints, such as the rounding radius and the minimal metal walls thickness between the hole apertures. In general, the best performances have been obtained with mirror D4 but, as already discussed in Section 3.2.6, this mirror presents some manufacturing problems due to its small thickness. Performances with mirror D5 (only for DSA23-B) are also good in terms of efficiency but not optimal in terms of XPD and it shares the same manufacturing problems of D4. All the other cases, apart from D1 and D6, exhibited quite satisfactory performances in the K band, except for the highest frequencies above 26.5 GHz, where their behaviour rapidly degrade due to a not optimal angular response of the correspondent dichroic at higher frequencies. Overall, as presented in Section 3.2 D1 and D6 designs showed the best performance and compromises for all the bands thus they have been selected among the others to be further extensively optimized before fabricating the samples to be measured.

A sensitivity analysis of D1 and D6 has been performed considering each of the mirror design parameter as a random variable characterized by a Gaussian probability function with a certain mean and standard deviation for testing the designs robustness in the presence of uncertainty (Section 3.2.9, *Sensitivity analysis*). Ohmic loss was also simulated using full-wave simulation tools taking into account aluminium as bulk material.

Then, the two breadboard prototypes were manufactured. A metrology and electromagnetic measurements campaigns have been carried out on each mirror to validate the two different fabrication techniques and evaluate their performance to confirm the simulated frequency response. Indeed, it is found values of μ and σ in line with the hypothesis made during the sensitivity analysis.

Regarding the measurement campaign, overall, having had to manufacture prototypes of

such small dimensions has revealed some problems that have undermined the fully success of the measurement campaign. Having tested them in different ways seems to point out that the problem is not in the inaccuracies of various setups (near/far field, amplitude/phase uniformity...), since they all gave the same results, but rather in something intrinsic to the samples themselves. Probably it has been underestimated the impact of having only about 15 cells per side. It might be that the periodicity is not completely defined and it could be that with such small samples the frequency for which the higher modes (i.e. grating lobes) are triggered, strongly linked to the periodicity, is not the correct one obtained from the simulations based on the theory of calculus for infinite periodic structures.

However, it was possible to focus on verifying and compare the different construction techniques. If milling was already known as a valid fabrication technique, from this study it has been verified that also wire erosion could achieve a good surface accuracy and therefore could be exploited for this type of application.

As a final step, each antenna new configuration was simulated in GRASP to evaluate their overall performance, as described in Section 3.1 (*Antenna simulations*). In particular for those configuration selected as best cases (i.e. those involving D1 and D6 mirrors), an optimization process was carried out to fine-tune each antenna lower BWG optic layout finding the optimal mutual position of both feed and mirrors. Thanks to this procedure it was possible to significantly reduce the impact of new dichroic mirror on the antenna and it was possible to compensate the main beam squint caused by the beam shift induced by the propagation inside its finite thickness.

Since the electromagnetic performance of these critical dichroic mirrors strongly affects the overall antenna noise temperature in K band, the differential contribution of mirror D6 with respect to mirror D1 on the overall G/T was estimated considering two possible best and worst case scenarios.

Considering all the different analyses for all the frequency bands described in this document and despite its slightly greater sensibility to manufacturing tolerances and impact on the G/T in K-band receiving channel central frequencies, D6 appears to be the best choice for the upgrade of each DSA.

Appendix A

Cycles summary and comments

A brief description of each cycle is hereafter reported

N.B. From middle of cycle 46 to cycle 49 there was a degradation of the cryogenic channel gain (channel 2) due to issues with the LNA compressor (was accidentally turned off). This loss is taken into account for the calculation of the theoretical level of the copolar signal at the input of the HRDFEP and for the XPD level. Thus, both residue and XPD reported for those cycles are coherent with the others. Instead, plots showing the measured HRDFEP input power level are not corrected, thus some of the curves in that plot for cycle 46 and all of them for cycle 47 to 49 are lower than the others.

From cycle 60 a failure of the polarisations switch forced the system to operate in TLE tracking mode, with considerable pointing losses affecting the signal reception especially for high elevation passes. Indeed, in parallel with pointing losses, many high peaks are recorded in the following cycles above 30 deg, even when weather seems good, because of this issue. Also under 30 deg of elevations is possible to appreciate many small peaks in parallel with the other graphs. For this reason, following descriptions shall be intended net of these peaks.

Cycle 23 This cycle comprises a small amount of passes because it started before the beginning of the operational phase. Highest attenuation recorded during the first part of the cycle likely due to a snow accumulation. Indeed, the recorded snow depth from the weather station is higher in that period. In the second half of the cycle estimated losses are minimum.

Cycle 24 Gain correction of the cryo channel implemented from middle cycle using the noise diode calibration (available only for the ambient channel yet). Higher losses recorded over 30 degrees of elevation after a snowfall (8th-12th December) and after a snowfall followed by a temperature increase near 0 °C (rightmost peak). Under 30 degrees the attenuation is on average around 1 dB with peaks up to 6 dB in parallel with more frequent precipitations (middle part).

Cycle 25 Lot of lost passes because of SCU issues. Lower attenuation recorded under 30 deg with respect to former cycles. Strong losses over 30 deg after a snowfall on 5th of january.

Cycle 26 High attenuation recorded at the beginning of the cycle while normal values for the rest of the cycle.

Cycle 27 Everything went nominal, no huge losses and no significant snowfalls. Strong precipitation recorded on 29th with no effect on residuals (probably haze).

Cycle 28 A couple of light snowfalls and moderate losses under 30 deg. Greater peaks over 30 deg. Passes lost because of no SCU data, empty HRDFEP file and no contact with ACU.

Cycle 29 For several passes at the end of this cycle the TLE prediction was out of date. Therefore, both angular errors and estimated pointing loss are not indicated for those passes because they are overestimated. Huge losses over 30 degrees for all passes at high elevation probably caused by a small snowfall on 27th of January. The continuously increasing length of the day and the sun radiation exposure is likely to cause a partial melting of the snow on top of the radome, inducing such high pointing losses. Under 30 deg losses remain low.

Cycle 30 One of the worst cycles. High losses for almost the whole cycle. Increased losses also at lower elevations after precipitations on 22nd of march. Gain correction implemented for both co- and cross-polar channels;

Cycle 31 Nominal cycle.;

Cycle 32 Increased losses under 30 deg in the initial part probably due to bad weather conditions (light precipitations recorded). Snowfall on 26th of April with a parallel increase in both atmospheric and pointing losses.

Cycle 33 Lost passes because of SCU problems in the middle of the cycle. Nominal recordings until 13th of May when precipitations induced above average losses.

Cycle 34 Snowfall on 26th of May with a parallel increase in the residue over 30 degrees. Losses under 30 degrees are on the average higher than in winter.

Cycle 35 Nominal cycle. Snow melts totally because of above 0°C temperature. Trend of losses under 30 degrees remains higher than in winter.

Cycle 36 Starting of the rainy season. Attenuation peaks under 30 deg concurrently with rainfalls and in general greater than other seasons.

Cycle 37 Average attenuation under 30 deg clearly increased because of greater cloud coverage. Attenuation peaks registered concurrently with rainfalls. Temperature constantly above 0°C.

Cycle 38 Recordings in line with previous summer cycle.

Cycle 39 Same as cycles before until a strong precipitation and a sudden snowstorm on 15th of August when high losses were recorded at all elevations.

Cycle 40 Interesting cycle when many attenuation peaks were recorded at all elevations concurrently with precipitations.

Cycle 41 Light rainfalls in the middle of the cycle;

Cycle 42 This cycle started nominally, with light rainfalls and average attenuation. On 27th of September there was a snowfall and starting from this date high attenuation were recorded in particular over 30 degrees of elevation. Daylight hours reduce significantly throughout September (from 19 to 10 hours of daylight with a maximum altitude between 20 and 10 degrees) and temperatures remain around 0 °C. This suggests that losses are due to the presence of wet snow, which melts during the day thanks to sunlight, or ice, which is formed from wet snow once the night or lower temperature come.

Cycle 43 First part of the cycle almost nominal. The second half is similar to cycle 42 after a snowfall around 17th of October.

Cycle 44 Moderate losses for elevation above 30 degrees, increasing from the previous cycle until the middle of this one. After a peak on 1st of November attenuation over 30 deg start to decrease. From 26th of October there is no more daylight.

Cycle 45 Moderate loss for higher elevations constantly decreasing until a snowfall on 22nd of November.

Cycle 46 Many attenuation peaks for higher elevations due to snow/ice on top of the radome.

Cycle 47 Many attenuation peaks for higher elevations due to snow/ice on top of the radome but decreasing with respect to the previous cycle. Loss increase under 30 deg at the end of the cycle because of a snowfall on 23rd of December.

Cycle 48 Still high losses at high elevation for most of the cycle. Losses are reduced suddenly around 7th of January probably thanks to the cleaning of the radome after Christmas holidays.

Cycle 49 Moderate losses for higher elevations.

Cycle 50 Low losses under 30 deg but moderate above.

Cycle 51 Constant losses over the whole cycle until 25th of February when attenuation peaks were recorded after precipitations.

Cycle 52 Nominal cycle with low and constant losses. Losses over are greater than losses under 30 deg probably because of a thin and uniform layer of ice/snow over the radome.

Cycle 53 Significant losses at all the elevations in parallel with precipitation recordings.

Cycle 54 Moderate losses for higher elevations;

Cycle 55 Nominal cycle. Snowfall at the end with increased losses just before, probably due to bad weather conditions;

Cycle 56 Almost nominal cycle. Both snow and rain precipitations occur at the end of the cycle with a moderate increase in losses;

Cycle 57 Light snowfall on 21th of May with parallel increase in both atmospheric and pointing losses. Temperature starts to rise and snow melts completely on 25th of May. Start of the rainy season;

Cycle 58 External temperature oscillates around 0° degrees. The average attenuation in nominal conditions is increased with respect to previous months likely due to a wetter atmosphere.

Cycle 59 In line with cycle 58.

Cycle 60 Losses under 30 deg are higher than the average but in line with the one expected in summer and recorded in previous summer cycles.

Cycle 61 After a first precipitation event with increased losses under 30 deg, the tend to decrease and remain low for the whole cycle.

Cycle 62 Losses remain low for the first part of the cycle until many little precipitation peaks were recorded with an increase in the average losses under 30 deg.

Cycle 63 Still many precipitations peaks, even snowfalls on 29th of August with parallel peaks of attenuation.

Cycle 64 Losses in this cycle are in line with the previous descriptions.

Cycle 65 The loss trend is increased in the middle of the cycle because of precipitations.

Cycle 66 Net of pointing losses everything is nominal.

Cycle 67 Same as cycle 66.

Cycle 68 Huge losses on 13th of November due to a snowfall and moderate losses at the end of the cycle.

Cycle 69 Last and very short cycle.

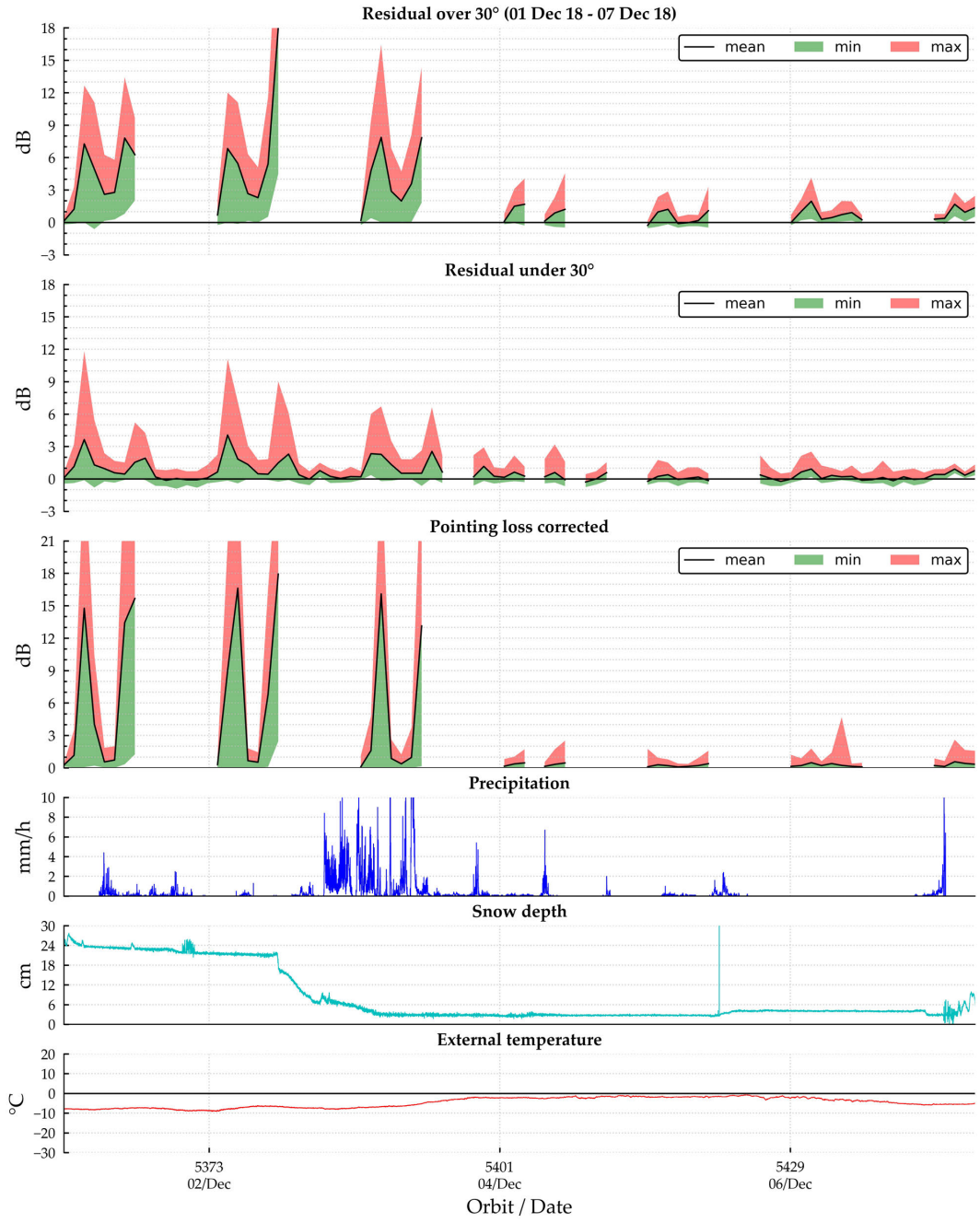

Figure A.1: Residuals and pointing loss comparison against weather effects for cycle 23

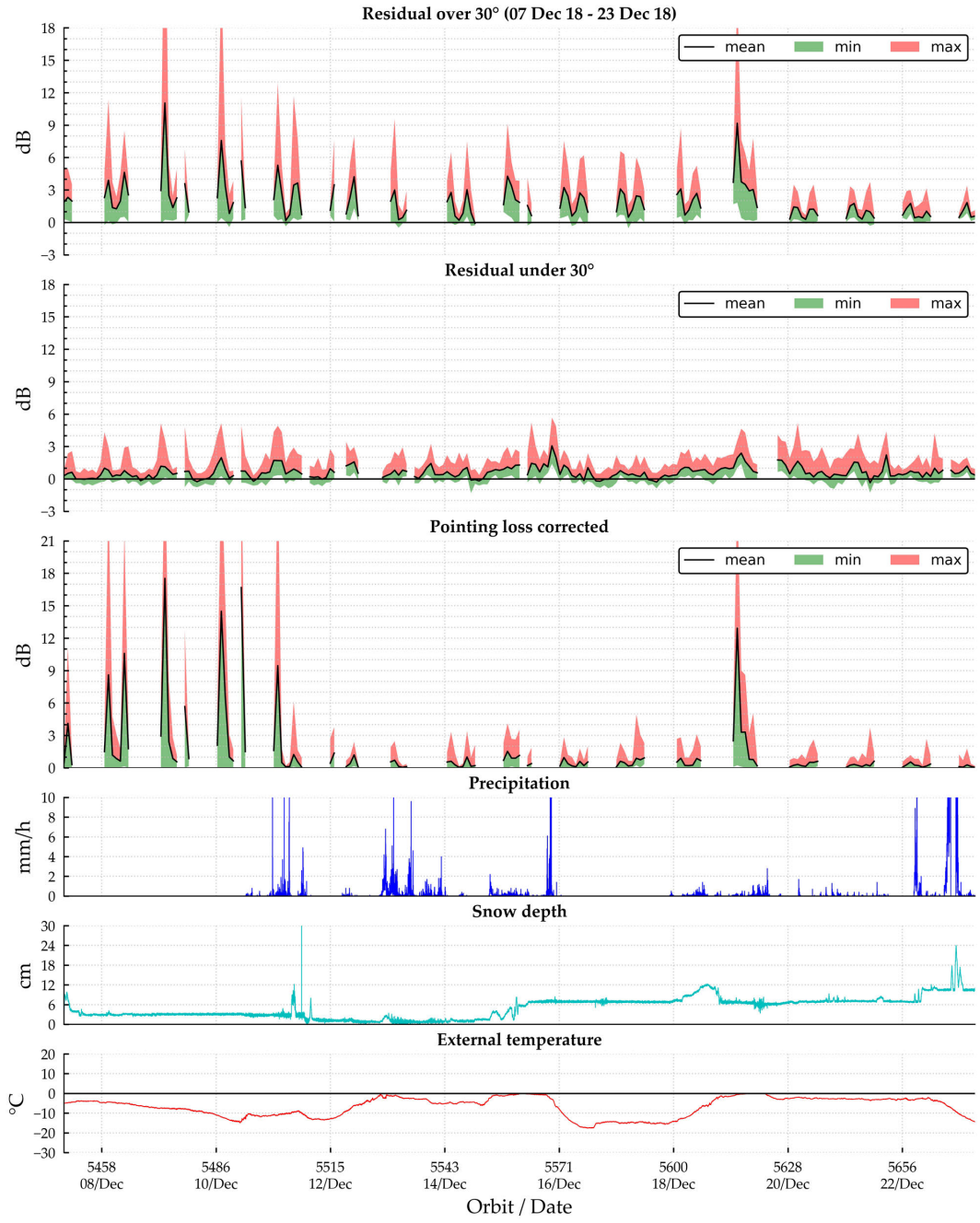

Figure A.2: Residuals and pointing loss comparison against weather effects for cycle 24

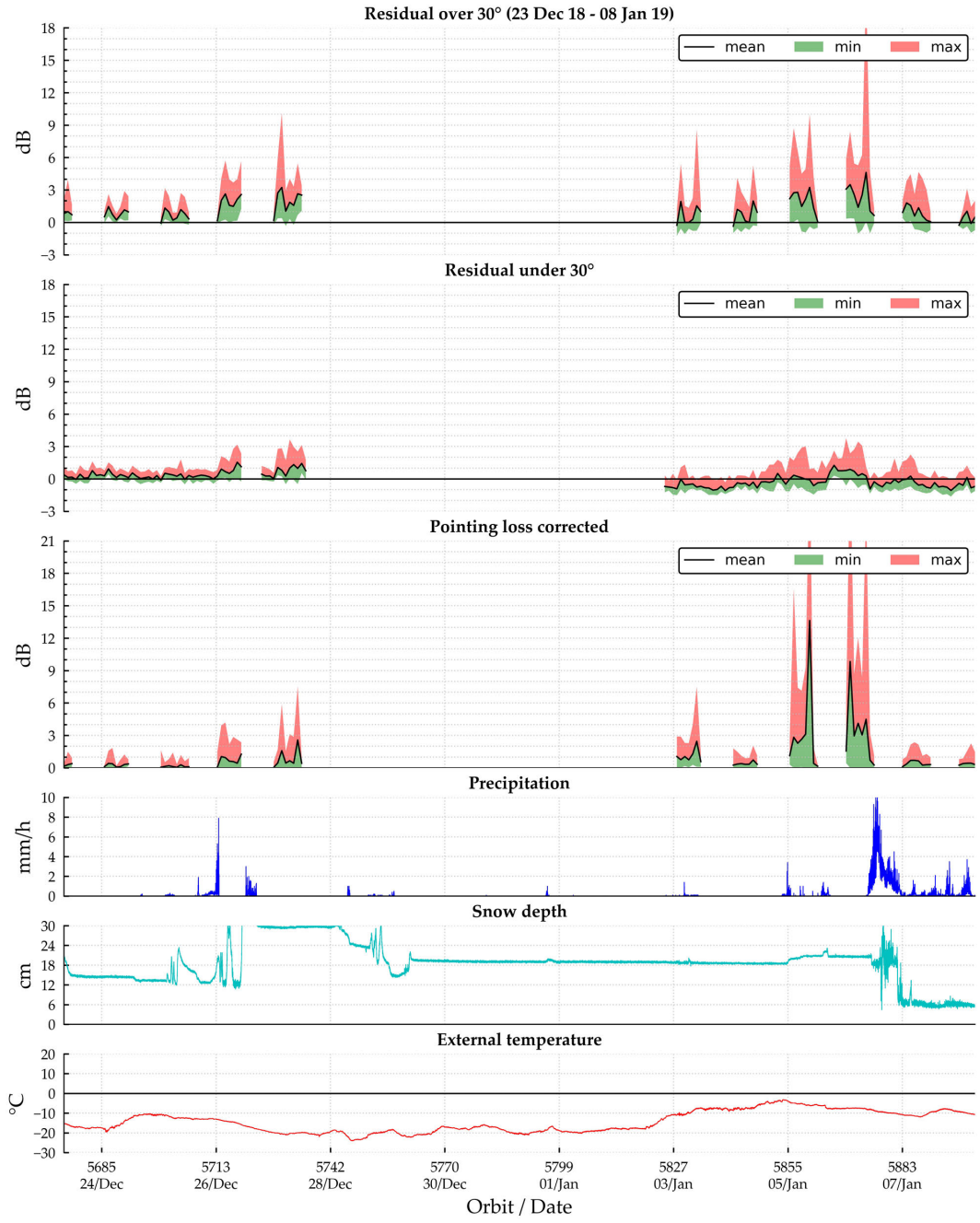

Figure A.3: Residuals and pointing loss comparison against weather effects for cycle 25

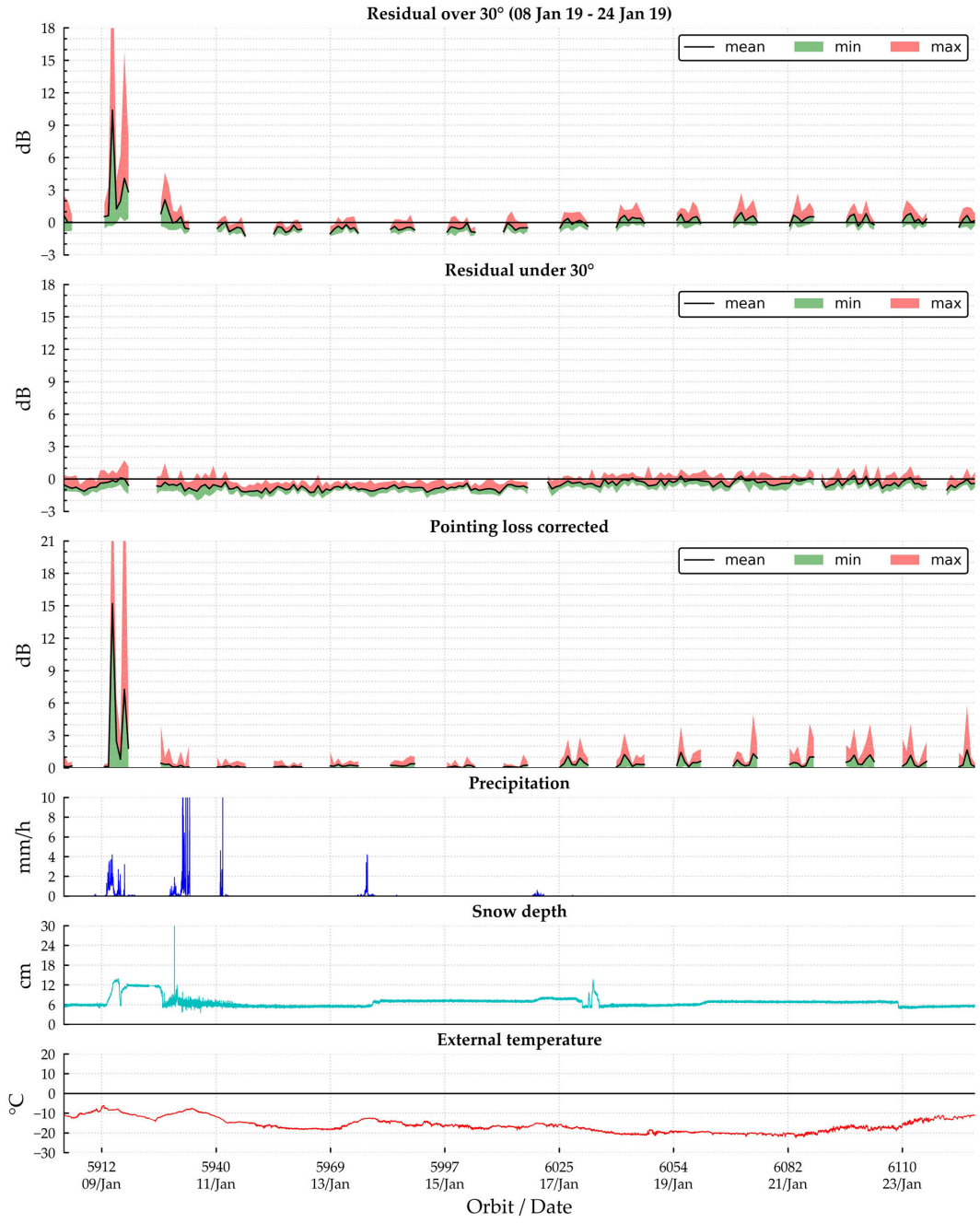

Figure A.4: Residuals and pointing loss comparison against weather effects for cycle 26

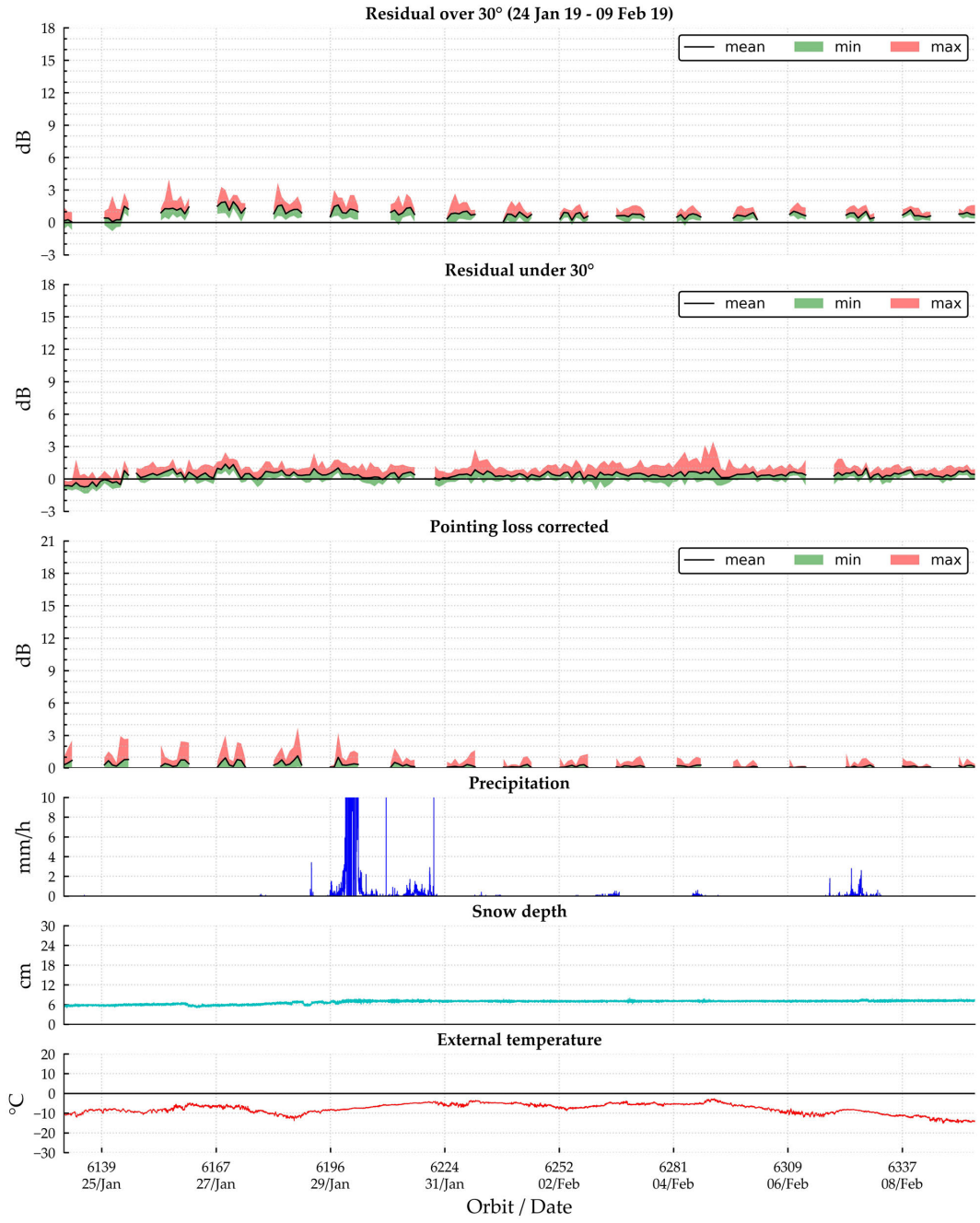

Figure A.5: Residuals and pointing loss comparison against weather effects for cycle 27

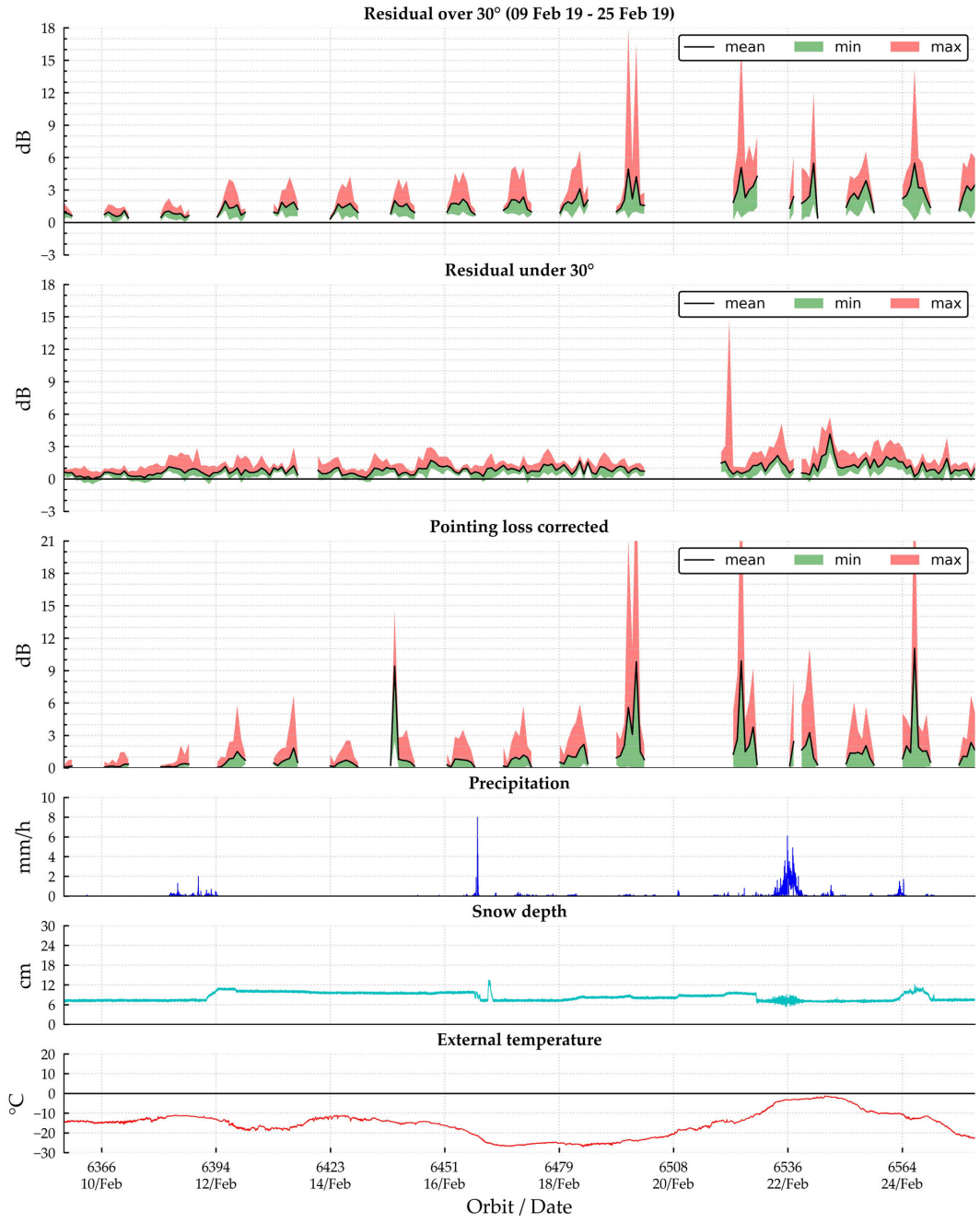

Figure A.6: Residuals and pointing loss comparison against weather effects for cycle 28

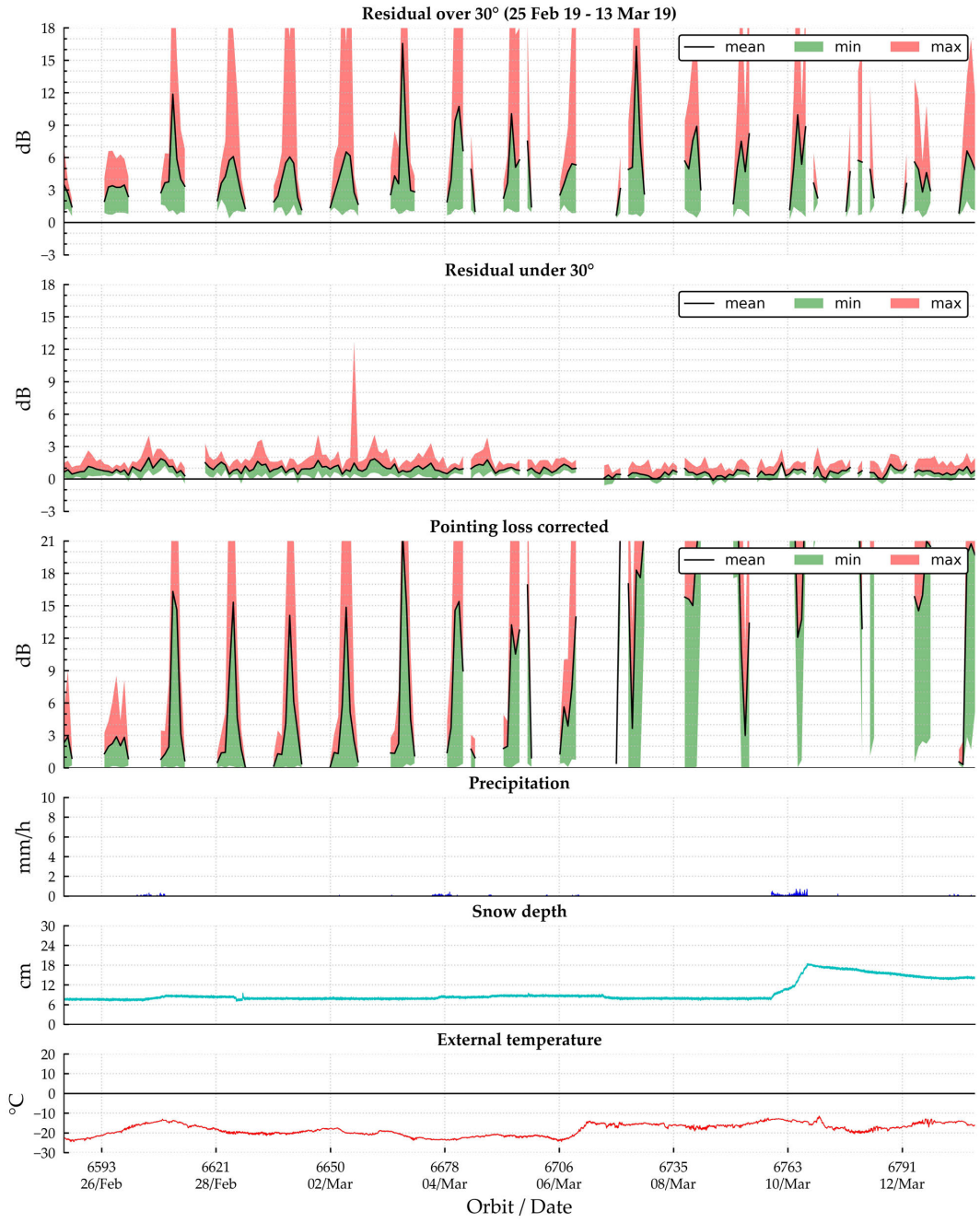

Figure A.7: Residuals and pointing loss comparison against weather effects for cycle 29

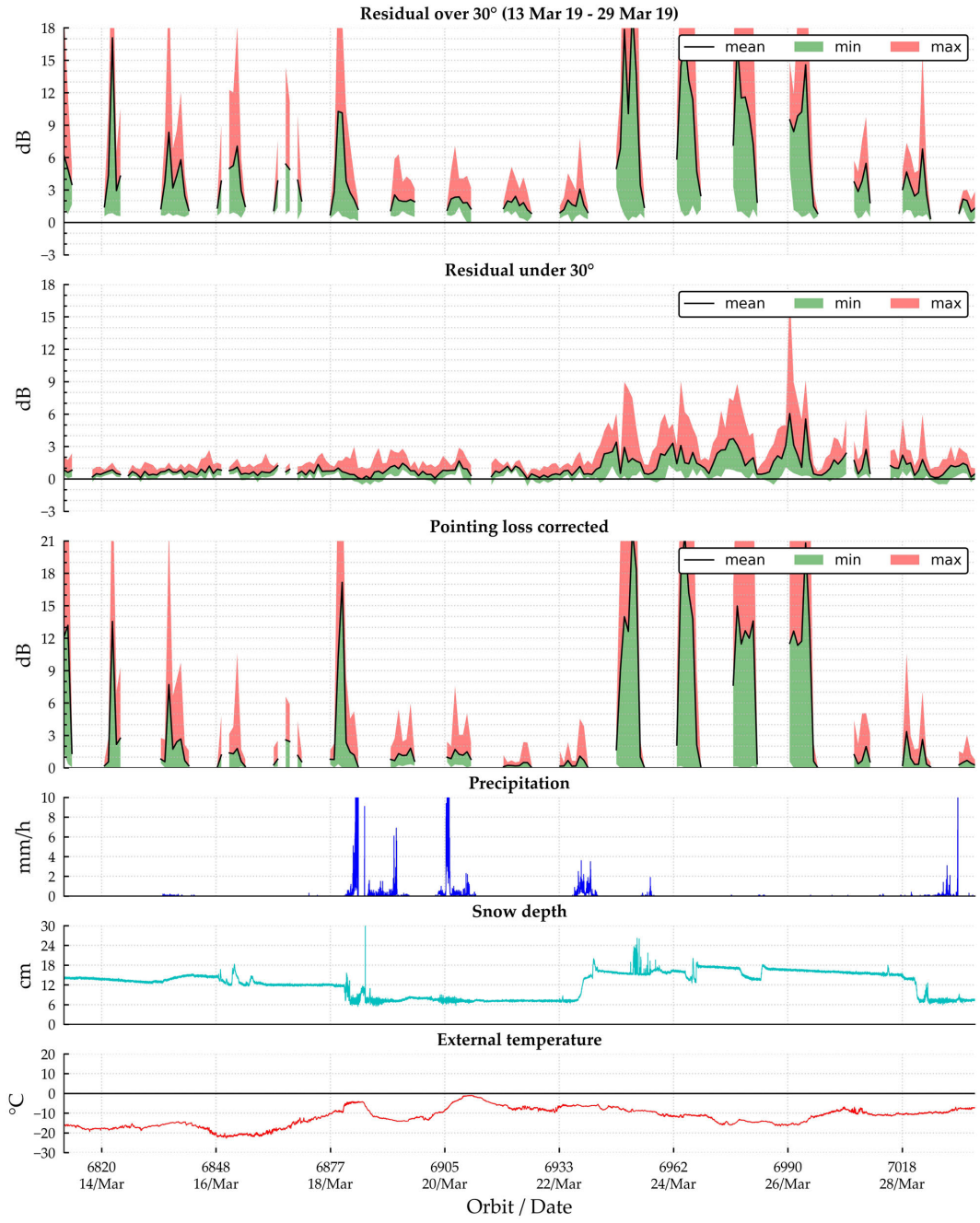

Figure A.8: Residuals and pointing loss comparison against weather effects for cycle 30

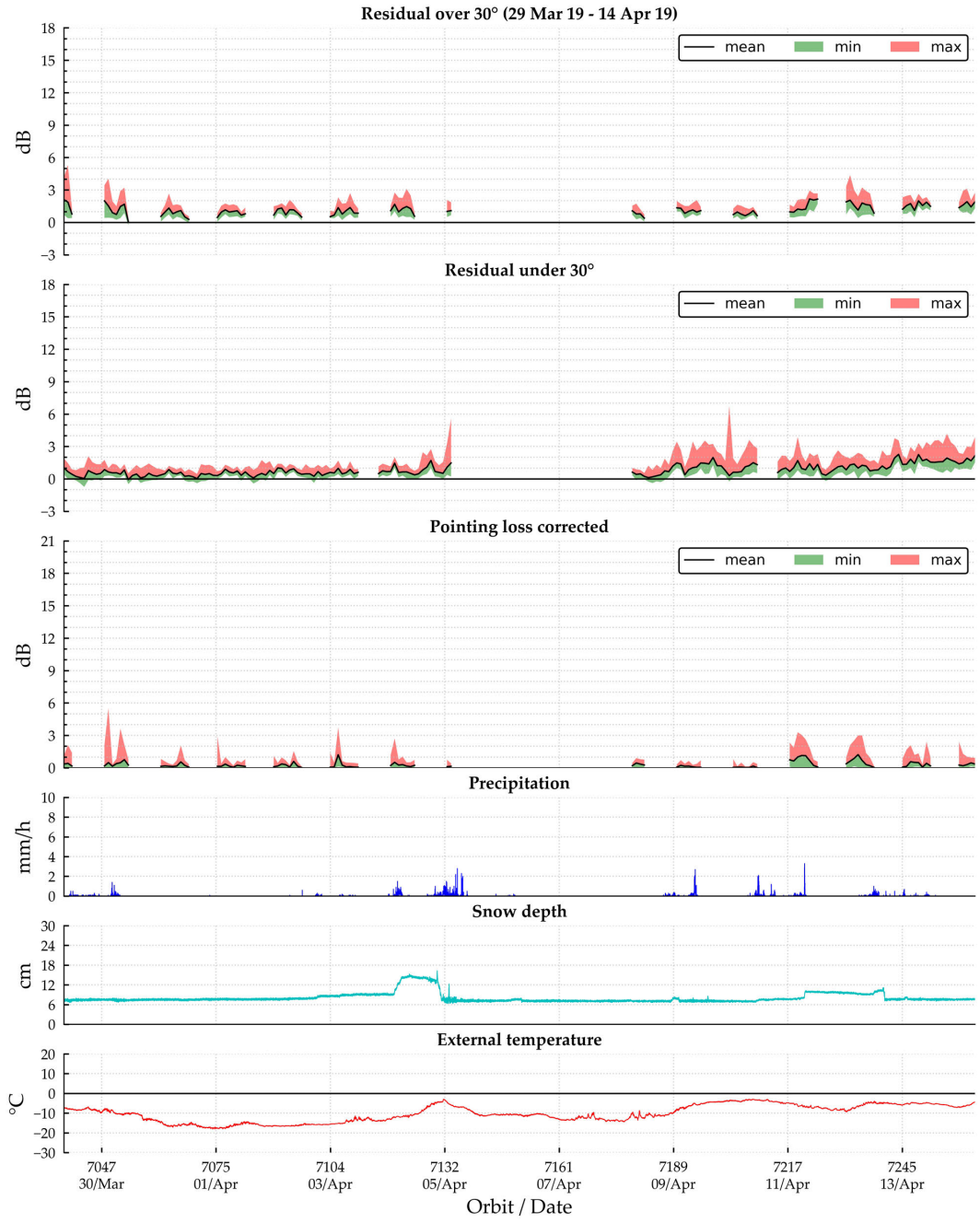

Figure A.9: Residuals and pointing loss comparison against weather effects for cycle 31

Figure A.10: Residuals and pointing loss comparison against weather effects for cycle 32

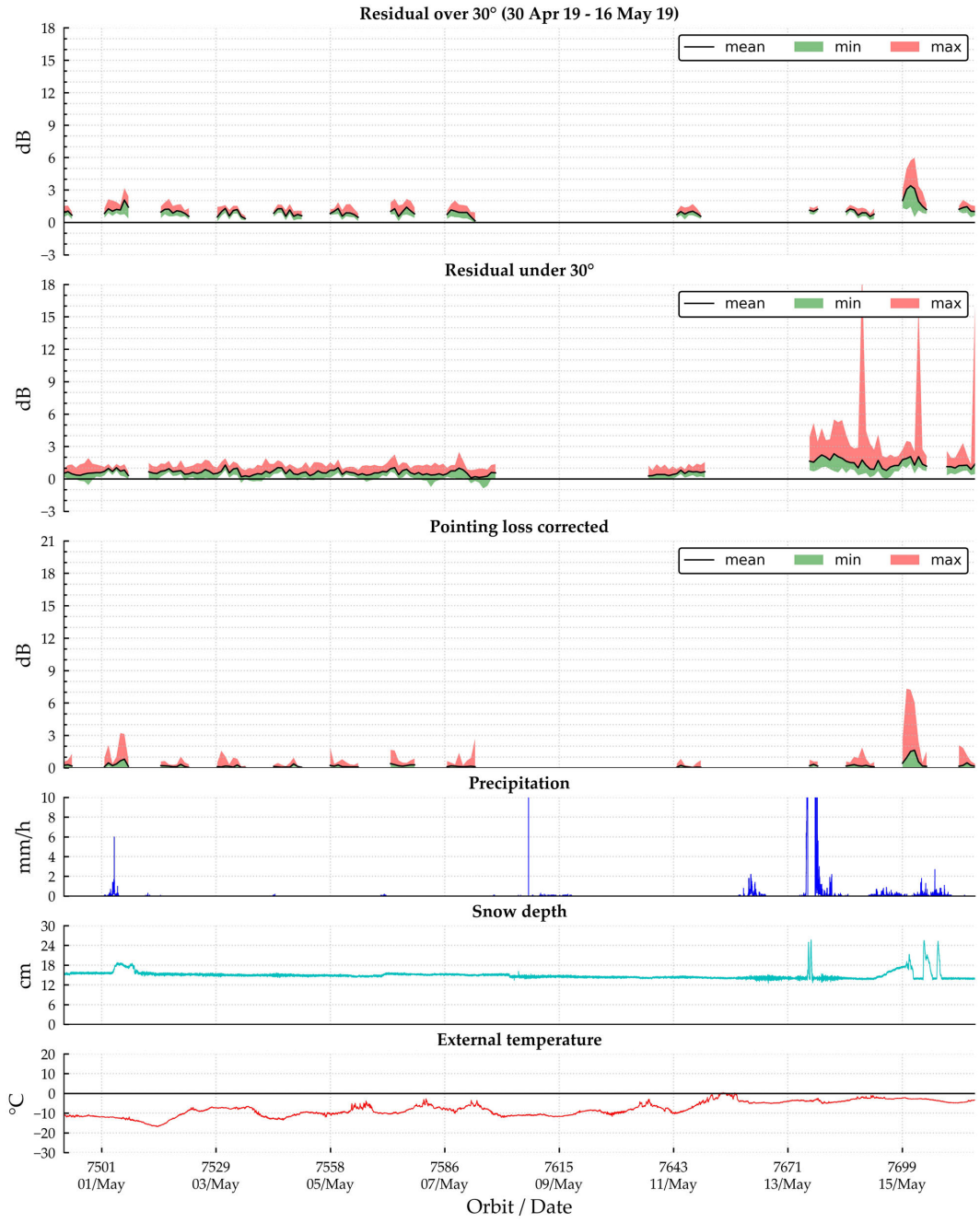

Figure A.11: Residuals and pointing loss comparison against weather effects for cycle 33

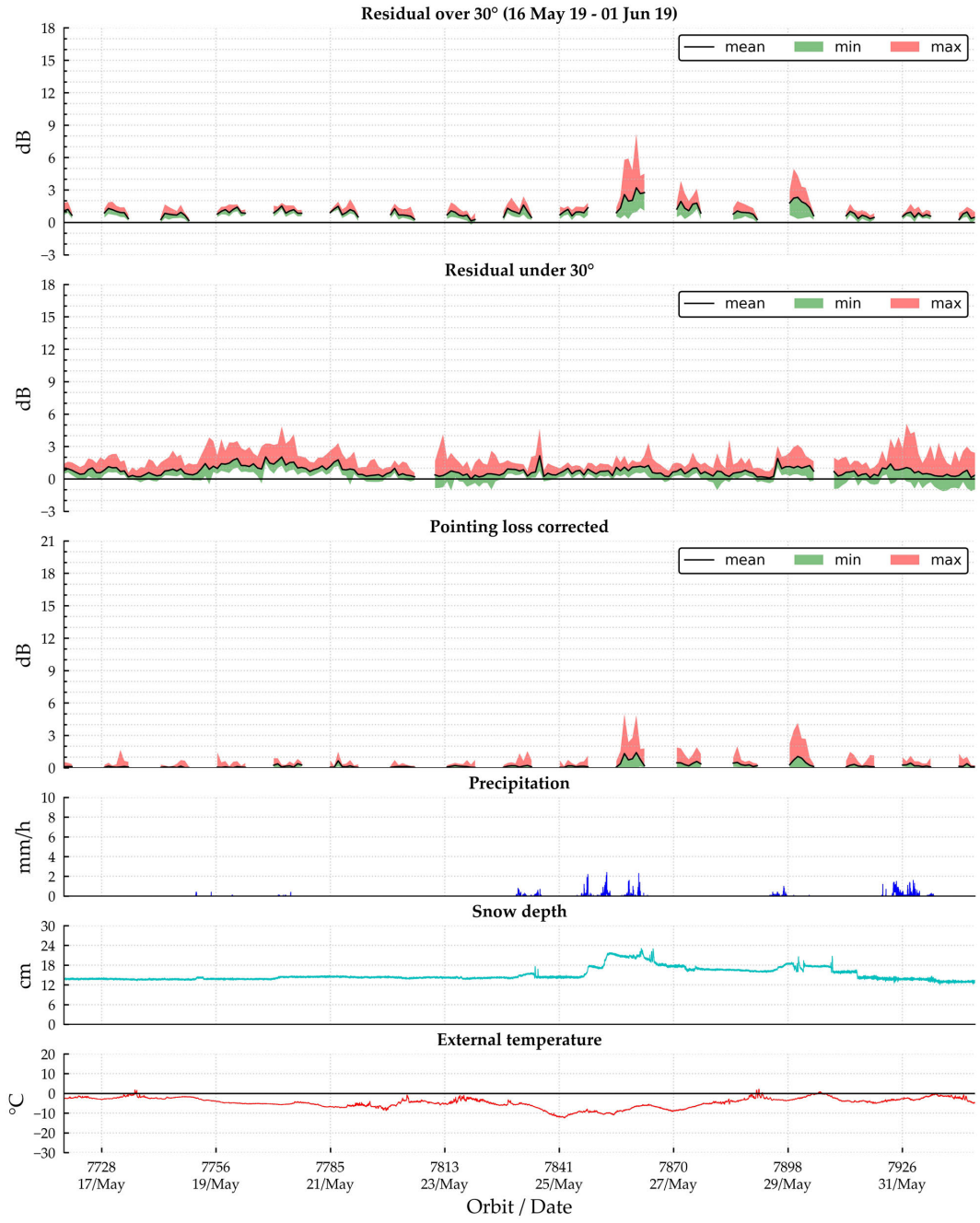

Figure A.12: Residuals and pointing loss comparison against weather effects for cycle 34

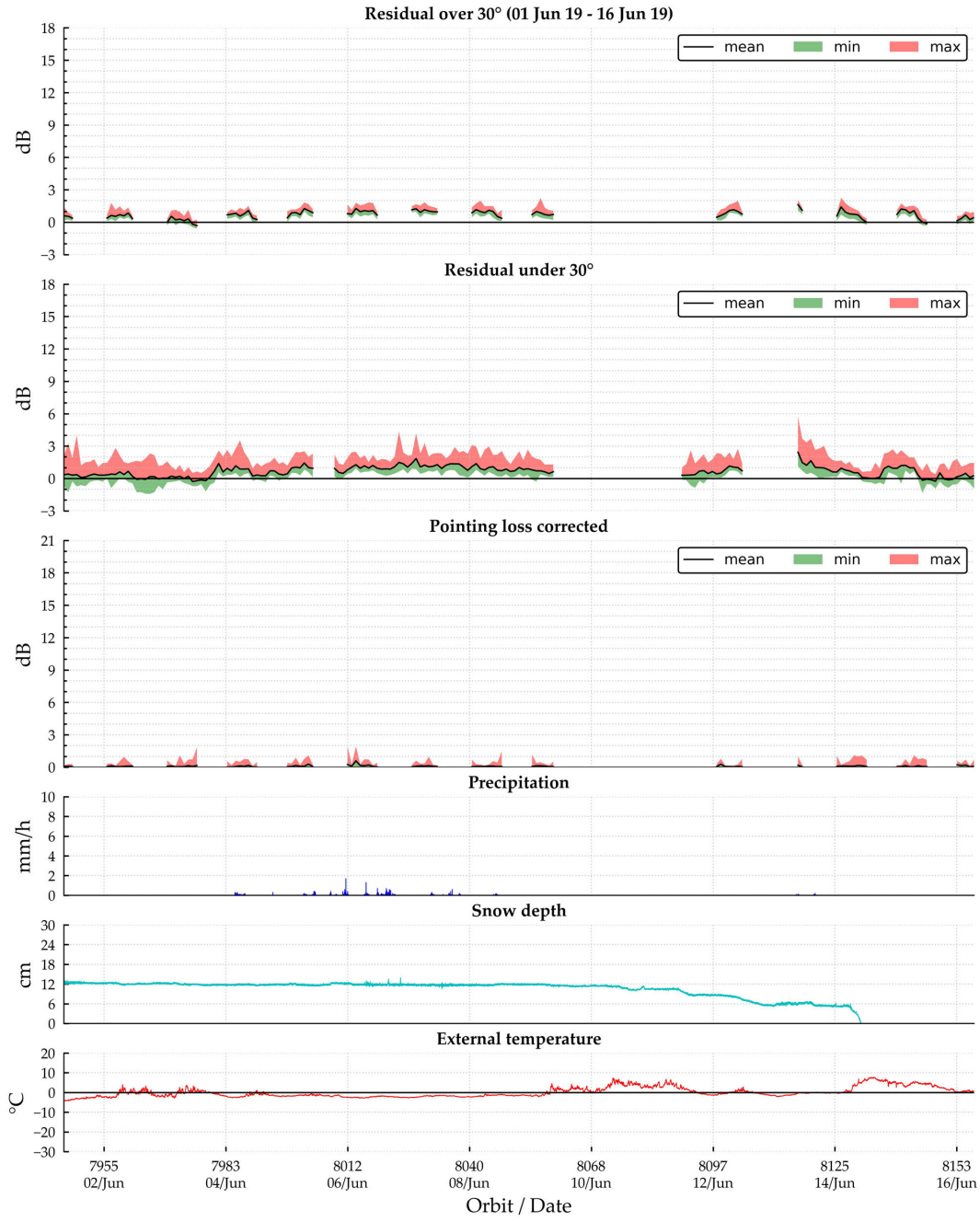

Figure A.13: Residuals and pointing loss comparison against weather effects for cycle 35

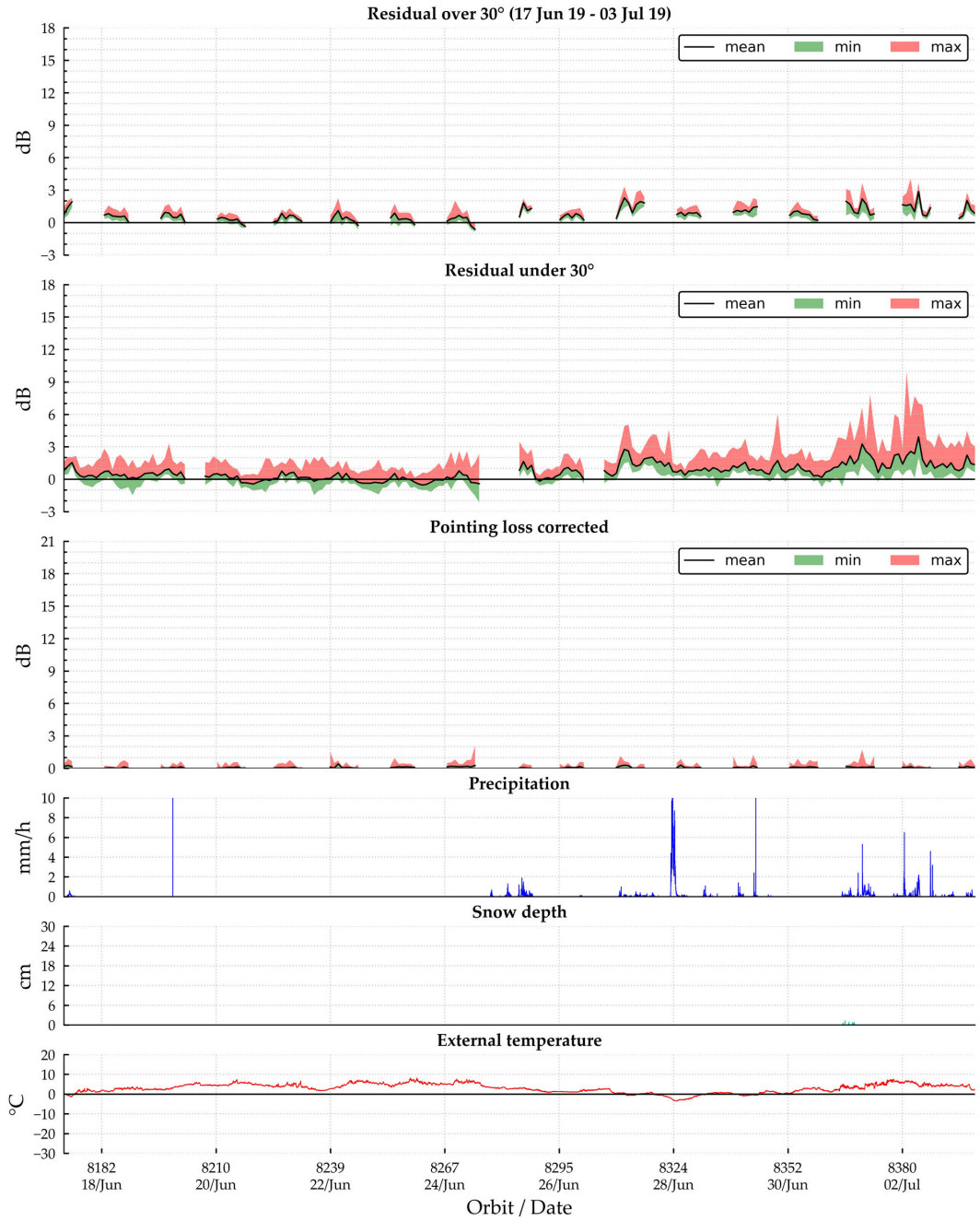

Figure A.14: Residuals and pointing loss comparison against weather effects for cycle 36

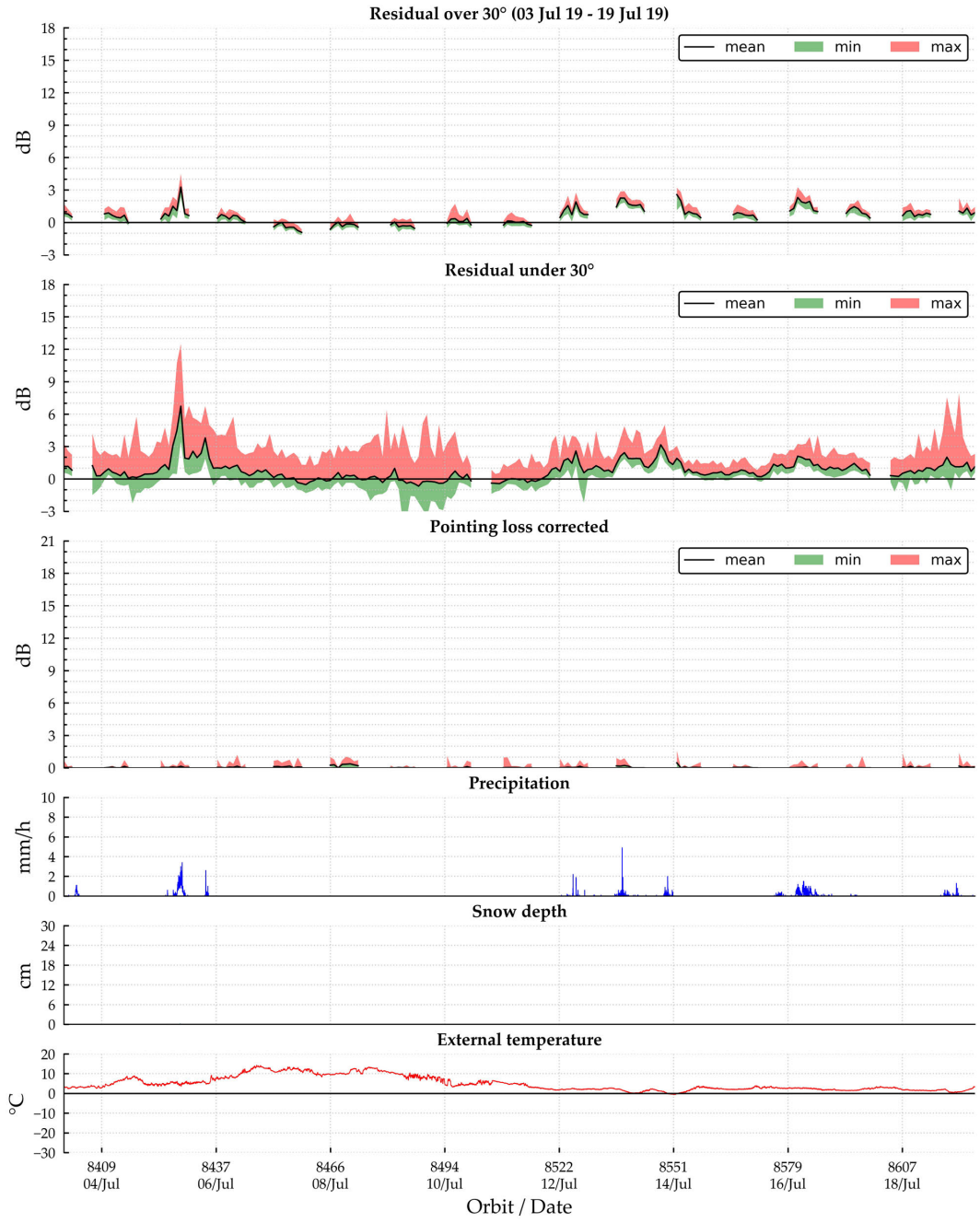

Figure A.15: Residuals and pointing loss comparison against weather effects for cycle 37

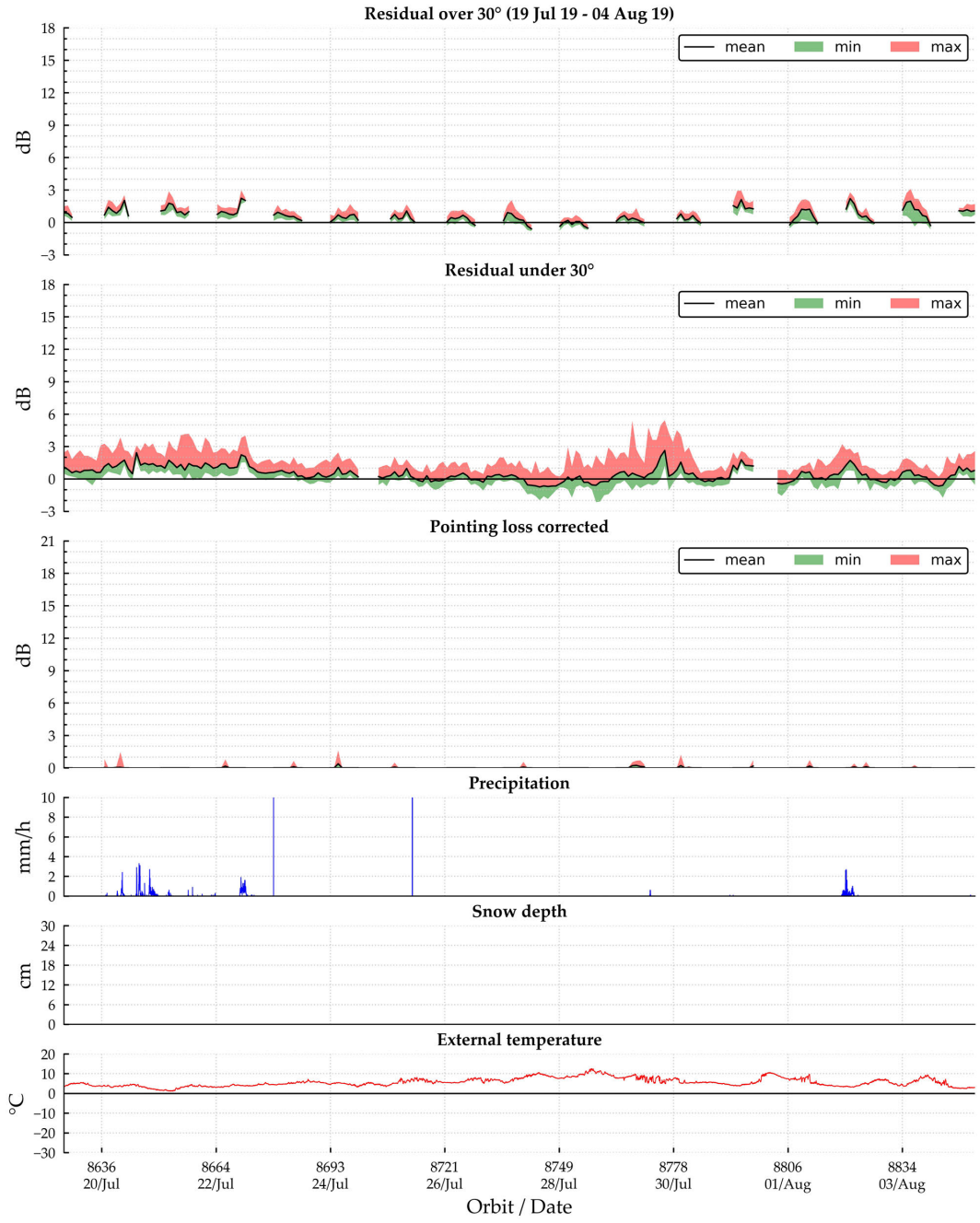

Figure A.16: Residuals and pointing loss comparison against weather effects for cycle 38

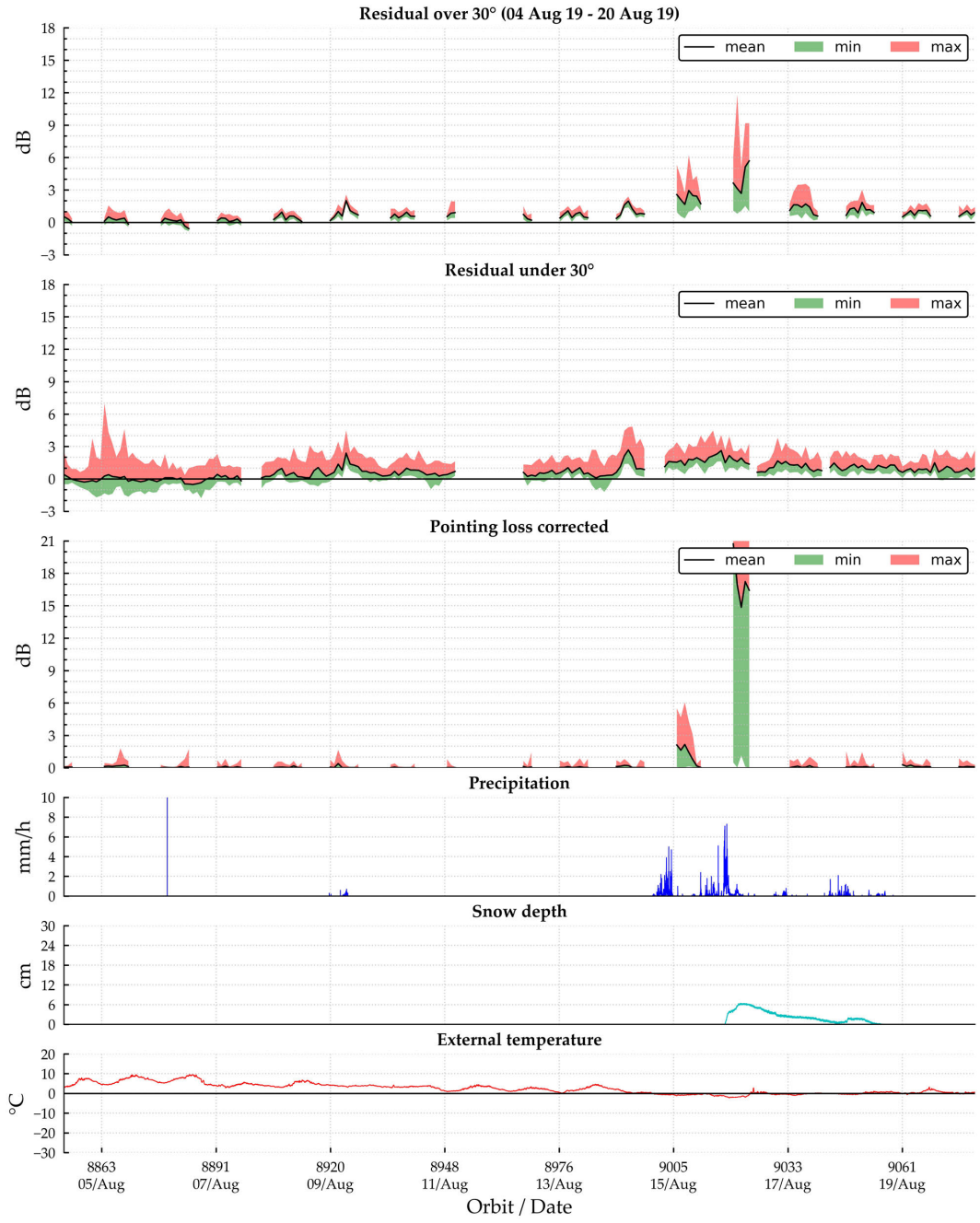

Figure A.17: Residuals and pointing loss comparison against weather effects for cycle 39

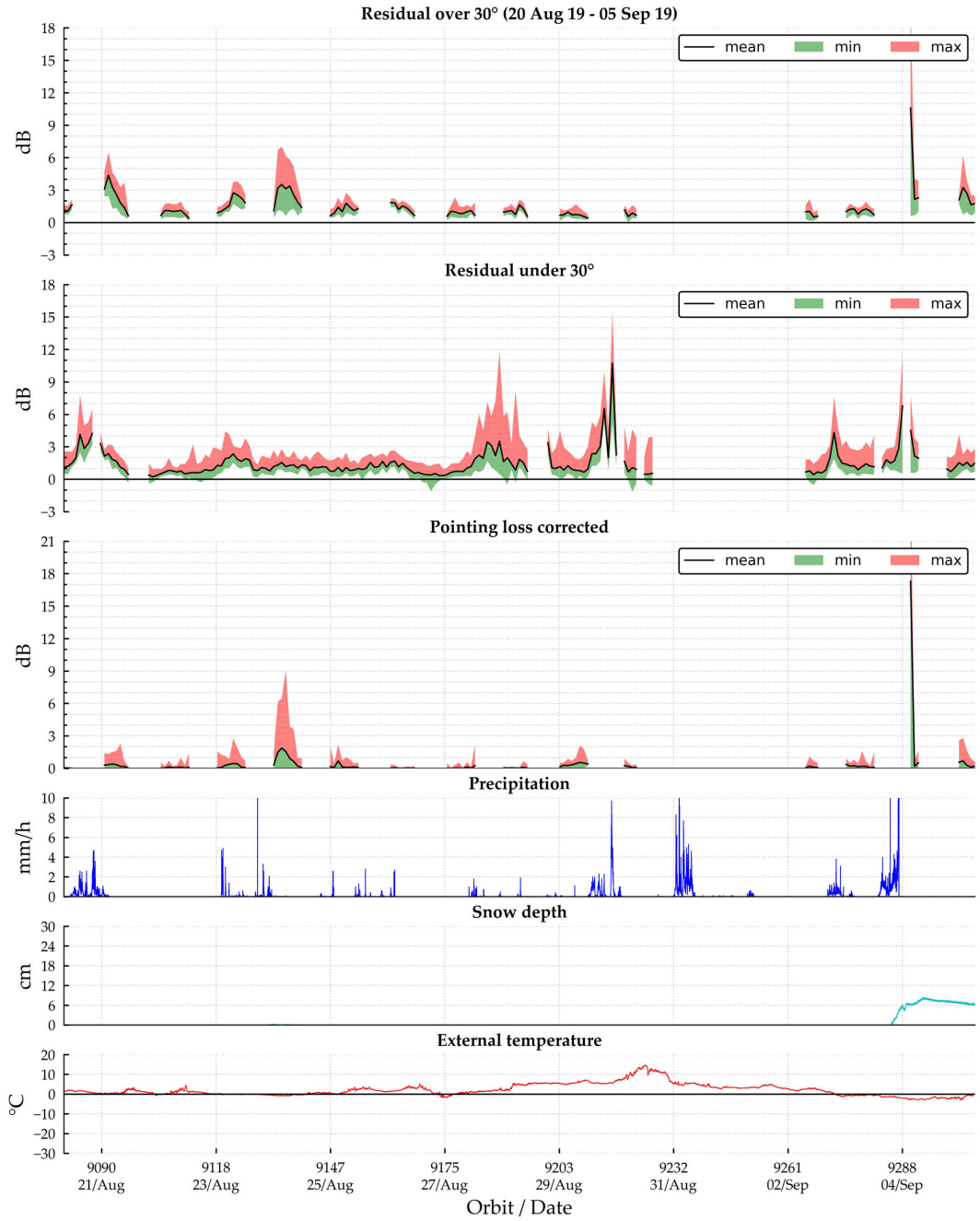

Figure A.18: Residuals and pointing loss comparison against weather effects for cycle 40

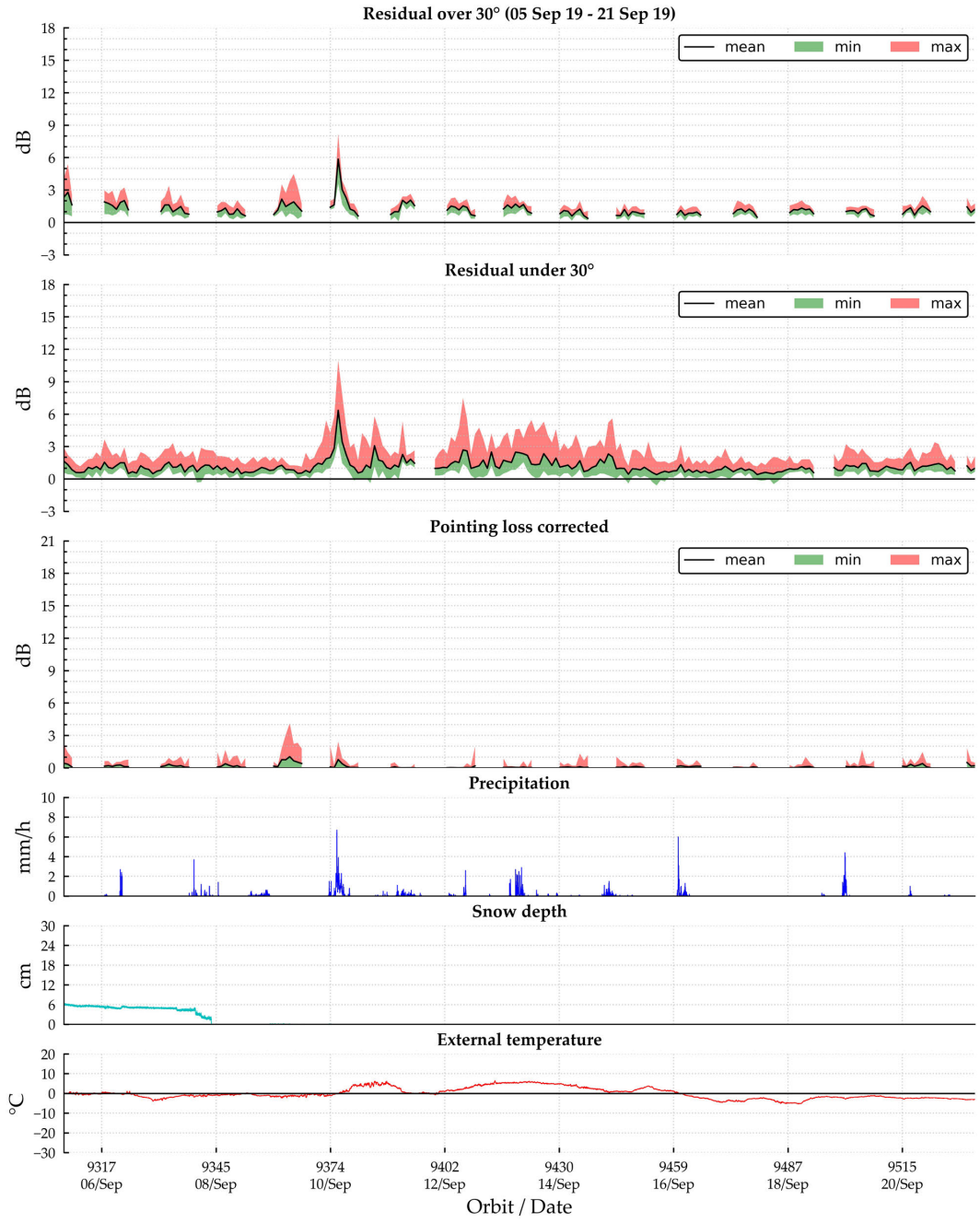

Figure A.19: Residuals and pointing loss comparison against weather effects for cycle 41

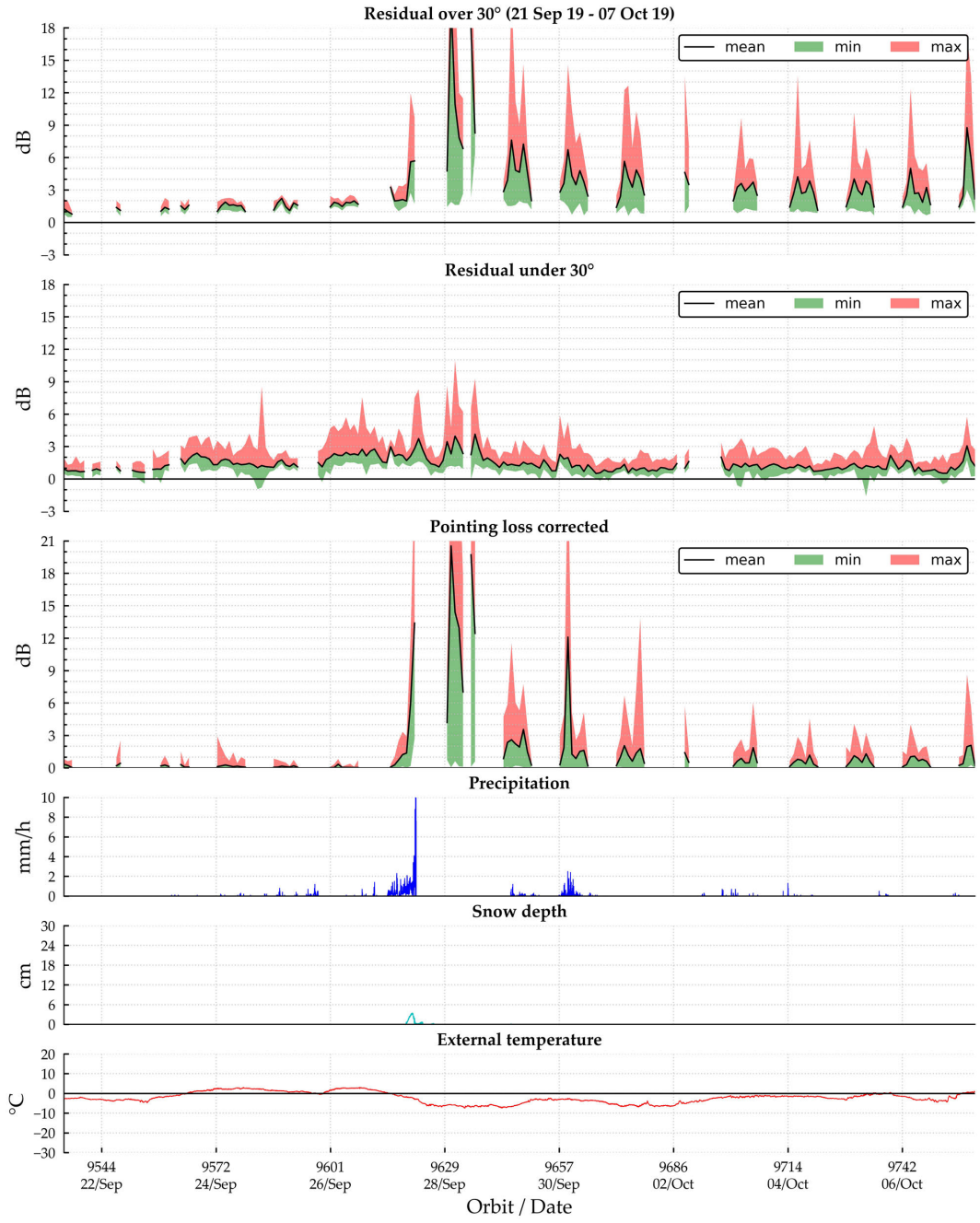

Figure A.20: Residuals and pointing loss comparison against weather effects for cycle 42

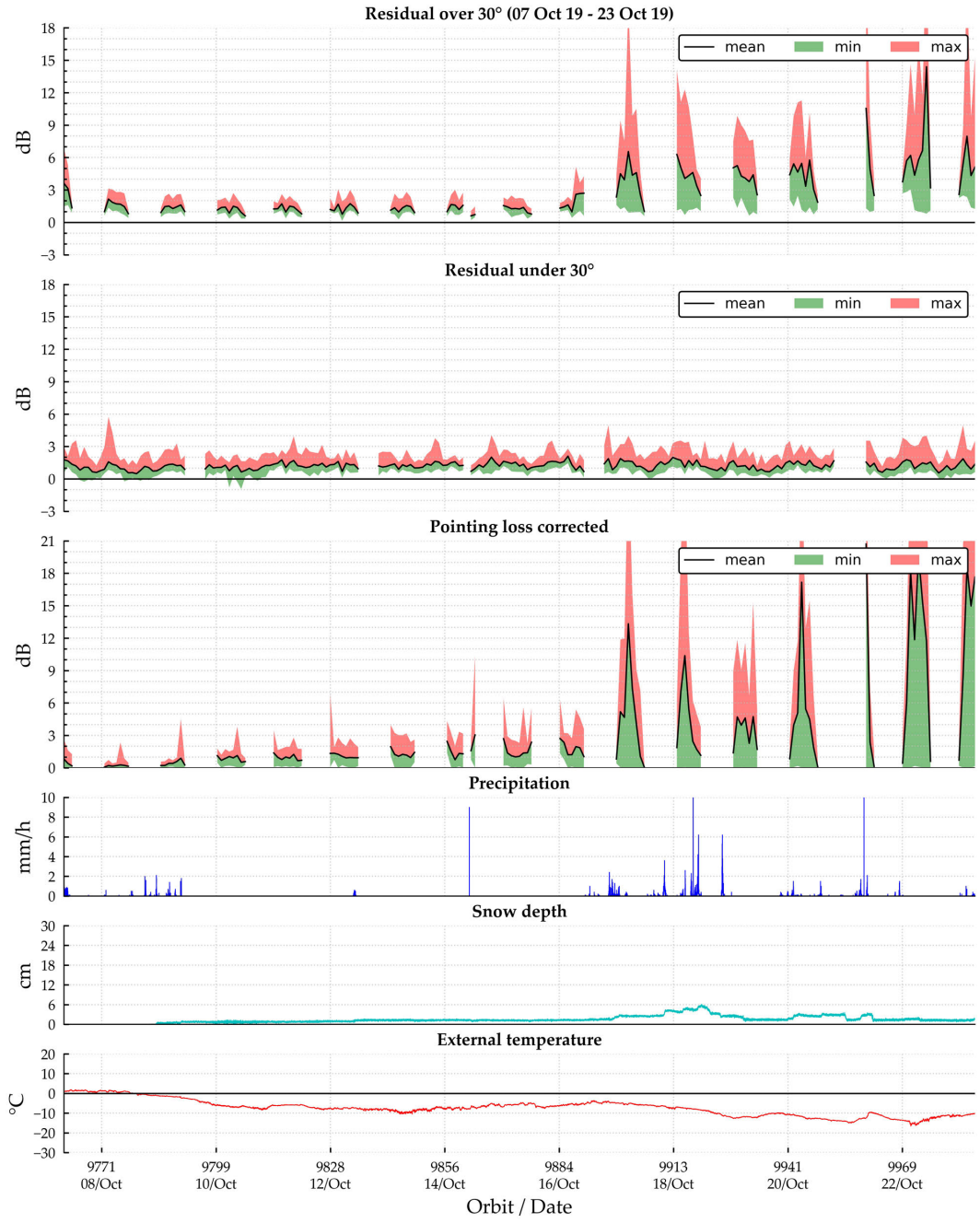

Figure A.21: Residuals and pointing loss comparison against weather effects for cycle 43

Figure A.22: Residuals and pointing loss comparison against weather effects for cycle 44

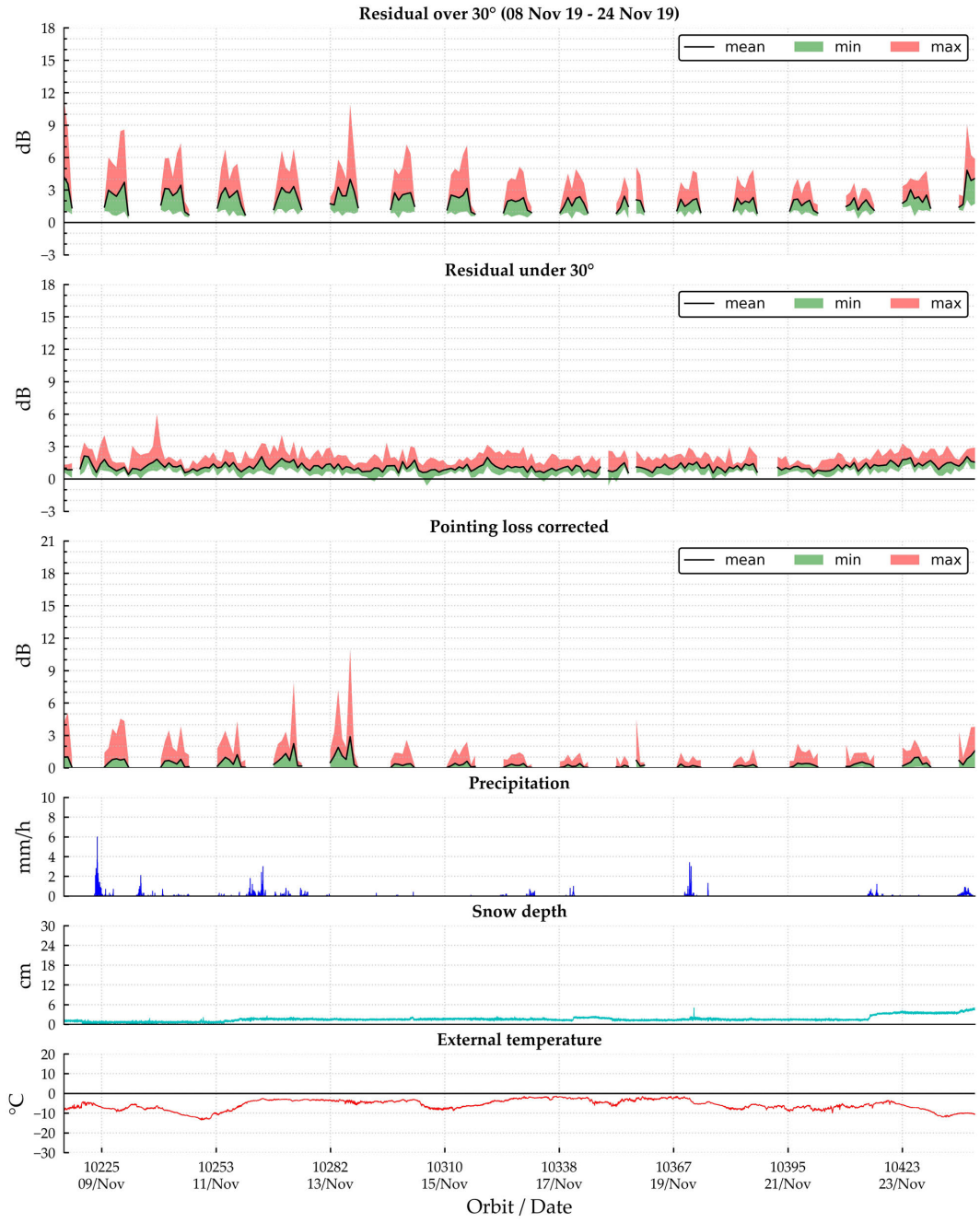

Figure A.23: Residuals and pointing loss comparison against weather effects for cycle 45

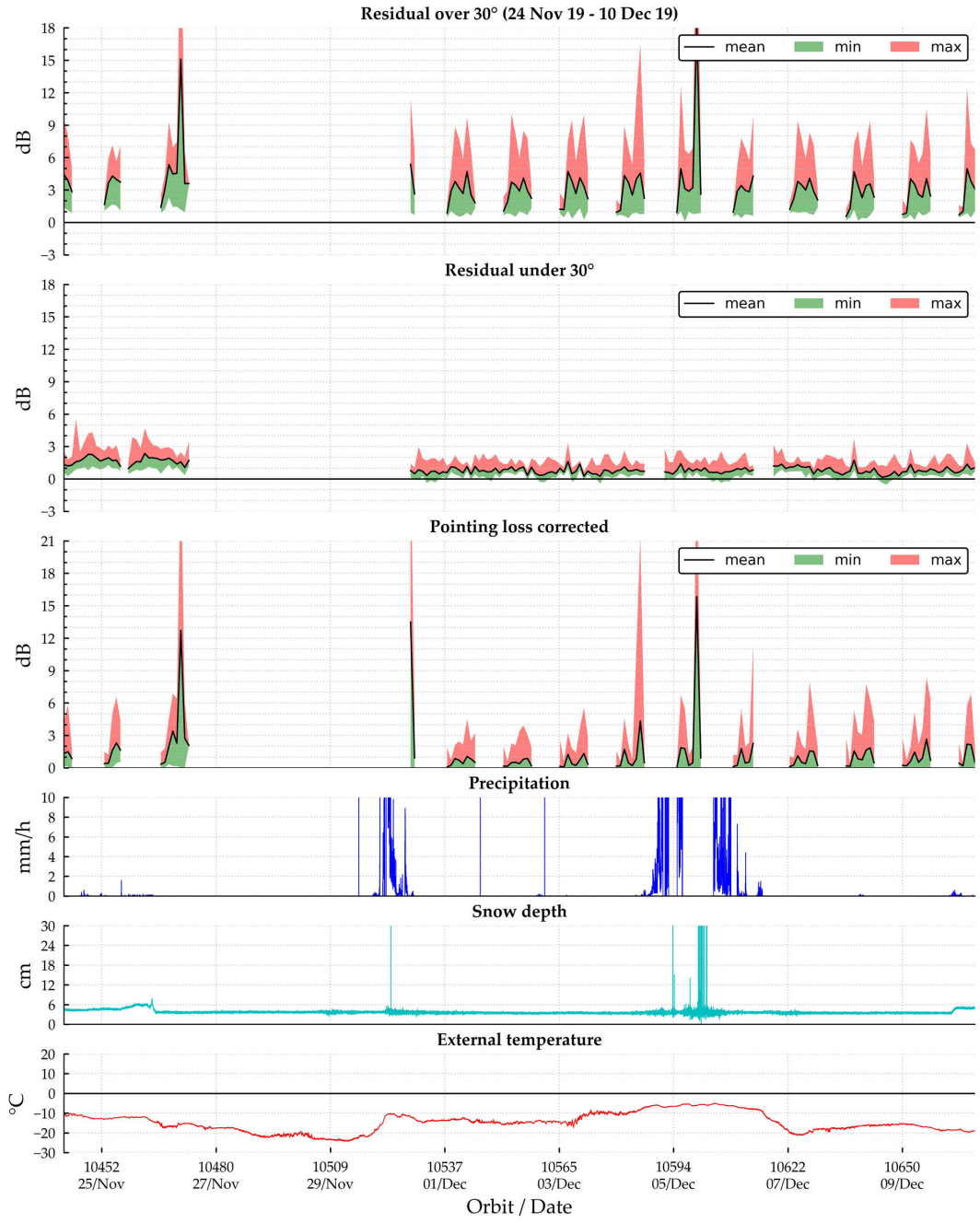

Figure A.24: Residuals and pointing loss comparison against weather effectsfor cycle 46

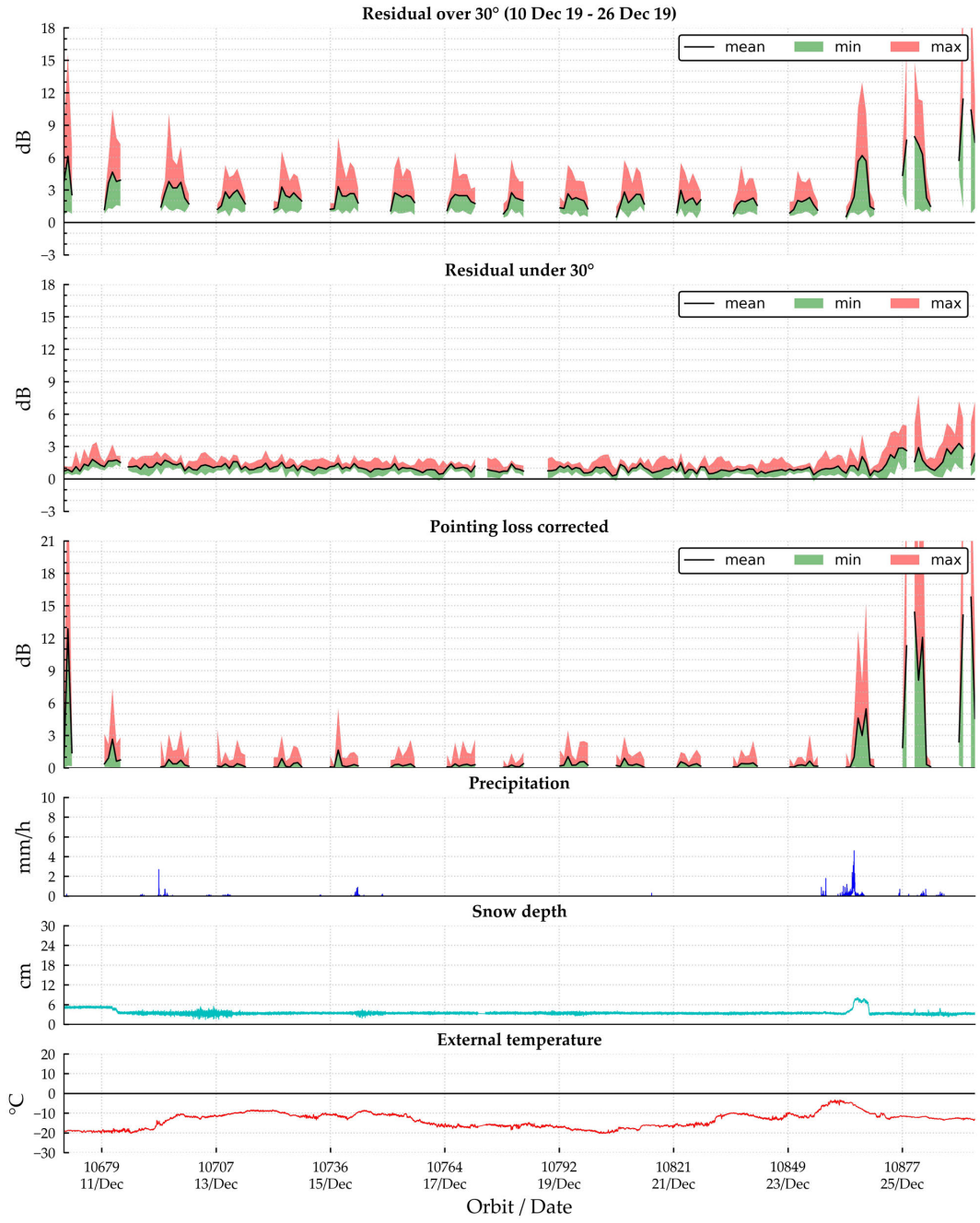

Figure A.25: Residuals and pointing loss comparison against weather effects for cycle 47

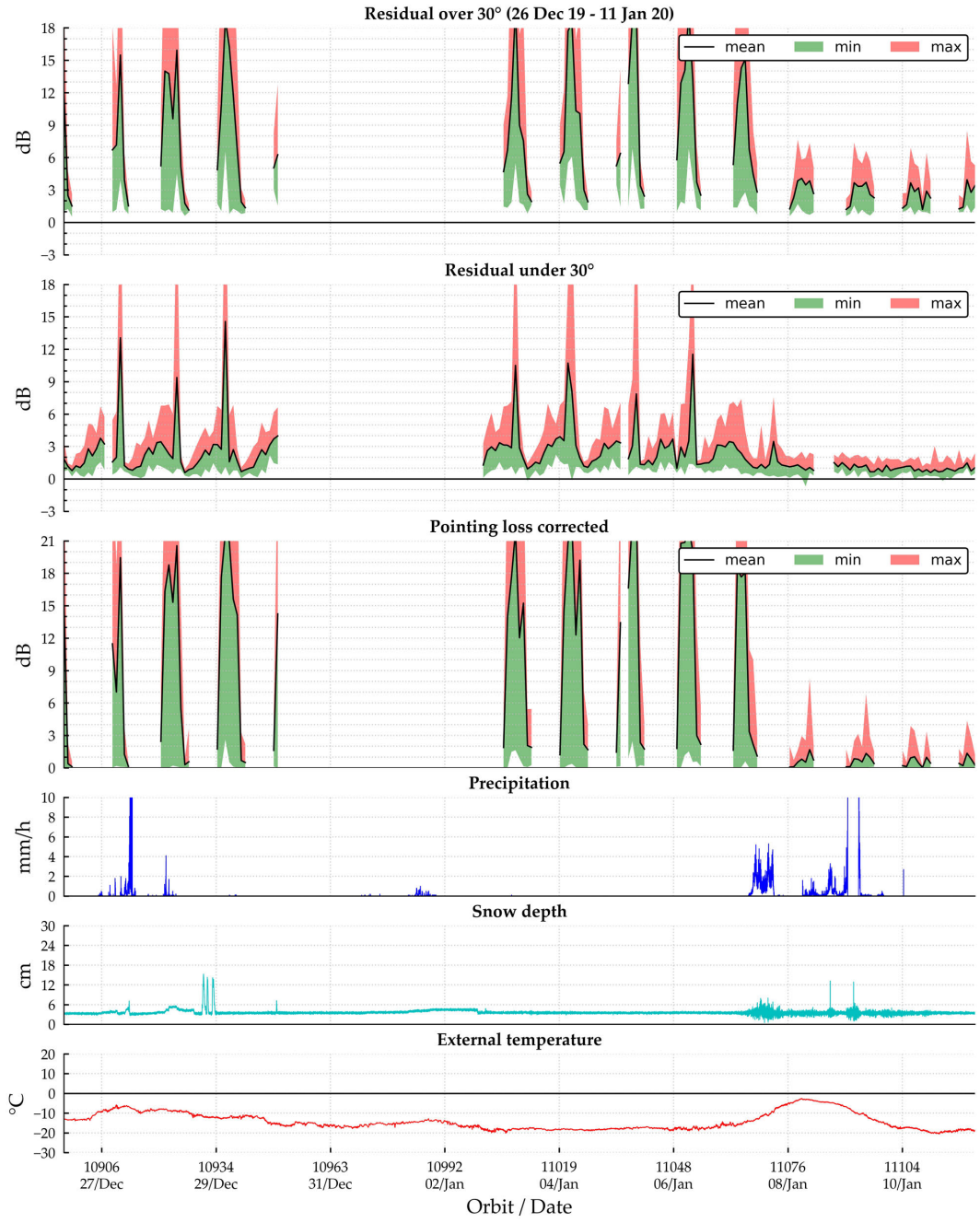

Figure A.26: Residuals and pointing loss comparison against weather effects for cycle 48

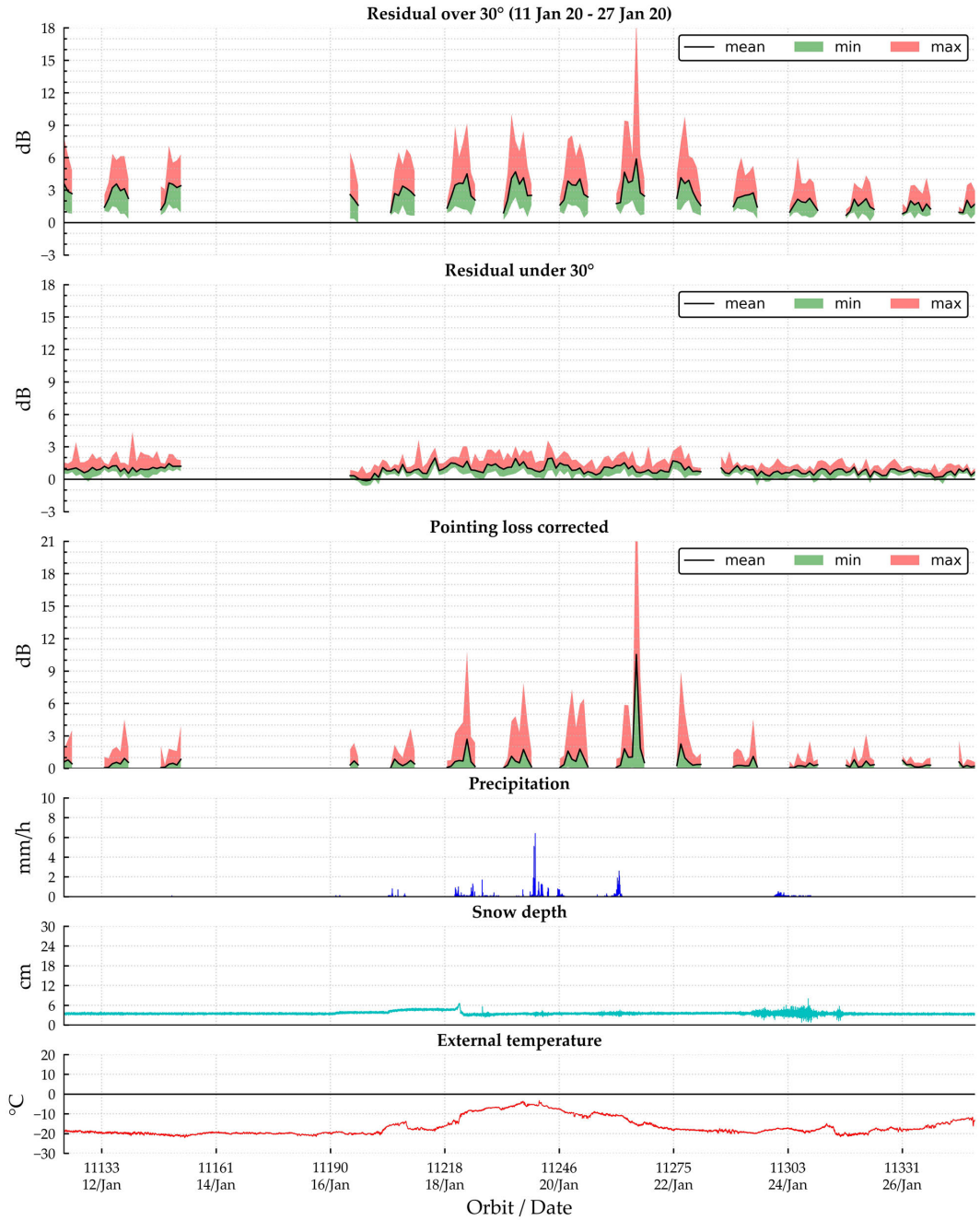

Figure A.27: Residuals and pointing loss comparison against weather effects for cycle 49

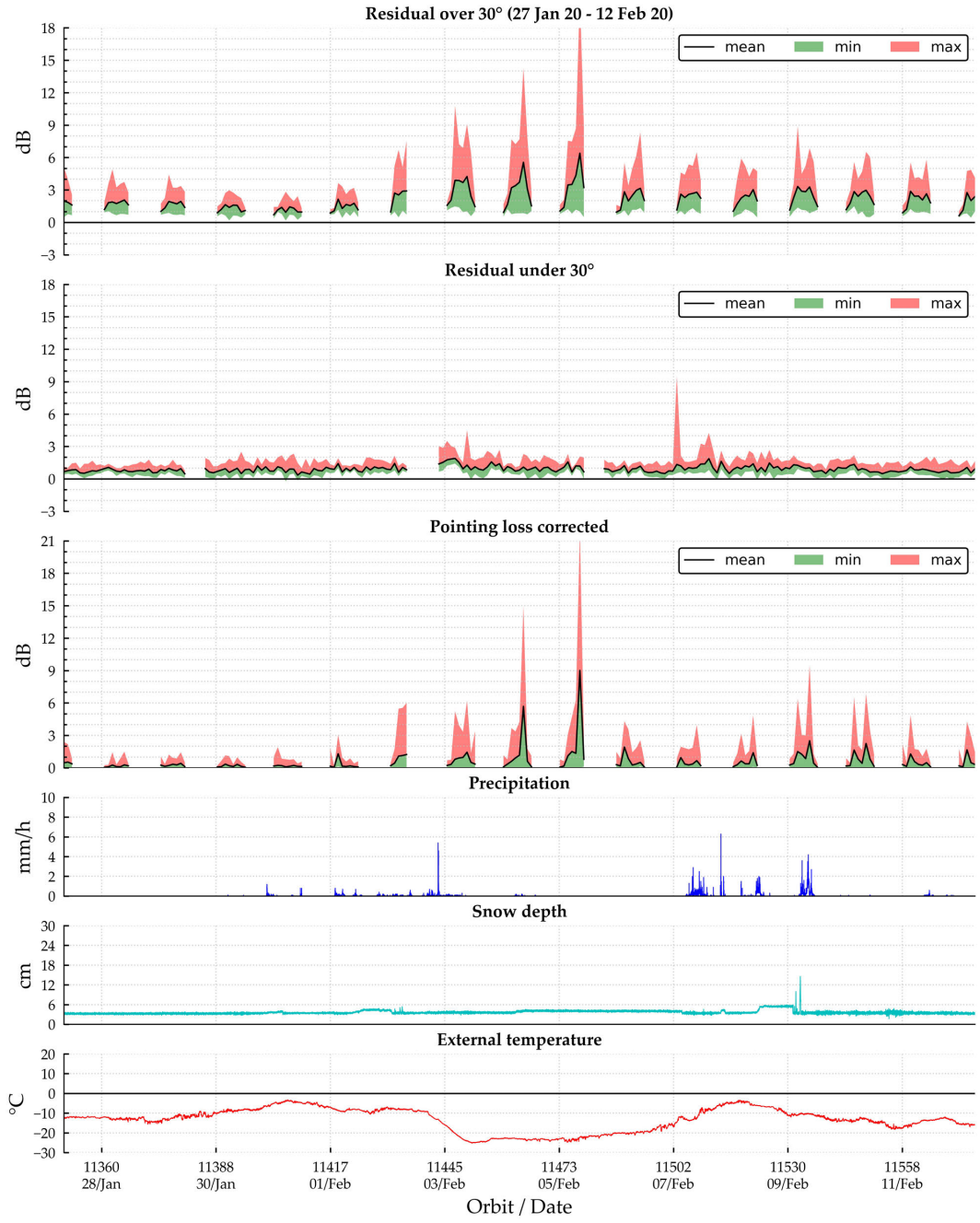

Figure A.28: Residuals and pointing loss comparison against weather effects for cycle 50

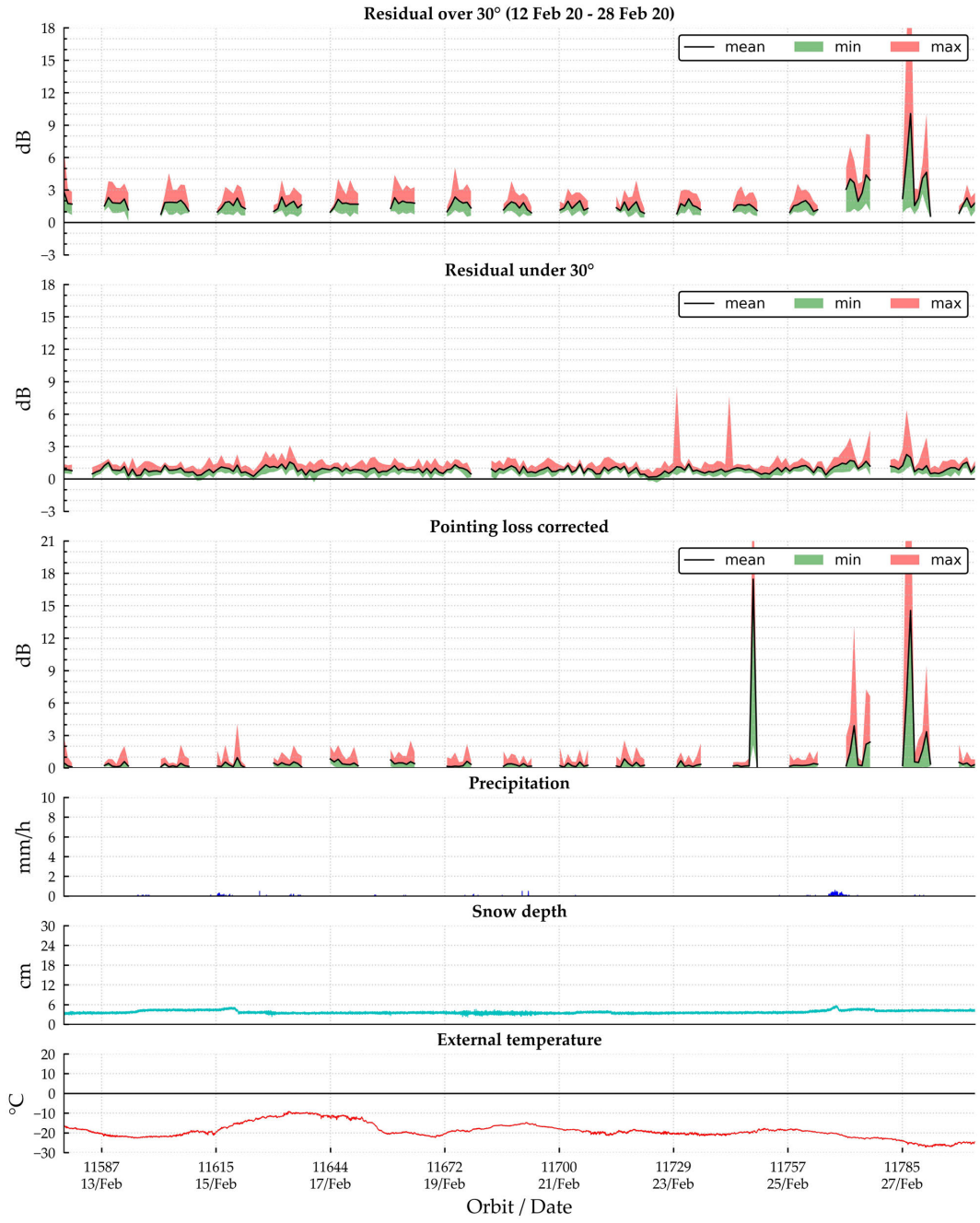

Figure A.29: Residuals and pointing loss comparison against weather effects for cycle 51

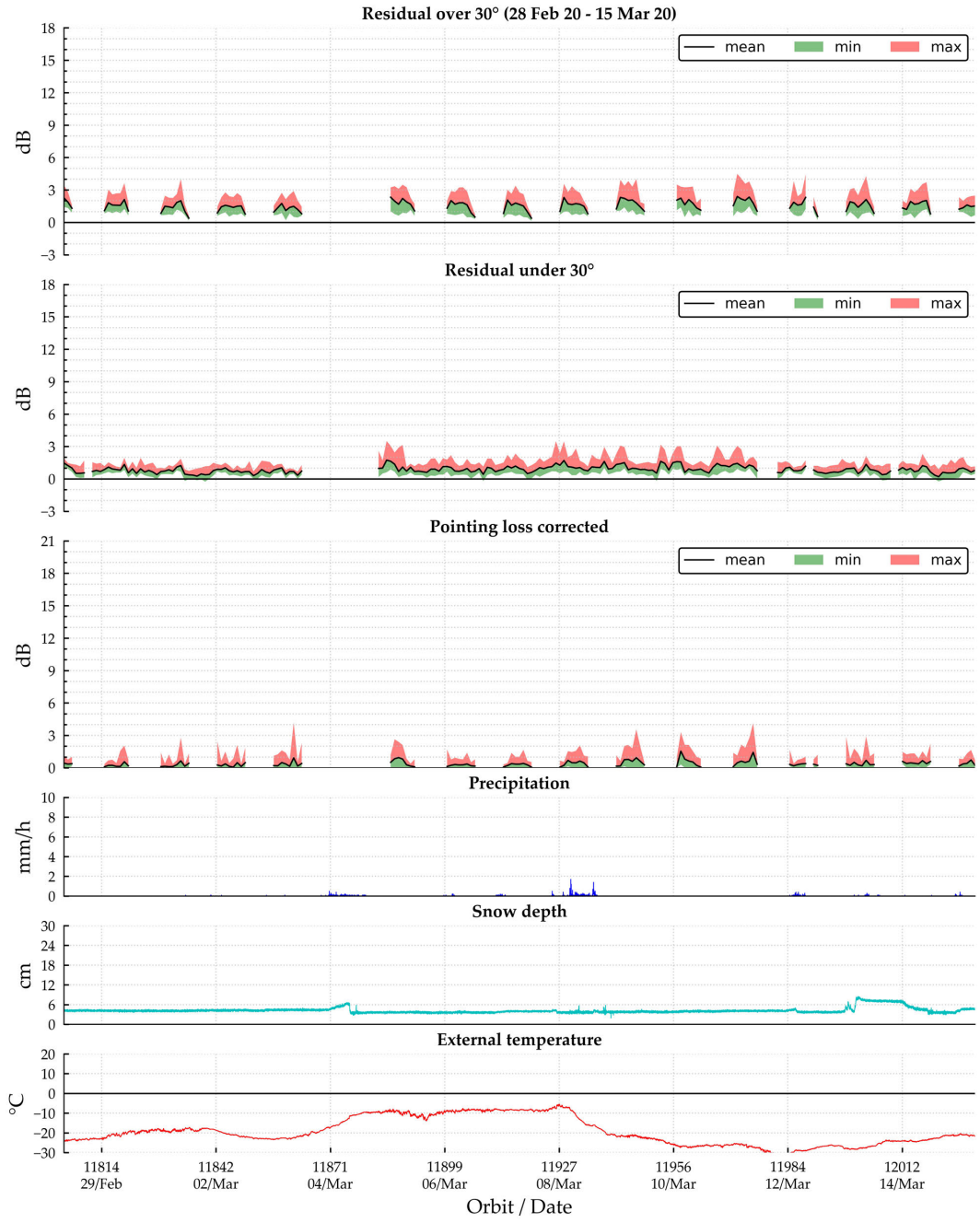

Figure A.30: Residuals and pointing loss comparison against weather effects for cycle 52

Figure A.31: Residuals and pointing loss comparison against weather effects for cycle 53

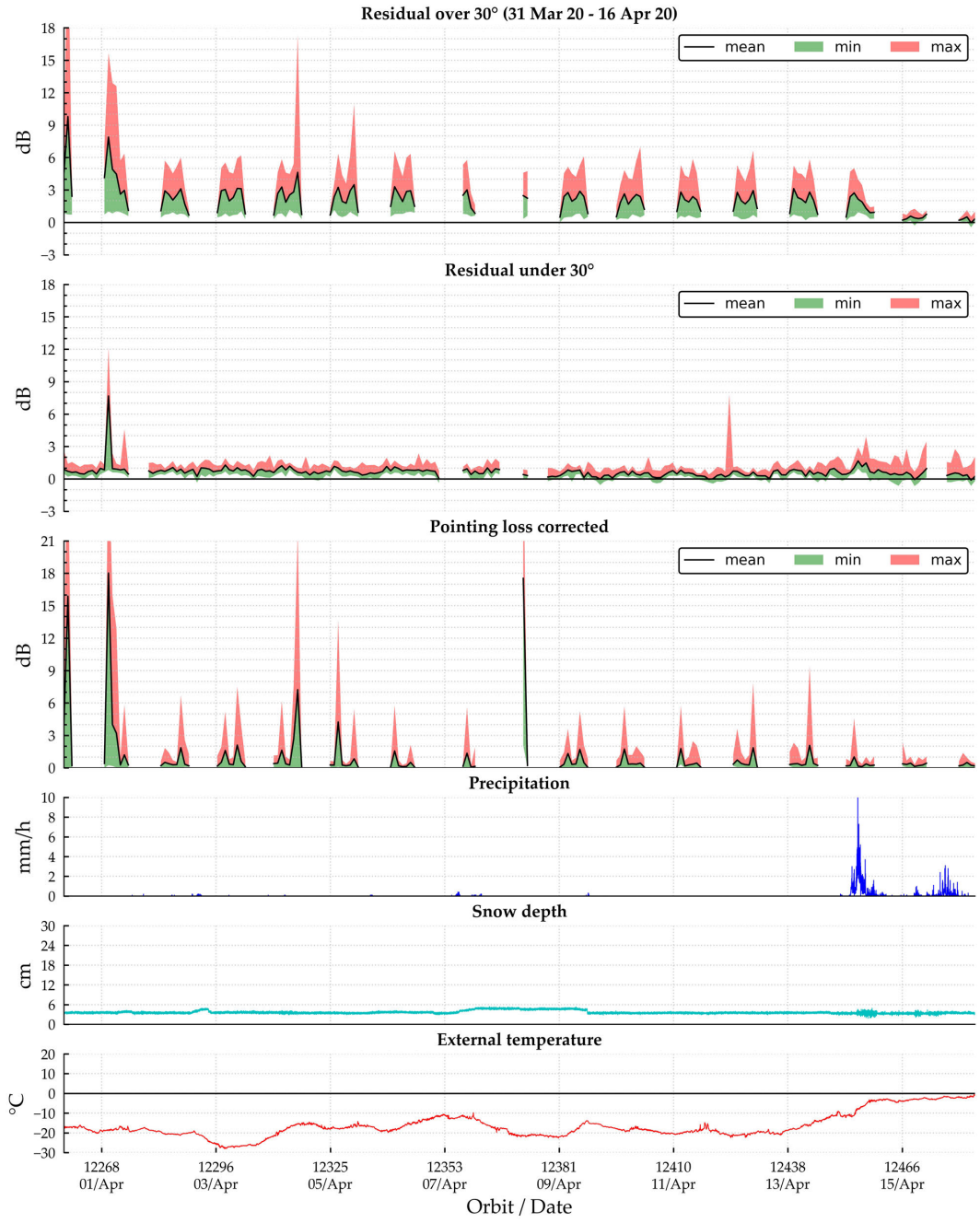

Figure A.32: Residuals and pointing loss comparison against weather effects for cycle 54

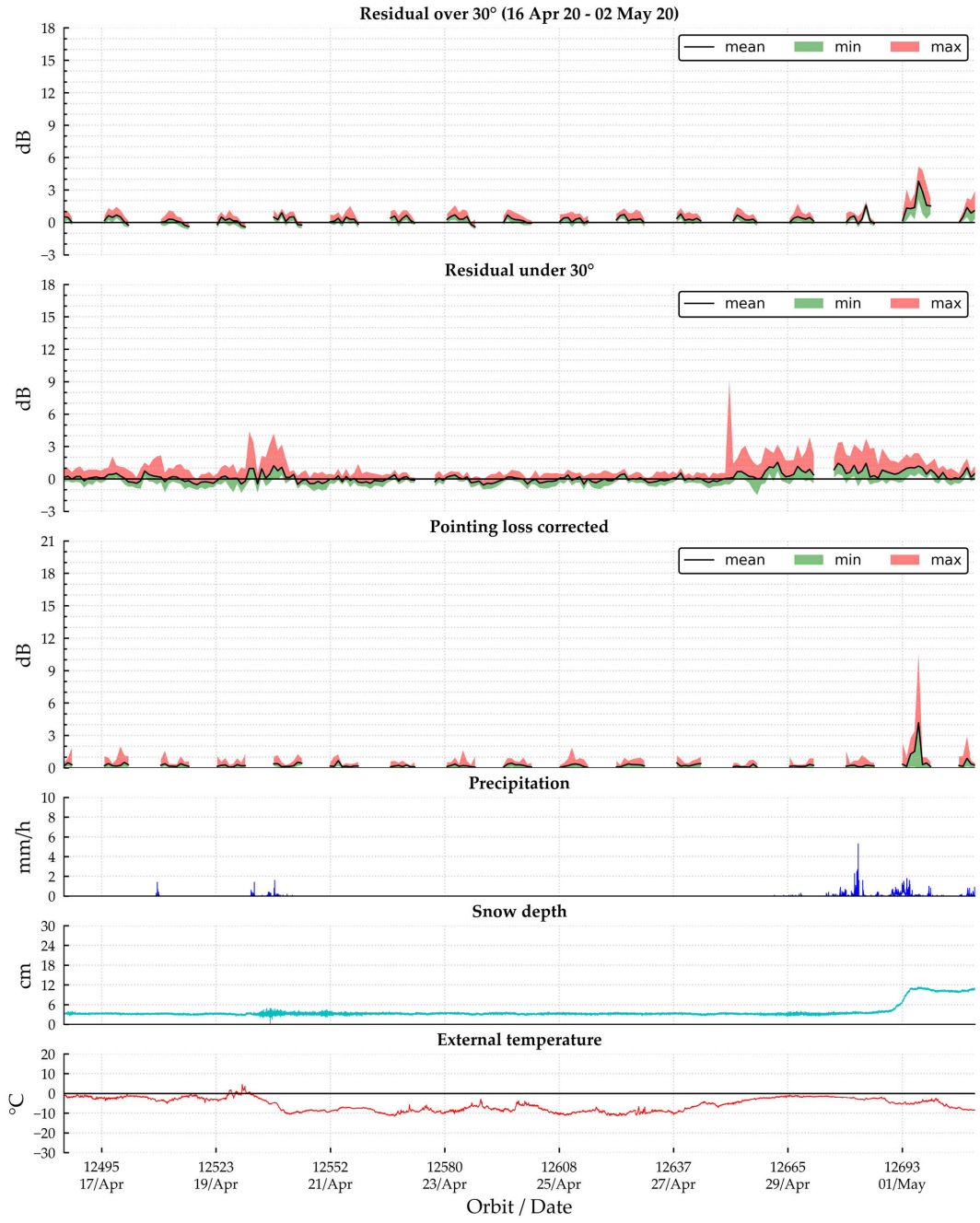

Figure A.33: Residuals and pointing loss comparison against weather effects for cycle 55

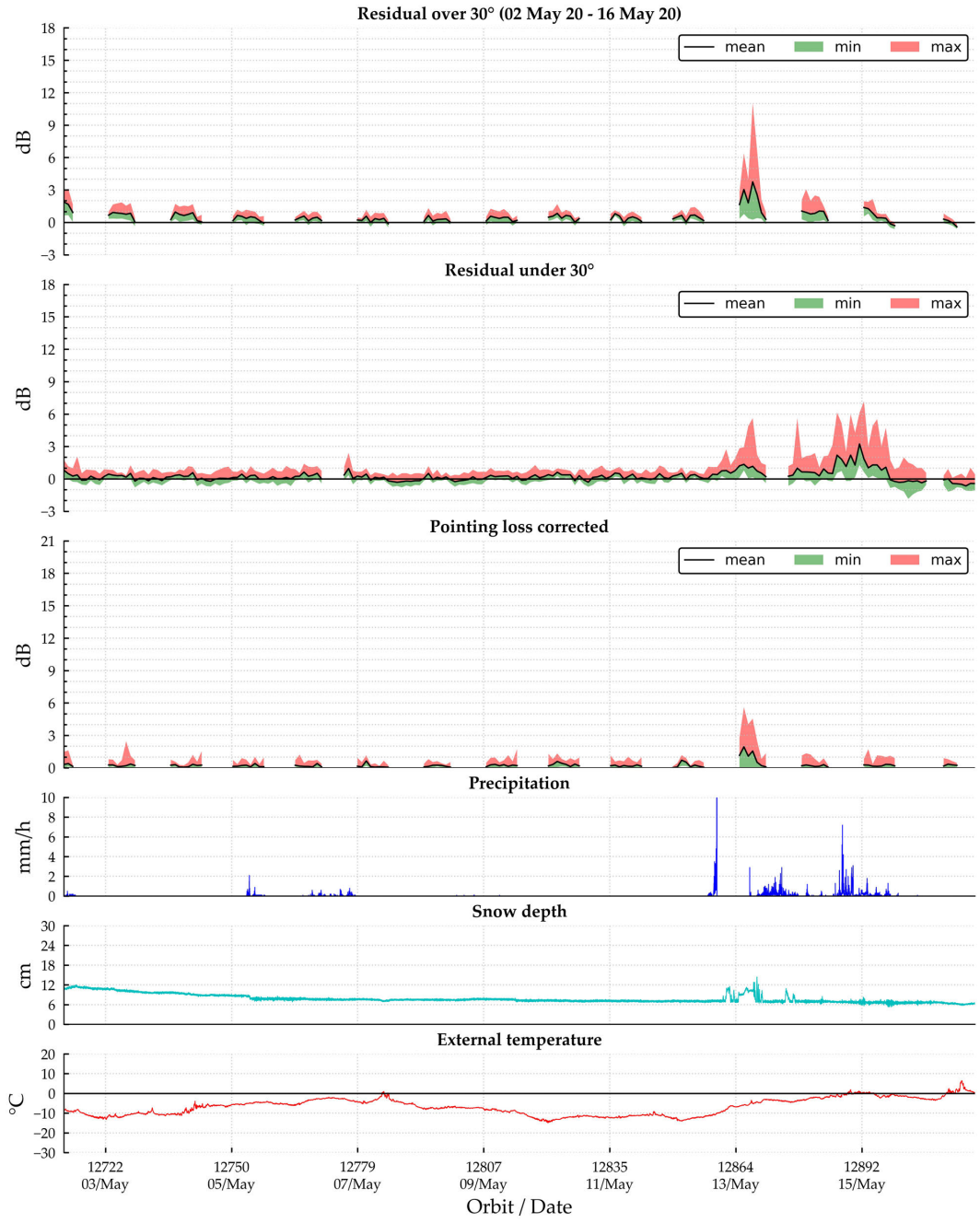

Figure A.34: Residuals and pointing loss comparison against weather effects for cycle 56

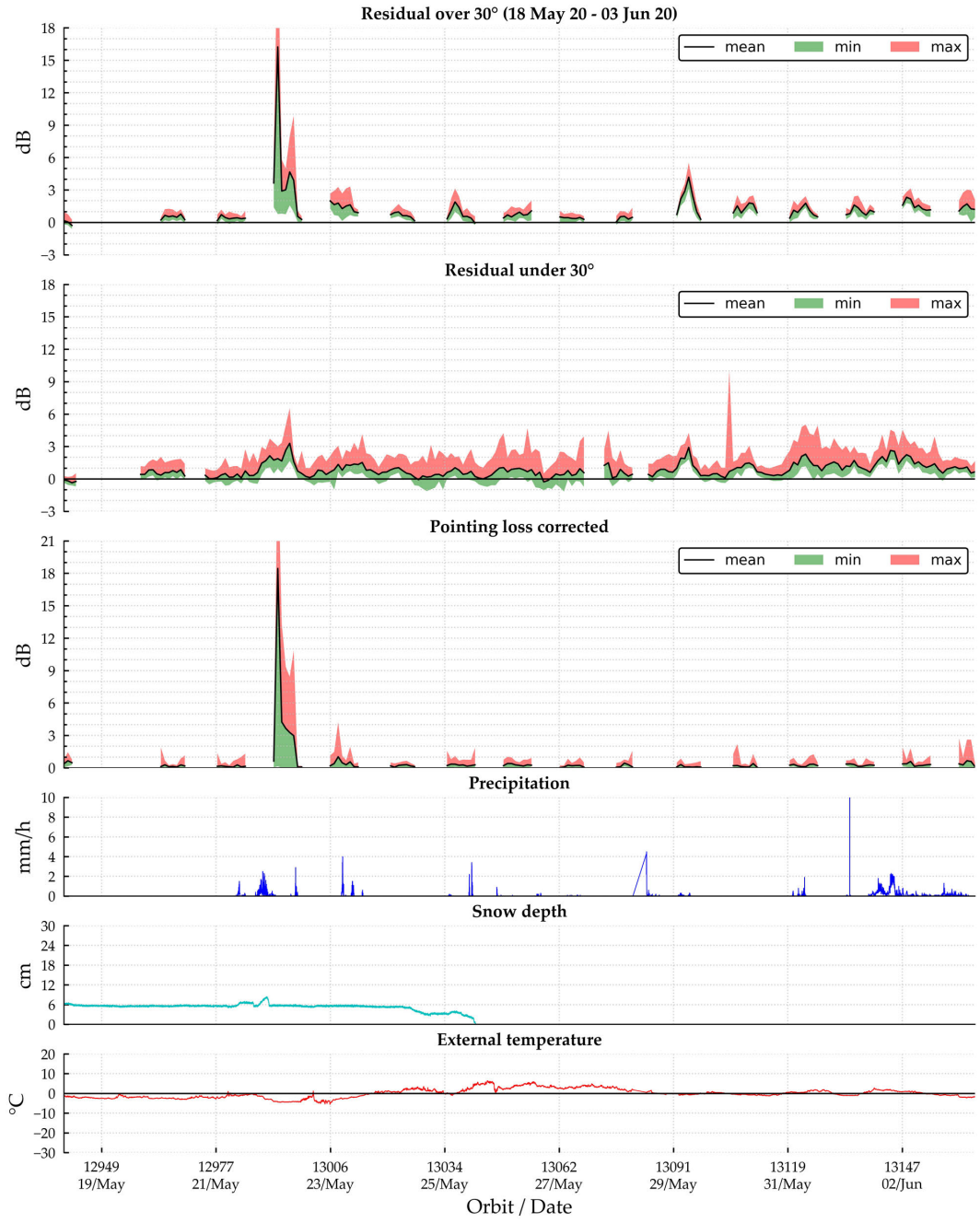

Figure A.35: Residuals and pointing loss comparison against weather effects for cycle 57

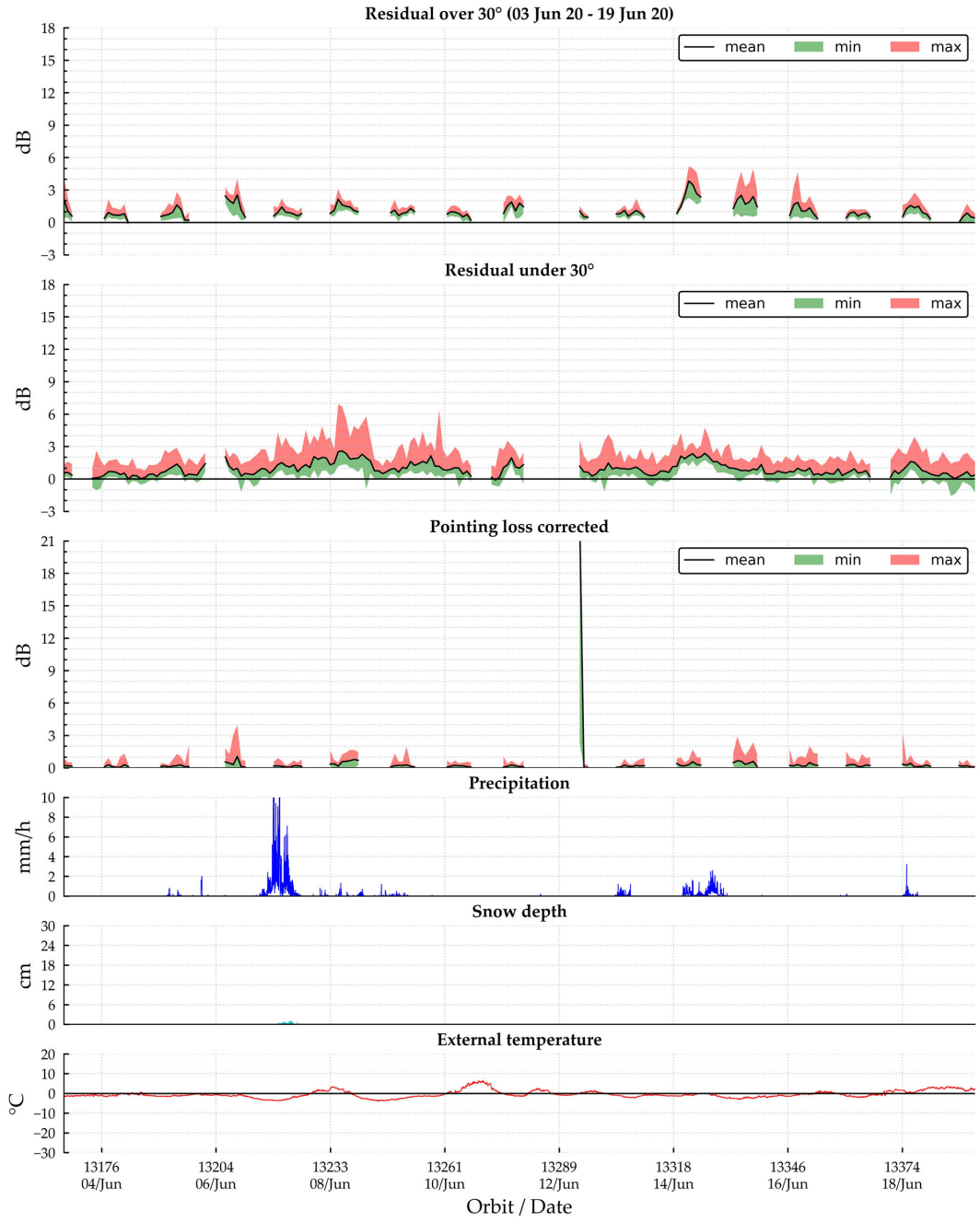

Figure A.36: Residuals and pointing loss comparison against weather effects for cycle 58

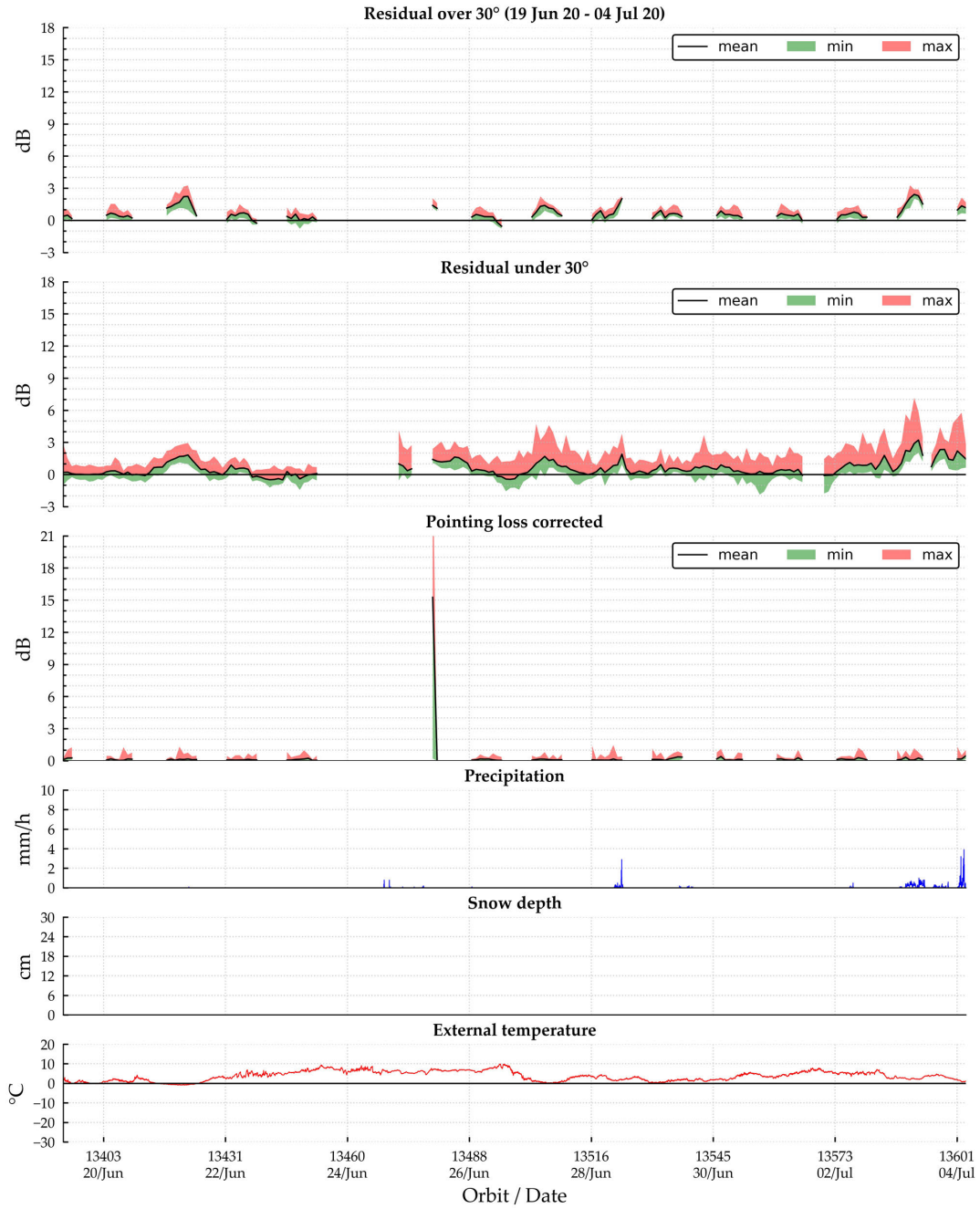

Figure A.37: Residuals and pointing loss comparison against weather effects for cycle 59

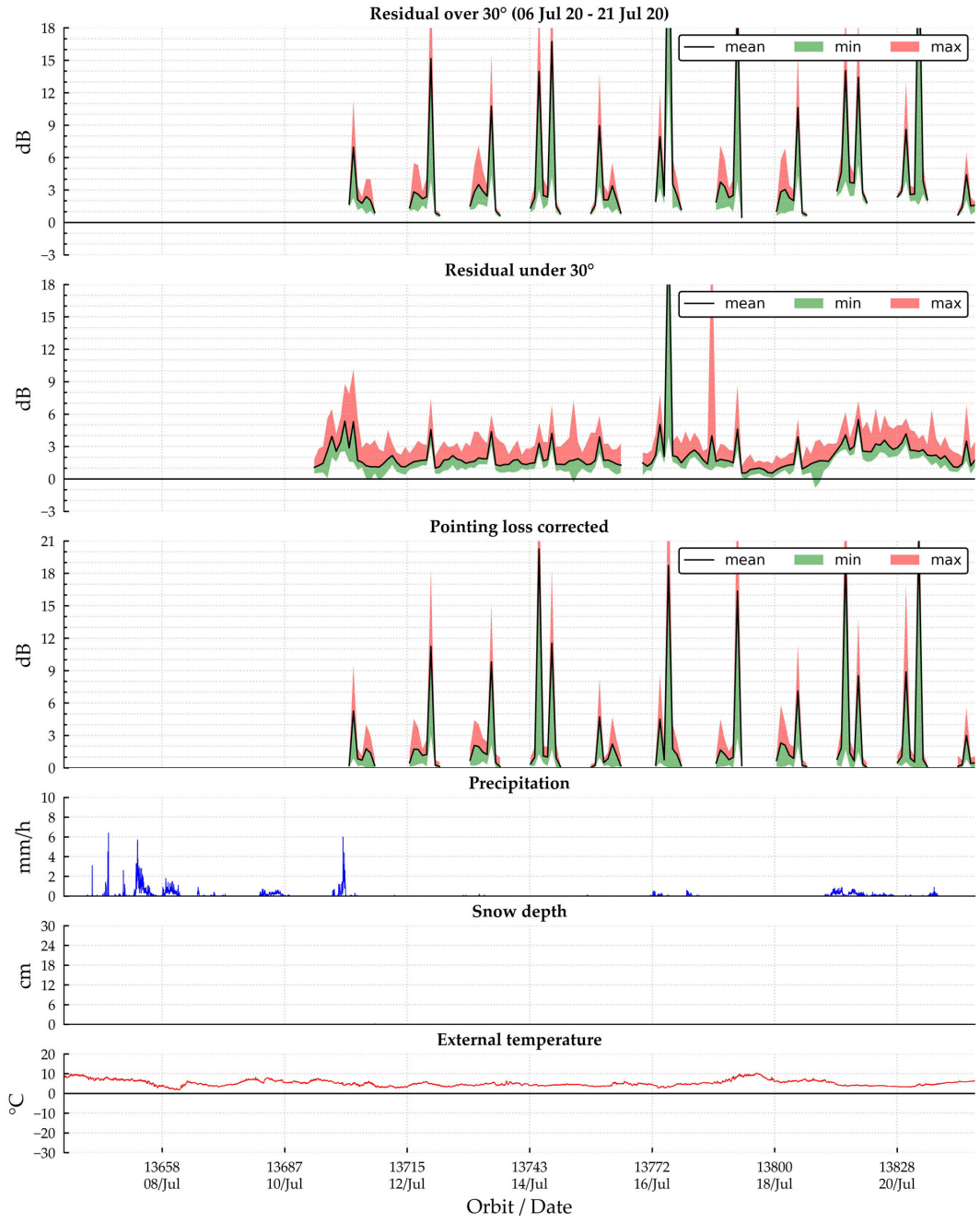

Figure A.38: Residuals and pointing loss comparison against weather effects for cycle 60

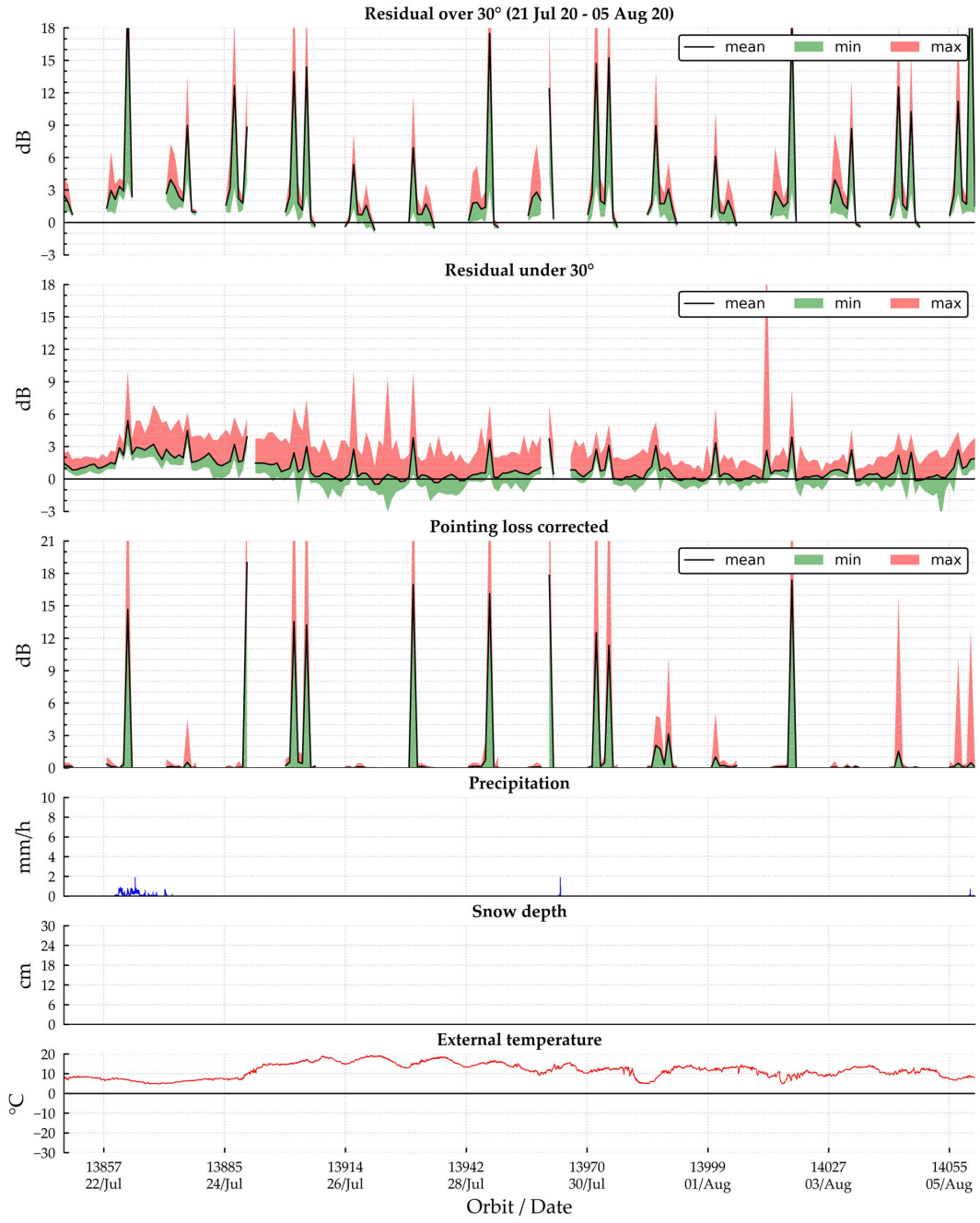

Figure A.39: Residuals and pointing loss comparison against weather effects for cycle 61

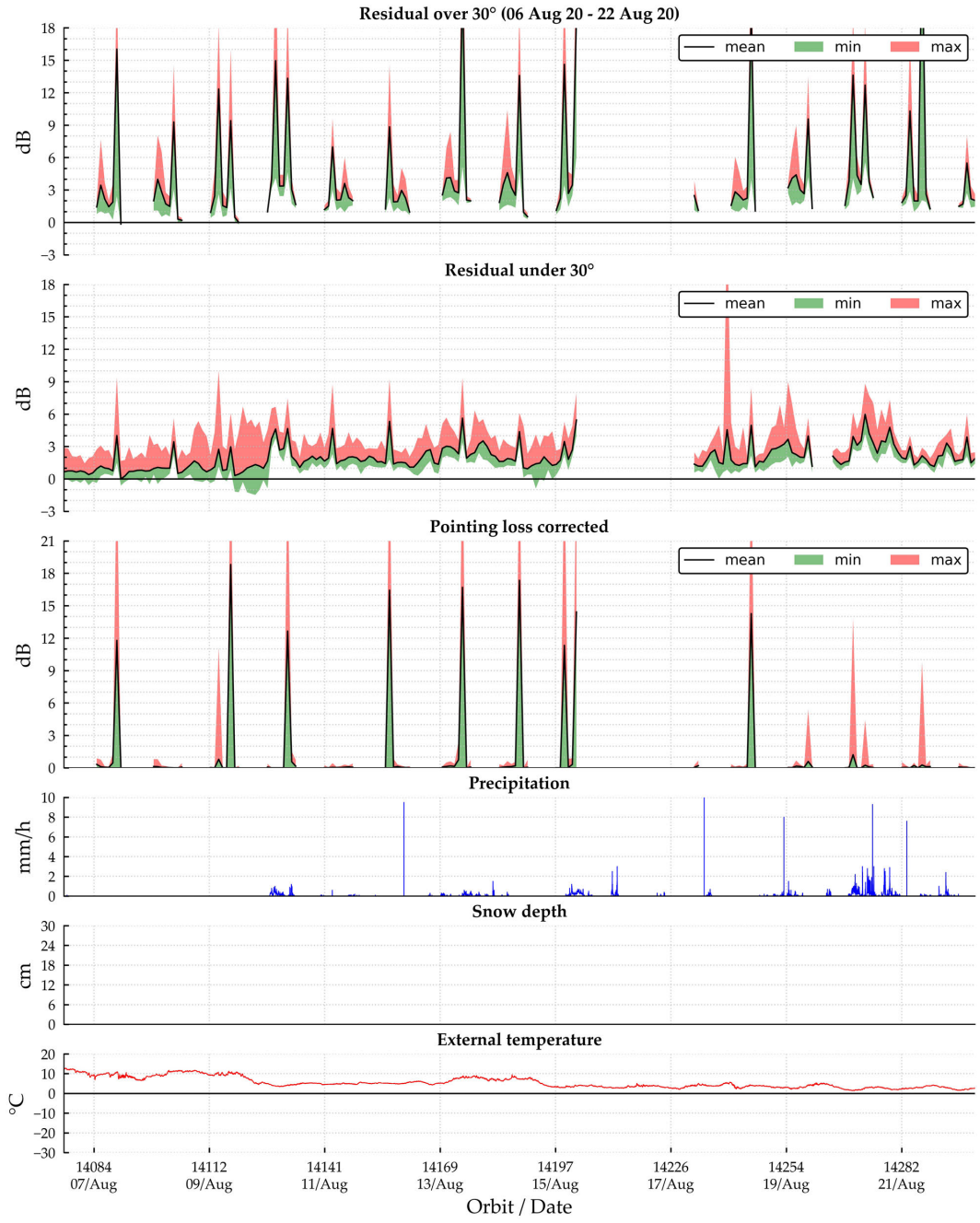

Figure A.40: Residuals and pointing loss comparison against weather effects for cycle 62

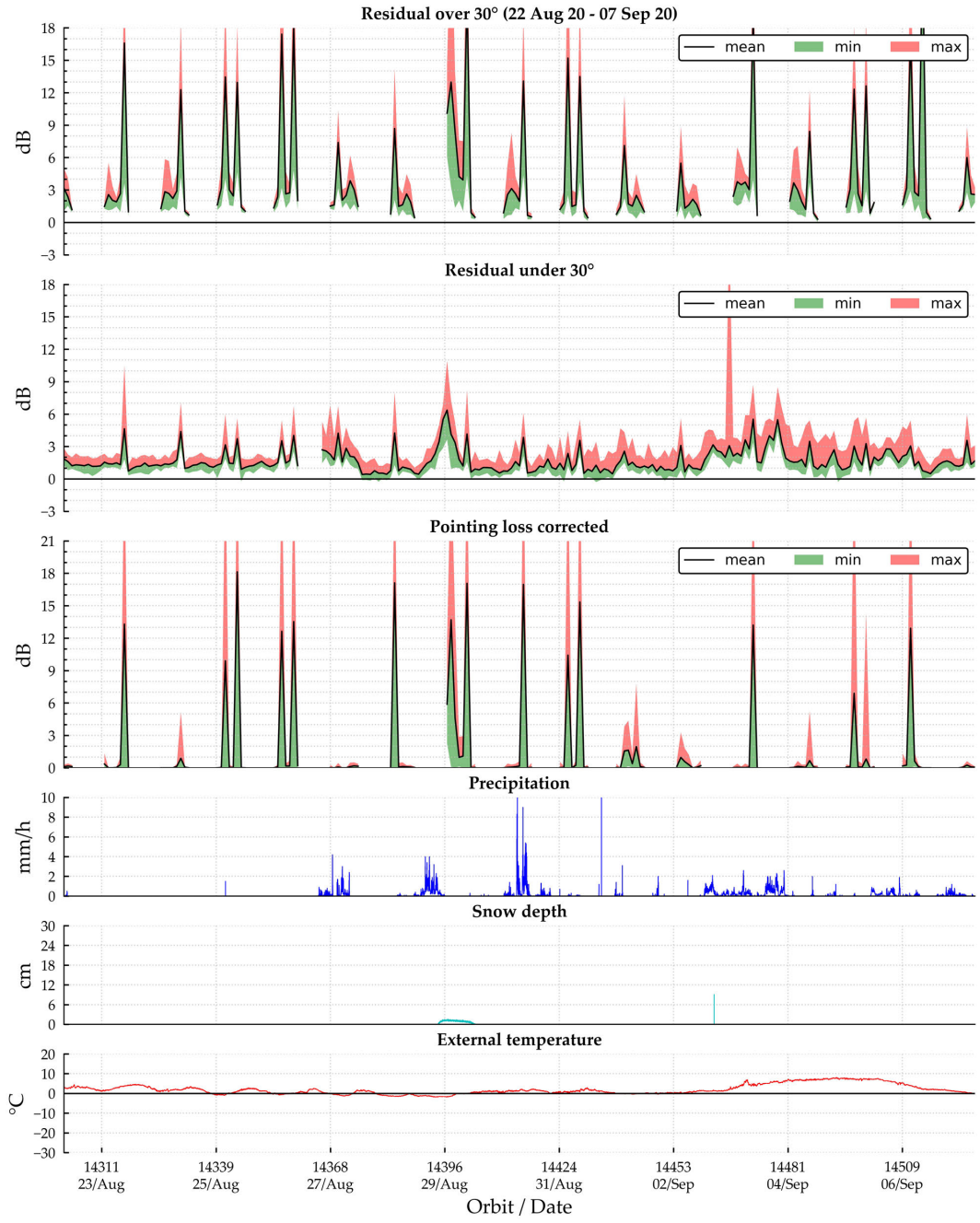

Figure A.41: Residuals and pointing loss comparison against weather effects for cycle 63

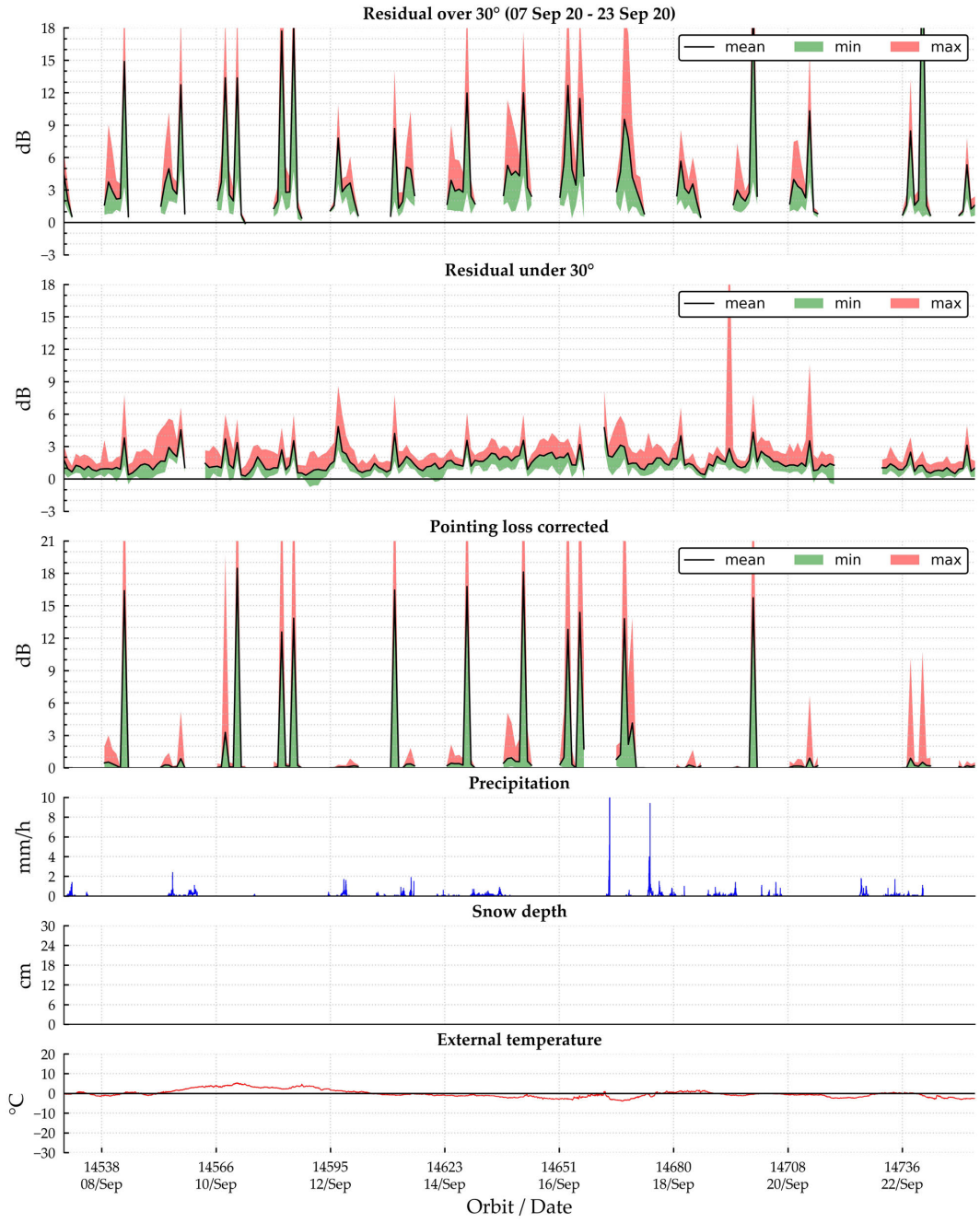

Figure A.42: Residuals and pointing loss comparison against weather effects for cycle 64

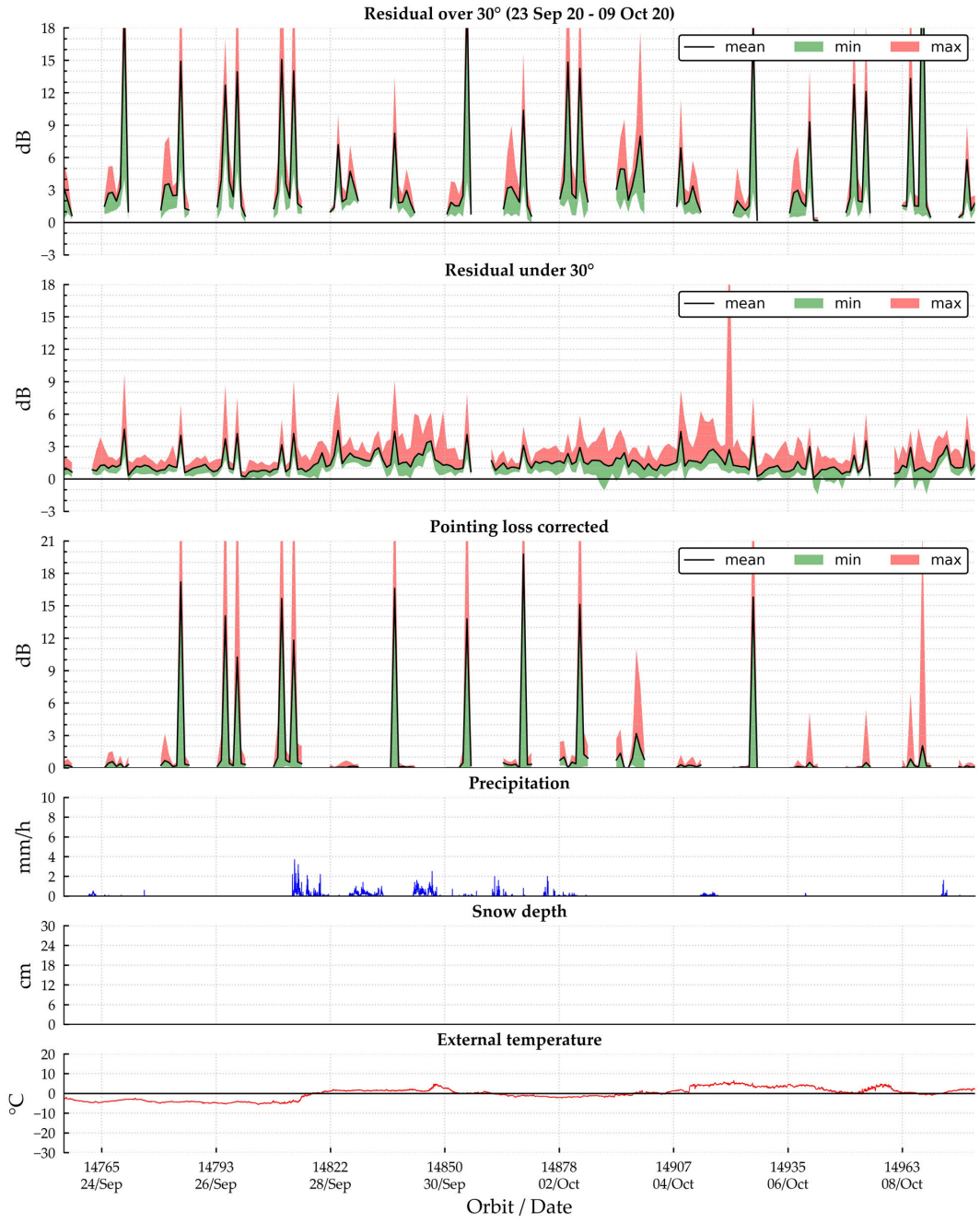

Figure A.43: Residuals and pointing loss comparison against weather effects for cycle 65

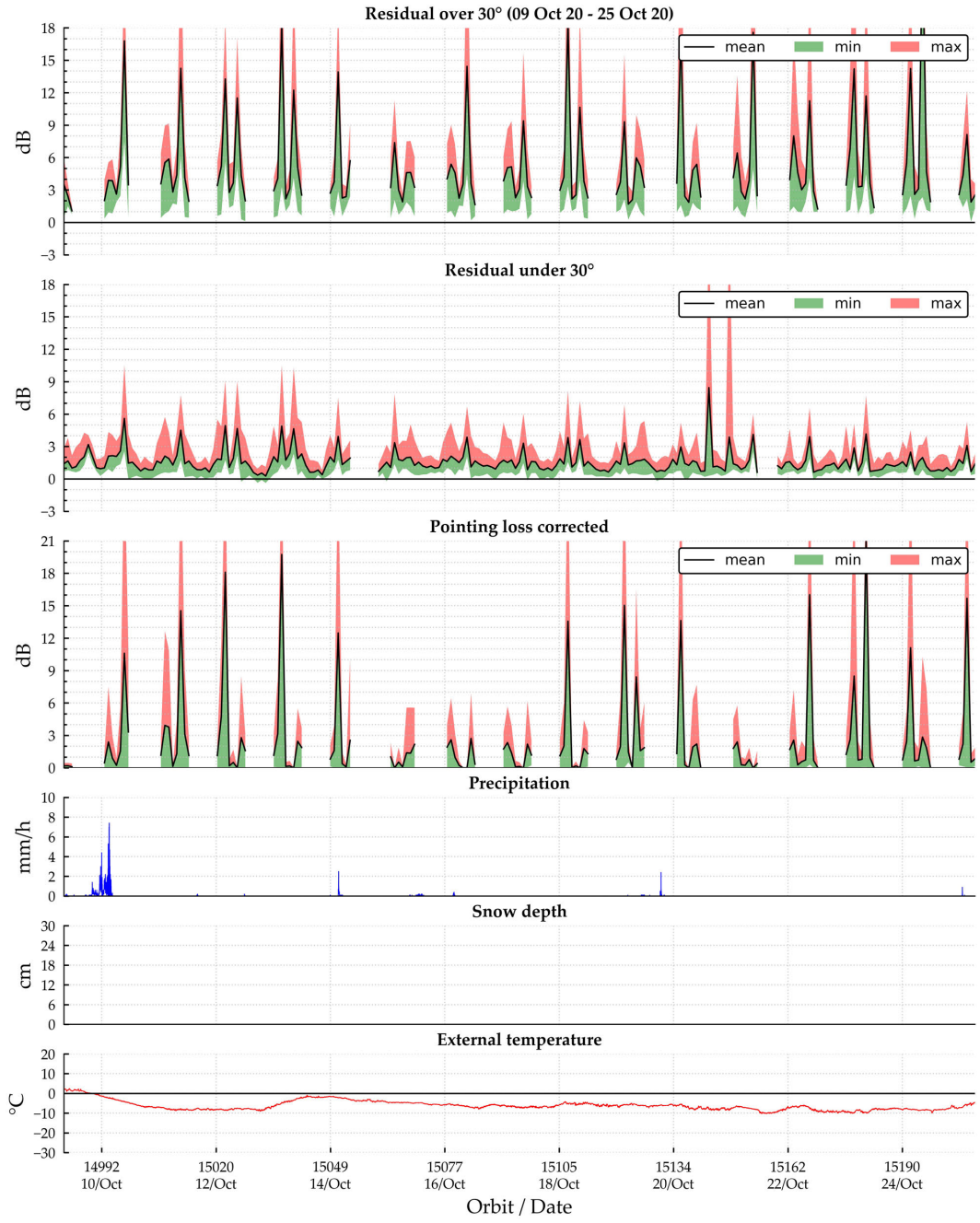

Figure A.44: Residuals and pointing loss comparison against weather effects for cycle 66

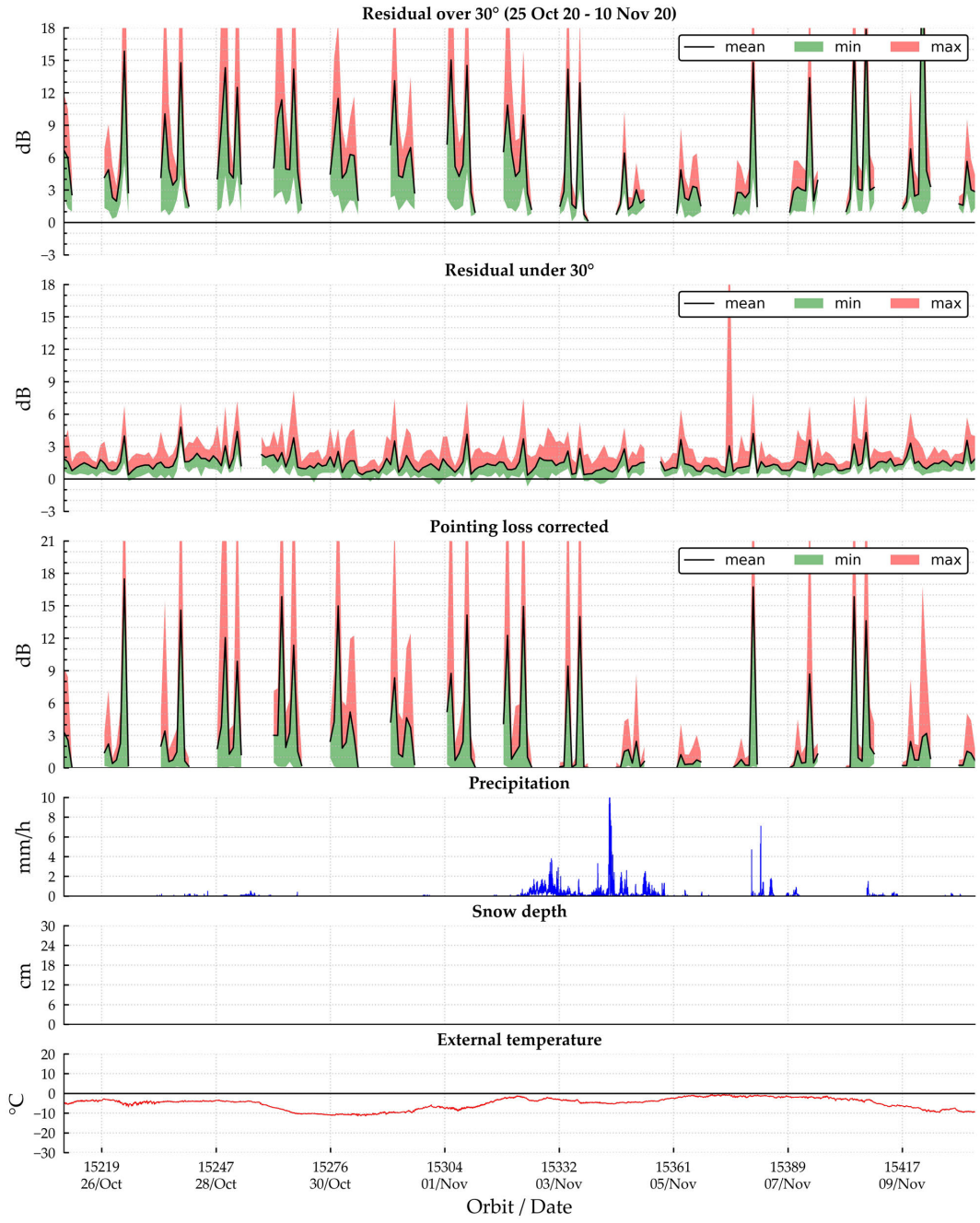

Figure A.45: Residuals and pointing loss comparison against weather effects for cycle 67

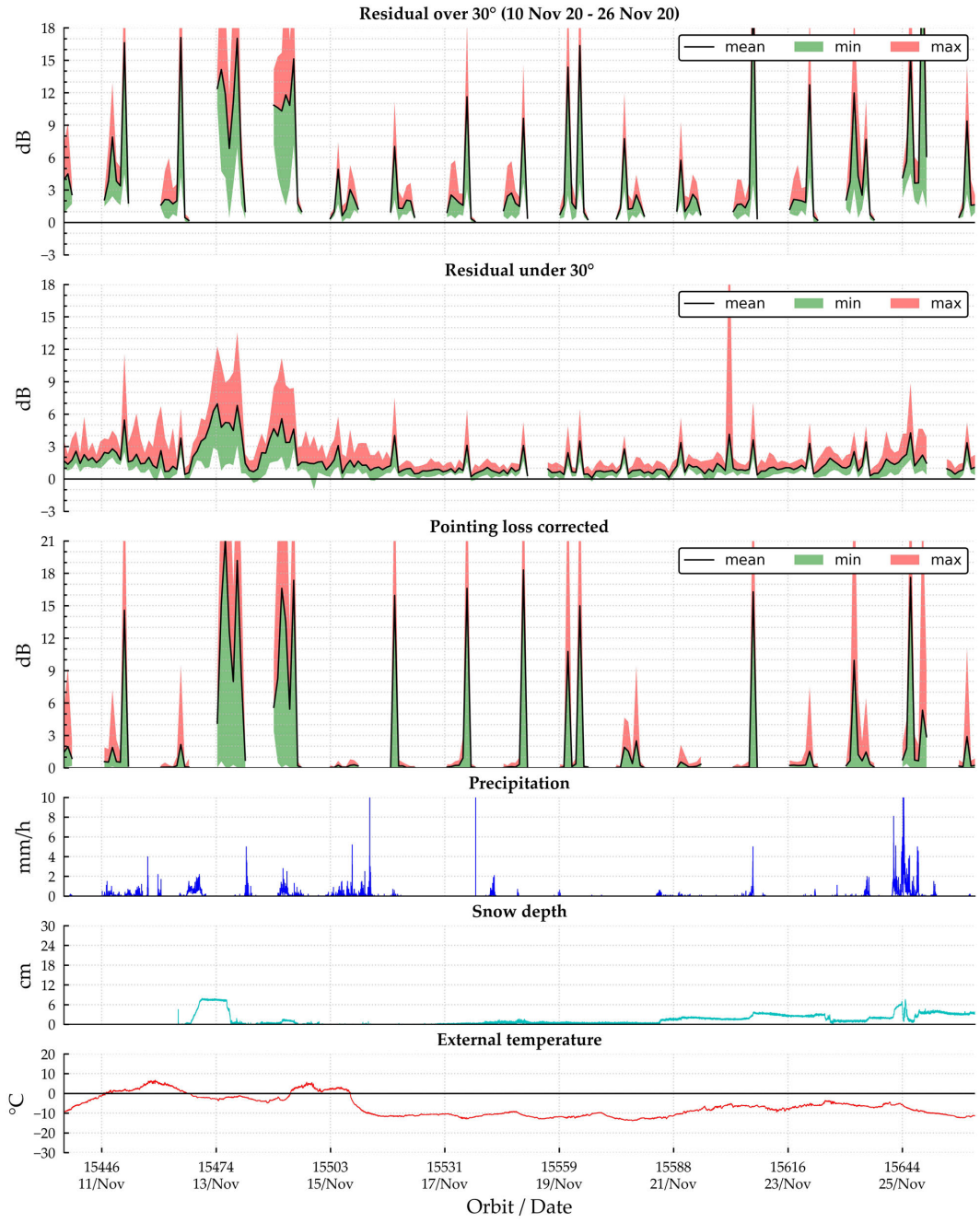

Figure A.46: Residuals and pointing loss comparison against weather effects for cycle 68

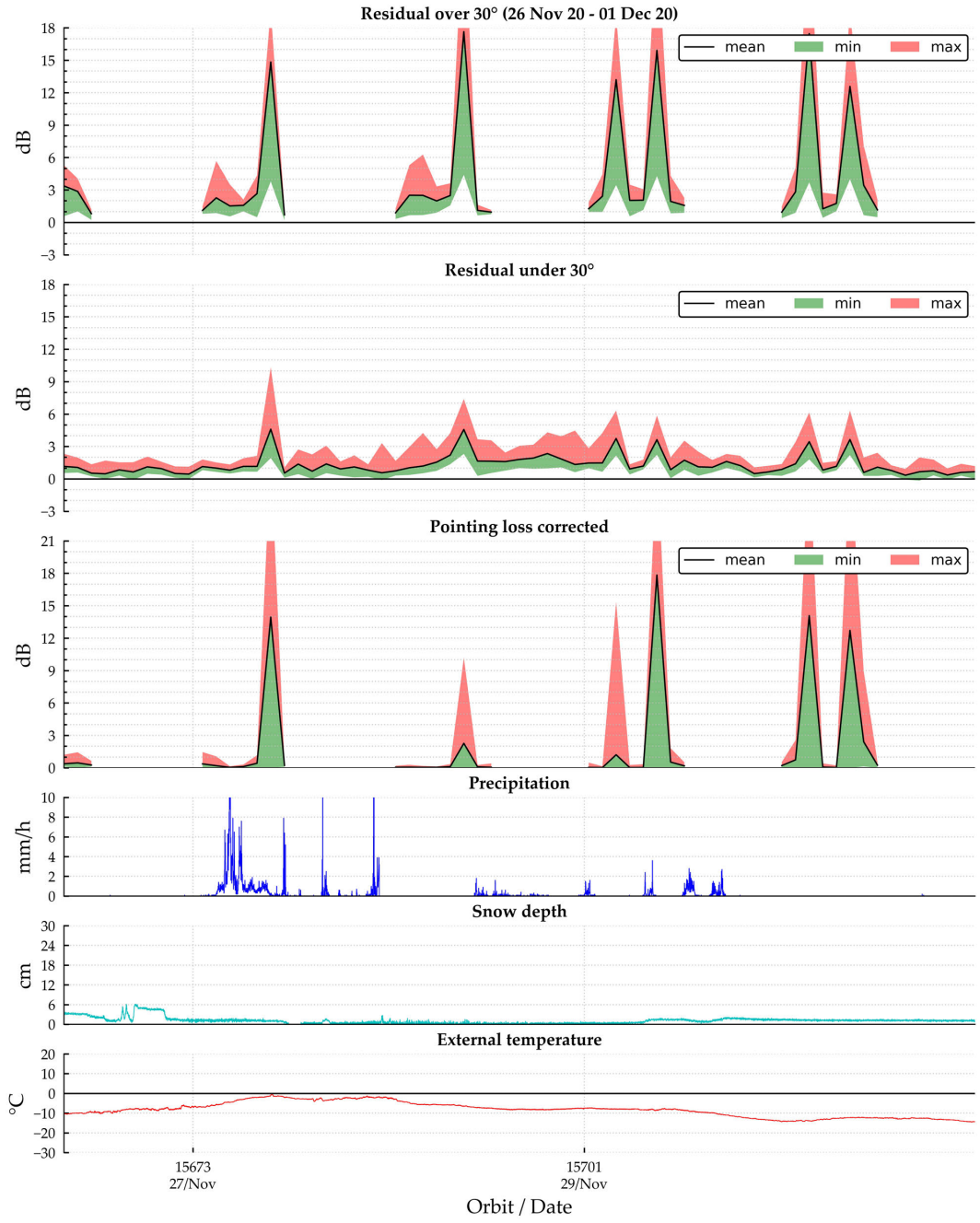

Figure A.47: Residuals and pointing loss comparison against weather effects for cycle 69

References

[1] M. Goldberg and L. Zhou, "The joint polar satellite system — Overview, instruments, proving ground and risk reduction activities," in *2017 IEEE International Geoscience and Remote Sensing Symposium (IGARSS)*, 2017, pp. 2776–2778. DOI: 10.1109/IGARSS.2017.8127573.

[2] K. Holmlund, B. Bojkov, D. Klaes, and P. Schlüssel, "The joint polar system: Towards the second generation eumetsat polar system," in *2017 IEEE International Geoscience and Remote Sensing Symposium (IGARSS)*, 2017, pp. 2779–2782. DOI: 10.1109/IGARSS.2017.8127574.

[3] D. J. Kozakoff, *Analysis of Radome-Enclosed Antennas*, 2nd ed., A. House, Ed. 2010.

[4] H.-P. Ip and Y. Rahmat-Samii, "Analysis and characterization of multilayered reflector antennas: rain/snow accumulation and deployable membrane," *IEEE Transactions on Antennas and Propagation*, vol. 46, no. 11, pp. 1593–1605, 1998. DOI: 10.1109/8.736606.

[5] B. Wang, D. Su, and J. Liu, "Analysis of snow covered radome with ray tracing method," in *2005 Asia-Pacific Microwave Conference Proceedings*, vol. 2, 2005, p. 3. DOI: 10.1109/APMC.2005.1606538.

[6] S. Nechitaylo, O. Sukharevsky, G. Khlopov, and O. Voitovich, "Method of pattern calculation for reflector antenna with surface partly covered by snow," in *2012 International Conference on Mathematical Methods in Electromagnetic Theory*, 2012, pp. 308–311. DOI: 10.1109/MMET.2012.6331252.

[7] O. I. Sukharevsky, S. V. Nechitaylo, G. I. Khlopov, and O. A. Voitovich, "Precipitations influence on reflector antenna radiation characteristics," in *2013 IX Internatioal Conference on Antenna Theory and Techniques*, 2013, pp. 447–449. DOI: 10.1109/ICATT.2013.6650807.

[8] M. Shimba, T. Sato, and H. Koike, "The antenna pattern degradation by snow accretion on the reflector surface," in *1988 IEEE AP-S. International Symposium, Antennas and Propagation*, vol. 2, 1988, pp. 871–874. DOI: 10.1109/APS.1988.94219.

[9] E. Salonen and P. Jokela, "The effects of dry snow on reflector antennas," in *1991 Seventh International Conference on Antennas and Propagation, ICAP 91 (IEE)*, vol. 1, 1991, pp. 17–20.

[10] C. Amaya, J.-M. Garcàa-Rubia, P. Bouchard, and T. Nguyen, "Experimental assessment of snow-induced attenuation on an Earth-space link operating at Ka-band," *Radio Science*, vol. 49, no. 10, pp. 933–944, 2014. DOI: 10.1002/2014RS005547.

[11] Rytir and J. Sander, "Attenuation due to snow accumulation on antenna at ka-band; effect and mitigation techniques," 25th Ka and Broadband Communications Conference, Sorrento, Italy, Sep. 30–Oct. 2, 2019.

[12] G. Maral and M. Bousquet, *Satellite Communications Systems*, 5th ed., Wiley, Ed. 2009.

[13] E. Vassallo, R. Martin, R. Madde, M. Lanucara, P. Besso, P. Droll, G. Galtie, and J. De Vicente, "The European Space Agency's Deep-Space Antennas," *Proceedings of the IEEE*, vol. 95, no. 11, pp. 2111–2131, 2007. DOI: 10.1109/JPROC.2007.905189.

[14] P. Besso, "Present and future feed systems for ESA Deep Space Antennas," in *2015 International Conference on Electromagnetics in Advanced Applications (ICEAA)*, 2015, pp. 12–15. DOI: 10.1109/ICEAA.2015.7297063.

[15] M. Bozzi, M. Cametti, M. Fornaroli, P. Maguire, S. Marti, M. Pasian, L. Perregrini, and S. Rawson, "Future Architectures for European Space Agency Deep Space Ground Stations," *IEEE Antennas and Propagation Magazine*, vol. 54, no. 1, Feb. 2012.

[16] P.-D. Arapoglou, M. Bertinelli, P. Concari, A. Ginesi, and M. Lanucara, "Benchmarking the future of RF in space missions: From low earth orbit to deep space," in *2017 IEEE MTT-S International Microwave Symposium (IMS)*, 2017, pp. 388–390. DOI: 10.1109/MWSYM.2017.8058575.

[17] A. Heske, "Advancements in ESA's future science missions," in *2014 IEEE Aerospace Conference*, 2014, pp. 1–11. DOI: 10.1109/AERO.2014.6836364.

[18] G. D. Racca, R. Laureijs, L. Stagnaro, J.-C. Salvignol, J. L. Alvarez, G. S. Criado, L. G. Venancio, A. Short, P. Strada, T. Bönke, C. Colombo, A. Calvi, E. Maiorano, O. Piersanti, S. Prezelus, P. Rosato, J. Pinel, H. Rozemeijer, V. Lesna, P. Musi, M. Sias, A. Anselmi, V. Cazaubiel, L. Vaillon, Y. Mellier, J. Amiaux, M. Berthé, M. Sauvage, R. Azzollini, M. Cropper, S. Pottinger, K. Jahnke, A. Ealet, T. Maciaszek, F. Pasian, A. Zacchei, R. Scaramella, J. Hoar, R. Kohley, R. Vavrek, A. Rudolph, and M. Schmidt, "The Euclid mission design," in *Space Telescopes and Instrumentation 2016: Optical, Infrared, and Millimeter Wave*, H. A. MacEwen, G. G. Fazio, M. Lystrup, N. Batalha, N. Siegler, and E. C. Tong, Eds., International Society for Optics and Photonics, vol. 9904, SPIE, 2016, pp. 235–257. DOI: 10.1117/12.2230762. [Online]. Available: https://doi.org/10.1117/12.2230762.

[19] F. Pasian, J. Hoar, M. Sauvage, C. Dabin, M. Poncet, and O. Mansutti, "Science ground segment for the ESA Euclid Mission," in *Software and Cyberinfrastructure for Astronomy II*, N. M. Radziwill and G. Chiozzi, Eds., International Society for Optics and Photonics, vol. 8451, SPIE, 2012, pp. 21–32. DOI: 10.1117/12.926026. [Online]. Available: https://doi.org/10.1117/12.926026.

[20] A. Martellosio, M. Pasian, L. Perregrini, L. Piffer, R. Riccardi, F. Concaro, and P. Besso, "High-Frequency Radomes for Polar Region Ground Stations, The State of the Art and Novel Developments of Radome Technologies," *IEEE Antennas and Propagation Magazine*, vol. 59, no. 6, pp. 88–101, Dec. 2017, ISSN: 1045-9243. DOI: 10.1109/MAP.2017.2752694.

[21] F. Concaro, F. A. Lopez, B. Sanadgol, A. Martellosio, M. Marchetti, M. Pasian, and A. Nylund, "The SNOWBEAR Project: a Svalbard Ground Station for Wide-band Earth Observation Data Reception," 15th International Conference on Space Operations, Marseille, France, May 28–Jun. 1, 2018.

[22] M. Marchetti, D. Lospalluto, F. Concaro, F. Romano, D. Cimini, and M. Pasian, "Performance trends at 26 GHz for a receiving ground station at polar latitudes: the SNOWBEAR project," 14th European Conference on Antennas and Propagation (EuCAP), Copenhagen, Denmark, Mar. 15–20, 2020.

[23] M. Marchetti, D. Arenare, F. Concaro, and M. Pasian, "Snow on polar radomes and performance deterioration at 26 GHz for a receiving ground station: the SNOWBEAR project," 15th European Conference on Antennas and Propagation (EuCAP), Düsseldorf, Germany, Mar. 22–26, 2021.

[24] F. Concaro, M. Marchetti, and M. Pasian, "The SNOWBEAR project: performance and statistics analysis of the 26-GHz Earth-observation receive channel for a ground station at Svalbard," 16th International Conference on Space Operations, Cape Town, South Africa, May 3–5, 2021.

[25] E. C. for Space Standardzation, *Space engineering Radio frequency and modulation*, edition, ECSS-E-ST-50-05C Rev. 2, Noordwijk, The Netherlands: ESA Requirements and Standards Division, 2011.

[26] NASA, *Joint Polar Satellite System 1 (JPSS-1) Spacecraft Stored Mission Data (SMD) to Ground Segment (GS) Radio Frequency (RF) Interface Control Document (ICD)*, Jan. 2015.

[27] "IEEE Standard Definitions of Terms for Antennas," *IEEE Std 145-1993*, pp. 1–32, Jul. 1993. DOI: 10.1109/IEEESTD.1993.119664.

[28] (2018). "ITU-R P. Recommendations," International Telecommunication Union, [Online]. Available: https://www.itu.int/rec/R-REC-P/.

[29] Recommendation ITU-R P.618-13, *Propagation data and prediction methods required for the design of Earth-space telecommunication systems*, Geneva, Dec. 2017.

[30] Recommendation ITU-R P.531-14, *Ionospheric propagation data and prediction methods required for the design of satellite networks and systems*, Geneva, Aug. 2019.

[31] Recommendation ITU-R P.676-12, *Attenuation by atmospheric gases*, Geneva, Aug. 2019.

[32] Recommendation ITU-R P.835-6, *Reference standard atmospheres*, Geneva, Dec. 2017.

[33] A. Giannini, *Analytical formulation for ground emission contribution to the overall antenna noise temperature*, ESA, Jun. 2017.

[34] (). "Kongsberg Satellite Services website," [Online]. Available: https://www.ksat.no/.

[35] (). "MT Mechatronics website," [Online]. Available: https://www.mt-mechatronics.com/.

[36] A. martellosio, "Analysis and design of protective structures for feed and reflector antennas," Doctoral thesis, University of Pavia, 2017.

[37] (). "FDS Italy s.r.l.," [Online]. Available: http://www.fdsradomes.com/home.html.

[38] (). "Noise Figure Measurement Accuracy: The Y-Factor Method," [Online]. Available: http://literature.cdn.keysight.com/litweb/pdf/%205952-3706E.pdf.

[39] (). "Ansys HFSS," [Online]. Available: https://www.ansys.com/it-it/products/electronics/ansys-hfss.

[40] M. Hallikainen, F. Ulaby, and M. Abdelrazik, "Dielectric properties of snow in the 3 to 37 GHz range," *IEEE Transactions on Antennas and Propagation*, vol. 34, no. 11, pp. 1329–1340, 1986. DOI: 10.1109/TAP.1986.1143757.

[41] (). "PROPA Library," [Online]. Available: https://logiciels.cnes.fr/fr/node/32?type=desc.

[42] W. A. Imbriale, S. (Gao, and L. Boccia, *Antennas for Deep Space Applications*. 2012, pp. 664–694. DOI: 10.1002/9781119945147.ch17.

[43] P. Noschese, "Antennas for Deep Space: Design and Technology Challenges," in *2018 IEEE International Symposium on Antennas and Propagation USNC/URSI National Radio Science Meeting*, 2018, pp. 1223–1224. DOI: 10.1109/APUSNCURSINRSM.2018.8609393.

[44] M. Bozzi, L. Perregrini, J. Weinzierl, and C. Winnewisser, "Efficient Analysis of Quasi-Optical Filters by a Hybrid MoM/BI-RME Method," *IEEE Transactions on Antennas and Propagation*, vol. AP-49, no. 7, pp. 1054–1064, Jul. 2001.

[45] M. Bozzi and L. Perregrini, "Analysis of Multilayered Printed Frequency Selective Surfaces by the MoM/BI-RME Method," *IEEE Transactions on Antennas and Propagation*, vol. AP-51, no. 10, pp. 2830–2836, Oct. 2003.

[46] P. Besso, M. Bozzi, L. Perregrini, L. SalghettiDrioli, and W. Nickerson, "Deep Space Antenna for Rosetta Mission: Design and Testing of the S/X-Band Dichroic Mirror," *IEEE Transactions on Antennas and Propagation*, vol. AP-51, no. 3, pp. 388–394, Mar. 2003.

[47] M. Pasian, M. Formaggi, M. Bozzi, F. Carli, L. Perregrini, G. Philippou, and G. Dauron, "Multiphysics Design and Experimental Verification of a Quad-Band Dichroic Mirror for Deep Space Ground Stations," *IET Microwaves, Antennas and Propagation*, vol. 7, no. 6, pp. 391–398, Apr. 2013.

[48] P. Besso, M. Bozzi, M. Formaggi, S. Germani, M. Pasian, and L. Perregrini, "A Novel Technique for the Accurate Design of Dichroic Mirrors for Focused Beam Waveguide Deep-Space Antennas," *Proceedings of the European Microwave Association*, vol. 2, no. 4, pp. 333–342, Dec. 2006.

[49] P. Besso, M. Bozzi, L. Perregrini, L. Drioli, and W. Nickerson, "Deep-space antenna for Rosetta mission: design and testing of the S/X band dichroic mirror," *IEEE Transactions on Antennas and Propagation*, vol. 51, no. 3, pp. 388–394, 2003. DOI: 10.1109/TAP.2003.808528.

[50] T. Kitsuregawa, *Satellite Communications Antennas,* A. House, Ed., p. 83.

[51] P. Besso, M. Bozzi, M. Formaggi, S. Germani, and L. Perregrini, "On the performance of dichroic mirrors with hexagonal holes," *Microwave and Optical Technology Letters*, vol. 48, no. 9, pp. 1858–1862, 2006. DOI: https://doi.org/10.1002/mop.21767.

[52] *A simple model for calculating ESA Deep Space Stations G/T performance*, Technical Note, ESA, Mar. 23, 2020.

[53] W. Veruttipong and M. M. Franco, *A technique for computation of noise temperature due to a beam waveguide shroud*, TDA progress report, JPL, Sep. 6, 2013.

Personal publications

Submitted: "On the de-pointing effects caused by snow accumulation on the radome for ground stations working at K band", IEEE Antennas and Propagation Magazine

F. Concaro, M. Marchetti, and M. Pasian, "The SNOWBEAR project: performance and statistics analysis of the 26-GHz Earth-observation receive channel for a ground station at Svalbard, " The 16th International Conference on Space Operations, May 3-5, 2021

M. Marchetti, D. Arenare, F. Concaro and M. Pasian, "Snow on Polar Radomes and Performance Deterioration at 26 GHz for a Receiving Ground Station: the SNOWBEAR Project", 15th European Conference on Antennas and Propagation (EuCAP 2021), Düsseldorf, Germany, March 22-26, 2021

D. Cimini et al., "Applicability of the Langley Method for Non-Geostationary In-Orbit Satellite Effective Isotropic Radiated Power Estimation," in IEEE Transactions on Antennas and Propagation, doi: 10.1109/TAP.2020.3048479.

M. Marchetti, D. Lospalluto, F. Concaro, F. Romano, D. Cimini and M. Pasian, "Performance trends at 26 GHz for a receiving ground station at polar latitudes: the SNOWBEAR project," 2020 14th European Conference on Antennas and Propagation (EuCAP), Copenhagen, Denmark, 2020, pp. 1-5, doi: 10.23919/EuCAP48036.2020.9135624

M. Marchetti, F. Concaro, F. Pelorossi, L. Perregrini and M. Pasian, "Upgrade to the K-band uplink channel for the ESA Deep Space Antennas: Analysis of the optics and preliminary dichroic mirror design," 2020 14th European Conference on Antennas and Propagation (EuCAP), Copenhagen, Denmark, 2020, pp. 1-5, doi: 10.23919/EuCAP48036.2020.9135708

F. Concaro, M. Marchetti, and M. Pasian, "Preliminary analysis of the performance metrics for the 26 GHz band receiving channel of the SNOWBEAR project," 8th ESA International Workshop on Tracking, Telemetry and Command Systems for Space (TTC2019), ESA-ESOC, Darmstadt, Germany, September 24-27, 2019

F. Concaro, F. Alvarez Lopez, B. Sanadgol, A. Martellosio, M. Marchetti, M. Pasian, and A. Nylund, "The SNOWBEAR Project: a Svalbard Ground Station for Wide-band Earth Observation Data Reception," The 15th International Conference on Space Operations, Marseille, France, May 28-June 1, 2018